

# Optimization of high peak power few-cycle optical parametric chirped pulse amplifier systems

PhD thesis

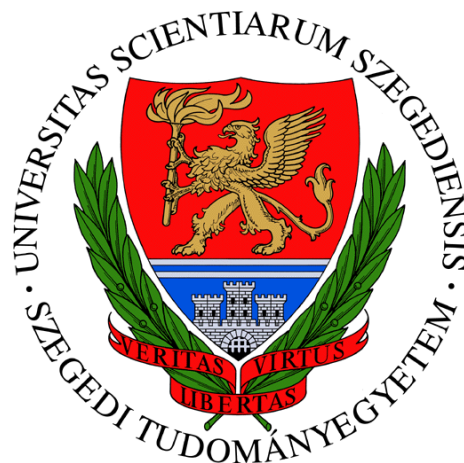
by

**Szabolcs Tóth**

Supervisor

**Dr. Károly Osvay**

*associate professor*



Doctoral School of Physics  
Department of Optics and Quantum Electronics  
Faculty of Science and Informatics  
University of Szeged  
Szeged  
2021

# Contents

<b>Abbreviations</b>	<b>4</b>
<b>1 Introduction</b>	<b>6</b>
1.1 Motivation and aim of this work	9
<b>2 Scientific background</b>	<b>10</b>
2.1 Description of pulses	10
2.1.1 Compressibility	12
2.1.2 Strehl ratio	13
2.2 Pulse propagation	15
2.2.1 Dispersion	16
2.2.2 Nonparaxial spatial phase shift	17
2.2.3 Propagation in anisotropic crystals	19
2.3 Propagation in nonlinear crystals	21
2.3.1 Second order nonlinear processes	21
2.3.2 Effective nonlinear coefficient	22
2.3.3 Coupled wave equations	24
2.3.4 Analytical solutions in case of OPA	24
Undepleted pump approximation	25
Exact analytical solution	25
2.3.5 CEP and phase in OPA	26
2.4 Phase-matching	27
Angle tuning	28
Temperature tuning	29
Quasi phase-matching	29
2.4.1 Noncollinear phase-matching	30
2.4.2 Broadband phase-matching geometry	31
2.5 Conversion efficiency of OPCPA	34
2.6 Techniques for improving OPCPA bandwidth	37
2.7 Spatiotemporal couplings (STCs) during OPA	38
2.8 Modeling of OPCPA systems	40
2.8.1 Numerical simulation of OPCPA	40
2.8.2 Numerical simulation of linear propagation	44
2.9 Overview of a few nonlinear crystals	46
2.9.1 $\beta$ -barium borate (BBO)	47
2.9.2 Deuterated potassium dihydrogen phosphate (DKDP)	50
2.9.3 Lithium triborate (LBO)	52
2.9.4 Potassium titanyl arsenate (KTA)	55

<b>3</b>	<b>Results</b>	<b>59</b>
3.1	Cascaded-extraction OPA	59
3.1.1	Modeling parameters	60
3.1.2	Improvement of conversion efficiency	62
3.1.3	Pulse properties of OPA and CE-OPA	65
3.1.4	Summary	67
3.2	Few-cycle OPCPA development	68
3.2.1	SYLOS system and the upgrade strategy	68
3.2.2	Potential broadband amplifier configurations	70
3.2.3	Numerical examination of the first OPCPA stage	72
	Double-BBO in configuration 1	73
	Double-BBO in configuration 2	75
	LBO in broadband configuration	77
	Pump recycling in a second LBO	78
3.2.4	Numerical examination of the second OPCPA stage	80
	Double-BBO in configuration 1	81
	Double-BBO in configuration 2	82
	Examination of LBO	83
	Conclusions in NOPCPA2	84
3.2.5	Numerical examination of the third OPCPA stage	85
	Double-BBO in configuration 1	86
	Double-BBO in configuration 2	87
	Examination of LBO	87
	Conclusions in NOPCPA3	88
3.2.6	Numerical examination of the fourth OPCPA stage	88
	Double-BBO in configuration 1	89
	Double-BBO in configuration 2	90
	Examination of LBO	91
	Conclusions in NOPCPA4	92
3.2.7	Influence of the idler in the second crystal	93
3.2.8	Possible final configuration	95
3.2.9	Summary	96
3.3	Comparative study	97
3.3.1	Generation of CEP-stabilized few-cycle mid-IR pulses	97
3.3.2	Description of the modelled system	97
	Nonlinear crystal parameters	99
	Dispersion of the system	100
3.3.3	OPCPA optimization	101
	Optimization of crystal thickness	101
	Chirp optimization	103
3.3.4	Investigation of peak power asymmetry	105
3.3.5	Comparison of the idler and signal schemes	109
	Energy and energy stability	109
	Spectral and temporal characteristics	110
	CEP-stability	112
3.3.6	Summary	113
<b>4</b>	<b>Summary</b>	<b>115</b>

<b>5 Magyar nyelvű összefoglaló</b>	<b>117</b>
5.1 Bevezetés	117
5.1.1 Munkám motivációja és célja	119
5.2 Tudományos előzmények	120
5.2.1 Impulzusok jellemző mennyiségei	120
5.2.2 Impulzusok terjedése	121
5.2.3 Nemlineáris folyamatok	122
5.2.4 Fázisillesztés	123
5.2.5 OPCPA rendszerek modellezése	125
5.2.6 Az impulzus alakjának torzulásai	126
5.3 Eredmények	126
<b>References</b>	<b>127</b>
<b>Own publications</b>	<b>147</b>
<b>A Undepleted pump approximation</b>	<b>154</b>
<b>B Analytical solution of TWM</b>	<b>156</b>
<b>Acknowledgements</b>	<b>160</b>

# Abbreviations

AOPDF - acousto-optic programmable dispersive filter  
ASE - amplified spontaneous emission  
BBO - beta barium borate ( $\beta - BaB_2O_4$ )  
CEP - carrier-envelope phase  
CE-OPA - cascaded extraction optical parametric amplification  
CPA - chirped pulse amplification  
CW - continuous wave  
DC - direct current  
DFG - difference frequency generation  
DKDP - deuterated potassium dihydrogen phosphate  
ELI-ALPS - Extreme Light Infrastructure Attosecond Light Pulse Source  
FFT - Fast Fourier-transform  
FL - Fourier-limit  
FOD- Fourth order dispersion  
FS - fused silica  
FTL - Fourier transform limit  
FWHM - full width at half maximum  
GB - gigabytes  
GD - group delay  
GDD - group delay dispersion  
GS - grid size  
HHG - high harmonic generation  
HR - high reflection  
IR - infrared  
KDP - potassium dihydrogen phosphate  
KTA - potassium titanyl arsenate  
LBO - lithium triborate  
LIDT - light induced damage threshold  
MIR - middle infrared  
NL - nonlinear  
NOPA - noncollinear optical parametric amplifier  
NOPCPA - noncollinear optical parametric chirped pulse amplification  
OPA - optical parametric amplification  
OPG - optical parametric generation  
OPO - optical parametric oscillation  
OPCPA - optical parametric chirped pulse amplification  
OR - optical rectification  
PFT - pulse front tilt  
PM - phase-matching

PPLN - periodically poled lithium niobate  
PSF - parametric superfluorescence  
PVWC - Poyting vector walk-off compensation  
QPA - quasi parametric amplification  
QPM - quasi phase-matching  
RMS - root mean square  
SFG - sum frequency generation  
SHG - second harmonic generation  
SPM - self phase modulation  
SR - Strehl-ratio  
STC - spatiotemporal coupling  
SWIR - short wave infrared  
SYLOS - Single Cycle Laser  
TL - transform-limit  
TOD - third order dispersion  
TPM - tangential phase-matching  
TWM - three wave mixing  
UPPE - unidirectional pulse propagation equation  
UV - ultraviolet  
YAG - yttrium aluminium garnet

# Chapter 1

## Introduction

Optics, the behavior of light as it propagates through matter, has been studied since the era of Euclid. Fundamental laws, such as rectilinear propagation, reflection, refraction, dispersion could be established simply by using the Sun as a light source. The average intensity of sunlight on the Earth's surface is roughly  $0.14 \text{ W cm}^{-2}$ , at which level materials provide linear response. Compared to this, the first operational laser, demonstrated in 1960 [1], could reach an intensity level of a few-MW  $\text{cm}^{-2}$ . Laser light, having this level of intensity, can induce nonlinear material response during propagation. Consequently, the first nonlinear phenomenon, second-harmonic generation (SHG) [2], was observed already in 1961, a year after the invention of the laser.

In lasers, light is amplified by stimulated emission of radiation as it propagates through the active medium, where the energy is stored. The possibility of energy storage is made possible by the specially allocated, real energy levels of active materials. In case of solid state lasers their lifetime is in the  $\mu\text{s}$  to  $\text{ms}$  range [3]. In contrast to this, during nonlinear processes such as second-harmonic generation, there is no real energy level involved, which is denoted by the word parametric [4]. Instead, during parametric processes the population of the medium is transferred to a virtual energy level for a very short time interval ( $\Delta t$ ), defined by the uncertainty relation  $\Delta t \Delta E \geq \hbar/2$  [4]. Therefore, the lifetime of a virtual energy state in case of visible and near-infrared photons is in the order of a few hundred attoseconds. Consequently, parametric phenomena are considered to be instantaneous on the fs to ns time scale, where such processes are studied and utilized.

The possibility of light amplification by utilizing nonlinear material response was subjected to theoretical [5] and experimental examination, right after the demonstration of SHG [2]. This technique is called optical parametric amplification (OPA) and its first successful demonstration was accomplished by Wang and Racette in 1965 [6]. During OPA, there is an instantaneous energy transfer between the pump and signal waves. The mechanism of the process is that a pump photon splits into two lower energy photons, a signal and an idler. Therefore, the number of signal photons increases while the energy difference of the pump and signal photons is taken away by the idler photon. In contrast to this, in lasers the energy difference of the pump and signal photons (in case of optical pumping) is dissipated as heat in the active medium.

After its first successful demonstration, laser development followed two directions, pulsed and continuous wave (CW) operation. Pulsed lasers could provide

higher intensity than CW lasers, thus extreme conditions in the interaction volume. Moreover, short laser pulses were indispensable tools for time-resolved spectroscopic measurements as well. Therefore, serious efforts were made to shorten the pulses and increase their energy. By the year of 1965, the techniques of Q-switching [7] and then mode-locking [8] were established, which enabled scientists to reach energetic light bursts in the range of 0.1 ns to 100 ns and to access pulse durations below 1 ps. It is interesting to note that the first OPA was already pumped by a Q-switched ruby laser, which was intense enough to provide parametric gain [6].

Within a few years, as a result of the rapid progress in laser development, the peak intensity reached a level where the refractive index of the materials became intensity dependent. The intensity dependent refractive index causes self-phase-modulation (SPM) and self-focusing in the temporal and spatial domains, and ultimately beam break-up as a consequence of these two effects [9]. All these nonlinear effects prevented the further scaling of pulse intensity for almost a decade, until the concept of chirped pulse amplification (CPA) was successfully applied to laser pulses for the first time [10]. The basic concept of chirped pulse amplification is that the ultrashort pulses are stretched to the 0.1 ns to 1 ns range before amplification. This way the pulse energy can be increased by 6 to 12 orders of magnitude without reaching the intensity limit of nonlinear effects. Amplification is followed by the re-compression of the pulse to the initial value [11]. In conventional CPA systems the amplifier medium is a laser active material. Ti:sapphire, a commonly used laser medium, has a very broad emission spectrum, thus supporting the amplification of sub-100 fs pulses. Using such system, 5.4 PW and 24 fs long pulses were demonstrated recently [12].

It was soon realized that instead of laser materials, parametric crystals can be also utilized in CPA systems. This is called optical parametric chirped pulse amplification (OPCPA). However, while the upper state lifetime of solid-state active materials is in the  $\mu\text{s}$  to ms range, OPA is an instantaneous process, and thus requires the precise temporal (and spatial) overlap of the pump and signal pulses. Therefore, precise synchronization is a prerequisite in OPCPA, while in conventional CPA the timing requirements are not that stringent. The first successful demonstration of the OPCPA concept was carried out by Dubietis et al. [13] by deriving the pump and signal pulses from the same master laser oscillator, thus ensuring passive synchronization. The technology was soon capable of delivering TW-level pulses [14]. Currently, the highest peak power achieved from a fully OPCPA based system is 4.9 PW, provided by a 18.6 fs pulse [15].

OPCPA has many beneficial properties over Ti:sapphire based CPA systems. For example, OPCPA gain bandwidth supports the amplification of sub-10 fs pulses, while gain narrowing in Ti:sapphire CPA, in the absence of special techniques [16–19], limits pulse duration to the 40 fs to 50 fs range. Parametric super-fluorescence (PSF) in case of OPCPA is confined to the temporal window of the pump pulse [20], while in Ti:sapphire the amplified spontaneous emission (ASE) is determined by the upper state lifetime of the laser material [21–23]. Consequently, if the pump and signal durations are matched, OPCPA provides better pulse contrast than Ti:sapphire CPA. Probably, the biggest advantage of OPCPA over conventional CPA is that during OPA the energy difference of pump and signal photons is taken away by the idler photon, while in laser amplification this energy difference is dissipated as heat. This allows OPCPA operation at much higher average power than conventional CPA.

On the other hand, OPCPA requires more demanding conditions than CPA. Due to the instantaneous nature of OPA, pump and signal pulses have to be precisely synchronised. Furthermore, the properties of the amplified signal are highly sensitive on the pump pulse quality [24, 25], which challenges pump technology. The ideal spatiotemporal pulse shape for pumping and seeding OPCPA is a cylinder, which is not straightforward to engineer [26–28]. Additionally to these, the pump-to-signal conversion efficiency in OPCPA is usually 10-25% [15, 29–31], while in Ti:sapphire based CPA systems, 50% can be reached with minor efforts [12, 19, 32, 33]. This is one of the main reasons why most of the PW-class systems are based on CPA and not OPCPA.

In the beginning, the spread of high peak power OPCPA systems was mainly prevented by the availability of suitable pump lasers, which provide high spatiotemporal quality pump pulses. This issue was overcome by the maturing of 1  $\mu\text{m}$  pump technology, mostly relying on Nd:YAG [28], Yb:YAG [34] and Nd:glass [35] lasers. Nowadays, the second-harmonics of these lasers can provide highly stable pump pulses with flat-top intensity distribution, which is ideal for driving OPCPA. Consequently, the number of OPCPA systems is rapidly increased in the past two decades.

One main driving force behind OPCPA development is that the technique can directly deliver pulses as short as a few oscillation cycle of the electric field, together with high peak and average power [36]. Such pulses are widely used in many scientific applications, which aim to explore ultrafast physical processes. For example, few-cycle, mJ-level pulses can be used to generate protons and ions from thin foils and accelerate them to few MeV energies [37, 38]. Recently, 1 fs, MeV electron beam was demonstrated which was driven by 3.4 fs multi-mJ pulses [39]. Such electron beams can be well used, for instance, in ultrafast imaging [40]. Sub-10 fs pulses are readily used in time-resolved spectroscopy as well [41, 42], as they can provide high temporal resolution. Beside all these applications, isolated attosecond pulse generation [43–45] is probably one of the greatest motivator of the development of high peak power, carrier-envelope-phase (CEP) stabilised few-cycle sources.

Another beneficial property of OPCPA is that the gain spectrum can be tuned over the whole transparency range of the nonlinear crystals, while in laser materials the tuning range is restricted to their emission spectrum. This is particularly useful when the goal is the generation of ultrashort pulses in the mid-IR spectral range. It was recognized that many strong field physical and spectroscopic experiments benefit from long wavelength driving fields [46], which induced a fast evolution in the territory of mid-IR OPCPA systems. By the utilization of this wavelength range the cutoff photon energy during high-harmonic-generation (HHG) can be extended to the keV range and allows the generation of the shortest as pulses [47–49]. It was proven experimentally that the intensity threshold for observing relativistic HHG was  $10^{17} \text{ W cm}^{-2}$  in case of mid-IR drivers which is lower by two orders than in case of near-IR pulses [50]. Electron acceleration to MeV energies using mid-IR pulses was also recently demonstrated [51]. The rotational and vibration transitions of many molecules are located in the mid-IR spectral range, consequently these sources have huge importance in trace gas detection, examination of biomedical samples and breath analysis [52–55].

## 1.1 Motivation and aim of this work

All the aforementioned scientific applications call for high peak and average power, ultrashort pulses in the visible, near-IR and mid-IR spectral ranges. Due to the previously described advantageous properties, OPCPA is probably the most suitable amplification technique for this, therefore OPCPA development was the main motivation of my work.

OPCPA systems can be developed based on empirical observations and simple analytical calculations, however the expenses of research and development can be reduced by first performing an extensive numerical examination. During simulations, many parameters, such as crystal thickness, seed pulse duration and beam diameter can be continuously varied without the additional cost and time required for the rearrangement of an experimental setup.

Numerical codes which consider every feature of OPCPA are very complex [56–58]. Furthermore, the computational requirements are exponentially increasing in case of large beam sizes and longer than 10 ps pulse durations. However, even with 2D models, which take into account the temporal shape of the pulse and the interaction distance  $(t, z)$  [59, 60] or those which neglect some features, for example dispersion [61], can provide useful information. The effectiveness of 4D models  $(x, y, t, z)$  during the design of OPCPA systems operating in the few picosecond temporal range, has been proven by many authors [62–65]. In addition, these numerical codes can provide an insight into the spatiotemporal shape of the amplified signal pulse, which is possible, but not straightforward to measure [66].

To model OPCPA during my work I used a 4D numerical code. It was developed by Andrianov et al. and utilizes a special algorithm for highly chirped pulses [67]. Thanks to this algorithm the computational requirements have significantly reduced, which enables the numerical simulation of OPCPA systems operating in the  $\geq 10$  ps range without approximations. This work focuses on the 4D numerical simulation of broadband OPCPAs operating in the 100 ps and 1 ns range. To the best of my knowledge, in this range no full-featured simulations have been presented in literature so far.

The aims of my work are the following:

- Examine the idea of a special OPA arrangement which could potentially increase conversion efficiency.
- Examine a broadband OPCPA configuration which can broaden the gain spectrum.
- Determine the optimal OPCPA configuration during the upgrade of the Single-Cycle Laser (SYLOS 2) laser in ELI-ALPS.
- Optimize a mid-IR OPCPA and answer a very basic, yet so far unanswered question, which is related to the position of the frequency up-conversion stage in an OPA chain.

I will present all these results in detail under the results section of this works. Before that, I will provide a scientific overview to summarize the theoretical knowledge crucial for the understanding of the numerical code and the operation of OPCPA systems.

# Chapter 2

## Scientific background

### 2.1 Description of pulses

Pulses are electromagnetic wave packets which can be considered as the superposition of monochromatic waves, according to the inverse Fourier transform defined by Eq. 2.1.

$$E(t) = \frac{1}{2\pi} \cdot \int_{-\infty}^{\infty} E(\omega) \cdot e^{-i\omega t} d\omega = \mathcal{F}^{-1}[E(\omega)] \quad (2.1)$$

The function  $E(\omega)$  is the complex spectrum of the wave packet, which can be calculated by applying the Fourier-transform, Eq. 2.2, on the electric field  $E(t)$ .

$$E(\omega) = \int_{-\infty}^{\infty} E(t) \cdot e^{i\omega t} dt = \mathcal{F}[E(t)] \quad (2.2)$$

In this definition  $E(t)$  is real function and the complex Fourier-amplitude  $E(\omega)$  is extended to negative frequencies, which does not have a physical meaning. In the numerical simulations presented in this work,  $E(\omega)$  is considered to be zero if  $\omega < 0$ , which results in the complex representation of the wave packet  $E(t)$  [68]. Therefore, from now on  $E(t)$  will define a complex function and the real field can be calculated according to  $E_{real} = 2\Re\{E(t)\}$  [68]. In both temporal and spectral domains the field amplitude and phase can be obtained by taking the absolute value and argument of the complex field according to Eq. 2.3.

$$E(\omega) = |E(\omega)| e^{i\phi(\omega)} \quad (2.3)$$

The fast oscillating electric field of a wave packet can be decomposed into an envelope function  $A(t)$  and a harmonic wave oscillating at an  $\omega_0$  carrier frequency according to Eq. 2.4.

$$E(t) = A(t) \cdot e^{-i\omega_0 t} \cdot e^{i\phi_0} \quad (2.4)$$

The choice of the carrier frequency is arbitrary but usually it is defined as the center of mass of the field spectrum according to Eq. 2.5.

$$\omega_0 = \frac{\int_{-\infty}^{\infty} \omega \cdot |E(\omega)|^2 d\omega}{\int_{-\infty}^{\infty} |E(\omega)|^2 d\omega} \quad (2.5)$$

The constant  $\phi_0$  phase offset in Eq. 2.5 is called the carrier-envelope phase (CEP), which is defined as the phase difference between the peaks of the pulse envelope and the electric field [69, 70].

The pulse intensity is proportional to the square of the field absolute value, which can be calculated by using Eqs. 2.6 and 2.7 in the temporal and spectral domains, respectively [68].

$$I(x, y, t) = 2\epsilon_0 cn |E(x, y, t)|^2 \quad (2.6)$$

$$I(x, y, \omega) = \frac{\epsilon_0 cn}{\pi} \cdot |E(x, y, \omega)|^2 \quad (2.7)$$

The pulse intensity provides information about the spatiotemporal or spatio-spectral distribution of the pulse energy. Thus the pulse energy can be calculated from the intensity by temporal (or spectral) and spatial integration according to Eq. 2.8.

$$W = \iiint I(x, y, t) dt dx dy = \iiint I(x, y, \omega) d\omega dx dy \quad (2.8)$$

Another two often used quantities are fluence ( $J[\text{J m}^{-2}]$ ) (energy density per unit area) and power ( $P[\text{W}]$ ) of the optical pulse, which can be calculated by temporal (or spectral) and spatial integration of the intensity distribution according to Eqs. 2.9 and 2.10 [68].

$$J(x, y) = \int_{-\infty}^{\infty} I(x, y, t) dt = \int_{-\infty}^{\infty} I(x, y, \omega) d\omega \quad (2.9)$$

$$P(t) = \iint I(x, y, t) dx dy \quad (2.10)$$

Similarly to the pulse power, the power spectrum (which is usually measured by a spectrometer) can be obtained by the spatial integration of the spatio-spectral intensity, as in Eq. 2.11.

$$P(\omega) = \iint_{-\infty}^{\infty} I(x, y, \omega) dx dy \quad (2.11)$$

The full width at half maximum (FWHM) of the pulse intensity (or pulse power) is a widely used quantity for the characterization of pulse duration or the spectral bandwidth. This, however, is difficult to interpret in case of a structured temporal profile or spectral shape, therefore in this work the width of an intensity distribution is often quantified by the root means square (RMS) deviation [68] defined by Eq. 2.12, where  $t$  is the time coordinate, but it could be frequency or a spatial coordinate as well.

$$\tau_{RMS} = \sqrt{\frac{\int_{-\infty}^{\infty} t^2 \cdot I(t) dt}{\int_{-\infty}^{\infty} I(t) dt} - \left( \frac{\int_{-\infty}^{\infty} t \cdot I(t) dt}{\int_{-\infty}^{\infty} I(t) dt} \right)^2} \quad (2.12)$$

If the phase of the complex field is zero ( $\phi(\omega) = 0$ ), then the pulse is Fourier- or transform-limited in the temporal domain. The FWHM of the Fourier limited pulse shape is the Fourier limited pulse duration, and in this work it is often denoted as  $\tau_{FL}$ . This is the shortest achievable pulse duration and it is directly related to the bandwidth of the pulse spectrum, through the duration-bandwidth product, defined by Eq. 2.13, where the constant  $K$  depends on the pulse shape [68].

$$\tau_{FL} \Delta\omega = 2\pi K \quad (2.13)$$

In literature, the Fourier limited pulse duration is often expressed by the number of oscillation cycles under the pulse envelope. According to the definition, a pulse duration is  $n$ -cycles if there are  $n$  oscillations during the *FWHM* duration of the pulse intensity[71]. Their relation is expressed by Eq.2.14, in which  $\lambda_0$  is the central wavelength and  $c$  is the speed of light.

$$n = \tau_{FL} \cdot \frac{c}{\lambda_0} \quad (2.14)$$

If the phase is nonzero ( $\phi(\omega) \neq 0$ ), then the pulse is chirped. In this case the pulse is longer than the Fourier limited duration and the pulse frequency continuously varies in time according to Eq. 2.15, where  $\phi(t)$  is the phase in time domain.

$$\omega(t) = \omega_0 - \frac{d\phi(t)}{dt} \quad (2.15)$$

The pulse is said to be positively or negatively chirped if  $\omega(t)$  is an increasing or decreasing function of time.

Beside the spatiotemporal  $(x, y, t)$  and spatio-spectral  $(x, y, \omega)$  domains, the electric field can also be represented in the transverse wave vector  $(k_x, k_y, t)$  or  $(k_x, k_y, \omega)$  domains. The spatial and transverse wave vector domains are related through the two-dimensional Fourier-transforms according to Eqs. 2.16 and 2.17 [72].

$$E(k_x, k_y, \omega) = \iint E(x, y, \omega) \cdot e^{-i(k_x x + k_y y)} dx dy = \Phi[E(x, y, \omega)] \quad (2.16)$$

$$E(x, y, \omega) = \frac{1}{(2\pi)^2} \iint E(k_x, k_y, \omega) \cdot e^{i(k_x x + k_y y)} dk_x dk_y = \Phi^{-1}[E(k_x, k_y, \omega)] \quad (2.17)$$

The inverse 2D Fourier-transform, Eq. 2.17, expresses the fact that an arbitrary wave can be considered as the superposition of plane waves.

In the ideal case, the 3D electric field  $E(x, y, t)$ , which describes a wave packet, can be decoupled according to the spatial and temporal coordinates. In reality this is usually not possible and the spatial and temporal coordinates are coupled. The most common spatiotemporal couplings (STC) are spatial chirp, angular dispersion and pulse front tilt. All of these are first order couplings and they can be represented in spatio-spectral  $(x, y, \omega)$ , transverse wave vector and spectral  $(k_x, k_y, \omega)$  and spatiotemporal  $(x, y, t)$  domains [73]. There are also higher order couplings which do not have specific names. In this work spatiotemporal distortions of all orders are characterized by pulse compressibility and the Strehl ratio.

### 2.1.1 Compressibility

In experimental conditions, the Fourier limited pulse duration is often calculated from the spatially integrated spectrum  $P(\omega)$ , according to Eq. 2.18, where  $P(\omega)$  is defined by Eq. 2.11. The FWHM of  $P(t)$  is denoted by  $\tau_\omega$ , where the subscript  $\omega$  denotes that the pulse duration is calculated from the integrated spectrum. This definition disregards spatiotemporal distortions.

$$P(t) = \left| \frac{1}{2\pi} \cdot \int_{-\infty}^{\infty} \sqrt{P(\omega)} \cdot e^{-i\omega t} d\omega \right|^2 \quad (2.18)$$

The proper method for calculating the Fourier limited pulse duration would be to first Fourier-transform the absolute value of the spatio-spectral field and then to calculate the Fourier limited, 3D intensity distribution  $I_{FL}$  according to Eq. 2.19.

$$I_{FL}(x, y, t) = \left| \frac{1}{2\pi} \cdot \int_{-\infty}^{\infty} |E(x, y, \omega)| \cdot e^{-i\omega t} d\omega \right|^2 \quad (2.19)$$

From  $I_{FL}$  we can extract a spatially dependent Fourier limited pulse duration  $\tau_{FL}(x, y)$ , or the pulse duration at the center of mass  $(x_c, y_c)$  of the spatial profile, which is denoted by  $\tau_{x_c, y_c}$ . Moreover, the Fourier limited pulse duration can also be calculated from the spatially integrated pulse shape  $P_{FL}$ , according to Eq. 2.10, which is denoted by the number  $\tau_{FL}$ . In the presence of STCs  $\tau_\omega$ ,  $\tau_{x_c, y_c}$  and  $\tau_{FL}$  are not equal, therefore their ratio can quantify spatio-spectral couplings of the electric field.

By taking the absolute value of the spatio-spectral field,  $E(x, y, \omega)$ , the phase distortions are neglected. In case of STCs the spatio-spectral phase ( $\phi(x, y, \omega)$ ) is not necessarily uniform across the spatial profile. Therefore, during pulse compression it is not possible to perfectly compensate the phase at every spatial position. In the best case, the spectral phase is perfectly compensated at the center of mass  $(x_c, y_c)$  of the spatial profile ( $\phi(x_c, y_c, \omega)$ ). By subtracting  $\phi(x_c, y_c, \omega)$  from the spectral phase at every other spatial position it is possible to simulate pulse compressibility in the presence of STCs, according to Eq. 2.20.

$$I_c(x, y, t) = \left| \frac{1}{2\pi} \cdot \int_{-\infty}^{\infty} E(x, y, \omega) e^{-i\phi(x_c, y_c, \omega)} \cdot e^{-i\omega t} d\omega \right|^2 \quad (2.20)$$

From the compressed pulse shape,  $I_c(x, y, t)$ , one can calculate the spatially integrated compressed pulse shape,  $P_c(t)$ , according to Eq. 2.10. The FWHM of  $P_c(t)$  is the compressed pulse duration, which is denoted by  $\tau_c$ , while the maximum value of  $P(t)$  represents the maximum achievable peak power.

In conclusion, the effect of spatiotemporal distortions on pulse duration can be quantified by the comparison of the following four quantities:

1.  $\tau_\omega$  - Fourier limited duration obtain from the spectrum
2.  $\tau_{x_c, y_c}$  - Fourier limited duration at the center of mass of the beam profile
3.  $\tau_{FL}$  - Fourier limited duration obtained from the pulse power
4.  $\tau_c$  - pulse duration in case of perfect temporal compression

## 2.1.2 Strehl ratio

The wavefront aberrations are usually characterized by the Strehl ratio (SR), which, according to the original definition, is the ratio of the central irradiances of the aberrated and unaberrated point-spread functions [74]. The Strehl ratio is an important parameter of laser pulses since it quantifies the achievable peak intensity in the focal plane of a perfect focusing element. In the original definition, SR is defined for only a single wavelength component. Consequently, if it is utilized for a broadband pulse, then a frequency dependent SR function ( $SR(\omega)$ ) can be obtained according

to Eqs. 2.21-2.23. The fields  $E_{\Phi}$  and  $E_{\Phi=0}$  correspond to the field distribution in the focal plane in case of aberrated and unaberrated phase fronts, respectively.

$$E_{\Phi}(k_x, k_y, \omega) = \iint E(x, y, \omega) \cdot e^{-i(k_x x + k_y y)} dx dy \quad (2.21)$$

$$E_{\Phi=0}(k_x, k_y, \omega) = \iint |E(x, y, \omega)| \cdot e^{-i(k_x x + k_y y)} dx dy \quad (2.22)$$

$$SR(\omega) = \frac{|E_{\Phi}(0, 0, \omega)|^2}{|E_{\Phi=0}(0, 0, \omega)|^2} \quad (2.23)$$

In OPCPA or CPA systems, the phase front of the broadband pulses is usually characterized by a wavefront sensor [75], which can provide either the averaged value of  $SR(\omega)$  or the SR of a single spectral component ( $SR(\omega_0)$ ). The latter one can be achieved by utilizing a narrow band-pass filter before the sensor. Wavefront aberrations, thus  $SR(\omega_0)$  in such a system can be reduced by using adaptive optics [36, 76] capable of correcting the spatial phase of a given frequency component  $\phi(x, y, \omega_0)$ .

During numerical simulations, instead of the previous  $SR(\omega)$  function, it would be more practical to express a SR which takes into account imperfect compressibility and quantifies the achievable peak intensity of the compressed pulses in the focal plane of a perfect focusing element. Therefore, during calculating the aberrated field distribution at the focal plane, the spectral phase at the center of mass of the spatial profile ( $\phi(x_c, y_c, \omega)$ ) has to be subtracted from the total phase, according to Eq. 2.24. Additionally, both the  $E_{\Phi}$  and  $E_{\Phi=0}$  fields are transformed into the temporal domains. This way it is possible to obtain a realistic SR (Eq. 2.26), which quantifies the achievable peak intensity in case of residual spectral phase and phase front aberrations.

$$E_{\Phi}(k_x, k_y, t) = \frac{1}{2\pi} \iiint E(x, y, \omega) e^{-i\phi(x_c, y_c, \omega)} \cdot e^{-i(k_x x + k_y y + \omega t)} dx dy d\omega \quad (2.24)$$

$$E_{\Phi=0}(k_x, k_y, t) = \frac{1}{2\pi} \iiint |E(x, y, \omega)| \cdot e^{-i(k_x x + k_y y + \omega t)} dx dy d\omega \quad (2.25)$$

$$SR = \frac{\max(|E_{\Phi}(k_x, k_y, \omega)|^2)}{\max(|E_{\Phi=0}(k_x, k_y, \omega)|^2)} \quad (2.26)$$

The SR defined by Eq 2.26 or Eq. 2.23, can be used only to quantify phase aberrations of ultrashort pulses, as it disregards pulse front distortions. In order to quantify spatiotemporal couplings, a further modification has to be incorporated during the calculation of the Strehl ratio [77, 78]. It was proposed by Giree et al. [77] that the field with spatiotemporal couplings and phase distortions ( $E_{\Phi}$ ) should be referenced to a distortion free field ( $E_{df}$ ), which is separable in all three coordinates ( $x, y, \omega$ ). Such a distortion free field can be constructed by spectrally and spatially averaging the absolute value of the distorted field, according to Eq. 2.27, where  $\mathcal{N}$  is a normalization constant [77]. The normalization constant ensures that  $E_{df}(x, y, \omega)$  and  $E(x, y, \omega)$  have the same energy.

$$E_{df}(x, y, \omega) = \mathcal{N} \int |E(x, y, \omega)| d\omega \cdot \iint |E(x, y, \omega)| dx dy \quad (2.27)$$

The far-field distribution of the distortion free field ( $E_{df}(k_x, k_y, t)$ ), can be calculated similarly to Eq. 2.25. Consequently, the influence of STCs on the achievable peak intensity in the focal plane can be quantified by the SR according to Eq. 2.28.

$$SR_{STC} = \frac{\max(|E_{\Phi}(k_x, k_y, \omega)|^2)}{\max(|E_{df}(k_x, k_y, \omega)|^2)} \quad (2.28)$$

During this work, the spatiotemporal quality of the amplified pulses was compared by using this latter method for calculating the SR.

## 2.2 Pulse propagation

The dynamics of the electromagnetic waves are governed by the Maxwell's equations [79], which relate four vector quantities: the electric and magnetic fields ( $\mathbf{E}$  and  $\mathbf{H}$ ), the electric displacement ( $\mathbf{D}$ ) and the magnetic induction ( $\mathbf{B}$ ) vectors. The material response on the applied electromagnetic field is described by another two vectors,  $\mathbf{P}$  and  $\mathbf{M}$ , which are equivalent to the density of the electric and magnetic dipole moments. The materials in this work are considered to be homogeneous, nonmagnetic and transparent dielectrics, therefore magnetic permeability is unity ( $\mu = 1$ ) and conductivity is zero ( $\sigma = 0$ ). Furthermore, the density of free charges and currents are also zero ( $\rho = 0$  and  $\mathbf{J} = 0$ ).

On the other hand, many of the materials considered during this work are anisotropic and provide considerable second order nonlinear response. In this case the displacement ( $\mathbf{D}$ ), electric field ( $\mathbf{E}$ ) and the nonlinear part of the electric polarization ( $\mathbf{P}^{NL}$ ) vectors are connected through the dielectric ( $\epsilon_{ij}$ ) and second-order susceptibility ( $\chi_{ijk}^{(2)}$ ) tensors, according to Eqs. 2.29 and 2.30 [68, 79].

$$D_i = \epsilon_0 \epsilon_{ij} E_j + P_i^{NL} \quad (2.29)$$

$$P_i^{NL} = \epsilon_0 \int \chi_{ijk}^{(2)}(\omega, \omega') E_j(\omega') E_k(\omega - \omega') d\omega' \quad (2.30)$$

Combining the Maxwell equations and the material equations (Eqs. 2.29 and 2.30) one can derive the wave equation which is valid in nonlinear anisotropic materials, Eq. 2.31 [79–81].

$$\nabla(\nabla\mathbf{E}) - \Delta\mathbf{E} - \frac{\omega^2}{c^2} \underline{\underline{\mu}} \mathbf{E} = \omega^2 \mu_0 \underline{\underline{\mu}} \mathbf{P}^{NL} \quad (2.31)$$

If anisotropy is disregarded then Eq. 2.31 simplifies to the nonlinear scalar wave equation, according to Eq. 2.32, where  $k(\omega)$  is the frequency dependent wave number defined by Eq. 2.33.

$$\Delta E + k^2 E = -\omega^2 \mu_0 \mu P^{NL} \quad (2.32)$$

$$k(\omega) = \frac{\omega}{c} n(\omega) \quad (2.33)$$

Using the 2D Fourier-transform (Eq. 2.16), the nonlinear wave equation, Eq. 2.32 can be written in the transverse wave vector domain, as it is expressed by Eq. 2.34, where  $k_z$  (Eq. 2.35) is the z-projection of the wave vector.

$$\left[ \frac{\partial^2}{\partial z^2} + k_z^2 \right] E = -\omega^2 \mu_0 \mu_r P^{NL} \quad (2.34)$$

$$k_z = \sqrt{k^2 - k_x^2 - k_y^2} \quad (2.35)$$

It can be shown that the left hand side of Eq. 2.34 describes the sum of a forward and backward propagating wave. In most cases of interest the backward propagating wave can be neglected, which results in a first order nonlinear differential equation, Eq. 2.36, called unidirectional pulse propagation equation (UPPE) [80].

$$\frac{\partial E}{\partial z} = ik_z E + i \frac{\omega^2 \mu_0 \mu_r}{2k_z} P^{NL} \quad (2.36)$$

UPPE is a nonparaxial propagation equation. The term containing  $k_z$ , on the right side of Eq. 2.36, describes the effects diffraction and dispersion. In case of linear propagation ( $P^{NL} \approx 0$ ), Eq. 2.36 has a simple analytical solution according to Eq. 2.37

$$E(k_x, k_y, \omega, z) = E(k_x, k_y, \omega, 0) \cdot e^{ik_z z} \quad (2.37)$$

Using Eq. 2.37 and the 2D Fourier-transforms, Eqs. 2.17 and 2.16 for switching between the spatial and transverse wave vector domains, linear pulse propagation can be easily simulated.

### 2.2.1 Dispersion

When pulses propagate through a medium, then different frequency components propagate with slightly different phase velocity, which results in changes in the pulse envelope. Dispersion is characterized by the phase derivatives. In order to derive these from UPPE, one must expand  $k_z$  into a Taylor series, as it is done in Eq. 2.38. This is equivalent to the usual paraxial approximation [80].

$$k_z(k_x, k_y, \omega) \approx k - \frac{k_x^2 + k_y^2}{2k} \quad (2.38)$$

Dispersion is usually studied with collimated beams, which means that diffraction can be neglected, so  $k_z \approx k$ . The phase derivatives are introduced by first expanding  $k(\omega)$  into Taylor series around the carrier frequency  $\omega_0$  according to Eq. 2.39

$$k(\omega) = k(\omega_0) + k'(\omega_0)(\omega - \omega_0) + \sum_{j=2}^{\infty} \frac{1}{j!} k^{(j)}(\omega_0)(\omega - \omega_0)^j \quad (2.39)$$

The first term  $\phi_0 = k(\omega)z$  shifts the carrier wave under the envelope. The second term is inversely proportional to the group velocity ( $v_g$ ), according to Eq. 2.40. It describes the temporal shift of the pulse envelope, therefore it is called group delay (GD).

$$GD = \phi'(\omega_0) = k'(\omega_0)z = \frac{z}{c} [n(\omega_0) + \omega_0 n'(\omega_0)] = \frac{n_g z}{c} = \frac{z}{v_g} \quad (2.40)$$

By calculating the temporal shape after  $z$  propagation using the inverse Fourier-transform (Eq. 2.1), one can show that propagation introduces a CEP offset according to Eq. 2.41 [82].

$$CEP = \phi(\omega_0) - GD \cdot \omega_0 \quad (2.41)$$

The second, third and fourth-order phase derivatives are called group delay dispersion (GDD), third-order dispersion (TOD) and fourth-order dispersion (FOD),

respectively. GDD is responsible for the temporal broadening of the pulse. TOD introduces side peaks, while FOD causes pedestals in the temporal intensity shape [82].

In numerical simulations it is practical to decompose the electric field ( $E(t, z)$ ) and nonlinear polarization ( $P^{NL}(t, z)$ ) into envelope and carrier functions, according to Eq. 2.4. Furthermore, it is advantageous to switch from the laboratory reference frame into a local frame, which co-propagates with the pulse with the same  $v_g$  group velocity. This can be achieved by introducing Eq. 2.42 into UPPE (Eq. 2.36), where  $\Omega = \omega - \omega_0$ .

$$E(\omega, z) = A(\Omega, z) e^{ik_0 z} e^{ik'_0 \Omega z} \quad (2.42)$$

This yields Eq. 2.43, which is UPPE for the field envelope in the local reference frame [80].

$$\frac{\partial A}{\partial z} = i[k_z - k_0 - k'_0 \Omega] A + i \frac{\Omega^2 \mu_0 \mu_r}{2k_z} \mathcal{P}^{NL} \quad (2.43)$$

### 2.2.2 Nonparaxial spatial phase shift

In a realistic laser system the spatial size of the pulses is often modified by a set of lenses or spherical mirrors. These focusing elements introduce spatial phase shift  $\phi(x, y, \omega)$  in the spatio-spectral domain. In case of a lens the phase shift is given by Eq. 2.44, where  $\Delta_0$  and  $\Delta(x, y)$  are the lens thickness and thickness function [72].

$$\phi(x, y, \omega) = \frac{\omega}{c} n(\omega) \Delta(x, y) + \frac{\omega}{c} [\Delta_0 - \Delta(x, y)] \quad (2.44)$$

The thickness function of a lens in the non-paraxial case can be calculated with Eq. 2.45 [72], where  $R_1$  and  $R_2$  are the radii of curvature of the front and rear surfaces.

$$\Delta(x, y) = \Delta_0 - R_1 \left( 1 - \sqrt{1 - \frac{x^2 + y^2}{R_1^2}} \right) + R_2 \left( 1 - \sqrt{1 - \frac{x^2 + y^2}{R_2^2}} \right) \quad (2.45)$$

In laser systems which deliver ultrashort and ultraintense laser pulses, the use of spherical mirrors are preferred over lenses. Spherical mirrors, on the other hand, can be used only at non-zero angles of incidence, which, in turn, introduces aberrations, especially astigmatism. Therefore, during the simulation of linear pulse propagation in realistic laser systems, the phase shift of an off-axis spherical mirror has to be taken into account instead of Eq. 2.44.

The spatial phase shift of an off-axis spherical mirror can be derived as shown in Fig. 2.1. In Fig. 2.1 (a) the green line indicates the 2D cross section of a sphere with the XZ plane in the reference frame of the incident laser pulse. The center of the sphere ( $x_0, y_0, z_0$ ) can be expressed using the radial ( $R$ ) distance, polar ( $\theta$ ) and azimuth ( $\phi$ ) angles as in Eq. 2.46. Due to the choice of the reference frame  $\phi = 180^\circ$  and  $\theta = 180^\circ - \alpha$ . The green shaded area illustrates the 2D cross section of the optical path difference across the spatial profile, which can be expressed by the  $z$ -coordinates of the sphere surface at different  $(x, y)$  spatial positions according to Eq. 2.47.

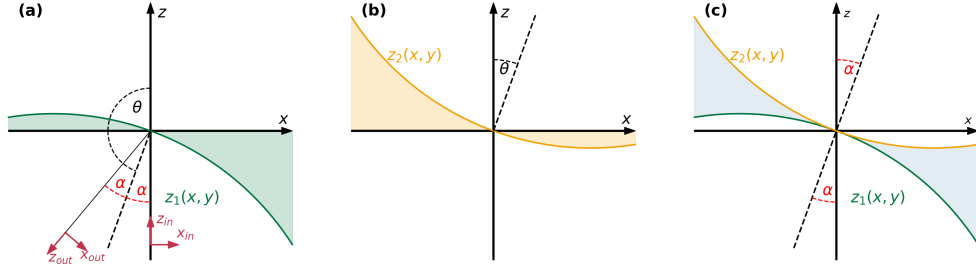


**Fig. 2.1.** Illustration of acquired optical path difference across the beam profile upon reflection on a tilted spherical mirror. Phase shift upon incidence (a), reflectance (b) and the sum of the total phase shift(c).

$$\begin{pmatrix} x_0 \\ y_0 \\ z_0 \end{pmatrix} = \begin{pmatrix} R \sin \theta \cos \phi \\ R \sin \theta \sin \phi \\ R \cos \theta \end{pmatrix} \quad (2.46)$$

$$z_1(x, y) = z_0 + \sqrt{R^2 - y^2 - (x - x_0)^2} = -R \sin \alpha + \sqrt{R^2 - y^2 - (x + R \sin \alpha)^2} \quad (2.47)$$

The directions of the  $x_{out}$  and  $z_{out}$  axes of the reflected pulse in the close vicinity of the sphere surface are illustrated by the small red coordinate system in Fig. 2.1 (a). According to this, the center of the sphere in the frame of the reflected pulse will be in the first quadrant of the XZ plane as it is already illustrated in Fig. 2.1 (b). Therefore, in this new frame  $\theta = \alpha$  and  $\phi = 0^\circ$ . The pulse as it departs from the sphere's surface given by yellow curve will also acquire a spatially dependent path length difference shown by the yellow shaded area. The spatially dependent optical path difference, similarly to the previous case, can be expressed by the  $z$ -coordinates of the sphere surface according to Eq. 2.48.

$$z_2(x, y) = z_0 - \sqrt{R^2 - y^2 - (x - x_0)^2} = R \sin \alpha - \sqrt{R^2 - y^2 - (x - R \sin \alpha)^2} \quad (2.48)$$

Based on these results, the total acquired spatial path length difference upon reflection on a concave (focusing) spherical mirror is  $z(x, y) = z_1 - z_2$ , as it is illustrated by the blue shaded area in Fig. 2.1 (c). In case of a convex (defocusing) spherical mirror, the order of  $z_1$  and  $z_2$  surfaces are interchanged, which results in the same spatial path length difference with the opposite sign. By adopting the usual sign convention for the radius of curvature in optical systems [72], namely  $R > 0$  and  $R < 0$  for convex (defocusing) and concave (focusing) spherical surfaces, the spatial path length difference in case of an off-axis spherical mirror can be written in the compact form of Eq. 2.49.

$$z(x, y) = R \cos \alpha \left[ 2 \tan \alpha - \sqrt{1 - \frac{x^2 + y^2}{R^2 \cos^2 \alpha} + \frac{2x \tan \alpha}{R \cos \alpha}} - \sqrt{1 - \frac{x^2 + y^2}{R^2 \cos^2 \alpha} - \frac{2x \tan \alpha}{R \cos \alpha}} \right] \quad (2.49)$$

This spatially dependent path length difference results in a spatial phase shift according to Eq. 2.50.

$$\phi(x, y, \omega) = \frac{\omega}{c} z(x, y) \quad (2.50)$$

The paraxial approximation of the spatial path length difference can be obtained by expanding Eq. 2.49 into a power series yielding Eq. 2.51, which, in case of  $\alpha = 0^\circ$ , equals to the paraxial approximation of the thickness function of a biconvex (or biconcave) lens [72].

$$z(x, y) \approx \frac{x^2 + y^2}{R \cos \alpha} + \frac{x^2 \tan^2 \alpha}{R \cos \alpha} \quad (2.51)$$

### 2.2.3 Propagation in anisotropic crystals

In anisotropic crystals the electric field  $\mathbf{E}$  and the displacement vectors  $\mathbf{D}$  are connected by the dielectric tensor  $\epsilon_{ij}$  according to Eq. 2.29. Therefore, these vectors are usually not parallel, and the electric field vector will have a longitudinal component. From Maxwell's equations the following statements can be derived [79, 81]:

1. The induction ( $\mathbf{B}$ ) and magnetic field ( $\mathbf{H}$ ) vectors are parallel, since the medium is considered to be magnetically isotropic. Furthermore, both fields are perpendicular to the propagation direction ( $\mathbf{k}$ ) due to  $\vec{k}\vec{B} = 0$ .
2. The displacement vector ( $\mathbf{D}$ ) is perpendicular to the propagation direction because of  $\vec{k}\vec{D} = 0$ , while in general the electric field vector ( $\mathbf{E}$ ) is no longer transversal due to Eq. 2.29.
3. The magnetic field vector ( $\mathbf{H}$ ) is perpendicular to the propagation direction ( $\mathbf{k}$ ) and the electric field ( $\mathbf{E}$ ), which follows from  $\mathbf{k} \times \mathbf{E} = \omega \mu_0 \mu_r \mathbf{H}$ .
4. The displacement vector ( $\mathbf{D}$ ) is perpendicular to  $\mathbf{k}$  and  $\mathbf{H}$  due to  $\mathbf{k} \times \mathbf{H} = -\omega \mathbf{D}$ .
5. The Poynting vector ( $\mathbf{S}$ ) (direction of energy flow) is perpendicular to  $\mathbf{E}$  and  $\mathbf{H}$ , due to  $\mathbf{S} = \mathbf{E} \times \mathbf{H}$ .
6. As a consequence of points 3, 4 and 5, the vectors ( $\mathbf{D}$ ,  $\mathbf{H}$ ,  $\mathbf{k}$ ) and ( $\mathbf{E}$ ,  $\mathbf{H}$ ,  $\mathbf{S}$ ) form an orthogonal system and the vectors ( $\mathbf{D}$ ,  $\mathbf{E}$ ,  $\mathbf{k}$ ,  $\mathbf{S}$ ) are coplanar.
7. From point 6 it follows that the direction of energy flow ( $\mathbf{S}$ ) is different from the propagation direction ( $\mathbf{k}$ ). The angles between vectors ( $\mathbf{D}$ ,  $\mathbf{E}$ ) and ( $\mathbf{k}$ ,  $\mathbf{S}$ ) are the same, and are often called as the "walk-off" angle ( $\rho$ ).

The dielectric tensor is symmetric ( $\epsilon_{ij} = \epsilon_{ji}$ ), which is the consequence of the energy conservation of electromagnetic fields [79]. Due to this property, the dielectric tensor has real eigenvalues and orthogonal eigenvectors. In the principal coordinate system, defined by the eigenvectors, the dielectric tensor is diagonal (Eq. 2.52) [79]. The diagonal elements are equal to the square of the principal refractive indices.

$$\underline{\underline{\epsilon}} = \begin{bmatrix} \epsilon_x & 0 & 0 \\ 0 & \epsilon_y & 0 \\ 0 & 0 & \epsilon_z \end{bmatrix} = \begin{bmatrix} n_x^2 & 0 & 0 \\ 0 & n_y^2 & 0 \\ 0 & 0 & n_z^2 \end{bmatrix} \quad (2.52)$$

Based on the principal refractive indices, the refractive index can be determined in every  $\mathbf{k}(\theta, \phi)$  propagation direction. In order to determine the directions of the electric field and displacement vectors of a wave propagating in an arbitrary direction, Eq. 2.31 must be written in the Fourier space (by applying  $\mathbf{F}[\partial_x f(x)] =$

$ik_x F(k_x)$  for every spatial coordinate) according to Eq. 2.53, where the nonlinear term is neglected.

$$k^2 \mathbf{E} - \mathbf{k} (\mathbf{kE}) = \omega^2 \mu_0 \mu_r \mathbf{D} \quad (2.53)$$

Using Eqs. 2.53, 2.29 and by utilizing that  $\mathbf{k} = \frac{\omega}{c} n \mathbf{m}$ , where  $\mathbf{m}$  is a unit vector which points into the propagation direction (Eq. 2.54), the components of the electric field and displacement vectors can be expressed with Eq. 2.55 [81].

$$\mathbf{m} = \begin{pmatrix} m_x \\ m_y \\ m_z \end{pmatrix} = \begin{pmatrix} \sin \theta \cos \phi \\ \sin \theta \sin \phi \\ \cos \theta \end{pmatrix} \quad (2.54)$$

$$\begin{aligned} e_x &= \frac{n^2 m_x \sin \rho}{n^2 - n_x^2} & d_x &= \frac{n_x^2 m_x \tan \rho}{n^2 - n_x^2} \\ e_y &= \frac{n^2 m_y \sin \rho}{n^2 - n_y^2} & d_y &= \frac{n_y^2 m_y \tan \rho}{n^2 - n_y^2} \\ e_z &= \frac{n^2 m_z \sin \rho}{n^2 - n_z^2} & d_z &= \frac{n_z^2 m_z \tan \rho}{n^2 - n_z^2} \end{aligned} \quad (2.55)$$

Utilizing the fact that  $\mathbf{m} \cdot \mathbf{d} = 0$ , an equation quadratic in  $n^2$  ( $An^4 - Bn^2 + C = 0$ ) can be obtained which has two roots for  $n^2$ , according to Eq. 2.56 [81].

$$\begin{aligned} n_s &= \sqrt{\frac{B + D}{2A}} \\ n_f &= \sqrt{\frac{B - D}{2A}} \\ A &= n_x^2 m_x^2 + n_y^2 m_y^2 + n_z^2 m_z^2 \\ B &= n_x^2 m_x^2 (n_y^2 + n_z^2) + n_y^2 m_y^2 (n_x^2 + n_z^2) + n_z^2 m_z^2 (n_x^2 + n_y^2) \\ C &= n_x^2 n_y^2 n_z^2 \\ D &= \sqrt{B^2 - 4AC} \end{aligned} \quad (2.56)$$

Based on this result, for a given propagation direction ( $\mathbf{m}$ ) there are two possible waves propagating with phase velocities  $v_s = \frac{c}{n_s}$  and  $v_f = \frac{c}{n_f}$ . Since  $n_s > n_f$ , therefore  $v_s < v_f$ . Consequently, they are called as "slow" and "fast" waves, which is denoted by the subscripts "s" and "f", respectively. It can be shown that the  $\mathbf{D}$  vectors of the slow and fast waves are perpendicular ( $\mathbf{D}_s \cdot \mathbf{D}_f = 0$ ) [79, 81], which comes from the fact that in the reference frame of the propagating wave ( $\mathbf{D}, \mathbf{k}, \mathbf{D} \times \mathbf{k}$ )  $\mathbf{D}_s$  and  $\mathbf{D}_f$  are the eigenvectors of the eigenvalues  $n_s$  and  $n_f$ , respectively [79]. The electric field vectors  $\mathbf{E}_s$  and  $\mathbf{E}_f$  are, in general, not orthogonal [79, 81]. Because of this and since the Poynting vectors of the slow and fast waves,  $\mathbf{S}_s$  and  $\mathbf{S}_f$ , are perpendicular to  $\mathbf{E}_s$  and  $\mathbf{E}_f$  respectively,  $\mathbf{S}_s$  and  $\mathbf{S}_f$  point into different directions. Consequently, a wave which has arbitrary polarization and propagation direction ( $\mathbf{k}$ ), will split into two waves having polarization directions  $\mathbf{E}_s$  and  $\mathbf{E}_f$  and energy flow into directions  $\mathbf{S}_s$  and  $\mathbf{S}_f$ . This is called double refraction. The walk-off angle ( $\rho$ ) between the propagation direction ( $\mathbf{k}$ ) and the Poynting vector ( $\mathbf{S}$ ) can be calculated according to Eq. 2.57, by replacing  $n$  with  $n_s$  or  $n_f$  in case of slow and fast waves, respectively [81].

$$\sin \rho = \frac{1}{n^2 \sqrt{\left(\frac{m_x}{n^2 - n_x^2}\right)^2 + \left(\frac{m_y}{n^2 - n_y^2}\right)^2 + \left(\frac{m_z}{n^2 - n_z^2}\right)^2}} \quad (2.57)$$

If the propagation direction  $\mathbf{k}$  is oriented along one of the principal axes, there is no double refraction ( $\rho = 0$ ), so both  $\mathbf{S}_s$  and  $\mathbf{S}_f$  are parallel to  $\mathbf{k}$ . In anisotropic crystals there are two special directions, called the optical axes. In the direction of the optical axes there is no double refraction and additionally the phase velocities of the slow and fast waves are equal. The optical axes are always located in the XZ principal plane due to  $n_x < n_y < n_z$  or  $n_x > n_y > n_z$  and the Z principal axis is the bisector of the angle between the two optical axes [81]. The angle ( $\Omega$ ) between the Z and one of the optical axes can be calculated according to Eq. 2.58 [81].

$$\tan \Omega = \frac{n_z}{n_x} \sqrt{\frac{n_x^2 - n_y^2}{n_y^2 - n_z^2}} \quad (2.58)$$

Crystals with two optical axes are called biaxial crystals. If two out of the three principal refractive indices are equal,  $n_x = n_y \neq n_z$ , then there is only one optical axis which coincides with the Z principal axis. These crystals are called uniaxial crystals. Both crystal types can be positive or negative. Uniaxial crystals are said to be positive or negative if  $n_z > n_x$  or  $n_z < n_x$ , respectively. In case of positive and negative biaxial crystals the angle  $2\Omega$  between the optical axes is acute or obtuse respectively [81].

During the derivation of the UPPE equation, crystal anisotropy was neglected. However, it can be shown that for the eigenwaves in anisotropic crystals UPPE is valid if we take into account that the refractive index is direction dependent, so  $n = n(k_x, k_y, \omega)$ . By expanding  $k_z$  into power series, one can show that the terms describe the walk-off effect and asymmetric diffraction [56, 65].

## 2.3 Propagation in nonlinear crystals

### 2.3.1 Second order nonlinear processes

When the amplitude of the electromagnetic waves is sufficiently high, then the response of the materials will be the nonlinear function of the electric field which is expressed by Eq. 2.30. The nonlinear polarization ( $\mathbf{P}^{NL}$ ), according to Eq. 2.31, will be the source term of new frequency components.

Second order nonlinear processes - on the femtosecond to nanosecond time scale, where they are utilized - are well described by an instantaneous nonlinear response. This means that the susceptibility tensor is independent of frequency and the nonlinear polarization will be the convolution of the fields in the spectral domain (Eq. 2.30), which reduces to a simple multiplication in the temporal domain, according to Eq. 2.59 [68].

$$P_i^{NL}(t) = \epsilon_0 \chi_{ijk}^{(2)} E_j(t) E_k(t) \quad (2.59)$$

The number of second-order nonlinear processes are introduced by considering an electric field which consists of two monochromatic components  $\mathbf{E}(t) = \mathbf{E}_1 e^{-i\omega_1 t} + \mathbf{E}_2 e^{-i\omega_2 t} + c.c.$  Inserting this into Eq. 2.59 yields Eq. 2.60, providing 5 terms which oscillate at different frequencies [4].

$$\begin{aligned}
P_i^{NL}(t) = \epsilon_0 \chi_{ijk} \{ & E_{1j} E_{1k} e^{-i2\omega_1 t} + E_{2j} E_{2k} e^{-i2\omega_2 t} + \\
& + [E_{1j} E_{2k} + E_{1k} E_{2j}] e^{-i(\omega_1 + \omega_2)t} + \\
& + [E_{1j} E_{2k}^* + E_{1k} E_{2j}^*] e^{-i(\omega_1 - \omega_2)t} + \\
& + [E_{1j} E_{1k}^* + E_{2j} E_{2k}^*] + c.c. \} \quad (2.60)
\end{aligned}$$

The first two terms in Eq. 2.60 oscillate at double frequencies ( $2\omega_1$  and  $2\omega_2$ ). These terms describe second harmonic generation (SHG). The third and fourth terms oscillate at the sum and difference of the two frequencies, therefore they describe sum and difference frequency generation (SFG and DFG), respectively. However, if  $\omega_2 = 0$ , the terms describe the Pockels effect, which is the modulation of light by a DC electric field. The last term corresponds to a DC electric field and it is known as optical rectification (OR). In case of degeneracy,  $\omega_1 = \omega_2$ , the third and fourth term will contribute to SHG and OR, respectively [4, 81].

During optical parametric amplification, two photons having frequency of  $\omega_3$  and  $\omega_2$  ( $< \omega_3$ ), enter the nonlinear medium, where they generate a new photon at their difference frequency,  $\omega_1 = \omega_3 - \omega_2$ . This newly generated photon ( $\omega_1$ ) can also interact with the highest energy photon ( $\omega_3$ ) and generate an additional photon at  $\omega_2 = \omega_3 - \omega_1$ . Therefore, the number of  $\omega_2$  photons increases, which results in the amplification of the  $\omega_2$  field. Additionally, a new wave at  $\omega_1$  frequency appears at the output, which is called the idler. If only the highest frequency field ( $\omega_3$ ) enters the medium (the amplitude of  $\omega_2$  is zero), then it is called optical parametric generation (OPG), which is the amplification of zero-point electromagnetic fluctuations [81]. OPG is the source of parametric super-fluorescence (PSF). When OPG takes place inside an optical resonator then a coherent emission can build up from the noise and this is called optical parametric oscillation (OPO).

Second-order nonlinear processes are only observable in non-centrosymmetric materials. The nonlinear susceptibility tensor ( $\chi_{ijk}^{(2)}$ ) has 27 components, but due to symmetry properties (intrinsic permutation symmetry, full permutation symmetry and Kleinman's symmetry) their number is significantly reduced [4, 81].

### 2.3.2 Effective nonlinear coefficient

In practice, instead of  $\chi_{ijk}^{(2)}$ , a simplified tensor with contracted notation  $d_{il}$  is used, which can be derived by using the above mentioned symmetry conditions. The un-contracted  $d_{ijk}$  tensor is defined by Eq. 2.61 [4, 81].

$$d_{ijk} = \frac{1}{2} \chi_{ijk}^{(2)} \quad (2.61)$$

The indices in the contracted notation and the shape of  $d_{il}$  tensor is indicated by Table 2.1 and Eq. 2.62 [4, 81].

$$d = \begin{pmatrix} d_{11} & d_{12} & d_{13} & d_{14} & d_{15} & d_{16} \\ d_{16} & d_{22} & d_{23} & d_{24} & d_{14} & d_{16} \\ d_{15} & d_{24} & d_{33} & d_{23} & d_{13} & d_{14} \end{pmatrix} \quad (2.62)$$

By using the contracted notation, the nonlinear polarization vectors during a non-degenerate ( $\omega_1 \neq \omega_2$ ) three-wave mixing process are described by Eq. 2.63,

**Table 2.1.** Indices in the contracted and un-contracted notation.

$\mathbf{jk}$	11	22	33	23	31	12
$\mathbf{l}$	1	2	3	4	5	6

where the vector  $\mathbf{u}(\omega_1, \omega_2)$  is constructed from the polarization components of the interacting waves according to Eq. 2.64 [81].

$$\begin{aligned}
P_{i,\omega_3}(t) &= 4\epsilon_0 d_{il} u_l(\omega_1, \omega_2) E_1 E_2 \\
P_{i,\omega_2}(t) &= 4\epsilon_0 d_{il} u_l(\omega_1, \omega_3) E_1^* E_3 \\
P_{i,\omega_1}(t) &= 4\epsilon_0 d_{il} u_l(\omega_2, \omega_3) E_2^* E_3
\end{aligned} \tag{2.63}$$

$$\mathbf{u}(\omega_a, \omega_b) = \begin{pmatrix} e_x(\omega_a) e_x(\omega_b) \\ e_y(\omega_a) e_y(\omega_b) \\ e_z(\omega_a) e_z(\omega_b) \\ e_y(\omega_a) e_z(\omega_b) + e_z(\omega_a) e_y(\omega_b) \\ e_z(\omega_a) e_x(\omega_b) + e_x(\omega_a) e_z(\omega_b) \\ e_x(\omega_a) e_y(\omega_b) + e_y(\omega_a) e_x(\omega_b) \end{pmatrix} \tag{2.64}$$

During the three-wave mixing interactions, which are relevant in the current work (DFG and OPA), the oscillation directions of the interacting waves are parallel to the directions of the slow and fast waves of nonlinear crystals. The vector components of the slow and fast waves, propagating in an arbitrary direction  $\mathbf{m}$  in the birefringent crystal, can be determined by using Eq. 2.55 and the corresponding refractive index  $n_s$  or  $n_f$  (Eq. 2.56).

The fact that the interacting waves are either slow or fast waves can be used to simplify the tensor relation between the nonlinear polarization and electric field vectors (Eqs. 2.63, 2.64) to simple scalar equations. This can be achieved by considering the projection of the nonlinear polarization vector on the oscillation direction of the generated field according to Eq. 2.65 [81].

$$\begin{aligned}
P_{\omega_3}^{(NL)}(t) &= \mathbf{e}(\omega_3) \cdot \mathbf{P}^{(NL)}(t) = 4\epsilon_0 [\mathbf{e}(\omega_3) \cdot \underline{\underline{d}} \cdot \mathbf{u}(\omega_1, \omega_2)] E_1(t) E_2(t) \\
P_{\omega_2}^{(NL)}(t) &= \mathbf{e}(\omega_2) \cdot \mathbf{P}^{(NL)}(t) = 4\epsilon_0 [\mathbf{e}(\omega_2) \cdot \underline{\underline{d}} \cdot \mathbf{u}(\omega_1, \omega_3)] E_1^*(t) E_3(t) \\
P_{\omega_1}^{(NL)}(t) &= \mathbf{e}(\omega_1) \cdot \mathbf{P}^{(NL)}(t) = 4\epsilon_0 [\mathbf{e}(\omega_1) \cdot \underline{\underline{d}} \cdot \mathbf{u}(\omega_2, \omega_3)] E_2^*(t) E_3(t)
\end{aligned} \tag{2.65}$$

The expressions in the square brackets in Eqs. 2.65 provide a scalar number which is the effective nonlinear coefficient ( $d_{eff}$ ). In general, the value of  $d_{eff}$  is different in each case. However, if Kleinman's symmetry condition is satisfied, the indices of the nonlinear tensor can be freely permuted and it can be shown that the effective nonlinear coefficient takes the same value in case of each nonlinear polarization in Eq. 2.65. Therefore, the effective nonlinear coefficient can be calculated with Eq. 2.66 [81].

$$d_{eff} = \mathbf{e}(\omega_3) \cdot \underline{\underline{d}} \cdot \mathbf{u}(\omega_1, \omega_2) \tag{2.66}$$

In general, each field ( $E_1, E_2$  and  $E_3$ ) can have both fast and slow polarization directions, which means that there are 8 possible polarization combinations. By using Eq. 2.66, the effective nonlinear coefficient can be calculated for each of them,

however due to phase-matching conditions, which is discussed in a later section, only three possibilities are used. These three combinations are ssf, sff and fsf, where the first, second and third letters indicate the polarization (slow or fast) of the  $\omega_1 < \omega_2 < \omega_3$  waves.

### 2.3.3 Coupled wave equations

According to the Eq. 2.65, the nonlinear polarization couples the propagation of three waves. The nonlinear propagation of each wave can be described by three coupled UPPE equations. Since UPPE is written in the Fourier space  $(k_x, k_y, \omega)$  (Eq.2.36), therefore the nonlinear polarization (Eq. 2.65), which is expressed in the spatiotemporal domain, has to be transformed into the Fourier space as well. This will result in the three coupled wave equation according to Eq. 2.67, where  $\Phi$  and  $\mathcal{F}$  denote 2D and 1D Fourier transformations, respectively.

$$\begin{aligned}\frac{\partial E_1}{\partial z} &= ik_{z1}E_1 + i\frac{2\omega_1^2 d_{eff}}{c^2 k_1} \Phi [\mathcal{F} [E_2^* E_3]] \\ \frac{\partial E_2}{\partial z} &= ik_{z2}E_2 + i\frac{2\omega_2^2 d_{eff}}{c^2 k_2} \Phi [\mathcal{F} [E_1^* E_3]] \\ \frac{\partial E_3}{\partial z} &= ik_{z3}E_3 + i\frac{2\omega_3^2 d_{eff}}{c^2 k_3} \Phi [\mathcal{F} [E_1 E_2]]\end{aligned}\tag{2.67}$$

If two waves with amplitudes  $E_1$  and  $E_2$  enter into the nonlinear medium, then all the processes described by Eq. 2.60 (SHG, SFG, DFG, OR) can take place, however their efficiency will be significantly different. The efficiency of an arbitrary three-wave mixing (TWM) process after a propagation length  $L$  is greatly influenced by the phase difference of the three propagating waves, which is determined by the  $z$  projection of the wave vector ( $k_z$ ). If the waves generated at different  $z$  coordinates are out of phase, they cannot add up coherently, thus spoil efficiency.

According to Eq. 2.38, in case of negligible diffraction  $k_z \approx k$ . This way the phase-mismatch, which is a vector quantity, is defined by Eq. 2.68.

$$\vec{\Delta k} = \vec{k}_3 - \vec{k}_2 - \vec{k}_1\tag{2.68}$$

### 2.3.4 Analytical solutions in case of OPA

The coupled differential equations, Eqs. 2.67, can be simplified by assuming monochromatic plane waves and by disregarding dispersion, diffraction and walk-off. This yields Eqs. 2.69, where  $A_j$  is the complex field amplitude of a monochromatic component [5, 81].

$$\begin{aligned}\frac{\partial A_1}{\partial z} &= i\frac{2\omega_1^2 d_{eff}}{c^2 k_1} A_2^* A_3 e^{i\Delta k z} \\ \frac{\partial A_2}{\partial z} &= i\frac{2\omega_2^2 d_{eff}}{c^2 k_2} A_1^* A_3 e^{i\Delta k z} \\ \frac{\partial A_3}{\partial z} &= i\frac{2\omega_3^2 d_{eff}}{c^2 k_3} A_1 A_2 e^{-i\Delta k z}\end{aligned}\tag{2.69}$$

### Undepleted pump approximation

In the undepleted pump approximation the amplitude of the pump wave is considered to be constant ( $A_3(z) = A_3(0)$ ) during interaction. This provides a simple solution for the intensity and phase of the idler and signal pulses, which can be utilized during phase-matching optimization and are often used throughout this work. The detailed derivation of the equations is presented in Appendix A.

The intensity gain for the idler ( $G_i$ ) and signal ( $G_s$ ) pulses is expressed by Eqs. 2.70 and 2.71, where  $\lambda_1$  and  $\lambda_2$  are the idler and signal wavelengths,  $z$  is the crystal length,  $I_{20}$  is the intensity of the signal pulse at  $z = 0$ . The constants  $K$  and  $g$  can be calculated according to Eqs. 2.72, where  $I_p$  is the pump intensity.

$$G_i = \frac{I_1(z)}{I_{20}} = \frac{\lambda_2}{\lambda_1} (G_s - 1) \quad (2.70)$$

$$G_s = \frac{I_2(z)}{I_{20}} = 1 + \frac{K^2}{g^2} \sinh^2 gz \quad (2.71)$$

$$K^2 = \frac{8\pi^2 d_{eff}^2 I_p}{\epsilon_0 c n_1 n_2 n_3 \lambda_1 \lambda_2} \quad g = \sqrt{K^2 - \frac{\Delta k^2}{4}} \quad (2.72)$$

The phase evolution can be simply obtained by extracting the argument of Eqs. A.9 and A.10, which yields Eqs. 2.73 and 2.74, describing the phase of the idler and signal waves, respectively [83].

$$\phi_1(z) = \frac{\pi}{2} + \phi_{30} - \phi_{20} - \frac{\Delta kz}{2} \quad (2.73)$$

$$\phi_2(z) = \phi_{20} - \frac{\Delta kz}{2} + \arctan\left(\frac{\Delta k}{2g} \tanh gz\right) \quad (2.74)$$

According to Eq. 2.1, a wave packet can be considered as the superposition of monochromatic waves. Therefore, by applying Eqs. 2.70 and 2.71 for each monochromatic component of a broadband pulse, a frequency dependent gain distribution can be obtained. These are called spectral gain curves [84, 85]. The spectral gain curves are particularly useful for gain bandwidth optimization during the development of broadband OPCPA systems.

### Exact analytical solution

The simplified TWM equations, Eq. 2.69, can be solved analytically when pump depletion is also considered. The solution can be expressed by the Jacobian elliptic functions [81]. The detailed derivation can be found in Appendix B, here I only present the brief results.

The solution in case of OPA or DFG for the field intensities are shown by Eq. 2.75, where  $L$  is the crystal thickness,  $v_1$ ,  $v_2$  and  $v_3$  are proportional to the absolute value of the field amplitude as it can be seen in Eq. B.1. The constants  $s_a$  and  $s_b$  can be calculated from the initial conditions, according to Eq. B.16. Finally, the term  $y(L)$  is expressed by the Jacobian elliptic functions according to Eq. B.18.

$$\begin{aligned}
v_3(L)^2 &= (s_b - s_a) y(L)^2 + s_a \\
v_2(L)^2 &= v_2(0)^2 + v_3(0)^2 - (s_b - s_a) y(L)^2 - s_a \\
v_1(L)^2 &= v_1(0)^2 + v_3(0)^2 - (s_b - s_a) y(L)^2 - s_a
\end{aligned} \tag{2.75}$$

Due to the Jacobian elliptic functions, the solution for the field intensities is periodic in propagation distance  $z$ . Periodicity is determined by the initial pump and signal intensities and the phase-mismatch. According to the solutions, beginning from  $z = 0$  the intensity of the signal and idler waves increase until they reach a maximum value at a certain  $z = L_{opt}$  crystal thickness. At this thickness, pump intensity decreases to zero and the pump is said to be depleted. In case of further propagation, the process reverses and turns into sum-frequency generation (SFG). This means that the idler and signal waves recombine into a pump wave, so the intensity of the signal and idler wave decreases, while the pump intensity grows. This is called re-conversion. In case of non-zero phase mismatch, the efficiency of the process decreases and the spatial periods of the field intensities will be much shorter than in case of perfect phase-matching.

The solutions for the phase are indicated by. Eqs 2.76 and 2.77, where  $\phi_j(0)$  is the initial phase of the waves and  $\Delta k$  is the phase-mismatch.

$$\phi_1(L) = \frac{\pi}{2} + \phi_3(0) - \phi_2(0) + \frac{\Delta k L}{2} \tag{2.76}$$

$$\phi_{2,3}(L) = \phi_{2,3}(0) + \frac{\Delta k L}{2} \int_0^1 \frac{v_3^2(0) - v_3^2(\xi)}{v_{2,3}^2(\xi)} d\xi \tag{2.77}$$

Equations 2.77 and 2.76 are of great importance for the operation of all OPA systems. According to Eq. 2.77, the phase of the signal wave does not depend on the phase of the pump wave. This means that phase front aberrations or the temporal chirp of the pump wave do not transfer into the signal wave. On the other hand, in case of non-zero phase-mismatch, the signal phase depends on the pump and signal intensities [83]. Due to this, in order to ensure a flat signal wavefront, the spatial intensity profile of the pump and signal waves has to be uniform.

According to Eq. 2.76, in case of phase-matched DFG ( $\Delta k = 0$ ) the phase of the idler depends on the initial phase difference of the pump and signal waves. This property of DFG is exploited during passive carrier-envelope-phase (CEP) stabilization [69, 86].

### 2.3.5 CEP and phase in OPA

The CEP of the ultrashort pulses can be decoupled into two terms according to Eq. 2.78, where  $\phi_0$  is a static phase offset and  $\Delta\phi$  represents the pulse-to-pulse phase fluctuations [87].

$$CEP = \phi_0 + \Delta\phi \tag{2.78}$$

If the pump and signal pulses have the same pulse-to-pulse fluctuations ( $\Delta\phi$ ), then, according to Eq. 2.76, the phase of the difference frequency (idler pulse) in case of perfect phase-matching will be constant, as it is indicated by Eq. 2.79, where  $\phi_{op}$

and  $\phi_{0s}$  are the static phase offset of the pump and signal waves [69]. This way at a given interaction plane the phase of the idler wave will be constant.

$$CEP = \phi_1 = \frac{\pi}{2} + \phi_{0p} + \Delta\phi - \phi_{0s} - \Delta\phi = \frac{\pi}{2} + \phi_{0p} - \phi_{0s} \quad (2.79)$$

A well-established way to provide pump and signal pulses with the same phase slippage ( $\Delta\phi$ ) is to derive the signal pulse from the pump wave. This can be done by splitting a small fraction of the available pump energy for self-phase modulation (SPM) in bulk material. SPM is a phase preserving, third-order ( $\chi^{(3)}$ ) nonlinear effect, during which new spectral components are generated. This results in the large scale extension of the pump spectrum. Thereafter, the signal spectrum can be chosen by the spectral filtering of the broadened pump wave [69, 86]. This allows for the generation of a pump and signal wave with the same phase slippage ( $\Delta\phi$ ), therefore they can be mixed in a nonlinear crystal to produce passively CEP stabilized idler pulses.

Passive CEP stabilization is an essential technique for the production of energetic, CEP-stabilized ultrashort pulses and it is widely used in present-day state-of-the-art optical parametric chirped pulse amplifier (OPCPA) systems [36, 88]. A commonly used scenario in these systems is that the phase stabilized idler pulse is further amplified in OPCPA, followed by the pulse compression to achieve the shortest possible pulse duration and highest peak power [88, 89]. For efficient pulse compression it is essential to know the spectral phase (chirp) of the CEP stable idler pulse and how to manipulate it. According to Eq. 2.1, the electric field of a broadband pulse can be written as a superposition of monochromatic waves. Therefore, Eq. 2.76, which describes the phase relation of the monochromatic pump, signal and idler waves can be applied for each frequency component of the broadband signal and idler pulses. Therefore, Eq. 2.76 is frequency dependent as it is indicated in Eq. 2.80 in case of perfect phase-matching ( $\Delta k = 0$ ).

$$\phi_i(\Omega_i) = \frac{\pi}{2} + \phi_p(\Omega_p) - \phi_s(\Omega_s) \quad (2.80)$$

According to Eq. 2.80, the initial spectral phase (chirp) of the signal and pump pulses determines the chirp of the idler pulse.

In most cases of interest the bandwidth of the pump is many times narrower than the bandwidth of the signal and idler pulses, therefore  $\phi(\Omega_p) \approx \phi_{p0}$ . By taking the  $n$ -th derivative of Eq. 2.80 and utilizing the fact that  $\frac{d\phi_s}{d\Omega_i} = -\frac{d\phi_s}{d\Omega_s}$ , one can obtain Eq. 2.81, which describes the relation between the higher order phase derivatives of the signal and idler pulses.

$$\frac{d^{(n)}\phi_1}{d\Omega_1^{(n)}} = (-1)^{n+1} \frac{d^{(n)}\phi_2}{d\Omega_2^{(n)}} \quad (2.81)$$

According to Eq. 2.81, the odd (GD, TOD, etc.) and even (GDD, FOD, etc.) order phase derivatives have the same and opposite signs, respectively. This is very crucial during the temporal compression of the CEP stabilized idler pulses.

## 2.4 Phase-matching

In the simplest geometrical case, the three interacting waves in a  $\chi^{(2)}$  material propagate collinearly. In order to achieve efficient frequency conversion, the phase

mismatch ( $\Delta k$ ) has to be zero, which results in Eq. 2.82.

$$k_3 = k_1 + k_2 \quad (2.82)$$

Using the dispersion relation (Eq. 2.33), the phase-matching condition can be written as in Eq. 2.83.

$$\frac{\omega_3}{c}n(\omega_3) = \frac{\omega_2}{c}n(\omega_2) + \frac{\omega_1}{c}n(\omega_1) \quad (2.83)$$

Due to the law of energy conservation,  $\omega_3 = \omega_2 + \omega_1$  must hold, thus, the phase-matching condition will be defined by Eq. 2.84 [4].

$$\omega_1 [n(\omega_1) - n(\omega_3)] = \omega_2 [n(\omega_3) - n(\omega_2)] \quad (2.84)$$

In case of normal dispersion, the refractive index is the increasing function of the frequency. Due to this, the left hand side of Eq. 2.84 is negative, while the right hand side is positive. Thus the phase-matching condition cannot be satisfied in the region of normal dispersion [4].

The phase-matching condition (Eq. 2.84) can be satisfied only if the refractive indices are ordered as  $n(\omega_1) < n(\omega_3) < n(\omega_2)$  or  $n(\omega_1) > n(\omega_3) > n(\omega_2)$ . This can be achieved by using those nonlinear crystals which are anisotropic as well. In birefringent crystals, as it was discussed in Section 2.2.3, a wave propagating in a general direction can experience two different refractive indices,  $n_f < n_s$ , depending on the polarization direction. Therefore, by choosing "fast" or "slow" polarization direction for the input wave, the refractive index can be either  $n_f$  or  $n_s$ . In order to provide phase-matching (Eq. 2.84), the highest frequency wave ( $\omega_3$ ) must have "fast" polarization direction. There are three polarization combinations for the two low frequency waves, which are "slow-slow" (ss), "fast-slow" (fs) and "slow-fast" (sf). Therefore, phase-matching is called Type I if the polarization directions of  $\omega_1$  and  $\omega_2$  fields are parallel, and it is denoted by "ssf", where the first, second and third letters indicate the polarization of the  $\omega_1 < \omega_2 < \omega_3$  waves. Phase-matching is called Type II if the polarization directions of the two low frequency waves are different. Consequently, during Type II phase-matching the three interacting waves are either sff or fsf [4, 81, 84].

There are two methods for the precise controlling of the refractive indices. One is called angle tuning and the other is temperature tuning.

### Angle tuning

During angle tuning, the crystal's orientation is changed with respect to the beam's propagation direction [4]. This can be easily illustrated on the example of Type I SHG in the YZ principal plane of a biaxial crystal. In the YZ principal plane of an arbitrary biaxial crystal, where the principal refractive indices are ordered as  $n_z < n_y < n_x$ , the formulas for calculating the fast and slow refractive indices (Eq. 2.56) are simplified to Eqs. 2.85 [81].

$$n_f^2(\theta) = \frac{n_z^2 n_y^2}{n_y^2 \sin^2 \theta + n_z^2 \cos^2 \theta} \quad n_s^2 = n_x^2 \quad (2.85)$$

In case of Type I phase-matching, the second harmonic ( $2\omega$ ) wave is a fast wave, while the fundamental wave ( $\omega$ ) is slow. In this case the collinear phase-matching condition (Eq. 2.84) reduces to Eq. 2.86.

$$n_f(2\omega) = n_s(\omega) \quad (2.86)$$

The introduction of Eqs. 2.85 into the phase-matching condition for SHG yields an equation (Eq. 2.87) for calculating the phase-matching angle  $\theta$  in the YZ plane.

$$\cos^2(\theta) = \frac{n_y^2(2\omega) [n_z^2(2\omega) - n_x^2(\omega)]}{n_x^2(\omega) [n_z^2(2\omega) - n_y^2(2\omega)]} \quad (2.87)$$

From Eqs. 2.55 and Eqs. 2.85 one can deduce that the direction of the electric field and displacement vectors of the slow wave are parallel, therefore the walk-off angle of the fundamental wave is zero [81]. The walk-off angle of the fast wave is non-zero and it can be calculated according to Eq. 2.57 or with its simplified form in Eq. 2.88 [81].

$$\tan \rho = \frac{(n_y^2 - n_z^2) \tan \theta}{n_z^2 + n_y^2 \tan^2 \theta} \quad (2.88)$$

The typical value of the walk-off angle is a few degrees, but it can cause the spatial separation of fundamental and second harmonic beams. This can lead to a spatially asymmetric second harmonic beam profile and decreased conversion efficiency.

### Temperature tuning

The refractive index is, in general, temperature dependent, thus the phase-matching condition (Eq. 2.84) can be satisfied by the temperature tuning of birefringent crystals. One advantage of temperature tuning over angle tuning is that the previously described beam walk-off effect can be prevented [4]. This can be achieved by propagating the interacting beams along one of the principal axes (X, Y, Z) of biaxial crystals or along the X or Y axes of uniaxial crystals. If the beam propagates along the Z axis of a biaxial crystal, where the refractive indices are ordered as  $n_z < n_y < n_x$ , the refractive indices of the fast and slow waves are  $n_y$  and  $n_x$ , respectively. In this case, according to Eqs. 2.55, the electric field and displacement vectors are parallel in case of both slow and fast waves, therefore the walk-off angle is zero for both the fundamental and SH beams. The phase-matching condition is described by Eq. 2.89, where  $T$  indicates the temperature dependence of the principal refractive indices. At certain  $T$  temperature, the refractive index of the fundamental and SH frequencies will be the same and SHG will be phase-matched.

$$n_y(2\omega, T) = n_x(\omega, T) \quad (2.89)$$

### Quasi phase-matching

There are highly nonlinear materials - for example gallium-arsenide (GaAs) [90], which has a very high nonlinear coefficient -, however they are isotropic, and therefore birefringent phase-matching is not possible. In other crystals, such as lithium niobate [91], the highest nonlinear coefficient in the nonlinear tensor ( $d_{33}$ ) is not accessible through birefringent phase-matching [4]. All these motivated the invention and development of the quasi-phase-matching (QPM) technique, which allows efficient frequency conversion in the absence of birefringent phase-matching.

In case of non-zero phase-mismatch, efficiency reaches its maximum at the coherence length defined by Eq. 2.90 [4].

$$L_c = \frac{\pi}{\Delta k} \quad (2.90)$$

Due to the periodicity the TWM processes, in the following  $L_c$  propagation distance the intensity of the wave will decrease until  $z = 2L_c$ . However, by changing the sign of the nonlinear coefficient after every  $L_c$  propagation distance, intensity can grow monotonically [4]. A possible method for the production of QPM gratings is to invert the orientation of ferroelectric domains using static electric field, which is called periodic poling (PP) [4, 92].

### 2.4.1 Noncollinear phase-matching

In real experimental situations it is common that the interacting beams propagate noncollinearly. In some cases, the usage of noncollinear interaction geometry is more advantageous than simple collinear phase-matching. For example, noncollinear propagation can compensate for the walk-off angle during frequency mixing, which can improve the beam profile after interaction. In case of the second harmonic generation of high power beams or the optical parametric amplification of high peak power pulses, the separation of the residual fundamental beam or the residual pump beam from the signal in collinear propagation is challenging as the intensity can exceed the light induced damage threshold (LIDT) of dichroic or polarization beam splitters. The usage of noncollinear geometry, however, enables the spatial separation of high peak and average power beams. Spatial separation is also useful for example in second or third order cross correlation measurements for the background free detection of measurement signals. Probably, the most useful feature of noncollinear phase-matching is that it can provide zero phase-mismatch over a very broad frequency range, which is essential in the production of energetic few cycle pulses [83].

In noncollinear geometry the phase-matching condition (Eq. 2.82) will be a vector equation according to Eq. 2.91, where the subscripts p, s and i denote pump, signal and idler waves.

$$\vec{k}_p = \vec{k}_s + \vec{k}_i \quad (2.91)$$

The noncollinear angle ( $\alpha$ ) is defined as the angle between the pump and signal pulses, as it is illustrated in Fig. 2.2.

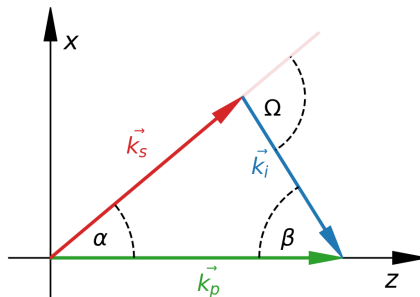


**Fig. 2.2.** Angle definitions in noncollinear phase-matching geometry.

The value of the noncollinear angle ( $\alpha$ ) needed to satisfy the phase-matching condition can be calculated by using the law of cosines, according to Eq. 2.92 [84].

$$\cos \alpha = \frac{k_p^2 + k_s^2 - k_i^2}{2k_p k_s} \quad (2.92)$$

The angle between the pump and idler waves, denoted by  $\beta$  in Fig. 2.2, depends on the angle  $\alpha$  and can be calculated by using one the equations in Eq. 2.93, which can be deduced from Fig. 2.2 by geometrical considerations.

$$\sin \beta = -\frac{k_s}{k_i} \sin \alpha \quad \cos \beta = \frac{k_p - k_s \cos \alpha}{k_i} \quad (2.93)$$

The angle between the signal and idler waves,  $\Omega$  in Fig. 2.2 can be expressed by using the law of cosines which yields Eq. 2.94.

$$\cos \Omega = \frac{k_p \cos \alpha - k_s}{k_i} \quad (2.94)$$

According to Eqs. 2.92, 2.93 and 2.94, the determination of noncollinear geometry requires the knowledge of the wave vectors. The wave vectors can be calculated with Eq. 2.33, by using the corresponding slow or fast refractive index values, depending on the interaction type (ssf, sff, fsf), as it is done in Eqs. 2.95 for a general case. In these equations  $\vec{m}_i, \vec{m}_s, \vec{m}_p$  are unit vectors pointing in the direction determined by the polar and azimuth angles.

$$\begin{aligned} \vec{k}_i(\omega_i) &= \frac{\omega_i}{c} n_{f,s}(\omega_i, \theta_i, \phi_i) \vec{m}_i(\theta_i, \phi_i) \\ \vec{k}_s(\omega_s) &= \frac{\omega_s}{c} n_{s,f}(\omega_s, \theta_s, \phi_s) \vec{m}_s(\theta_s, \phi_s) \\ \vec{k}_p(\omega_p) &= \frac{\omega_p}{c} n_f(\omega_p, \theta_p, \phi_p) \vec{m}_p(\theta_p, \phi_p) \end{aligned} \quad (2.95)$$

According to Eq. 2.95, the magnitudes of the wave vectors depend on the propagation direction, however, in order to determine the noncollinear propagation directions, one needs to determine the magnitudes of the wave vectors. Therefore, in a general case, this problem can be solved by numerical iterative algorithms [93].

If the interaction takes place in uniaxial crystals or in the principal planes of biaxial crystals the solution of the above problem greatly simplifies. For example, in case of Type I interaction in negative uniaxial crystals only the pump wave vector depends on the propagation direction, according to Eqs. 2.96.

$$\begin{aligned} k_i(\omega_i) &= \frac{\omega_i}{c} n_o(\omega_i) \\ k_s(\omega_s) &= \frac{\omega_s}{c} n_o(\omega_s) \\ k_p(\omega_p, \theta) &= \frac{\omega_p}{c} n(\omega_p, \theta) \end{aligned} \quad (2.96)$$

In this simple case, for fixed pump, signal and idler frequencies, there is a direct relation between the noncollinear and phase-matching angles ( $\alpha(\theta)$ ).

## 2.4.2 Broadband phase-matching geometry

In the previous sections it was shown how to achieve phase-matching for three monochromatic waves, but the spectral dependence of a given arrangement was

not examined. During the frequency mixing of broadband pulses it is important to provide efficient conversion for a broad frequency range and not just at the carrier wavelengths.

The central frequencies are related through energy conservation, according to Eq. 2.97.

$$\omega_{0p} = \omega_{0s} + \omega_{0i} \quad (2.97)$$

In most cases, especially during OPA, the pump has a much narrower bandwidth than the signal and idler pulses, therefore it can be considered to be monochromatic. Energy conservation must hold for other  $\omega_{0s} + d\omega_s$  and  $\omega_{0i} + d\omega_i$  frequency pairs in the signal and idler spectra which interact with the same pump frequency  $\omega_{0p}$ , according to Eq. 2.98.

$$\omega_{0p} = \omega_{0s} + d\omega_s + \omega_{0i} + d\omega_i \quad (2.98)$$

By comparing Eqs. 2.97 and 2.98, one can find Eq. 2.99, which means that a  $d\omega_s$  shift of the signal frequency results in the same shift of the idler frequency in the opposite direction. Moreover, this also implies that the bandwidth of the signal and idler pulses should be equal in the absence of absorption.

$$d\omega_s = -d\omega_i \quad (2.99)$$

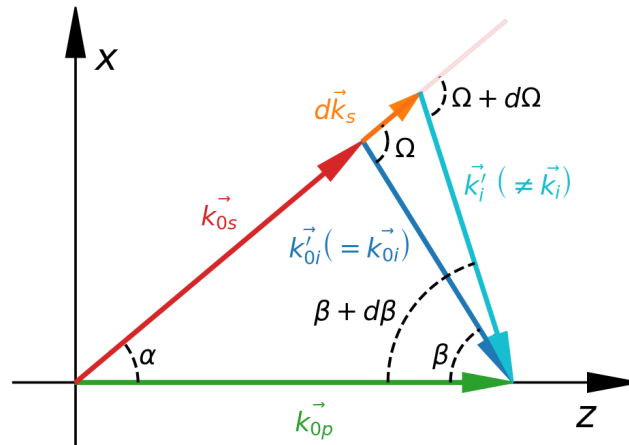


**Fig. 2.3.** Noncollinear phase-matching in case of a broadband signal pulse.

The noncollinear geometry in case of a monochromatic pump and broadband signal and idler pulses is illustrated in Fig. 2.3. An  $\omega_{0s} + d\omega_s$  frequency component of the signal pulse will provide a wave vector which has  $k_{0s} + dk_s$  magnitude. By using the law of cosines, for a given noncollinear angle  $\alpha$ , it is possible to calculate a hypothetical idler wave vector  $k'_i$ , which would provide zero phase-mismatch, and represents the shortest distance between the endpoints of the pump and signal wave vectors. According to Fig. 2.3, different frequency components of the broadband signal pulse will provide different hypothetical wave vectors  $k'_i$ . In case of the central

frequencies, the magnitude of  $k'_{0i}$  is equal to the real magnitude of the idler wave vector  $k_{0i}$ , which can be obtained from the dispersion relation in Eq. 2.96. However, for general signal and idler frequency pairs the magnitude of  $k'_i$  and  $k_i$  is not necessarily equal. This results in a phase-mismatch which is defined as the difference of the real ( $k_i$ ) and hypothetical ( $k'_i$ ) idler wave vectors, according to Eq. 2.100 [94].

$$\Delta k = k_i - \sqrt{k_p^2 + k_s^2 - 2k_p k_s \cos \alpha} \quad (2.100)$$

The real  $k_i$  vector has to be parallel to the hypothetical  $k'_i$  vector, because this configuration provides the minimal phase-mismatch ( $\Delta k$ ), which assures the most efficient generation of the idler frequency components. Consequently, OPA of broadband signal pulses in noncollinear geometry results in the generation of a broadband idler pulse which has angular dispersion.

The angular dispersion of the idler can be calculated by using Eq. 2.93 or Eq. 2.94 with the hypothetical idler wave vector  $k'_i$ , according to Eqs. 2.101.

$$\begin{aligned} \sin \beta(\omega_i) &= -\frac{k_s \sin \alpha}{\sqrt{k_p^2 + k_s^2 - 2k_p k_s \cos \alpha}} \\ \cos \beta(\omega_i) &= \frac{k_p - k_s \cos \alpha}{\sqrt{k_p^2 + k_s^2 - 2k_p k_s \cos \alpha}} \\ \cos \Omega(\omega_i) &= \frac{k_p \cos \alpha - k_s}{\sqrt{k_p^2 + k_s^2 - 2k_p k_s \cos \alpha}} \end{aligned} \quad (2.101)$$

The bandwidth of the frequency conversion process is determined by the phase-mismatch parameter  $\Delta k$ . The phase-mismatch where the gain decreases to half of the maximum value can be obtained from Eq. A.16 by assuming a large gain ( $KL \gg 1$ ). This leads to Eq. 2.102, where the constant  $K$  is determined by Eq. A.3 and  $L$  is the crystal thickness [95].

$$\Delta k_{\frac{1}{2}} \approx 2\sqrt{\ln 2} \sqrt{\frac{K}{L}} \quad (2.102)$$

The phase-matching bandwidth in terms of frequency can be obtained by expanding  $\Delta k$  into a power series around the central frequency  $\omega_{0s}$ .

$$\Delta k(\omega_s) = \Delta k(\omega_{0s}) + \left. \frac{d\Delta k}{d\omega_s} \right|_{\omega_{0s}} \Delta\omega_s + \frac{1}{2} \left. \frac{d^2\Delta k}{d\omega_s^2} \right|_{\omega_{0s}} \Delta\omega_s^2 + \dots \quad (2.103)$$

term zero (Eq. 2.104) is the phase-mismatch at the central frequencies, which, according to the previous paragraphs, is equal to zero.

$$\Delta k(\omega_{0s}) = k_i(\omega_{0i}) - \sqrt{k_p^2 + k_s^2(\omega_{0s}) - 2k_p k_s(\omega_{0s}) \cos \alpha} = 0 \quad (2.104)$$

Therefore, the phase-matching bandwidth is mainly influenced by the first term in the Taylor series of  $\Delta k$ . The first derivative of the phase-mismatch can be derived by differentiating Eq. 2.100 according to  $\omega_s$  and utilizing that  $d\omega_s = -d\omega_i$ , which yields Eq. 2.105, where the last term accounts for the angular dispersion of the signal pulse.

$$\begin{aligned} \frac{d\Delta k}{d\omega_s} &= -\frac{dk_i}{d\omega_i} + \frac{k_p \cos \alpha - k_s}{\sqrt{k_p^2 + k_s^2 - 2k_p k_s \cos \alpha}} \frac{dk_s}{d\omega_s} - \frac{k_p k_s \sin \alpha}{\sqrt{k_p^2 + k_s^2 - 2k_p k_s \cos \alpha}} \frac{d\alpha}{d\omega_s} = \\ &= -\frac{dk_i}{d\omega_i} + \cos \Omega \frac{dk_s}{d\omega_s} - k_s \sin \Omega \frac{d\alpha}{d\omega_s} \end{aligned} \quad (2.105)$$

The phase-matching bandwidth can be increased by zeroing the first derivative of the phase-mismatch at the central frequency of the signal pulse ( $d_{\omega_s} \Delta k(\omega_{0s}) = 0$ ). This leads to Eq. 2.106 which is the condition of broadband phase-matching [83, 95, 96].

$$\left. \frac{\cos \Omega}{v_{gs}} - \frac{1}{v_{gi}} - k_{0s} \sin \Omega_0 \frac{d\alpha}{d\omega_s} \right|_{\omega_{0s}} = 0 \quad (2.106)$$

Eq. 2.106 offers three possibilities for achieving broadband phase-matching. The first option is to use collinear propagation ( $\Omega = 0$ ) at wavelength degeneracy ( $\omega_{0s} = \omega_{0i}$ ) in which case  $v_{gi} = v_{gs}$ , therefore the phase-mismatch is zeroed up to the second order [95, 97].

During the second option, noncollinear geometry is utilized, without signal angular dispersion ( $d_{\omega_s} \alpha = 0$ ). This leads to Eq. 2.107, which is called group-velocity matching [83].

$$v_{gs} = v_{gi} \cos \Omega \quad (2.107)$$

During group velocity matching, according to Eq. 2.107, the projection of the idler's group-velocity on the signal propagation direction has to be equal with the signal's group velocity [83].

The third option is to introduce angular dispersion into the signal pulse, which, according to Eq. 2.106, compensates for the group-velocity mismatch of the signal and idler pulses [96].

Using one of the above mentioned techniques to cancel the first order phase-mismatch term, the phase-matching bandwidth will be determined by the second and higher order terms. These can be derived by differentiating Eq. 2.105 according to  $\omega_s$ . By neglecting the angular dispersion, this yields Eq. 2.108, which formulates the condition for achieving ultrabroadband phase-matching [95].

$$\left. \frac{d^2 \Delta k}{d\omega_s^2} \right|_{\omega_{0s}} = \left. \frac{d^2 k_i}{d\omega_i^2} \right|_{\omega_{0i}} + \cos \Omega_0 \left. \frac{d^2 k_s}{d\omega_s^2} \right|_{\omega_{0s}} - \frac{\sin^2 \Omega_0}{k_{i0} v_{gs}^2} = 0 \quad (2.108)$$

In general, for a given nonlinear crystal it is possible to zero the phase-mismatch terms up to the fourth order [95]. However, this will add another criterion for the central wavelength of the interacting pulses, which is not always achievable in experimental conditions.

## 2.5 Conversion efficiency of OPCPA

The typical pump-to-signal conversion efficiency in Ti:sapphire based CPA systems is 40-50% [12, 19, 32, 33], while in OPCPAs it is 20-25% [15, 29–31]. The theoretically achievable pump-to-signal conversion efficiency in both laser and parametric amplification equals the quantum efficiency. The quantum efficiency ( $\eta_q$ ) is defined as the ratio of the pump ( $\lambda_p$ ) and signal ( $\lambda_s$ ) central wavelengths:

$$\eta_q = \frac{\lambda_p}{\lambda_s} \quad (2.109)$$

In the above-mentioned PW class systems the central wavelengths of the pump and signal pulses are 527 nm and 800 nm, respectively, which according to 2.109, corresponds to a quantum efficiency of 65.9%. The remaining pump energy heats the active material or in case of parametric amplifiers it is converted into idler wave. Deviation from the theoretical efficiency in Ti:sapphire is caused by the improper absorption of the pump energy, while in OPCPAs the situation is more complex. The most detrimental parameter is the phase-mismatch of the three interacting waves, which is usually minimized over a broad wavelength range, by group velocity matching [83]. The second influencing factor is the crystal thickness as the intensity gain during parametric amplification is periodic in the propagation distance. Consequently, there is an optimal crystal length where conversion efficiency and the energy stability are maximal. The optimal crystal thickness is determined by the phase-mismatch and by the peak intensity of the pump and signal pulses. Therefore, in case of non-uniform spatial and temporal intensity distribution (for example Gaussian distribution) the optimal crystal thickness will be different at different spatial and temporal coordinates. As a consequence, the pump pulse cannot be fully depleted, which results in low conversion efficiency. The typical pump-to-signal conversion efficiency in OPCPAs where the pump has a spatiotemporally Gaussian shape is 15% [98, 99].

A further issue with pump pulses having a Gaussian temporal shape is that they limit the achievable amplified signal bandwidth by gain narrowing. In case of chirped pulses, the spectrum is mapped into the temporal domain, which means that in time the short and long wavelength components are located at the leading or trailing edge of the pulse. If the pump is Gaussian in time, these spectral components overlap with the low intensity parts of the pump pulse. Consequently, the gain at the spectral edges is lower than at the center of the spectrum, which means that the bandwidth after amplification is narrower and the compressed pulse duration is longer than before OPA. In order to moderate this effect, the signal has to be stretched to a small fraction of the pump pulse duration [100]. However, this will reduce the temporal overlap of the two pulses, which will result in reduced conversion efficiency. So there is a trade-off between the amplified pulse energy and bandwidth. The optimal seed pulse duration is determined by the application of the laser pulse itself and in most cases the signal stretching factor is optimized to produce pulses with the highest peak power.

Improving the conversion efficiency of OPA has been subjected to many theoretical and experimental investigations and several techniques have been developed which address various aspects of the process.

The most widely used method relies on spatiotemporal pump pulse shaping [26–28, 101–105]. The ideal pump shape for OPCPA has a spatiotemporally flat-top intensity distribution as it provides equal gain at every spatial and temporal coordinate, and such pump pulse could be depleted almost uniformly. Consequently, the pump energy extraction is higher than in case of a spatiotemporally Gaussian pump pulse. For example, pump-to-signal conversion efficiency as high as 40% was demonstrated in an OPCPA system which was driven by spatiotemporally shaped pump pulses[106].

Depletion of an arbitrarily shaped pump can be enhanced by using conformal profiles for the interacting waves [107, 108]. During this method the spatiotemporally shaped signal has a complementary shape of the pump pulse, which results

in equalized signal gain and pump depletion at every spatial and temporal coordinate. For example, the complementary shape for a flat-top pump is a flat-top seed. Similarly, the complementary seed shape for a spatially and temporally Gaussian pump is a signal which has a "U" and "doughnut" shape in time and space, respectively. Beside the shaping techniques referenced in the previous paragraph, the seed pulse can be shaped by an OPCPA stage operated in the deep back-conversion regime. The resulting amplified signal pulse will have the complementary shape of a Gaussian pump. Hence, in the following stage conversion efficiency will increase and additionally, gain narrowing will reduce [83, 109].

**Table 2.2.** Efficiencies of different techniques.  $\eta_{dpl}$  - level of pump depletion,  $\tau$  - compressed signal duration

Ref.	$\eta_{dpl}$ (%)	$\tau$ (fs)	Technique
Ma et al.[110]	70	100	QPA
Li et al.[111]	70	100	Special QPM
Begishev et al.[108]	67	-	Complementary seed
Matousek et al.[109]	64.5	21	Complementary seed
Guardalben et al.[106]	61	$10^3 - 10^5$	Pump shaping
Elu et al.[89]	54.4	97	Pump-recycling
Fattahi et al.[62]	49.5	9.5	Pump-recycling
Deng et al.[62, 112]	49.5	9.5	Controlled energy dep.
Schultze et al.[113]	36.4	5.7	Pump-recycling
Wnuk et al.[114]	22.5	23	Time-shear

During pump-recycling, conversion efficiency is increased by reusing the residual pump energy after the first crystal in a second one [62, 89, 113, 115]. Usually, this method is used when the pump shape is Gaussian both temporally and spatially. During the technique, the first crystal is operated under conditions that provide the highest efficiency and stability. At this point, a small, but considerable portion of the pump wave is reconverted from the signal and idler at the center of the pulse. So a small central lobe is formed which is surrounded by the remains of the original pump. The two regions are separated by a small depleted region. The goal during recycling is to reuse the central lobe only as it has a smoother envelope than the whole pump. Since the intensity of this part is lower than it was prior amplification, the residual pump has to be focused to a smaller diameter in the second crystal. Additionally, the signal's beam size has to be matched to that of the pump lobe.

Time-shear amplification is a particularly useful scheme if the pump pulse duration is in the few nanoseconds range, while the stretched seed pulse is at least three-times shorter than the pump [114]. During this scheme, the seed pulse overlaps with different temporal sections of the pump in subsequent nonlinear crystals. Each crystal is operated under conditions to provide the highest pump depletion, so in the end most of the pump energy is converted into signal and idler.

An opposite approach controls energy deposition from a few-picosecond pump into a few-times longer stretched signal pulse [62, 112]. In this method the pump overlaps with different temporal sections of the long signal in subsequent crystals. This way the spectral shape can be controlled by the gain of the individual crystals and high pump depletion can be achieved.

Pump re-conversion, which decreases conversion efficiency, could be prevented by

extracting the idler wave from the crystal during interaction thus preventing back-conversion. Quasi-parametric-amplification (QPA) utilizes this idea by doping the nonlinear material with ions which are absorbing at the idler wavelength range [110, 116]. Using this technique a 47% pump-to-signal conversion efficiency was achieved, thus approaching Ti:Sapphire based amplifiers. The drawback of this scheme is that the biggest advantage of OPCPA, namely the low heat load, is lost due to idler absorption. Consequently, this method can be used at low repetition rates only.

The idea of idler separation is used in a specially designed QPM crystal where the idler wave strays away from the pump and signal pulses during interaction [111]. The numerical simulation of this scheme predicts a 70% pump depletion, which corresponds to a 47% pump-to-signal conversion efficiency.

Quantum efficiency (Eq.(2.109)), and hence pump-to-signal conversion efficiency, depend on the carrier frequency of the interacting pulses. This complicates the comparison of the above-mentioned OPCPA systems operating at different central wavelengths. However, the pump energy extraction efficiency or pump depletion level ( $\eta_{dpl}$ ) is wavelength independent. The pump depletion level and its relation to the pump-to-signal conversion efficiency is described by equation (2.110), where  $E_{rp}$  and  $E_{p0}$  are the residual and initial pump energy,  $\eta_{p-s}$  is the pump-to-signal conversion efficiency,  $\lambda_p$  and  $\lambda_s$  are the central wavelengths of the pump and signal pulses.

$$\eta_{dpl} = \left(1 - \frac{E_{rp}}{E_{p0}}\right) \approx \eta_{p-s} \cdot \frac{\lambda_s}{\lambda_p} \quad (2.110)$$

In order to compare the above-mentioned techniques, the pump depletion level was calculated in case of each work, by using Eq. 2.110. All of the above-mentioned techniques and the achievable pump depletion levels are summarized in Table 2.2.

## 2.6 Techniques for improving OPCPA bandwidth

The gain bandwidth of OPA is mainly determined by the phase-matching properties of the nonlinear crystals. It was already discussed in Section 2.4.2 that by matching the group velocities of the signal and idler pulses, phase-mismatch can be minimized over a very broad wavelength range enabling the amplification of 10 fs pulses. This condition is naturally satisfied at wavelength degeneracy [95, 97, 117], but it can be easily realized in noncollinear phase-matching geometry as well. Noncollinear phase-matching is utilized in every state-of-the-art few-cycle OPCPA systems [36, 98, 99, 118–120].

Another less commonly used method to minimize the phase-mismatch over a broad wavelength range is to introduce angular dispersion into the signal pulse before OPA [96, 121–124]. Using this method, the amplification of a sub-2 cycle bandwidth was demonstrated in the sub-mJ energy range [121, 124].

Group velocity matching or the introduction of signal angular dispersion compensates for the phase-mismatch up to the second order in the Taylor expansion of  $\Delta k(\omega)$ . Further gain bandwidth extension requires the minimization of the quadratic and higher order phase-mismatch terms. This can be achieved by the proper choice of the pumping wavelength. It was demonstrated by Adachi et al. [118] that BBO pumped by 450 nm pulses can amplify over a bandwidth corresponding to 5.5 fs. The pump source in their work was the second harmonic of a Ti:sapphire laser in which the central wavelength was tuned from 800 nm to 900 nm. There is an

ideal pumping wavelength for every nonlinear crystal, however in practice usually this is a fixed parameter.

Broadband pump pulses with carefully optimized temporal chirp also offers a possibility to increase the gain bandwidth in OPA [97, 117].

The usage of short nonlinear crystals for OPA allows to reach broader gain bandwidth due to the  $L^{-\frac{1}{2}}$  relation between the phase-matching bandwidth and crystal thickness [95]. Since the efficiency of the process depends on the crystal thickness, the usage of short crystals requires increased pump intensity to compensate for the energy drop. Above 10 ps pump pulse duration the safe intensity level for nonlinear crystals is typically below  $10 \text{ GW cm}^{-2}$ , while in case of few-ps pulses, produced by thin-disk pump technology, crystals accept much higher pump intensities [119]. Consequently, NOPCPA systems driven by 0.5 ps to 2 ps pump pulses can reach  $< 7$  fs pulse duration [98, 99, 115, 119], while in case of pump pulses with a duration of few tens of picoseconds 7.5 fs is the lower limit [36, 125, 126]. On the other hand, systems driven by short ps pump pulses have to be operated in vacuum [98], otherwise nonlinear effects in air will limit the usable pump energy, and consequently the output signal pulse energy [99].

It is possible to use multiple pump beams to pump a single nonlinear crystal and each beam amplifies a slightly different part of the signal spectrum. This is called multibeam pumping [127–130], and it has been demonstrated both theoretically and experimentally that it can significantly increase the OPA bandwidth [131–135]. When this technique is applied, energy losses caused by parametric diffraction [136–138] have to be taken into account.

In multistage OPCPA systems, instead of pumping a single crystal with multiple beams it is also possible to utilize a slightly different phase-matching geometry in subsequent stages, thus amplifying slightly different spectral bands. The demonstration of this technique provided an amplified bandwidth corresponding to 4.3 fs in the Fourier limit [119].

In case of two-color pumping [131, 135], the subsequent OPCPA stages are pumped by different pump wavelengths. During the realization of this technique the subsequent stages were pumped by the second and third harmonics of a Nd:YAG laser. This way 75 mJ sub-5 fs compressed pulses were generated [120].

During Fourier-Domain Optical Parametric Amplification (FOPA) [139], the spectrum of a broadband signal pulse is spatially dispersed using a grating and a spherical mirror. In the focal plane of the spherical mirror (Fourier plane) the different spectral bands are amplified in different crystals. Using this method, 1.43 mJ two-cycle pulses were demonstrated.

In field synthesizers [119, 140, 141] broadband seed pulses are separated by dichroic beamsplitters into multiple individual OPCPA channels. Each channel is pumped at a different wavelength and amplifies a dedicated spectral band. After amplification, the channels are recombined and as a result, sub-cycle fields can be synthesized. Using this concept sub-mJ level 0.6-cycle pulses were demonstrated [141].

## 2.7 Spatiotemporal couplings (STCs) during OPA

It was pointed out in Section 2.3.4, during the analytical solution of the TWM equations, that all three-wave mixing processes are periodic in the propagation distance. The periodicity of the process is governed by the  $\theta$  function in Eq. B.4,

which is influenced by the amplitudes of the interacting waves. During OPA, when the amplitude of the pump wave decreases to zero (pump is depleted), then the direction of the energy flow reverses ( $\sin \theta > 0$ ). This means that in case of further propagation, the signal and idler photons recombine into pump photons. This is called back-conversion. The propagation distance where back-conversion starts depends on the initial intensity of the pump and signal waves. Therefore, in case of spatiotemporal Gaussian pump and signal pulses, the pump periphery (where the intensity is low) will be depleted in a longer propagation distance. Due to the uneven pump intensity depletion, the central portions of the pulses enter the back-conversion regime as soon as the highest conversion efficiency is reached. It is known that intensity back-conversion deteriorates the spatiotemporal quality of the amplified signal pulses, which is even more pronounced in case of high gain amplifiers [77, 142]. On the other hand, the highest energy stability is reached when the amplifier stage is operated beyond the point of the highest conversion efficiency which is in the back-conversion regime [106]. Since high intensity gain enhances spatiotemporal distortions, it is advantageous to decrease the gain by splitting the available pump energy into multiple amplification stages. This way it is possible to simultaneously obtain high conversion efficiency and good spatiotemporal quality [77, 106, 142].

Another factor which has an impact on the spatial shape is the walk-off effect, which arises due to the crystal's anisotropy [77]. For example, in case of the *fsf* phase-matching type in KTA crystals, the signal pulse demonstrates extraordinary behavior. Therefore, during collinear propagation it walks off from the pump and idler pulses, resulting in an elongated beam profile along the direction of the walk-off plane due to gain guiding [142]. This effect is even more pronounced in case of high gain and if the beam size is small compared to the crystal thickness.

A set of first order spatiotemporal couplings (STCs)[73, 143, 144] are introduced during amplification in noncollinear OPA (NOPA). In general, noncollinear phase-matching geometry induces pulse front tilt (PFT) in the spatiotemporal domain of the signal pulse, because the pulse fronts of the pump and signal pulses are not parallel during amplification [145, 146]. PFT, when considered in the spectral domain, can be caused by angular dispersion or by the combination of temporal chirp and spatial dispersion [143, 144]. If the signal pulse is transform-limited during amplification, then PFT is equivalent to angular dispersion [145, 146]. However, if the signal pulse is highly chirped, then the different spectral components overlap with the tilted pump pulse at different spatial locations, which causes spatial chirp. In this case PFT is mainly caused by temporal chirp and spatial dispersion [146]. PFT can be eliminated from the signal if the beam diameter and physical length of the pump pulse are matched during amplification[146]. Above 1 ps pump pulse duration, both spatial and angular dispersion vanishes [146], so OPCPA systems driven by long, 10 ps to 100 ps pulses are free from PFT [145]. In case of NOPAs which operate in the 100 fs to 1000 fs range (fs-NOPA), in order to avoid PFT, either the physical length and beam diameter of the pump must be matched or the pulse front of the pump must be tilted [98, 145, 147].

It was pointed out in the previous paragraph that in case of fs-NOPAs the beam diameters must be matched to the physical length of the pump pulses to avoid PFT. For example, a 200 fs pulse duration corresponds to a physical length of  $\approx 50 \mu\text{m}$  inside the nonlinear crystal. A Gaussian beam with FWHM diameter of  $50 \mu\text{m}$  corresponds to an angular spread of  $\pm 0.5^\circ$ . Since the intensity gain is

angular dependent, during amplification the spatial and optical frequencies ( $k_x, \omega$ ) will be coupled. In spite of the fact that the physical dimensions of the pump are matched, this coupling will result in angular dispersion, consequently PFT [78]. It was shown experimentally that this kind of spatiotemporal distortion is eliminated at the noncollinear angle which corresponds to the broadest gain bandwidth [78].

Based on the effects described so far one can conclude that OPA, if not implemented properly, can introduce several spatiotemporal distortions [77]. Therefore, during numerical optimization it is crucial to check the spatiotemporal quality of the amplified pulses. Throughout this work, the spatiotemporal quality of the amplified pulses is characterized by the compressibility and the Strehl ratio.

## 2.8 Modeling of OPCPA systems

In general, an optical parametric chirped pulse amplification (OPCPA) system consists of five main parts:

1. Front-end, which produces low-energy, broadband seed pulses;
2. Pump laser, which is synchronized to the front and provides pump pulses for the OPCPA stages;
3. Pulse stretcher;
4. Multiple OPCPA stages;
5. Pulse compressor;

During pulse stretching and compression, the spectral phase of the signal pulse is manipulated by introducing a path difference between different spectral components. This process can be well described by 1D linear propagation models and the spectral phase derivatives introduced in Section 2.2.1 [148, 149]. Therefore, during this work, the simulation of pulse stretching and compression was carried out by applying the spectral phase shift introduced by dispersive elements.

The numerical simulation of the OPCPA stages can be divided into two parts, i.e. the numerical simulation of the OPA process in birefringent nonlinear crystals and the simulation of the linear propagation of the amplified pulses between the subsequent OPCPA stages.

### 2.8.1 Numerical simulation of OPCPA

The code, which was used for the numerical simulation of OPCPA throughout in this work, was developed in C++ language in the Institute of Applied Physics of the Russian Academy of Sciences. It utilizes a special algorithm for calculating the Fourier transform of highly chirped pulses [67]. The code solves the three coupled UPPE equations, which describe TWM (Eq. 2.67), by the second order split-step method [9, 58]. The linear part of Eq. 2.67 is calculated in the transverse wave vector spectral domain ( $k_x, k_y, \Omega$ ), while the nonlinear term is solved in the spatial temporal domain ( $x, y, t$ ) using the second-order Runge-Kutta method. Since the code solves Eq. 2.67, it is a 4D ( $x, y, t, z$ ), nonparaxial model, which takes into account dispersion and diffraction. The crystal's anisotropy is considered via the

direction dependent refractive index  $n(k_x, k_y, \omega)$  [56, 65], which also includes the walk-off effect. Therefore it is possible to simulate TWM in an arbitrary propagation direction in biaxial crystals. The model includes refraction on crystal surfaces which can be tilted with respect to each other, therefore wedged crystals can be considered too. The incidence angle of each beam can be changed independently, therefore TWM interactions can be simulated with arbitrary noncollinear angles. Parametric superfluorescence (PSF) is also considered in the model by adding noise to the initial signal and idler fields [150]. After completing the simulation, the 3D complex fields of idler, signal and pump pulses are obtained and they can be used in a further OPCPA stage.

The numerical simulation of noncollinear OPCPA is challenging in terms of computational capacity due to the fine resolution ( $dt$ ) and high number of points ( $N_t$ ) on the temporal grid which is required to accommodate both the Fourier limited and stretched pulse shapes. In addition, noncollinear phase-matching geometry results in the angular dispersion of the idler pulse. Angular dispersion is equivalent to high spatial frequencies in the idler field. In order to resolve these frequencies, fine spatial resolution ( $dx$ ) is needed, which increases the number of the spatial grid points ( $N_x$ ) in case of large beams. According to the sampling theorem [151], the highest frequency of the pulse envelope spectrum ( $\Omega_m$ ) should be less than the Nyquist critical frequency ( $\Omega_c$ ), according to Eq. 2.111, where  $\Omega = \omega - \omega_0$ .

$$\Omega_m < \Omega_c = \frac{\pi}{dt} \quad (2.111)$$

The same is also true for the spatial resolution  $dx$  and the maximal spatial frequency  $k_{xm}$  (Eq. 2.112).

$$k_{xm} < k_c = \frac{\pi}{dx} \quad (2.112)$$

For example, in case of BBO the bandwidth-optimized spectral gain (Fig. 2.6) ranges from 700 nm to 1100 nm and the center of the frequency grid corresponds to 850 nm. According to the sampling theorem, Eq. 2.111, the temporal resolution must be less than 7 fs. If the pump pulse duration is 1 ns, then the size of the temporal grid must be  $N_t = 2^{18}$ . The spectrum of the idler ranges from 1000 nm to 2200 nm. The angular deviation of the 1000 nm component with respect to the central wavelength of 1425 nm is  $3.6^\circ$ . According to Eq. 2.112, the required spatial resolution must be less than 11  $\mu\text{m}$  in the dimension parallel to the phase-matching plane (x-dimension). A typical crystal size in a power amplification OPCPA stage is 10 mm to 20 mm, thus  $N_x = 2^{10}$  is a minimum requirement. Along the y-dimension the wave vector spread is small, therefore  $N_y = 128$  is sufficient. Based on this, the memory requirements in GB can be calculated according to Eq. 2.113, where the numbers 3, 2 and 8 indicate the number of pulses (idler, signal, pump), the real and imaginary parts of the complex numbers and the memory space in bytes, occupied by 1 double precision number.

$$RAM = \frac{N_x \times N_y \times N_t \times 3 \times 2 \times 8}{1024^3} GB \quad (2.113)$$

In the above example, the occupied memory would be 1.536 TB, which is only available in supercomputer nodes. This huge memory requirement can be significantly reduced by using the advanced Fourier-transform algorithm for highly chirped pulses, developed by Andrianov et al. [67].

This algorithm utilizes the fact that the biggest contribution in the spectral phase of the stretched signal pulse comes from the quadratic phase, GDD. This can be factored out from the phase, according to Eq. 2.114, where  $\psi$  is the residual spectral phase containing the contribution from high-order phase derivatives (TOD, FOD, etc.) [67].

$$\begin{aligned} A(\Omega) &= |A(\Omega)| e^{i\phi(\Omega)} e^{-i\frac{GDD}{2}\Omega^2} e^{i\frac{GDD}{2}\Omega^2} = \\ &= |A(\Omega)| e^{i\psi(\Omega)} e^{i\frac{GDD}{2}\Omega^2} = \\ &= A'(\Omega) e^{i\frac{GDD}{2}\Omega^2} \end{aligned} \quad (2.114)$$

The complex spectrum  $A'(\Omega)$  corresponds to a GDD-compensated temporal pulse shape,  $A'(t)$ , which fits into a much shorter temporal window, according to Eq. 2.115.

$$A'(t) = \frac{1}{2\pi} \int_{-\infty}^{\infty} A'(\Omega) e^{-i\Omega t} d\Omega \quad (2.115)$$

The relation between the stretched ( $A(T)$ ) and GDD compensated ( $A'(t)$ ) pulse shapes can be derived by going through the steps in Eq. 2.116, where in the last step the frequency dependent terms were integrated according to  $\Omega$

$$\begin{aligned} A(T) &= \frac{1}{2\pi} \int_{-\infty}^{\infty} A(\Omega) e^{-i\Omega T} d\Omega = \\ &= \frac{1}{2\pi} \int_{-\infty}^{\infty} A'(\Omega) e^{i\frac{GDD}{2}\Omega^2} e^{-i\Omega T} d\Omega = \\ &= \frac{1}{2\pi} \iint_{-\infty}^{\infty} A'(t) e^{i\frac{GDD}{2}\Omega^2} e^{-i\Omega T} e^{i\Omega t} d\Omega dt = \\ &= \sqrt{\frac{i}{2\pi GDD}} e^{-i\frac{T^2}{2GDD}} \int_{-\infty}^{\infty} A'(t) e^{-i\frac{t^2}{2GDD}} e^{it\frac{T}{GDD}} dt \end{aligned} \quad (2.116)$$

Based on Eqs. 2.114, 2.115 and 2.116, the stretched pulse shape ( $A(T)$ ) can be calculated from the complex spectrum ( $A(\Omega)$ ) by applying two Fourier transformations according to Eq. 2.117.

$$\begin{aligned} A'(t) &= \frac{1}{2\pi} \int_{-\infty}^{\infty} A(\Omega) e^{-i\frac{GDD}{2}\Omega^2} e^{-i\Omega t} d\Omega \\ A(T) &= \sqrt{\frac{i}{2\pi GDD}} e^{-i\frac{T^2}{2GDD}} \int_{-\infty}^{\infty} A'(t) e^{-i\frac{t^2}{2GDD}} e^{it\frac{T}{GDD}} dt \end{aligned} \quad (2.117)$$

This will result in two temporal grids ( $t$  and  $T$ ) for the GDD-compensated ( $A'(t)$ ) and stretched ( $A(T)$ ) pulses. In case of fast-Fourier-transform algorithm, the temporal resolution of the two grids ( $dt$  and  $dT$ ) are connected through Eq. 2.118 [67].

$$dT = GDD \cdot \frac{2\pi}{N_t dt} \quad (2.118)$$

According to Eqs. 2.117, if the spectral phase only has second order contribution, then  $A'(t)$  can fit a small temporal grid as the Fourier limited pulse shape. Sticking to the above example, the spectral gain provided by BBO supports the amplification of sub-10 fs pulses. Therefore, with  $dt = 7$  fs resolution,  $N_t = 128 = 2^7$  grid points

can conveniently accommodate both the Fourier limited and stretched pulse shapes. Using the same spatial resolution as in the above example, the minimum memory requirement considerably decreases, from 1.536 TB to 768 MB.

In real OPCPA or CPA systems, there is a considerable amount of TOD, which requires more points on the temporal (and spectral) grid even in the case of the special algorithm (Eq. 2.117). The minimum grid size requirement can be determined from the fact that the spectral (and also temporal) phase difference between the adjacent grid points must be less than  $\pi$  in order to avoid aliasing during FFT [67], expressed by Eq. 2.119.

$$\max \left( \frac{d\phi}{d\Omega} \right) \cdot \Delta\Omega < \pi \quad (2.119)$$

In the advanced algorithm GDD is factored out, thus the biggest contribution in the spectral phase originates from TOD. Based on this and Eq. 2.119, the minimum grid requirement can be expressed as Eq. 2.120.

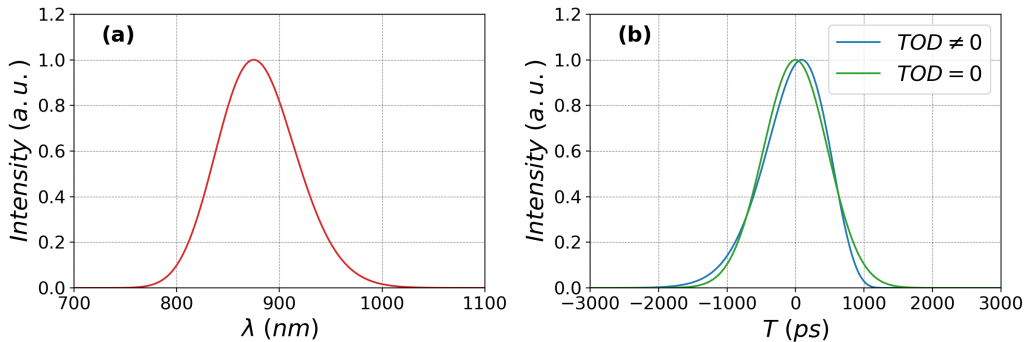
$$N_t > \frac{TOD \cdot \Omega_{max}^2}{dt} \quad (2.120)$$

In the above example, to stretch a sub-10 fs, Fourier limited pulse to 1 ns, roughly  $1 \times 10^6 \text{ fs}^2$  GDD is needed. This large stretching factor can be easily provided by grating pairs [152, 153], which can have a TOD-GDD ratio as large as  $\approx -2 \text{ fs}$ . In this case the spectral phase will contain  $-2 \times 10^6 \text{ fs}^3$  TOD. According to Eq. 2.120, this increases the minimum number of grid points to  $N_t = 2^{17}$  and the memory requirement to 768 GB. Although it seems large, but it is by a factor of two lower than without the advanced algorithm.

The number of grid points, thus the memory requirements for the numerical simulation of OPCPA, are highly influenced by the interaction geometry, spectral bandwidth and stretching ratio. These data are summarized in Table 2.3, for a few typical OPCPA configurations. The numerical simulation of PW class, noncollinear OPCPA has the highest memory needs due to the high TOD-GDD ratio and the large crystal aperture. In terms of computational capacity, the less demanding is the simulation of GW class, collinear, KTA crystal based OPCPA, which is pumped by 1 ps to 1.5 ps pump pulses. It can be noted in Table 2.3 that by neglecting TOD in case of the advanced algorithm, the memory requirements are highly reduced. This enables the numerical simulation of PW-class OPCPAs on desktop computers. Fig. 2.4 (a) and (b) illustrates a scenario when a broadband pulse (10 fs Fourier limited pulse duration) is stretched to  $\approx 1 \text{ ns}$ . According to Fig. 2.4 (b), there is just a minor difference in the pulse shape when TOD is neglected (green curve). Consequently, disregarding TOD will have minor influence on the output results, which is a reasonable price for the reduction of computational requirements.

**Table 2.3.** Minimum memory requirements for the numerical simulation of various OPCPA configurations.

Crystal OPCPA class	BBO TW	DKDP PW	LBO TW	KTA GW
Crystal aperture (mm)	15	500	15	5
Noncollinear angle ( $^\circ$ )	2.35	1.06	1.26	0
Max. $dx$ ( $\mu\text{m}$ )	11	52	24	—
$N_x$	$2^{11}$	$2^{14}$	$2^{10}$	$2^7$
$N_y$	$2^7$	$2^7$	$2^7$	$2^7$
Pump window (ps)	150	1500	150	1.5
Spectral range (nm)	700-1100	770-1000	740-1150	1450-1650
$TOD/GDD$ (fs)	0.75	-2	0.75	0.75
Max. $dt$ (fs)	6.7	12	7	50
$N_t$	$2^{14}$	$2^{17}$	$2^{14}$	$2^6$
$N_{t,Advanced}$	$2^{11}$	$2^{15}$	$2^{11}$	$2^6$
$N_{t,Advanced,TOD=0}$	$2^8$	$2^8$	$2^8$	$2^6$
$RAM$ (GB)	192	12288	96	$< 1$
$RAM_{Advanced}$ (GB)	24	3072	12	$< 1$
$RAM_{Advanced,TOD=0}$ (GB)	3	24	1.5	$< 1$

**Fig. 2.4.** (a) Spectrum corresponding to 10 fs Fourier limited pulse duration. (b) Stretched pulse shape which is calculated with (blue) and without (green) TOD.  $GDD = 5 \times 10^6 \text{ fs}^2$ ,  $TOD = -10 \times 10^6 \text{ fs}^3$ 

## 2.8.2 Numerical simulation of linear propagation

The advanced Fourier transform proposed by Andrianov et al. [67] can be applied to switch between the spatial and transverse wave vector domains, when the spatial phase has large second-order contribution.

This can be particularly useful when the goal is to numerically simulate the linear propagation of a converging (focusing) or diverging pulse. In the focal plane, for example, much higher spatial resolution is needed than at the plane of the focusing lens or spherical mirror. This can result in large spatial grid size, as well as increased computational time and capacity.

Another example is the numerical simulation of linear pulse propagation through a telescope which is used for beam expansion and consists of two or three spherical

mirrors. In this case, high spatial resolution is needed to keep the spatial phase difference between adjacent nodes below  $\pi$ . Otherwise aliasing [151] will occur during the usage of FFT.

The spatial phase shift of a spherical mirror is expressed by Eq. 2.50, where  $z(x, y)$  is the optical path difference across the spatial profile, given by Eq. 2.49. According to the Taylor expansion of the path difference, Eq. 2.51, the spatial phase shift of a spherical mirror mainly consists of second order contribution. Similarly to Eq. 2.114, the second order contribution can be factored out, which provides a residual phase ( $\psi_L$ ), defined by Eq. 2.121, where  $\alpha = \frac{k}{f}$  and  $f = \frac{R}{2}$  is the focal distance.

$$\psi_L(x, y, \omega) = k \cdot z(x, y) - \alpha \cdot \frac{x^2 + y^2}{2} \quad (2.121)$$

This provides a smoother spatial phase profile which can be sampled with lower resolution without aliasing, thereby relaxing the spatial grid requirements. As a result of factorization, switching between the spatial  $(x, y, \omega)$  and transverse wave vector  $(K_x, K_y, \omega)$  domains is accomplished by two subsequent, 2D Fourier transformations, according to Eq. 2.122. The second Fourier transform can be either forward or backward transformation, depending on the sign of  $\alpha$ .

$$\begin{aligned} A'(k_x, k_y, \omega) &= \iint_{-\infty}^{\infty} A(x, y, \omega) e^{i\psi_L} e^{-i(k_x x + k_y y)} dx dy \\ A(K_x, K_y, \omega) &= \frac{i}{2\pi\alpha} e^{-i\frac{K_x^2 + K_y^2}{2\alpha}} \iint_{-\infty}^{\infty} A'(k_x, k_y, \omega) e^{-i\frac{k_x^2 + k_y^2}{2\alpha}} e^{i(k_x \frac{K_x}{\alpha} + k_y \frac{K_y}{\alpha})} dk_x dk_y \end{aligned} \quad (2.122)$$

Linear pulse propagation can be simulated in the transverse wave vector frequency domain (Fourier-domain), by using Eqs. 2.37. According to the Taylor expansion of  $k_z(k_x, k_y, \omega)$ , the spatial phase in the Fourier domain has mainly second-order contribution (Eq. 2.38). Similarly to the previous case, the second-order phase contribution can be factored out, leading to a residual phase ( $\psi_P$ ) defined by Eq. 2.123, where  $\beta = -\frac{z}{k}$ .

$$\psi_P(k_x, k_y, \omega) = z \cdot k_z - \beta \frac{k_x^2 + k_y^2}{2} \quad (2.123)$$

As a result of factorization, the resolution requirements are relaxed and switching between the Fourier and spatial domains is accomplished in two subsequent Fourier transformations according to Eqs. 2.124.

$$\begin{aligned} A'(x, y, \omega) &= \frac{1}{4\pi^2} \iint_{-\infty}^{\infty} A(k_x, k_y, \omega) e^{i\psi_P} e^{i(k_x x + k_y y)} dk_x dk_y \\ A(X, Y, \omega) &= \frac{i}{2\pi\beta} e^{-i\frac{X^2 + Y^2}{2\beta}} \iint_{-\infty}^{\infty} A'(x, y, \omega) e^{-i\frac{x^2 + y^2}{2\beta}} e^{i(x\frac{X}{\beta} + y\frac{Y}{\beta})} dx dy \end{aligned} \quad (2.124)$$

The advanced 2D Fourier transformations, Eqs. 2.122-2.124, can be combined to efficiently simulate an optical system consisting of a sequence of spherical mirrors (or lenses) and free space propagation.

First, the residual spatial phase shift of the focusing element ( $\psi_L$ ) must be applied on the field  $A(x, y, \omega)$ , which is then transformed into the Fourier domain by using Eqs. 2.122. It must be noted that the field,  $A(K_x, K_y, \omega)$ , contains a second

order phase term. This must be considered during the calculation of the residual propagation phase  $\psi_p$ , through the modified definition of  $\beta$  (Eq. 2.125).

$$\beta = -\frac{z + f}{k} \quad (2.125)$$

In the second step, the residual propagation phase ( $\psi_P$ ) is applied on the field,  $A(K_x, K_y, \omega)$ , in the Fourier domain. After this, by using the advanced 2D Fourier transform, Eqs. 2.124, one can calculate the field distribution ( $A(X, Y, \omega)$ ) in a plane which is at  $z$  distance from the lens or mirror. According to Eqs. 2.124, the field  $A(X, Y, \omega)$  contains a second-order phase term. Similarly to the previous case, this must be taken into account during the calculation of the residual spatial phase-shift of the next spherical mirror, through the modified definition of  $\alpha$ , Eq. 2.126.

$$\alpha = k \left( \frac{1}{f_2} + \frac{1}{z + f_1} \right) \quad (2.126)$$

In real OPCPA systems, telescopes are often used to increase the beam size between pre- and power-amplification stages. In the simplest case, a telescope consists of two spherical mirrors in a confocal arrangement. For example, if the beam size has to be increased from 5 mm to 10 mm, then a telescope consisting of  $f_1 = -0.5$  m and  $f_2 = -1$  m spherical mirrors separated by 1.5 m can be used for this purpose. In case of simple Fourier transform, at least a  $15 \text{ mm} \times 15 \text{ mm}$  grid must be defined to accommodate the beam size after the telescope. The criterion that the phase difference between adjacent nodes has to be less than  $\pi$  leads to Eq. 2.127, where  $\lambda_{min}$  is the smallest wavelength component in the spectrum and  $GS$  is the grid size.

$$dx < \frac{\lambda_{min} f}{GS} \quad (2.127)$$

In the current example, if the smallest wavelength is 700 nm, then the spatial resolution must be less than  $23 \mu\text{m}$ . This means that the grid will consist of  $N_x \times N_y = 1024 \times 1024$  data points. By using the special Fourier transform, Eq. 2.122, the only restriction for the spatial resolution is posed by the sampling theorem, Eq. 2.112. According to Eq. 2.112, the spatial resolution must be less than  $780 \mu\text{m}$ . Therefore, the minimum requirement for the grid size is  $N_x \times N_y = 32 \times 32$ , which is a considerable gain in computational time and capacity.

In this work, during the modeling of multistage OPCPA systems, pulse propagation through beam magnifying telescopes was numerically simulated by using the special Fourier transformations defined by Eqs. 2.122 and 2.124. These algorithms were implemented in my own Python code, which was used to simulate the propagation of the complex 3D fields, provided by the OPCPA code. This method enabled the numerical simulation of entire OPCPA systems under realistic circumstances.

## 2.9 Overview of a few nonlinear crystals

In this section, I give an overview about four commonly used nonlinear crystals, which are also used throughout this work. These are beta barium borate (BBO), deuterated potassium dihydrogen phosphate (DKDP), lithium triborate (LBO) and potassium titanyl arsenate (KTA) crystals. The equations derived in the previous sections for calculating slow and fast refractive indices, effective nonlinear coefficients, phase-matching angles will be directly applied here in case of commonly used pump wavelengths.

### 2.9.1 $\beta$ -barium borate (BBO)

Beta barium borate (BBO) is a negative uniaxial crystal belonging to the  $3m$  point group [154]. The transparency window of BBO is in the range of 200 nm to 3500 nm [155]. In negative uniaxial crystals ( $n_z = n_e < n_o (= n_x = n_y)$ ), thus the equations for calculating the refractive indices of the slow and fast waves (Eqs. 2.56) can be simplified to Eq. 2.128.

$$n_s = n_o \quad n_f(\theta) = \frac{n_o n_e}{\sqrt{n_o^2 \sin^2 \theta + n_e^2 \cos^2 \theta}} \quad (2.128)$$

According to Eq. 2.128, the refractive index of the slow wave does not depend on the propagation direction, and the walk-off angle is zero (Eq. 2.57). The oscillation directions of the electric field and displacement vectors (Eq. 2.55) of the slow wave are parallel and they are perpendicular to the plane defined by the optical axis (Z-axis) and the propagation direction ( $\mathbf{k}$ ) [81]. Due to these properties, the slow wave in negative uniaxial crystals is called ordinary wave [4, 81].

The refractive index of the fast wave depends on the polar angle ( $\theta$ ) (Eq. 2.128), therefore it is called extraordinary wave. From Eqs. 2.55, 2.29 and from the sixth point of Section 2.2.3 it follows that the displacement ( $\mathbf{D}_f$ ), electric field ( $\mathbf{E}_f$ ), wave ( $\mathbf{k}_f$ ) and Poynting ( $\mathbf{S}_f$ ) vectors of the fast wave and the Z-principal axis (optical axis) are coplanar. Furthermore, the polar angle  $\theta$  and the angle between Z-axis and  $\mathbf{S}$ , denoted by  $\theta'$ , are related through Eq. 2.129 [81].

$$\tan \theta' = \left( \frac{n_o}{n_e} \right)^2 \tan \theta \quad (2.129)$$

Due to Eq. 2.129, in negative uniaxial crystals ( $n_e < n_o$ )  $\theta' > \theta$ . This means that the wave vector ( $\mathbf{k}$ ) is between the optical axis and the Poynting vector ( $\mathbf{S}$ ). The walk-off angle ( $\rho = \theta' - \theta$ ) can be calculated according to Eq. 2.130 [81].

$$\tan \rho = \frac{(n_o^2 - n_e^2) \tan \theta}{n_e^2 + n_o^2 \tan^2 \theta} \quad (2.130)$$

Consequently, the directions of the electric field and displacement vectors can be expressed according to Eq. 2.131 [81].

$$\mathbf{d}_s = \mathbf{e}_s = \begin{pmatrix} \sin \phi \\ -\cos \phi \\ 0 \end{pmatrix} \quad \mathbf{d}_f = \begin{pmatrix} -\cos \theta \cos \phi \\ -\cos \theta \sin \phi \\ \sin \theta \end{pmatrix} \quad \mathbf{e}_f = \begin{pmatrix} -\cos(\theta + \rho) \cos \phi \\ -\cos(\theta + \rho) \sin \phi \\ \sin(\theta + \rho) \end{pmatrix} \quad (2.131)$$

The wavelength dependence of the principal refractive indices of BBO are given by the Sellmeier equations (Eqs. 2.132), which were measured by Zhang et al. at room temperature [156].

$$n_o^2(\lambda) = 2.7359 + \frac{0.01878}{\lambda^2 - 0.01822} - 0.01471\lambda^2 + 0.0006081\lambda^4 - 0.00006740\lambda^6 \quad (2.132)$$

$$n_e^2(\lambda) = 2.3753 + \frac{0.01224}{\lambda^2 - 0.01667} - 0.01627\lambda^2 + 0.0005716\lambda^4 - 0.00006305\lambda^6$$

The temperature dependence of the refractive indices in the range of 20 °C to 80 °C (Eq. 2.133) are obtained by Nikogosyan et al. [157].

$$\begin{aligned}\frac{dn_o}{dT} &= -16.6 \cdot 10^{-6} \frac{1}{^\circ\text{C}} \\ \frac{dn_e}{dT} &= -9.3 \cdot 10^{-6} \frac{1}{^\circ\text{C}}\end{aligned}\quad (2.133)$$

The contracted nonlinear tensor ( $d$ ) is given by Eq. 2.134 [158, 159].

$$d = \begin{pmatrix} 0 & 0 & 0 & 0 & 0.08 & 2.2 \\ 2.2 & -2.2 & 0 & 0.08 & 0 & 0 \\ 0.08 & 0.08 & 0.04 & 0 & 0 & 0 \end{pmatrix}\quad (2.134)$$

BBO is probably one of the most widely used nonlinear crystal in OPCPA systems which produce few-cycle, near-IR pulses [36, 99, 115, 120, 125, 126, 160, 161]. Usually, BBO is pumped by the second harmonic wavelengths of Nd:YAG ( $\lambda_p = 532$  nm), Yb:YAG ( $\lambda_p = 515$  nm) or Ti:Sapphire ( $\lambda_p = 400$  nm) lasers. The first step during the design of a broadband OPCPA system is to determine the phase-matching type and the optimal interaction plane with respect to the principal coordinate system. One possible way to do this is to assume collinear propagation ( $\alpha = 0$ ) and calculate the phase-mismatch ( $\Delta k$ ) in all possible  $(\theta, \phi)$  directions and find those  $(\theta_c, \phi_c)$  pairs, where  $\Delta k$  is zero. This way it is possible to determine the propagation directions where efficient three-wave mixing can take place. These  $(\theta_c, \phi_c)$  pairs are indicated by the green curves in Fig. 2.5 (a)-(c) for *ssf*, *sff* and *fsf* type interactions. In this example, the central wavelength of the idler, signal and pump pulses are 1301 nm, 900 nm and 532 nm. The effective value of the nonlinear tensor ( $d_{eff}$ ) along these directions are calculated by using Eq. 2.66, and the results are indicated by the blue curves in Fig. 2.5 (a)-(c).

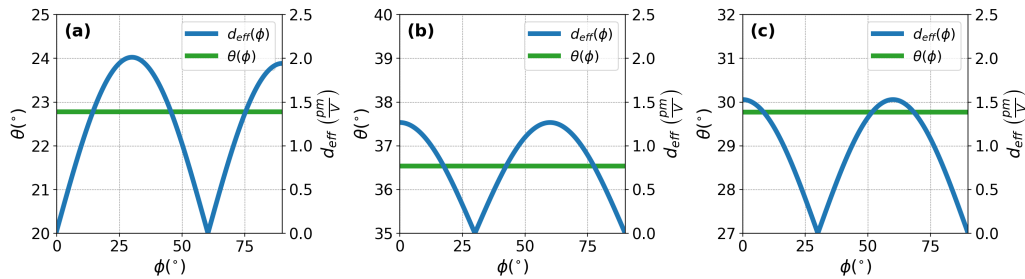


**Fig. 2.5.** Collinear propagation directions in BBO where  $\Delta k = 0$  (green curves) and the effective value of the nonlinear tensor ( $d_{eff}$ ) along these directions (blue curves) in case of *ssf* (a), *sff* (b) and *fsf* (c) type interaction ( $\lambda_i = 1301$  nm,  $\lambda_s = 900$  nm and  $\lambda_p = 532$  nm).

The optimal interaction plane for each phase-matching type can be determined by finding the  $(\theta, \phi)$  pair where the maximum value of  $d_{eff}$  is reached. These data are summarized in Table 2.4. The next step in the optimization of a broadband OPCPA is to determine which configuration provides the broadest gain bandwidth.

Broadband phase-matching can be achieved by matching the group velocities of signal and idler pulses in noncollinear geometry (Eq. 2.107). The required non-collinear and phase-matching angles can be easily obtained analytically in case of an

**Table 2.4.** Propagation direction  $(\theta, \phi)$  where the maximum value of  $d_{eff}$  occurs in case of each phase-matching type.

Type	$d_{eff}$ (pm V <sup>-1</sup> )	$\theta$ (°)	$\phi$ (°)
ssf	2	22.8	30
sff	1.27	36.5	60
fsf	1.53	29.8	60

*ooe* type interaction, however it becomes more complicated in case of two extraordinary waves and in some cases, when  $v_{gs} > v_{gi}$ , group velocity matching is not even possible.

Another approach is the numerical optimization of the noncollinear ( $\alpha$ ) and phase-matching ( $\theta$ ) angles on the broadest gain bandwidth. For this, one must calculate the spectral gain curves by using Eq. A.16 as a function of the phase-matching and noncollinear angles in the interaction plane which were previously determined by the collinear optimization. This results in a 3D function  $G(\omega_s, \theta, \alpha)$ . There are many possibilities to obtain the gain bandwidth from the spectral gain curves. One robust way is to define a super-Gaussian window function ( $W(\omega_s)$ ) on the spectral range to be amplified and then perform the integration defined by Eq. 2.135.

$$g(\theta, \alpha) = \int G(\omega_s, \theta, \alpha) \cdot W(\omega_s) d\omega_s \quad (2.135)$$

The  $(\theta, \alpha)$  position of the peak of  $g(\theta, \alpha)$  will correspond to the optimal phase-matching geometry, where the broadest gain bandwidth can be achieved.

The blue gain curves in Fig. 2.6 (a)-(c) illustrate the results of the gain bandwidth optimization on the 650 nm to 1200 nm spectral range, while the red curves indicate the spectral gain in case of collinear propagation. In case of *ssf* type phase-matching, at  $\alpha = 2.35^\circ$  noncollinear angle the group velocities of the idler and signal pulses can be matched. This results in an extremely broad gain bandwidth from 700 nm to 1060 nm, plotted by the blue curve in Fig. 2.6 (a). This configuration is utilized in all BBO based few-cycle OPCPA systems. The phase-matching parameters are summarized in Table. 2.5.

In case of Type II, *sff* interaction (Fig. 2.6 (b)) group velocity matching is not possible, and according to the bandwidth optimization, the broadest spectrum on the near-IR spectral range can be achieved at 1021 nm central wavelength. Finally, in case of *fsf* type phase-matching (Fig. 2.6 (c)), the broadest achievable spectrum spans from 1010 nm to 1120 nm. This corresponds to an idler pulse centered around 1057 nm (Table 2.5). The noncollinear angle in this configuration is  $8.2^\circ$ , which is unpractical in experimental conditions, furthermore, due to the large noncollinear angles, the value of  $d_{eff}$  decreases to 0.34 (Table 2.5).

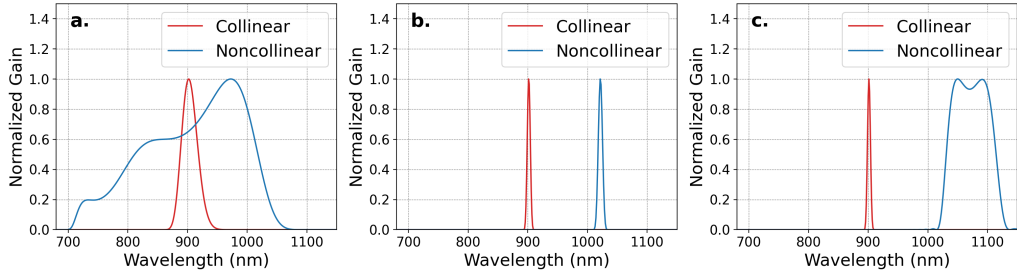


**Fig. 2.6.** Spectral gain curves provided by BBO in collinear (red) and noncollinear (blue) geometry using *ssf* (a), *sff* (b) and *fsf* (c) type phase-matching. The blue curves also represent the broadest achievable spectrum on the 650 nm to 1200 nm range in the corresponding interaction type.

**Table 2.5.** Phase-matching parameters in BBO provided by gain bandwidth optimization.

Type	ssf	sff	fsf
$\lambda_i$ (nm)	1301	1110	1057
$\lambda_s$ (nm)	900	1021	1071
$\lambda_p$ (nm)	532	532	532
$\theta_i$ ( $^\circ$ )	20.4	34.5	69.1
$\theta_s$ ( $^\circ$ )	26.2	31.8	48.1
$\theta_p$ ( $^\circ$ )	23.8	32.9	56.3
$\phi_i$ ( $^\circ$ )	30	60	60
$\phi_s$ ( $^\circ$ )	30	60	60
$\phi_p$ ( $^\circ$ )	30	60	60
$d_{eff}$ (pm V $^{-1}$ )	2	1.27	0.34

## 2.9.2 Deuterated potassium dihydrogen phosphate (DKDP)

Deuterated potassium dihydrogen phosphate (DKDP), is a negative uniaxial crystal, which belongs to the  $\bar{4}2m$  point group [162]. The transparency range of DKDP is 200 nm to 2000 nm [163]. DKDP is the isomorph of the potassium dihydrogen phosphate (KDP) crystal, where one hydrogen atom is replaced with a deuterium atom. Due to this, DKDP has a few beneficial properties over KDP. For example, DKDP has a broader transparency range [162] and broader gain bandwidth can be achieved by group velocity matching than in KDP [164]. The most favorable property of DKDP is that it can grow to very large apertures (90 cm) [163] which is necessary for the power amplifier stages of PW class OPCPA systems [31].

Since DKDP, similarly to BBO, a negative uniaxial crystal, therefore the formulas for calculating the refractive indices (Eq. 2.128), walk-off angle and polarization directions (Eq. 2.131) are the same as in the case of BBO.

The principal refractive indices of DKDP depend on the deuteration level ( $D$ ), and can be calculated according to Eq. 2.136, where  $n(0.96)$  and  $n(0)$  are the Sellmeier equations in case of  $D = 0.96$  and  $D = 0$  deuteration levels [164].

$$n^2(D, \lambda) = \frac{n^2(0.96, \lambda) - 0.04n^2(0, \lambda)}{0.96}D + (1 - D)n^2(0, \lambda) \quad (2.136)$$

The Sellmeier equations of the principal refractive indices at  $D = 0$  and  $D = 0.96$  deuteration levels [164] and the nonlinear tensor [158] are given by Eqs. 2.137 and 2.138.

$$\begin{aligned} n_o^2(0, \lambda) &= 2.259276 + \frac{0.010089562}{\lambda^2 - 0.012942625} + \frac{13.00522\lambda^2}{\lambda^2 - 400} \\ n_e^2(0, \lambda) &= 2.132668 + \frac{0.008637494}{\lambda^2 - 0.012281043} + \frac{3.2279924\lambda^2}{\lambda^2 - 400} \\ n_o^2(0.96, \lambda) &= 2.240921 + \frac{0.009676393}{\lambda^2 - 0.015620153} + \frac{2.2469564\lambda^2}{\lambda^2 - 126.920659} \\ n_e^2(0.96, \lambda) &= 2.126019 + \frac{0.008578409}{\lambda^2 - 0.011991324} + \frac{0.7844043\lambda^2}{\lambda^2 - 123.403407} \end{aligned} \quad (2.137)$$

$$d = \begin{pmatrix} 0 & 0 & 0 & 0.4 & 0 & 0 \\ 0 & 0 & 0 & 0 & 0.4 & 0 \\ 0 & 0 & 0 & 0 & 0 & 0.4 \end{pmatrix} \quad (2.138)$$

The temperature dependence of the constants in the Sellmeier polynomials were measured by Ghosh et al. and can be found in Ref. [165].

It was mentioned previously that DKDP can grow to large apertures, so it can be utilized in high peak power OPCPA systems in the near-IR spectral range [31]. Similarly to BBO, it can be pumped by the second harmonic wavelength of Nd:YAG or Yb:YAG lasers. Collinear phase-matching optimization presented in Fig. 2.7 (a)-(c) was carried out for 1186 nm, 910 nm and 515 nm idler, signal and pump wavelengths. The green and blue curves in Fig. 2.7 illustrate the  $\Delta k = 0$  directions and the corresponding value of  $d_{eff}$ . Similarly to BBO, the phase-mismatch depends only on the angle  $\theta$ . Based on this, the optimal phase-matching planes can be determined by finding the maximum value of the nonlinear coefficient. These parameters are summarized in Table. 2.6.

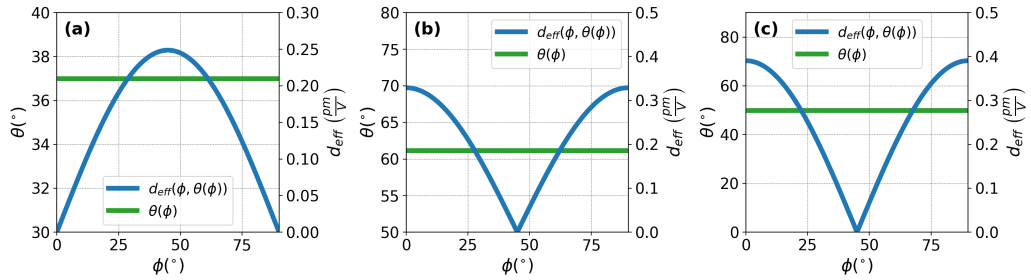


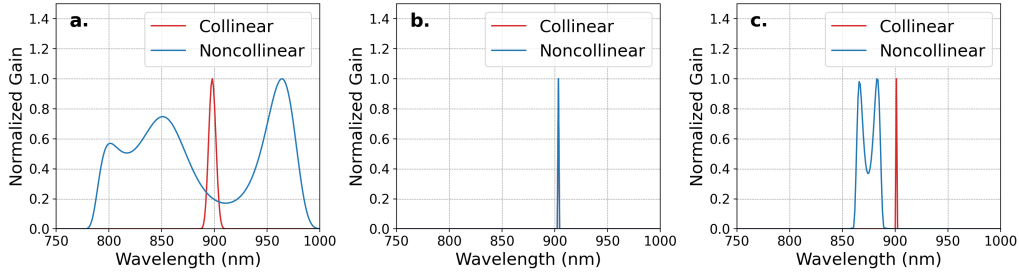
**Fig. 2.7.** Collinear propagation directions in DKDP where  $\Delta k = 0$  (green curve) and the corresponding value of the effective nonlinear coefficient (blue curves) in case of *ssf* (a), *sff* (b) and *fsf* (c) type interaction ( $\lambda_i = 1186$  nm,  $\lambda_s = 910$  nm and  $\lambda_p = 515$  nm).

According to the gain bandwidth optimization presented in Fig. 2.8 (a)-(c), the broadest spectrum is provided in noncollinear, *ssf* type phase-matching at  $\alpha = 1.06^\circ$ . This is illustrated by the blue curve in Fig. 2.8 (a). In case of *sff* type interaction, group velocity matching is not possible, therefore bandwidth optimization cannot provide a broader spectrum than it can be obtained in case of collinear propagation (Fig. 2.8 (b)). In *fsf* type phase-matching, noncollinear propagation can provide a broader bandwidth than in the collinear case, however, due to the large

**Table 2.6.** Propagation direction ( $\theta, \phi$ ) where the maximum value of  $d_{eff}$  occurs in case of each phase-matching type.

Type	$d_{eff}$ (pm V <sup>-1</sup> )	$\theta$ (°)	$\phi$ (°)	Comment
ssf	0.25	37.0	45	-
sff	0.33	61.1	0	XZ plane
fsf	0.39	49.85	0	XZ plane

noncollinear angles, the effective nonlinear coefficient decreases, as it is indicated in Table 2.7.

**Fig. 2.8.** Spectral gain curves provided by DKDP in collinear (red) and noncollinear (blue) geometry using *ssf* (a), *sff* (b) and *fsf* (c) type phase-matching. The blue curves also represent the broadest achievable spectrum on the 650 nm to 1200 nm range in the corresponding interaction type.**Table 2.7.** Phase-matching parameters in DKDP after gain bandwidth optimization.

Type	ssf	sff	fsf
Plane	$\phi = 45^\circ$	XZ	XZ
$\lambda_i$ (nm)	1186	1186	1252
$\lambda_s$ (nm)	900	900	875
$\lambda_p$ (nm)	515	515	515
$\theta_i$ (°)	36.04	61.1	78.78
$\theta_s$ (°)	38.49	61.1	92.6
$\theta_p$ (°)	37.43	61.1	86.7
$\phi_i$ (°)	45	0	0
$\phi_s$ (°)	45	0	0
$\phi_p$ (°)	45	0	0
$d_{eff}$ (pm V <sup>-1</sup> )	0.25	0.33	0.1

### 2.9.3 Lithium triborate (LBO)

Lithium triborate (LBO) is a negative biaxial crystal belonging to the  $mm2$  point group [154, 162]. The principal refractive indices of LBO are ordered as  $n_x < n_y < n_z$  and transparency ranges from 160 nm to 2600 nm [154].

The temperature dependent Sellmeier equations of the principal refractive indices at 20 °C are obtained by Kato [166] and listed under Eqs. 2.139 and 2.140.

$$\begin{aligned} n_x^2 &= 2.4542 + \frac{0.01125}{\lambda^2 - 0.01135} - 0.01388\lambda^2 \\ n_y^2 &= 2.5390 + \frac{0.01277}{\lambda^2 - 0.01189} - 0.01849\lambda^2 + 4.3025 \cdot 10^{-5}\lambda^4 - 2.9131 \cdot 10^{-5}\lambda^6 \\ n_z^2 &= 2.5865 + \frac{0.01310}{\lambda^2 - 0.01223} - 0.01862\lambda^2 + 4.5778 \cdot 10^{-5}\lambda^4 - 3.2526 \cdot 10^{-5}\lambda^6 \end{aligned} \quad (2.139)$$

$$\begin{aligned} \Delta n_x &= (-3.76\lambda + 2.3) \cdot 10^{-6} \cdot \left( \Delta T + 29.13 \cdot 10^{-3} (\Delta T)^2 \right) \\ \Delta n_y &= (6.01\lambda - 19.4) \cdot 10^{-6} \cdot \left( \Delta T - 32.89 \cdot 10^{-4} (\Delta T)^2 \right) \\ \Delta n_z &= (1.5\lambda - 9.7) \cdot 10^{-6} \cdot \left( \Delta T - 74.49 \cdot 10^{-4} (\Delta T)^2 \right) \end{aligned} \quad (2.140)$$

During calculations, the nonlinear tensor constructed by Roberts [167] was used (Eq. 2.141).

$$d = \begin{pmatrix} 0 & 0 & 0 & 0 & 0 & -0.67 \\ -0.67 & 0.04 & 0.85 & 0 & 0 & 0 \\ 0 & 0 & 0 & 0.85 & 0 & 0 \end{pmatrix} \quad (2.141)$$

LBO is another widely used nonlinear crystal in broadband near-IR OPCPA systems. Compared to DKDP, it has a higher nonlinear coefficient, and its feasibility in PW class OPCPA systems has been recently demonstrated [15, 29, 30]. The collinear optimization of LBO is presented in Fig. 2.9 (a)-(c) for *ssf*, *sff* and *fsf* phase-matching types. The maximum values of the effective nonlinear coefficients and the corresponding propagation directions are summarized in Table 2.8. According to Table 2.8, the highest  $d_{eff}$  values are achieved in the principal planes of LBO.

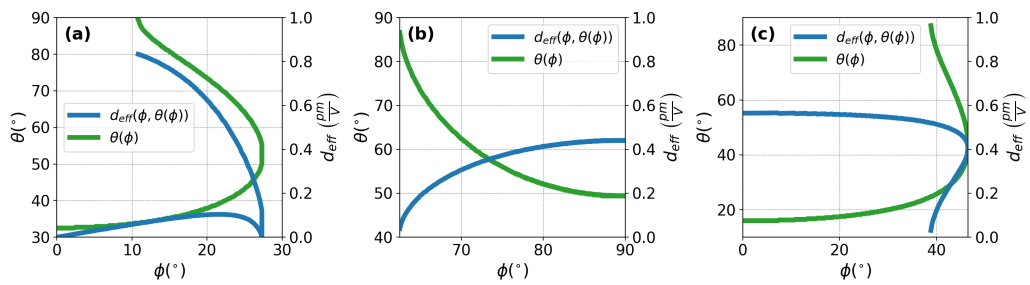


**Fig. 2.9.** Propagation directions where the phase-mismatch is zero ( $\Delta k = 0$ ) (green curves) and the effective nonlinear coefficients ( $d_{eff}$ ) along these directions (blue curves) in case of *ssf* (a), *sff* (b) and *fsf* (c) interaction type.

In the principal planes of biaxial crystals, the formulas for calculating the slow and fast indices, walk-off angles and the oscillation directions of the electric field and displacement vectors can be simplified similarly to the uniaxial case, according to Eqs. 2.142-2.150.

**XY principal plane** According to Fig. 2.9 and Table 2.8, the highest nonlinear coefficient in *ssf* type phase-matching is reached in the XY principal plane. According to Eqs. 2.142, 2.143 and 2.144 the idler, signal and pump waves are propagating

**Table 2.8.** Propagation direction  $(\theta, \phi)$  where the maximum value of  $d_{eff}$  occurs in case of each phase-matching type.

Type	$d_{eff}$ (pm V <sup>-1</sup> )	$\theta$ (°)	$\phi$ (°)	Comment
ssf	0.83	90	11	XY plane
sff	0.44	49.4	90	YZ plane
fsf	0.56	16	0	XZ plane

as ordinary, ordinary and extraordinary waves (*ooe*). Due to Eq. 2.144, the wave vector of the fast wave  $\mathbf{k}_f$  is located between the X axis and the Poynting vector  $\mathbf{S}_f$ .

$$n_s = n_z \quad n_f = \frac{n_x n_y}{\sqrt{n_x^2 \cos^2 \phi + n_y^2 \sin^2 \phi}} \quad (2.142)$$

$$\rho_s = 0 \quad \tan \rho_f = \frac{(n_y^2 - n_x^2) \tan \phi}{n_x^2 + n_y^2 \tan^2 \phi} \quad (2.143)$$

$$\mathbf{d}_s = \mathbf{e}_s = \begin{pmatrix} 0 \\ 0 \\ 1 \end{pmatrix} \quad \mathbf{d}_f = \begin{pmatrix} \sin \phi \\ -\cos \phi \\ 0 \end{pmatrix} \quad \mathbf{e}_f = \begin{pmatrix} \sin(\phi + \rho) \\ -\cos(\phi + \rho) \\ 0 \end{pmatrix} \quad (2.144)$$

**YZ principal plane** According to Fig. 2.9 and Table 2.8, the highest nonlinear coefficient in *sff* (Type II) phase-matching is reached in the YZ principal plane. The idler, signal and pump waves propagate as extraordinary, ordinary and ordinary waves (*ooo*). Due to Eq. 2.147, the Poynting vector of the slow wave  $\mathbf{S}_s$  is located between the Z axis and the wave vector  $\mathbf{k}_s$ .

$$n_s = \frac{n_y n_z}{\sqrt{n_y^2 \sin^2 \theta + n_z^2 \cos^2 \theta}} \quad n_f = n_x \quad (2.145)$$

$$\tan \rho_s = \frac{(n_z^2 - n_y^2) \tan \theta}{n_z^2 + n_y^2 \tan^2 \theta} \quad \rho_f = 0 \quad (2.146)$$

$$\mathbf{d}_s = \begin{pmatrix} 0 \\ \cos \theta \\ -\sin \theta \end{pmatrix} \quad \mathbf{e}_s = \begin{pmatrix} 0 \\ \cos(\theta - \rho) \\ -\sin(\theta - \rho) \end{pmatrix} \quad \mathbf{d}_f = \mathbf{e}_f = \begin{pmatrix} 1 \\ 0 \\ 0 \end{pmatrix} \quad (2.147)$$

**XZ principal plane** The optical axis of every birefringent crystals is located in the XZ principal plane. In case of LBO, the angle between the optical axis and the Z principal axis at 532 nm is  $V_z = 54.2^\circ$ . According to Table 2.8, the phase-matching angle in the XZ plane is  $\theta = 16^\circ$ , therefore  $\theta < V_z$ . In this case the slow wave will behave like an ordinary wave, while the refractive index of the fast wave will depend on the phase-matching angle according Eq. 2.148. (In case of  $\theta > V_z$  the opposite situation occurs.). In the XZ plane, according to Table 2.8, *fsf* (Type II) phase-matching provides the highest nonlinear coefficient. Consequently, the idler, signal and pump waves propagate as extraordinary, ordinary and extraordinary

waves ( $oeo$ ). Due to Eq. 2.150, the Poynting vector of the fast wave  $\mathbf{S}_f$  is located between the Z axis and the wave vector  $\mathbf{k}_f$ .

$$n_s = n_y \quad n_f = \frac{n_x n_z}{\sqrt{n_x^2 \sin^2 \theta + n_z^2 \cos^2 \theta}} \quad (2.148)$$

$$\rho_s = 0 \quad \tan \rho_f = \frac{(n_z^2 - n_x^2) \tan \theta}{n_z^2 + n_x^2 \tan^2 \theta} \quad (2.149)$$

$$\mathbf{d}_s = \mathbf{e}_s = \begin{pmatrix} 0 \\ 1 \\ 0 \end{pmatrix} \quad \mathbf{d}_f = \begin{pmatrix} \cos \theta \\ 0 \\ -\sin \theta \end{pmatrix} \quad \mathbf{e}_f = \begin{pmatrix} \cos(\theta - \rho) \\ 0 \\ -\sin(\theta - \rho) \end{pmatrix} \quad (2.150)$$

The blue gain curves in Fig. 2.10 (a)-(c) illustrate the results of the gain bandwidth optimization on the 650 nm to 1200 nm spectral range, while the red curves indicate the spectral gain in case of collinear propagation. In case of Type I,  $ssf$ , noncollinear phase-matching geometry (blue curve in Fig. 2.10 (a)), the group velocities of the idler and signal pulses can be matched. This results in an extremely broad gain bandwidth from 750 nm to 1150 nm. In case of Type II,  $fff$  interaction (Fig. 2.10 (b)) group velocity matching is not possible, and according to the bandwidth optimization, the broadest gain curve occurs in collinear propagation, but at a different central wavelength. Finally, in case of  $fsf$  phase-matching in the XZ plane (Fig. 2.10 (c)), the broadest achievable spectrum spans from 710 nm to 760 nm, therefore it is centered around 735 nm. This corresponds to an idler pulse which is centered around 1927 nm. It can be checked that the group velocities in this configuration satisfy Eq. 2.107. Therefore, group velocity matching can be achieved in Type II phase-matching too, but the resulting gain bandwidth is much narrower than in Fig. 2.10 (a). The phase-matching parameters after gain bandwidth optimization are summarized in Table. 2.9.

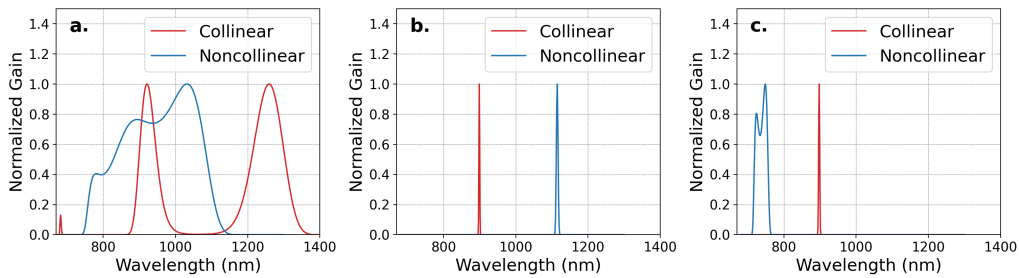


**Fig. 2.10.** Spectral gain curves provided by LBO in collinear (red) and noncollinear (blue) geometry using  $ssf$  (a),  $sff$  (b) and  $fsf$  (c) type phase-matching. The blue curves also represent the broadest achievable spectrum on the 650 nm to 1200 nm range in the corresponding interaction type.

### 2.9.4 Potassium titanyl arsenate (KTA)

Potassium titanyl arsenate (KTA) is a positive biaxial crystal belonging to the  $mm2$  point group [162]. KTA is transparent from 350 nm to 5000 nm [168] and the principal refractive indices are ordered as  $n_x < n_y < n_z$  [169]. Due to this latter property,

**Table 2.9.** Phase-matching parameters in LBO after gain bandwidth optimization.

Type	ssf	sff	fsf
Plane	XY	YZ	XZ
$\lambda_i$ (nm)	1301	1022	1927
$\lambda_s$ (nm)	900	1110	735
$\lambda_p$ (nm)	532	532	532
$\theta_i$ (°)	90	10.1	12.43
$\theta_s$ (°)	90	10.1	0.79
$\theta_p$ (°)	90	10.1	3.98
$\phi_i$ (°)	11.68	90	0
$\phi_s$ (°)	14.77	90	0
$\phi_p$ (°)	13.51	90	0
$d_{eff}$ (pm V <sup>-1</sup> )	0.82	0.66	0.64

the formulas for calculating refractive indices, walk-off angles and polarization directions of the slow and fast waves in the principal planes are the same as in case of LBO crystals. The temperature dependent Sellmeier equations of the principal refractive indices are obtained by Kato et al. [169] and indicated by Eqs. 2.151 and 2.152.

$$\begin{aligned}
n_x^2 &= 5.55552 + \frac{0.04703}{\lambda^2 - 0.0403} + \frac{602.9734}{\lambda^2 - 249.6806} \\
n_y^2 &= 5.70174 + \frac{0.04837}{\lambda^2 - 0.04706} + \frac{647.9035}{\lambda^2 - 254.7727} \\
n_z^2 &= 6.98362 + \frac{0.06644}{\lambda^2 - 0.05279} + \frac{920.3789}{\lambda^2 - 259.8645}
\end{aligned} \tag{2.151}$$

$$\begin{aligned}
\frac{dn_x}{dT} &= \left( \frac{0.6086}{\lambda^3} - \frac{1.2878}{\lambda^2} + \frac{0.9073}{\lambda} + 0.4294 \right) \cdot 10^{-5} \text{ } ^\circ\text{C}^{-1} \\
\frac{dn_y}{dT} &= \left( \frac{0.9568}{\lambda^3} - \frac{1.9496}{\lambda^2} + \frac{1.3307}{\lambda} + 0.6421 \right) \cdot 10^{-5} \text{ } ^\circ\text{C}^{-1} \\
\frac{dn_z}{dT} &= \left( \frac{1.5855}{\lambda^3} - \frac{4.2712}{\lambda^2} + \frac{4.1149}{\lambda} + 0.7051 \right) \cdot 10^{-5} \text{ } ^\circ\text{C}^{-1}
\end{aligned} \tag{2.152}$$

The elements of the nonlinear tensor (Eq. 2.153) were measured by Pack et al. [170].

$$d = \begin{pmatrix} 0 & 0 & 0 & 0 & 2.3 & 0 \\ 0 & 0 & 0 & 3.64 & 0 & 0 \\ 2.3 & 3.66 & 15.5 & 0 & 0 & 0 \end{pmatrix} \tag{2.153}$$

Since the transparency range of KTA extends up to 5  $\mu\text{m}$ , it is widely utilized for frequency up-conversion (DFG/OPA) into the mid-infrared (mid-IR) spectral range. Unlike most of the other mid-IR nonlinear crystals, KTA is highly transparent at 1  $\mu\text{m}$ . Therefore, it can be pumped by 1030 nm or 1064 nm wavelength pulses provided by the well-established neodymium (Nd) or ytterbium (Yb) based pump lasers [171–173].

The collinear phase-matching optimization of KTA in case of  $\lambda_i = 3110$  nm,  $\lambda_s = 1540$  nm and  $\lambda_p = 1030$  nm idler, signal and pump central wavelengths are shown in Fig. 2.11 (a)-(c) for *ssf*, *sff* and *fsf* type interactions.

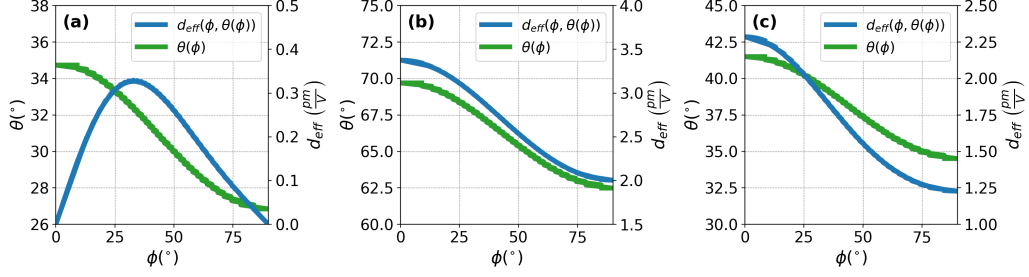


**Fig. 2.11.** Propagation directions where the phase-mismatch is zero ( $\Delta k = 0$ ) (green curves) and the values of the effective nonlinear coefficient ( $d_{eff}$ ) along these directions (blue curves) in case of *ssf* (a), *sff* (b) and *fsf* (c) interaction type.

The maximum values of the effective nonlinear coefficients and the corresponding propagation directions are summarized in Table. 2.10 in case of each phase-matching type. In case of Type I (*ssf*) interaction, the formulas for calculating the refractive

**Table 2.10.** Propagation direction ( $\theta, \phi$ ) where the maximum value of  $d_{eff}$  occurs in case of each phase-matching type.

Type	$d_{eff}$ (pm V <sup>-1</sup> )	$\theta$ (°)	$\phi$ (°)	Comment
ssf	0.33	32.5	32.93	-
sff	3.38	69.7	0	XZ plane
fsf	2.29	41.5	0	XZ plane

indices, walk-off angles and polarization directions (Eqs. 2.56, 2.57 and 2.55) cannot be simplified. Type II. phase-matching, on the other hand, can be most efficiently utilized in the XZ principal plane. The angle between the optical and Z principal axes is  $V_z = 15^\circ$ , so  $V_z < \theta$  in case of both *sff* and *fsf* type interactions. Therefore, in the XZ plane of KTA the opposite situation occurs as in the XZ plane of LBO where  $V_z > \theta$ . Consequently, the slow and fast subscripts have to be interchanged according to Eqs. 2.154, 2.155 and 2.156.

$$n_f = n_y \quad n_s = \frac{n_x n_z}{\sqrt{n_x^2 \sin^2 \theta + n_z^2 \cos^2 \theta}} \quad (2.154)$$

$$\rho_f = 0 \quad \tan \rho_s = \frac{(n_z^2 - n_x^2) \tan \theta}{n_z^2 + n_x^2 \tan^2 \theta} \quad (2.155)$$

$$\mathbf{d}_f = \mathbf{e}_f = \begin{pmatrix} 0 \\ 1 \\ 0 \end{pmatrix} \quad \mathbf{d}_s = \begin{pmatrix} \cos \theta \\ 0 \\ -\sin \theta \end{pmatrix} \quad \mathbf{e}_s = \begin{pmatrix} \cos(\theta - \rho) \\ 0 \\ -\sin(\theta - \rho) \end{pmatrix} \quad (2.156)$$

The blue gain curves in Fig. 2.12 (a)-(c) illustrate the results of gain bandwidth optimization on the 1400 nm to 1800 nm spectral range, while the red curves indicate

the spectral gain in case of collinear propagation. The phase-matching parameters are summarized in Table 2.11. In case of *ssf* (Fig. 2.12 (a)) and *sff* (Fig. 2.12 (b)) type interaction, group velocity matching is not possible, thus bandwidth optimization in noncollinear geometry provided the same output spectrum. In case of *fsf* type phase-matching (Fig. 2.12 (c)), the group velocities of the idler and signal pulses can be matched at  $\alpha = 3.6^\circ$  noncollinear angle, which results in a very broad gain spectrum ranging from 1430 nm to 1740 nm (blue curve in Fig. 2.12 (c)). Therefore, *fsf* type interaction in the XZ-plane can be well utilized for the amplification of broadband short-wave-infrared (SWIR) pulses or for the generation of mid-IR pulses by DFG. It must be noted that during DFG/OPA noncollinear propagation introduces angular dispersion into the mid-IR (idler) pulse, which has to be compensated [173, 174]. Another way to obtain angular dispersion free idler pulse is by using collinear propagation at the expense of gain bandwidth, which is illustrated by the red curve in Fig. 2.12 (c).

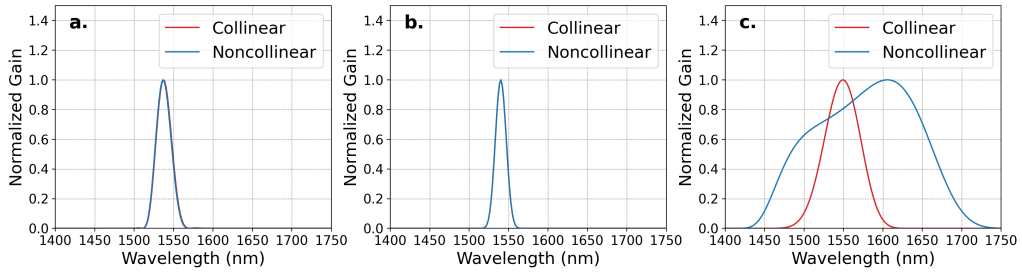


**Fig. 2.12.** Spectral gain curves provided by KTA in collinear (red) and noncollinear (blue) geometry using *ssf* (a), *sff* (b) and *fsf* (c) type phase-matching.

**Table 2.11.** Phase-matching parameters in KTA after gain bandwidth optimization.

Type Plane	ssf $\phi = 32.93^\circ$	sff XZ	fsf XZ
$\lambda_i$ (nm)	3110	3110	3110
$\lambda_s$ (nm)	1540	1540	1540
$\lambda_p$ (nm)	1030	1030	1030
$\theta_i$ ( $^\circ$ )	31.9	69.7	60.39
$\theta_s$ ( $^\circ$ )	33.1	69.7	49.2
$\theta_p$ ( $^\circ$ )	32.7	69.7	52.8
$\phi_i$ ( $^\circ$ )	32.93	0	0
$\phi_s$ ( $^\circ$ )	32.93	0	0
$\phi_p$ ( $^\circ$ )	32.93	0	0
$d_{eff}$ (pm V $^{-1}$ )	0.33	3.38	2.29

# Chapter 3

## Results

### 3.1 Cascaded-extraction OPA

One aim of this work is to examine further possibilities for the enhancement of OPCPA efficiency. In order to increase conversion efficiency, a cascaded-extraction OPA (CE-OPA) design was proposed.

CE-OPA consists of two crystals of the same type, crystallographic cut and orientation with respect to the laboratory frame. The difference between them is that the first is thicker than the second one, and there is a dielectric coating on the rear surface of the first crystal, which highly reflects (HR) the idler, but highly transmits (HT) the pump and signal (Fig. 3.1).

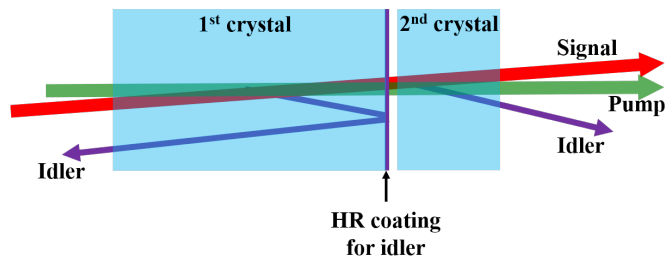


**Fig. 3.1.** Scheme of CE-OPA configuration. HR - high reflection coating [Adapted] with permission from [Ref. [T1]] © The Optical Society.

The main idea behind CE-OPA can be simply explained in the temporal domain with the help of a Gaussian shaped pump pulse. The strategy is to first extract the energy from the leading and trailing edge of the pump, where the intensity is low. If pump intensity is low, crystal thickness, which is needed to deplete the pump, is long. Therefore, the first crystal is longer than in a conventional OPA and this way the pump energy is extracted from the leading and trailing edge. The intensity at the central part of the pump is higher than at the edges. Therefore, it will be depleted sooner and by reaching the end of the first crystal, it will be almost completely re-generated. In the second step, the pump energy is extracted from this re-generated central region in the second crystal. Before the pulse enters the second crystal, it is necessary to separate the idler pulse with a HR coating to prevent its recombination with the signal in the following crystal. Therefore, in the second crystal the originally low intensity parts of the pump will remain empty and the energy from the central high intensity part will flow into the signal and the newly

generated idler pulses. Since an intense pump depletes sooner during interaction, the thickness of the second crystal is shorter than in a conventional OPA. This compact solution results in a highly depleted pump and increased pump-to-signal conversion efficiency.

CE-OPA combines the advantages of three techniques: complementary seed pulse shaping, pump-recycling and QPA, which are introduced in Section 2.5. During the amplification of the signal periphery in the first crystal, a complementary seed-pump shape is created which can efficiently interact in the second crystal. Similarly to QPA or the special QPM design, the idler is extracted during interaction to prevent signal back-conversion. It is important to note that in CE-OPA idler extraction will not induce heat, thus will not diminish the biggest advantage of OPA. Furthermore, unlike the previously mentioned QPM design, CE-OPA is based on simple nonlinear crystals available in large apertures, thus it can be applied in PW class OPCPA systems too. The similarity between pump-recycling and CE-OPA is that both techniques use two crystals, however their operational conditions are different. During pump-recycling the first crystal is a conventional OPA, which is operated under conditions to provide high efficiency, while the first crystal in CE-OPA is operated in the deep re-conversion regime to gain the energy from the pump periphery too.

### 3.1.1 Modeling parameters

Pump-to-signal conversion efficiency is an important aspect of every OPCPA, but its relevance in case of PW-class system is even more pronounced. Therefore, the operation of CE-OPA is numerically demonstrated on the example of a hypothetical PW OPCPA, but with realistic crystal and pulse parameters. These systems can be driven by the second harmonic of Nd:glass [15] or Yb:YAG pump lasers [175, 176]. In this modeling example the second harmonic of a kJ-level Yb:YAG laser was assumed as the pump source, delivering 1.2 ns pulses at 515 nm. Such pump parameters require a large aperture crystal to avoid damage. Deuterated potassium dihydrogen phosphate (DKDP) crystals can grow to an aperture as big as 90 cm [163], have a high damage threshold and can amplify over a broad bandwidth around 910 nm in noncollinear phase-matching geometry [177], as it is illustrated in Section 2.9.2. These properties make DKDP an ideal nonlinear material in PW class OPCPAs. The generation of an energetic seed around 910 nm is also straightforward by the pre-amplification of the spectrally broadened Ti:Sapphire [177] or Yb:KGW [36, 178] laser pulses. The phase-matching and pulse parameters are summarized in Table 3.1 and 3.2.

**Table 3.1.** Broadband phase-matching parameters in DKDP.

$\theta$ (°)		37.44
$\phi$ (°)		45
$\alpha$ (°)		1.06
$d_{eff}$ (pm/V)		0.25

During the simulations, three different scenarios were compared. In Case 0 spatiotemporal shaping is not involved, so the pump has a 3D Gaussian intensity dis-

tribution. In Case 1, only spatial shaping is applied to the pump, thus the temporal and spatial shapes are 1<sup>st</sup> and 6<sup>th</sup> order Gaussian distributions. Finally, in Case 2, the pump is a spatiotemporally shaped 3D 6<sup>th</sup> order Gaussian distribution. The peak intensity, the FWHM duration and the diameter of the pump were the same in all cases, consequently their energy was different. These parameters are summarized in Table 3.2.

The simulation of this PW-class OPCPA was carried out by using the numerical OPCPA code and methods described in Section 2.8.1.

**Table 3.2.** Pump and seed pulse parameters used for the modeling of PW-class OPCPA.

		Pump	Seed
$\lambda_C$ (nm)		515	910
$\Delta\lambda_{FWHM}$ (nm)	case 0	$3.2 \cdot 10^{-4}$	100
	case 1	$3.2 \cdot 10^{-4}$	
	case 2	$6.2 \cdot 10^{-4}$	
$GDD$ (ps <sup>2</sup> )		0	4.35
$\tau_{FWHM}$ (ns)		1.2	1
Temporal shape	case 0	1 <sup>st</sup> order Gauss	1 <sup>st</sup> order Gauss
	case 1	1 <sup>st</sup> order Gauss	
	case 2	6 <sup>th</sup> order Gauss	
$FWHM$ (cm)		40	30
Spatial shape	case 0	1 <sup>st</sup> order Gauss	1 <sup>st</sup> order Gauss
	case 1	6 <sup>th</sup> order Gauss	
	case 2	6 <sup>th</sup> order Gauss	
$Energy$ (J)	case 0	2311	2
	case 1	1580	
	case 2	1466	
$I_{PEAK}$ ( $\frac{GW}{cm^2}$ )		1	0.002

### 3.1.2 Improvement of conversion efficiency

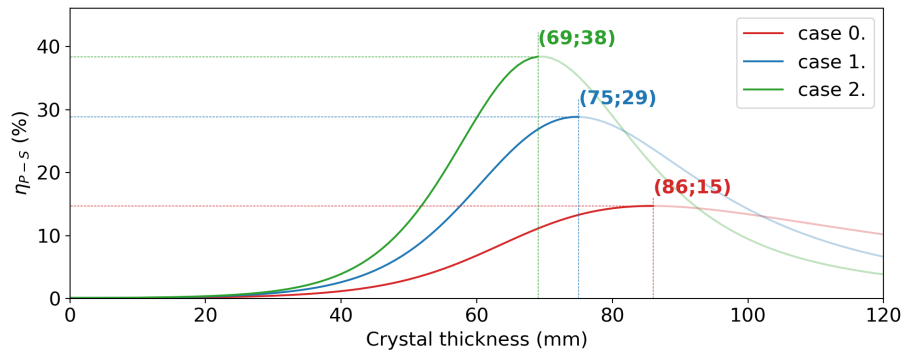


**Fig. 3.2.** Pump-to-signal conversion efficiency ( $\eta_{P-S}$ ) of conventional OPA as a function of the crystal thickness in case of different spatiotemporal pump shapes (details in Table 3.2). The values in the brackets indicate the maximum positions.

In Fig. 3.2 the pump-to-signal conversion efficiency is plotted as a function of DKDP crystal thickness in case of different spatiotemporal pump pulse shapes. The optimal crystal thicknesses for OPA are 86 mm, 75 mm and 69 mm in Cases 0, 1 and 2. The highest efficiency, 38%, is reached in Case 2, when the pump was shaped both spatially and temporally. The use of longer crystals results in strong pump re-conversion and decreased efficiency. In fact, at the point of maximum efficiency already a considerable portion of the pump is reconverted. This is illustrated in Fig. 3.4 (a) and (b), where the 1D spatial and temporal segments of pump and signal pulses are plotted in Case 1.

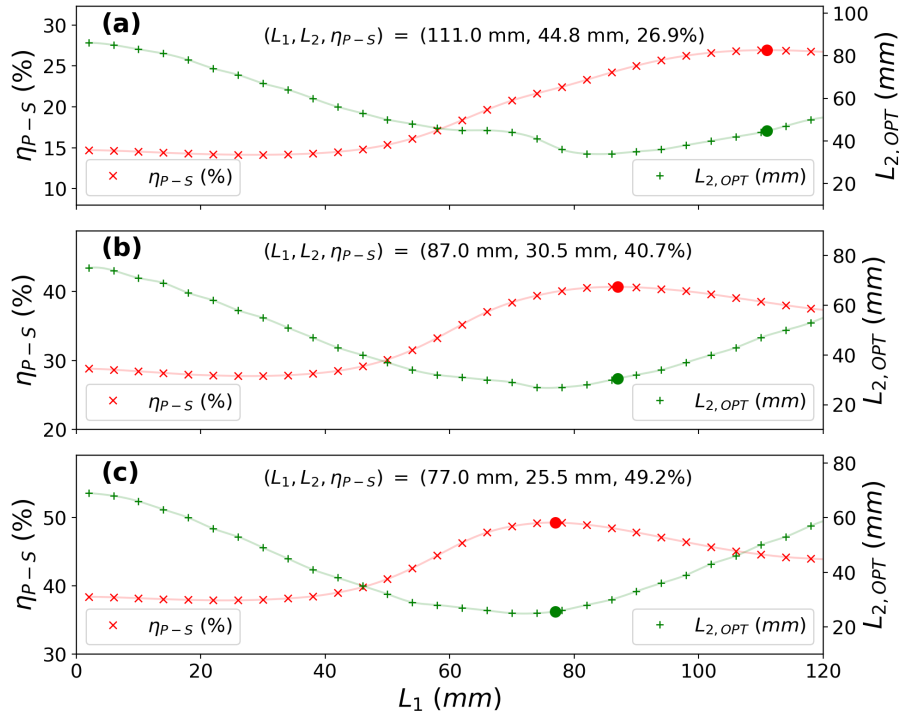


**Fig. 3.3.** CE-OPA optimization in Case 0 (a), Case 1 (b) and Case 2 (c). The red crosses (left axis) and green pluses (right axis) represent the pump-to-signal conversion efficiency ( $\eta_{P-S}$ ) and optimal thickness of the second crystal ( $L_{2,OPT}$ ) as a function of the first crystal thickness ( $L_1$ ). The red dots indicate the maximum values of conversion efficiency, achieved at crystal thicknesses indicated by the green dots.

In CE-OPA, the optimal crystal thicknesses can be determined by numerical optimization visualized in Fig. 3.3 for the three cases. The thickness of the first crystal ( $L_1$ ) is varied from 0 mm to 120 mm in steps of 4 mm, and for each value OPA was simulated in the first crystal. Before entering the second crystal, the idler was omitted and for every  $L_1$  the amplification in the second crystal was simulated and the optimum thicknesses ( $L_{2,OPT}$ ) were determined by finding the maximum positions of the efficiency curves. In Fig. 3.3 the pump-to-signal conversion efficiency ( $\eta_{P-S}$ ) and  $L_{2,OPT}$  are plotted as a function of  $L_1$  by red crosses and green pluses, respectively. The continuous lines are the cubic spline interpolations of the discrete data. Note that at  $L_1 = 0$  mm CE-OPA becomes a conventional OPA. The optimum configuration for CE-OPA is determined by the position ( $L_1, L_2$ ) where conversion efficiency has the maximum value. These positions are indicated by the red and green dots and their values are also printed on the graphs. The optimization curves (Fig.3.3) indicate that the first (second) crystal is always thicker (thinner) than the crystal thickness in a conventional OPA. The 1D spatial and temporal segments of pump and signal pulses in Case 1 after the first crystal of CE-OPA are plotted in Fig.3.4 (c) and (d). They indicate that the central part of the pump is almost reconverted and the depleted region is moved towards the peripheries, which means that more energy is extracted from those parts than in a conventional OPA. It can be also noted that the pump and signal shapes are conformal [108], which ensures high efficiency in the second crystal. The spatial and temporal shape of the pump and signal pulses after the second crystal in Case 1 are plotted in Fig. 3.4 (e) and (f).

The pump is more depleted and the signal is smoother than in a conventional OPA (Fig.3.4 (a) and (b)). The pump-to-signal conversion efficiencies of OPA and CE-OPA in the three cases are compared and summarized in Table 3.3. Based on these results, it can be concluded that the CE-OPA scheme increases the pump-to-signal conversion efficiency by 11%.

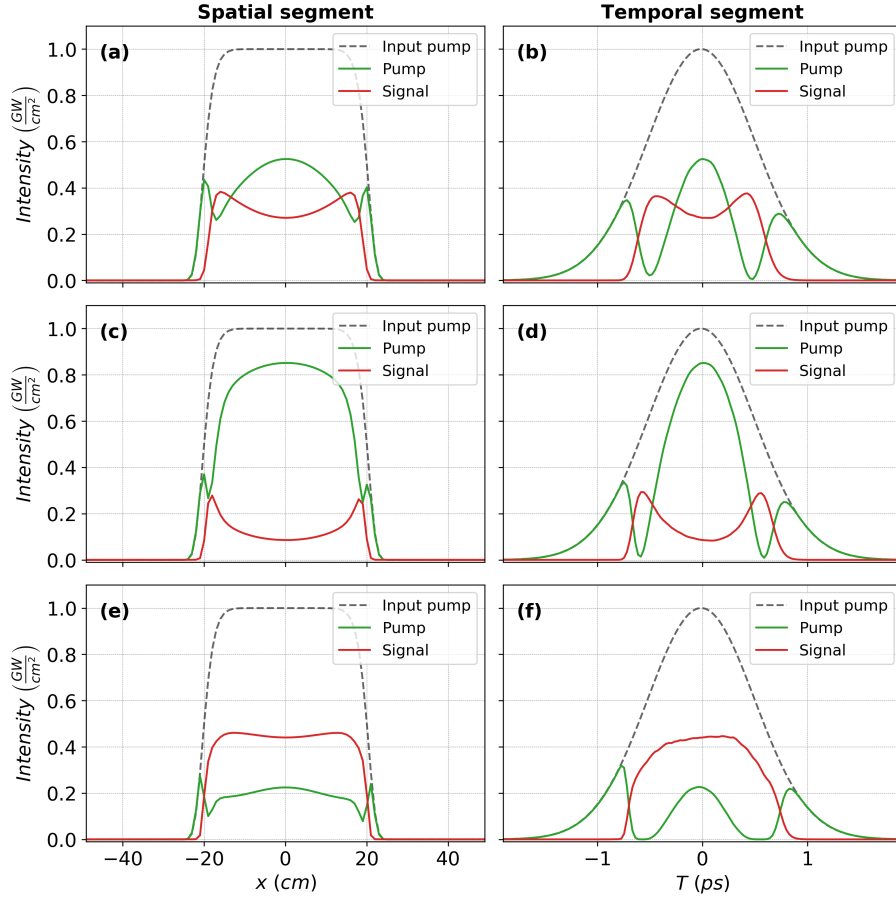


**Fig. 3.4.** Spatial (a-e) and temporal (b-f) segments of the pump (green) and signal (red) pulses in case 1, after OPA (a, b); 1<sup>st</sup> crystal of CE-OPA (c, d); and 2<sup>nd</sup> crystal of CE-OPA. The black dashed curve illustrates the input pump. [Adapted] with permission from [Ref. [T1]] © The Optical Society.

**Table 3.3.** Pump-to-signal conversion efficiency in OPA and CE-OPA under the same conditions.

		OPA	CE-OPA
$\eta_{P-S}$ (%)	case 0.	15	26.9
	case 1.	29	40.7
	case 2.	38	49.2

Figure 3.5 shows the spatiotemporal shape of the input (a, d, g) and the depleted pump pulses after OPA (b, e, h) and CE-OPA (c, f, i) in Case 0 (a, b, c), Case 1 (d, e, f) and Case 2 (g, h, i). The level of pump depletion is indicated in the figures in each case. According to Table 2.2, CE-OPA alone has similar efficiency as pump

recycling, but when combined with spatial or spatiotemporal pump shaping it can be the most efficient OPA scheme by extracting 86.6% of the total pump energy.

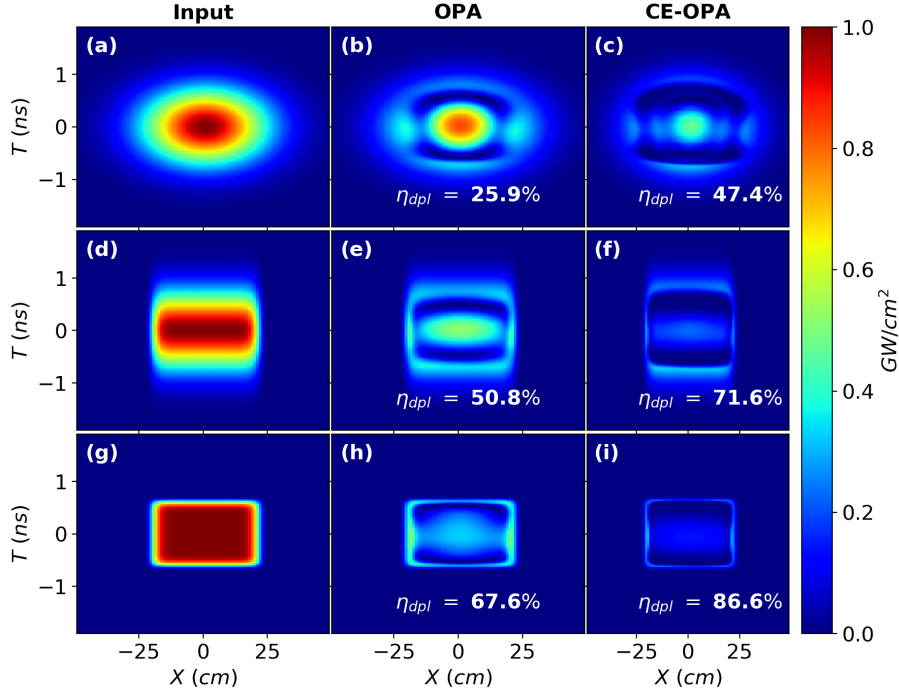


**Fig. 3.5.** Pump depletion level ( $\eta_{dpl}$ ) in OPA (b)-(h) and CE-OPA (c)-(i) in Case 0 (a)-(c), Case 1 (d)-(f) and Case 2 (g)-(i). The input spatiotemporal shapes are shown in subplots (a)-(g).

### 3.1.3 Pulse properties of OPA and CE-OPA

In the previous section I presented in detail how the CE-OPA scheme increases pump-to-signal conversion efficiency. It is also important to examine the properties of the amplified pulses such as pulse duration, compressibility, near-time contrast and the focusability of the amplified pulses.

The spectra after OPA and CE-OPA in the three cases are compared in Fig. 3.6 (a), (c) and (e). In all cases, CE-OPA provides a slightly broader bandwidth than conventional OPA. The bandwidth is quantified by the root-mean-square (RMS) deviation of the spectrum (Eq. 2.12), and the Fourier limited pulse durations, which are summarized in Table 3.4 for the three cases.

Usually, it is impossible to zero the spectral phase at every  $(x, y)$  coordinate of the spatio-spectral electric field  $E(x, y, \omega)$ , due to STCs. Therefore, the best-case compressibility is calculated by using Eq. 2.20 and compared to the Fourier limited pulse duration in Table 3.4.

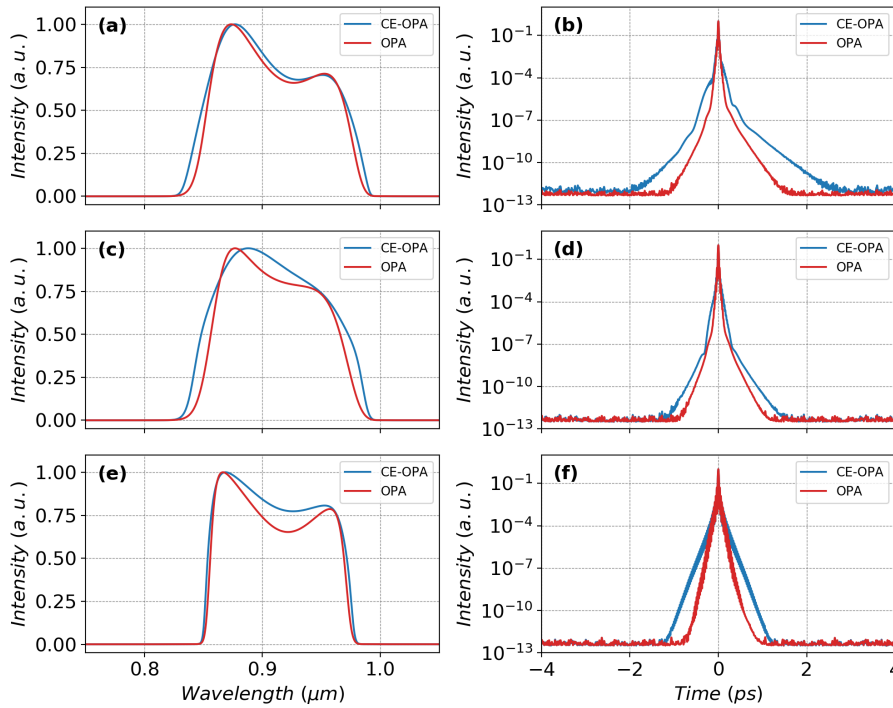
Based on Table 3.4, it can be concluded that CE-OPA can provide shorter compressed pulses ( $\tau_{comp}$ ) than OPA. Furthermore, by comparing the difference in the Fourier limited pulse durations calculated from the pulse power  $P(t)$  ( $\tau_{FL}$ ) and the pulse intensity at the center of mass  $I(x_c, y_c, t)$  ( $\tau_{x_c, y_c}$ ), it can be concluded that the amplified pulses after CE-OPA have a more homogeneous bandwidth and spectral phase across the beam profile than after OPA. The only exception is Case 2, where OPA and CE-OPA provides the same values due to the super-Gaussian spatiotemporal pump shape.

**Table 3.4.** Comparison of bandwidth, pulse duration and Strehl ratio of the signal after OPA and CE-OPA.

	Case 0		Case 1		Case 2	
	OPA	CE-OPA	OPA	CE-OPA	OPA	CE-OPA
$RMS_{\omega}$ (THz)	84.2	89.0	78.6	85.6	78.7	79.3
$\tau_{FL}$ (fs)	16.8	16.4	17.6	16.4	18.8	18.8
$\tau_{x_c, y_c}$ (fs)	14.4	14.8	16.4	16.0	18.4	18.4
$\tau_{comp}$ (fs)	17.0	16.6	17.6	16.6	19.0	19.0
Strehl ratio	0.97	0.93	0.99	0.98	0.99	0.99

The shape of the compressed pulses after OPA and CE-OPA in the three cases are plotted in Fig. 3.6 (b), (d) and (f) on a logarithmic scale. They illustrate that the steepening of the pulse spectrum in CE-OPA lead to longer pedestal in the time domain. As a consequence, the near-time contrast of CE-OPA is slightly deteriorated in the  $-2$  ps to  $2$  ps window compared to OPA, but during experiments it is still low enough to preserve the solid target conditions before the main pulse [179].

Finally, the most important parameter which determines the achievable peak intensity in the focus is the Strehl ratio. The Strehl numbers calculated by the modified definition (Eq. 2.28) are summarized in Table 3.4. Although the first crystal of CE-OPA operates in the back-conversion regime, the spatiotemporal quality of the amplified signal after the second crystal is not deteriorated significantly compared to OPA.

**Fig. 3.6.** Spectrum (a, c and e) and near-time contrast (b,d and f) of OPA (red) and CE-OPA (blue) in case 1 (a, b), case 2 (c, d) and case 3 (e, f). [Adapted] with permission from [Ref. [T1]] © The Optical Society.

### 3.1.4 Summary

**T1** I have numerically examined the properties of the cascaded-extraction optical parametric amplifier (CE-OPA) design and revealed that CE-OPA increases conversion efficiency by at least 10%, without deteriorating the spatiotemporal shape of the amplified signal[T1].

## 3.2 Few-cycle OPCPA development

### 3.2.1 SYLOS system and the upgrade strategy

The first development phase of the Single-Cycle laser system (SYLOS 1) in ELI-ALPS was the first TW-level system which operated at 1 kHz repetition rate and provided 5.5 TW, sub-9 fs pulses with passive CEP-stabilization [36]. The aim during the second development phase, SYLOS 2, was to improve compressed pulse duration close to 2 cycle. The details of both the SYLOS 1 and SYLOS 2 systems are well described in refs. [36] and [T2], therefore here I provide only a short summary about the most important aspects.

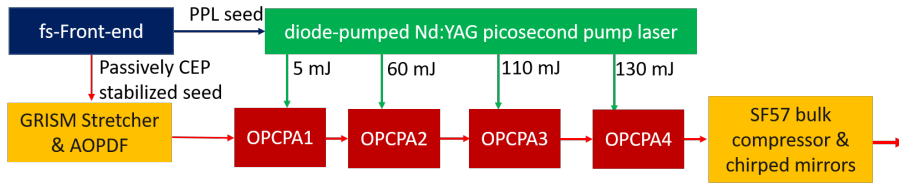


**Fig. 3.7.** Schematics of SYLOS system.

Figure 3.7 illustrates the simplified schematics of the system. The femtosecond front-end consists of a diode-pumped Yb:KGW oscillator and a regenerative amplifier (Pharos, Light Conversion Ltd.), which is extended by a CEP-module producing passively CEP-stabilized pulses at 2.4  $\mu\text{m}$  wavelength. These pulses are spectrally broadened in sapphire, and the near-IR part (700 nm to 1300 nm) of the broadband supercontinuum is amplified in two subsequent femtosecond noncollinear OPA stages (fs-NOPA) to 70  $\mu\text{J}$  energy level. Since both SPM and OPA are phase preserving nonlinear processes, the energetic seed pulses after fs-NOPA are also CEP-stable. The seed pulses are chirped negatively by the combination of a grism stretcher [148] and an acousto-optic programmable dispersive filter (AOPDF)[180]. A typical seed spectrum is plotted by the continuous red curve in Fig. 3.8. a. (the seed spectrum in case of the SYLOS 1 system is also visible as a reference). From the measured spectrum and the theoretical spectral phase of the stretcher I calculated the temporal shape of the signal pulse before amplification, which is shown by the red curve in Fig. 3.8. b. The measured spatial intensity distribution of the seed pulse after the stretcher is shown in Fig. 3.8. c. After amplification in four noncollinear OPCPA stages, the pulses are compressed using the combination SF57 and FS bulk glasses and eight pairs of positively chirped mirrors. The large positive second- and third-order dispersion (GDD and TOD) of the compressor glasses are mostly pre-compensated by the grism stretcher, while the higher phase orders are canceled by the AOPDF.

The seed for the picosecond pump laser (PPL) (Fig. 3.7) is also provided by the Yb:KGW oscillator. This ensures passive synchronization between pump and signal pulses in the OPCPA chain. The PPL consists of four diode pumped Nd:YAG regenerative amplifiers, which are followed by diode pumped Nd:YAG power amplifiers. This setup provides four pump channels for the four OPCPA stages. The envelope of the pump pulses in the first two pump lines are shaped by cascaded second harmonic generation [27], which results in a flattened temporal pump pulse shape as it is illustrated by the blue curve in Fig. 3.8.b. The temporal shape of

the pump in the last two channels can be well approximated by 1<sup>st</sup> order Gaussian functions, as it is illustrated by the green curve in Fig. 3.8.b.

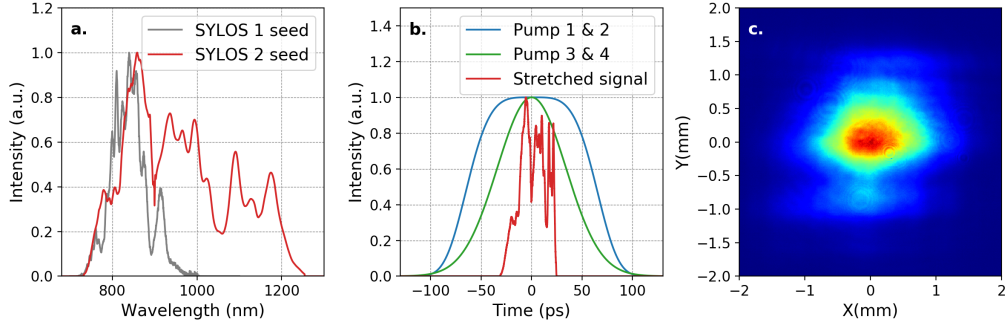


**Fig. 3.8.** a. Seed spectrum for the ps-OPCPA stages after the fs-NOPA front-end. b. Temporal shape of the pump in the first two (blue) and last two OPCPA stages (green) and the temporal shape of the stretched signal pulse before amplification. c. Seed beam profile after the stretcher. (Adopted from Ref. [T2])

The beam profile of the first pump channel in the plane of the first NOPCPA stage is shown in Fig. 3.9. a. The spatial profile of the pump pulses in the other three pump lines are shaped by spatially variable beam shapers [26], which provide a roughly 10<sup>th</sup>-order super-Gaussian spatial intensity distribution for the last three OPCPA stages. The measured pump beam profiles in the plane of the amplifier crystals are shown in Fig. 3.9.

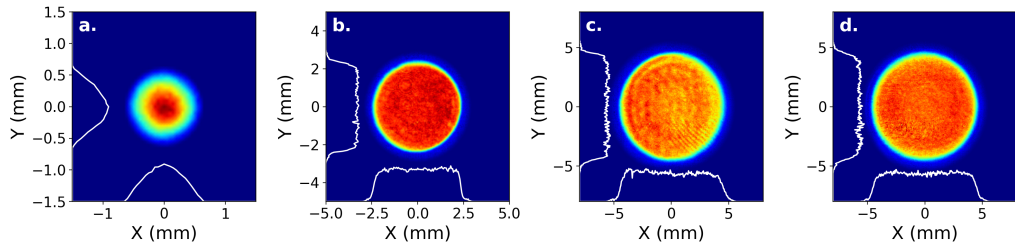


**Fig. 3.9.** Measured beam profiles of the pump in the 1<sup>st</sup> (a), 2<sup>nd</sup> (b), 3<sup>rd</sup> (c) and 4<sup>th</sup> (d) OPCPA stage. The white curves are the insets of the pump beams at the center of mass. (Adopted from Ref. [T2])

The upgrade strategy of the SYLOS 1 system was to shorten the compressed pulse duration while keeping the peak power at the few-TW level. The goal was to approach the 2-cycle pulse duration. In order to reach this, first of all, new fs-NOPA was installed which provides a broader seed bandwidth for the OPCPA chain as it is shown in Fig. 3.8. a. The increased bandwidth required the installation of a new AOPDF, shorter bulk compressor glasses and new chirped mirrors.

One of the greatest challenges was to redesign the ps OPCPA stages to support the amplification of the increased bandwidth, which, ultimately should yield 2-cycle compressed pulses. To optimize the amplifier configurations, I carried out extensive numerical simulations, which are going to be presented in the current chapter.

Among the various bandwidth enhancing techniques summarized in Section 2.6, two-color pumping would be very promising, as it was demonstrated that this technique can deliver TW-level sub-2 cycle pulses. However, the system described in

Ref. [99] operates at 10 Hz, while SYLOS provides pulses at 1 kHz repetition rate. At hundred times larger average power optical elements have lower resilience to UV light, thus at this repetition rate this would cause higher operational risks. Therefore, in case of SYLOS a different approach is used, where different parts of the broadband seed spectrum are amplified in separate crystals, oriented in different phase-matching geometries.

### 3.2.2 Potential broadband amplifier configurations

By using the gain curve optimization described in Section 2.9.1, I identified three phase-matching configurations which can be suitable for the broadband ps-OPCPA stages. In each configuration, the corresponding polar ( $\theta$ ), azimuth ( $\phi$ ) and non-collinear ( $\alpha$ ) angles and the Fourier limited pulse duration supported by the gain curve are summarized in Table 3.5.

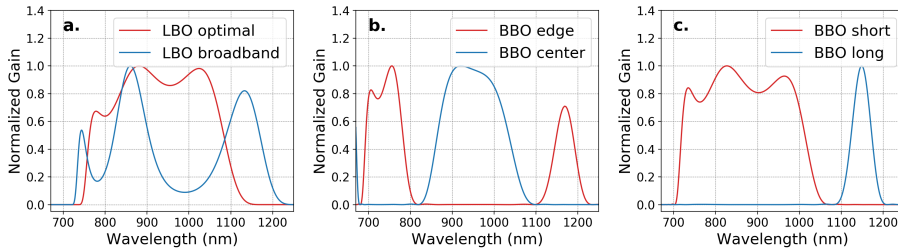


**Fig. 3.10.** Normalized spectral gain curves of single LBO (a), double-BBO in the first (b) and second (c) configurations.

The first candidate is single LBO in a slightly detuned noncollinear phase-matching geometry. The spectral gain curve of LBO in optimal configuration is plotted by the red curve in Fig. 3.10. a. Optimal configuration means that group velocity matching is satisfied, which results in a mostly flat gain curve (Section 2.9.3). In this configuration, the achievable Fourier limited pulse duration is 7 fs, which corresponds to 2.3 cycles at 900 nm central wavelength. A slight detuning of the noncollinear and phase-matching angles results in a broader, but modulated gain curve as it is illustrated by the blue curve in Fig. 3.10. a. This geometry decreases the overall conversion efficiency and leads to holes at 790 nm and 1000 nm. In turn the amplified bandwidth can support a sub-2 cycle pulse duration (Table 3.5).

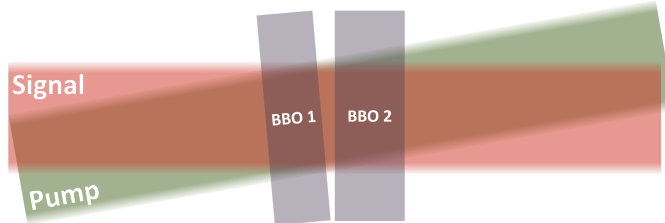


**Fig. 3.11.** Schematics of double-BBO configuration.

The other two candidates for the broadband ps-OPCPA stages are based on amplification in double-BBO pairs. The idea of the double-BBO is illustrated in Fig. 3.11. It consists of two identically cut, closely packed BBO crystals. The

noncollinear angle between the pump and signal pulses is the same in both crystals, but the phase-matching orientation is slightly different ( $\Delta\theta \approx 0.2^\circ$ ).

Bandwidth enhancement in a double-BBO can be realized in two possible configurations. In the first configuration (Fig. 3.10. (b)) one crystal amplifies the spectral edges (BBO edge: from 700 nm to 800 nm and from 1100 nm to 1200 nm) while the other one amplifies the center (BBO center: from 800 nm to 1100 nm) of the spectrum. The corresponding phase-matching and noncollinear angles are summarized in Table 3.5, where  $BBO_c$  and  $BBO_e$  refer to the orientation used for amplifying the center and edges of the spectrum.

In the second configuration (Fig. 3.10. (c)), one of the BBO crystals (BBO short) amplifies a broad wavelength range from 700 nm to 1050 nm. The phase-matching angle ( $\theta$ ) of the other crystal (BBO long) is slightly detuned so it amplifies a narrow peak around 1150 nm. The parameters of the second configuration are also summarized in Table 3.5.

**Table 3.5.** Phase-matching parameters of single-LBO and double-BBO configurations.

	LBO		Config. 1		Config. 2	
	Optimal	Broadband	$BBO_c$	$BBO_e$	$BBO_s$	$BBO_l$
$\theta$ ( $^\circ$ )	90	90	23.52	23.36	23.69	23.52
$\phi$ ( $^\circ$ )	13.42	12.63	90	90	90	90
$\alpha$ ( $^\circ$ )	1.24	1.06	2.0	2.0	2.2	2.2
$\tau_{FL}$ (fs)	7	5.3	5.3		6.1	
<i>Cycles</i>	2.3	1.8	1.74		2.06	

The gain bandwidth of a double-BBO in the first configuration is slightly larger than in the second one, consequently, they support 5.3 fs and 6.1 fs Fourier limited pulse durations. On the other hand, the second configuration can provide a spectrum with one spectral hole (at  $\approx 1070$  nm) instead of the two dips (at  $\approx 800$  nm and  $\approx 1100$  nm) of the first configuration (Fig. 3.10. (b) and Fig. 3.10. (c)). Modulations in the gain spectrum can result in modulations in the spectral phase too, making it difficult to compress the pulses.

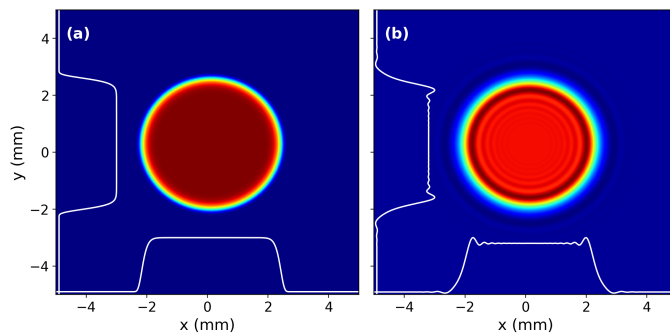


**Fig. 3.12.** Spatial intensity distribution of the pump pulse (a) in the plane of the nonlinear crystal and (b) in a plane 0.5 m farther away.

The usage of double-BBO for broadband amplification is particularly advantageous when the pump has a super-Gaussian beam profile as it is shown in Fig. 3.12. (a).

These pump pulses are delivered from the source to the nonlinear crystals by image relaying telescopes. The OPA crystals have to be placed at the image planes of these telescopes to ensure the most uniform spatial intensity distribution during amplification. Deviation from the image plane by 0.5 m results in the appearance of a diffraction pattern in the beam profile, which is illustrated in Fig. 3.12 (b). If two separated crystals were used instead of the double BBO, two additional image relaying telescopes (one for the signal and one for the pump) would be needed to avoid the diffraction pattern at the plane of the second crystal. This would increase the footprint and complexity of the setup. In the double-BBO configuration all these complications are avoided, because the plane of the second crystal is just a few millimeters behind the first one. Within this short propagation distance the pump beam preserves its super-Gaussian spatial shape.

I examined and numerically optimized the three broadband phase-matching configurations for each ps-OPCPA stage. The individual OPCPA stages were simulated by using the OPCPA code, described in Section 2.8.1, while linear pulse propagation was modeled by the methods described in Section 2.8.2. The nonparaxial spatio-spectral phase shift of spherical mirrors was taken into account as it is described in Section 2.2.2. The results of the modeling are presented in the following sections.

### 3.2.3 Numerical examination of the first OPCPA stage

The complex three-dimensional field of the signal pulse was constructed in the spatio-spectral domain from the measured spectrum (Fig. 3.8. (a)), the theoretical spectral phase of the stretcher (Table 3.6) and the measured seed beam profile (Fig. 3.8. (c)). In experimental conditions the seed pulse is loosely focused with a set of spherical mirrors, thus slightly converges as it propagates through the crystal. In the simulations the spatial phase shift introduced by a  $f = 2.5$  m spherical mirror was applied to the pulse in the spatio-spectral domain and propagated 0.5 m to have a slightly bigger size than the pump pulse. This way beam divergence was taken into account in the numerical simulations. The spatial shape of the seed and pump beams in the front surface of the nonlinear crystal are visualized in Fig. 3.13. (a) and (b). The spatiotemporal shape of the signal pulse is visualized in Fig. 3.13. (c). The seed pulse has an irregular temporal shape; therefore, the duration of the chirped signal pulse is determined at the temporal positions where the intensity drops to 1% of the peak intensity (Table 3.6). The spatiotemporal shape of the pump pulse at the input of the first stage is shown in Fig. 3.13. (d). The FWHM duration of the pump is 125 ps (Table 3.6), more than twice longer than the seed pulse. The reason for this low stretching ratio in the first stage is to avoid gain narrowing in the last stages, where the pump pulse duration is 90 ps.

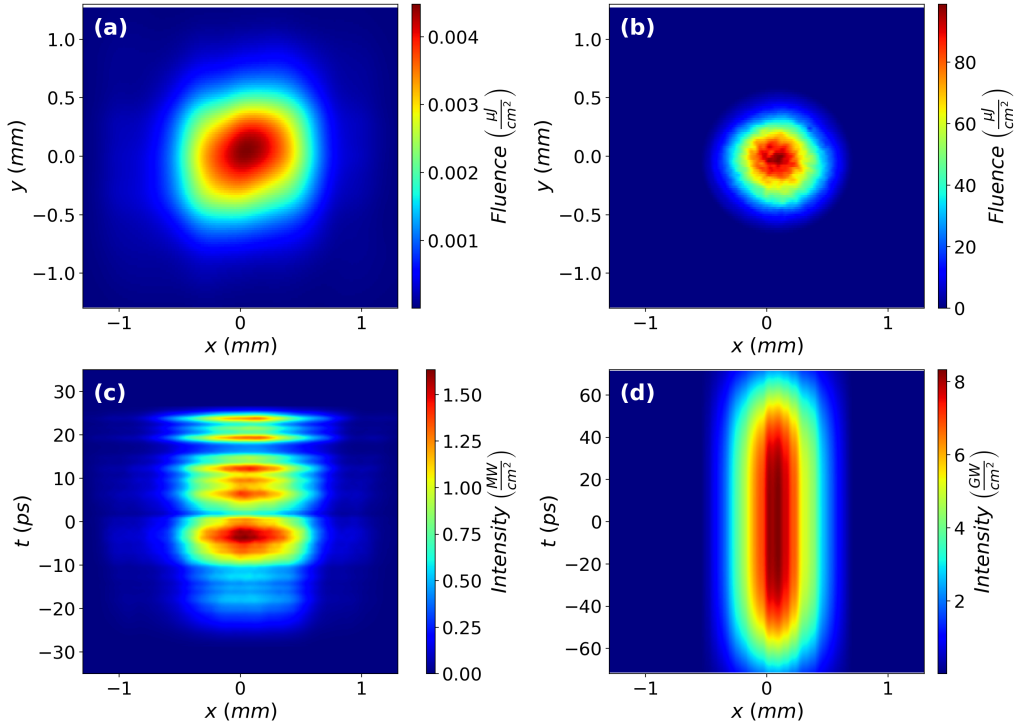


**Fig. 3.13.** Beam profile (a & b) and spatiotemporal shape (c & d) of the seed (a & c) and pump (b & d) pulses.

**Table 3.6.** Input pulse parameters of the 1<sup>st</sup> NOPCPA stage.

	Pump	Signal
Energy (mJ)	3.6	$0.45 \times 10^{-3}$
Pulse duration (ps)	125	50
FWHM (mm)	0.6	0.95
Diameter at $e^{-2}$ (mm)	1	1.5
Intensity ( $\text{GW cm}^{-2}$ )	8.4	$1.5 \times 10^{-3}$
GDD ( $\text{fs}^2$ )	-	-55000
TOD ( $\text{fs}^3$ )	-	-44000
FOD ( $\text{fs}^4$ )	-	3500

### Double-BBO in configuration 1

Fig. 3.14 (a) illustrates the energy (blue) and peak intensity (red) evolution during amplification in double-BBO. Energy saturation is reached by using a 6 mm and a 5 mm thick BBO crystal for the amplification of the edges ( $BBO_e$ ) and the central part of the spectrum ( $BBO_c$ ). The spectrum after the first ( $BBO_e$ ) and second ( $BBO_c$ ) crystal is shown in Fig. 3.14 (b) by the blue and red curves.

Despite conversion efficiency is maximized at these crystal thicknesses, the re-conversion process takes place, which results in the deterioration of spatiotemporal quality. The peak intensity (red curve in Fig. 3.14 (a)) at the spectral edges ( $BBO_e$ ) maximizes at 4.5 mm thickness. In the simulations, the order of the crystals was interchanged and it was verified that the intensity at the center of the spectrum also

reaches maximum value at 4.5 mm. Based on these result, in order to avoid signal back conversion and improve pulse quality, two 4.5 mm thick crystals are recommended. The beam profile, spatial and angular distribution of the amplified signal pulse in case of maximum conversion efficiency and peak intensity are visualized in Fig. 3.15 (a)-(c) and Fig. 3.16 (a)-(c). It can be observed that although spatio-spectral couplings are present, the intensity shape is smoother in case of shorter crystals Fig. 3.16 (b). This is proven by the Strehl numbers, which are 0.14 and 0.47 in the two cases.

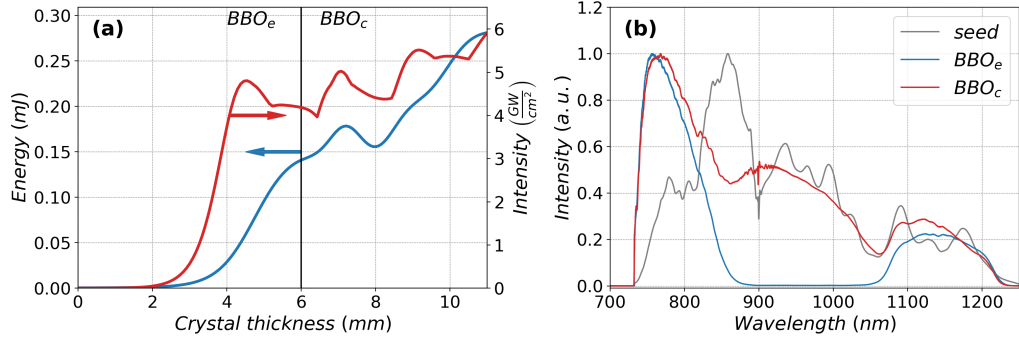


**Fig. 3.14.** Energy evolution (a) at the edges ( $BBO_e$ ) and central part ( $BBO_c$ ) of the signal spectrum (b). The grey curve illustrates the seed spectrum.

The duration of the Fourier limited pulse shape in case of the thinner crystals is 6 fs. This, however, is not identical with the best achievable compressed pulse duration due to differences in the spectral phase and shape taken at different spatial (X,Y) positions. According to Fig. 3.16 (b), the central part of the spectrum is located at a different spatial position from the edges of the spectrum. Due to the coupling of the spatial and spectral coordinates, the compressed pulse duration will be spatially dependent. In the ideal case these pulses can be compressed to 6.4 fs, which can be calculated by using Eq. 2.20. It must be noted that in case of longer crystals (6 mm + 5 mm) the duration of the Fourier limited and compressed pulse shapes are 5.6 fs and 16.2 fs, which also confirms that energy saturation has to be prevented by using thinner crystals.

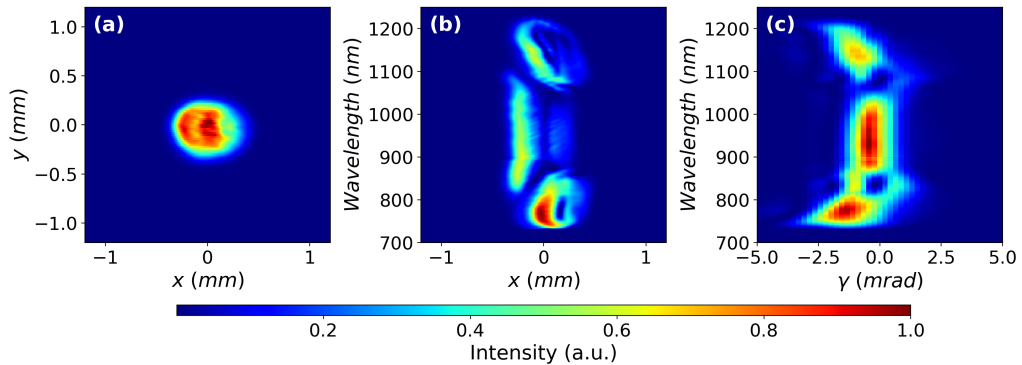


**Fig. 3.15.** Beam profile (a), spatial (b) and angular (c) distribution of the amplified signal pulse after 6 mm + 5 mm double-BBO.  $\gamma = \arcsin\left(\frac{k_x}{k}\right)$  is the propagation angle of the spectral components. The Strehl ratio is 0.14.

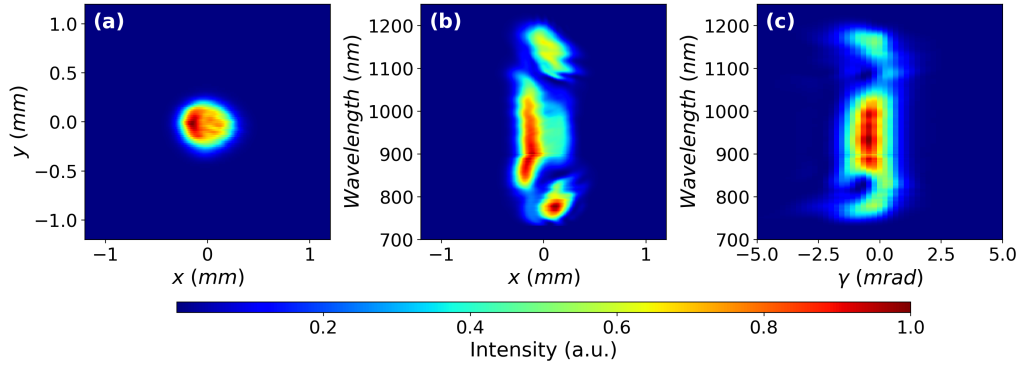


**Fig. 3.16.** Beam profile (a), spatial (b) and angular (c) distribution of the amplified signal pulse after 4.5 mm + 4.5 mm double-BBO in config. 1.  $\gamma = \arcsin\left(\frac{k_x}{k}\right)$  is the propagation angle of the spectral components. The Strehl ratio is 0.47.

Despite the improved pulse quality in case of shorter crystals, the spatial and spectral coordinates of the intensity distribution are still coupled, which is illustrated in Fig. 3.16 (b). The extent of such distortions are influenced by two factors:

1. The relationship between the spatial size of the interacting beams and the lateral pump beam displacement with respect to the signal pulse during propagation in the birefringent crystal.
2. The magnitude of the intensity gain.

The lateral displacement of the pump beam is caused by the noncollinear phase-matching geometry and the walk-off effect. There are two options to realize a noncollinear phase-matching geometry. In the first arrangement, the pump beam walks off towards the direction of the signal beam, thus improves the spatial overlap. This is called Poynting vector walk-off compensation (PVWC) scheme [181]. In the second arrangement, the pump beam moves away from the signal beam. This is called tangential phase-matching geometry (TPM) [181]. In case of the first double-BBO configuration the walk-off and noncollinear angles are  $3.36^\circ$  and  $2.02^\circ$ . In the numerical simulations (and also during experimental conditions) we use the PVWC, thus the angle between the signal propagation vector ( $\vec{k}$ ) and the Poynting vector of the pump is  $1.34^\circ$ . In a 4.5 mm thick BBO crystal this will result in a lateral shift of  $105\ \mu\text{m}$ , which is comparable to the pump beam's FWHM of  $600\ \mu\text{m}$ . The intensity gain in the first stage is on the order of  $10^3$ . Due to the high gain, the pump pulse will define the size and position of the amplified signal pulse on the output surface of the nonlinear crystal. Therefore, the pump and signal pulses on the input surface of the second crystal will perfectly overlap, however, by the end of the second crystal, the pump, thus the central part of the signal spectrum, will be spatially shifted by  $105\ \mu\text{m}$  compared to the spatial position of the edges of the spectrum. This effect is illustrated in Fig. 3.16 (b).

### Double-BBO in configuration 2

The energy and intensity evolution during amplification in the second double-BBO configuration are shown in Fig. 3.17 (a) by the blue and red curves. The energy saturates at 6 mm, while the intensity peaks at 4.5 mm thickness in case of both

BBO crystals. The spectrum after the first ( $BBO_l$ ) and second ( $BBO_s$ ) crystal is plotted in Fig. 3.17 (b).

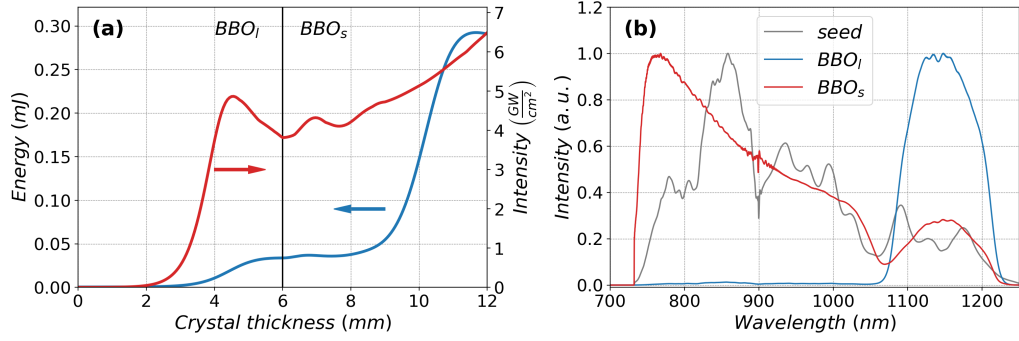


**Fig. 3.17.** Energy evolution (a) at the long ( $BBO_l$ ) and short wavelength part ( $BBO_c$ ) of the signal spectrum (b). The grey curve illustrates the seed spectrum.

Similarly to the previous configuration, the usage of two 4.5 mm BBO crystals results in improved spatio-spectral quality. The beam profile, spatial and angular distribution of the signal spectrum after 6 mm + 6 mm and 4.5 mm + 4.5 mm double-BBO are visualized in Fig. 3.15 (a)-(c) and Fig. 3.16 (a)-(c), respectively. The corresponding Strehl-numbers are 0.25 and 0.65.

The duration of the Fourier limited pulse shape is 6.4 fs, while in case of perfect phase compensation at the center of mass of the pulse profile, 6.7 fs can be reached.

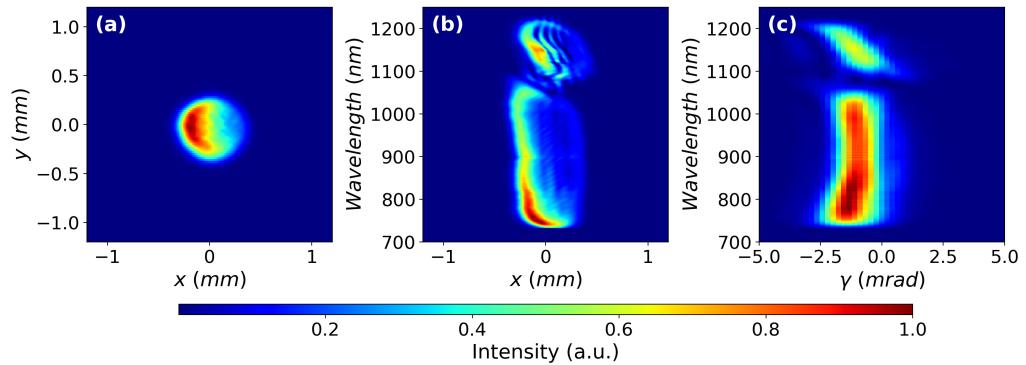


**Fig. 3.18.** Beam profile (a), spatial (b) and angular (c) distribution of the amplified signal pulse after 6 mm + 6 mm double-BBO. The Strehl ratio is 0.25.

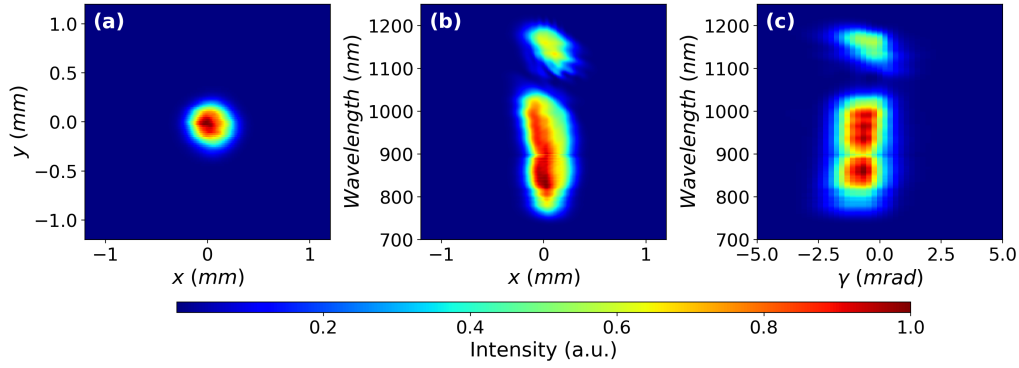


**Fig. 3.19.** Beam profile (a), spatial (b) and angular (c) distribution of the amplified signal pulse after 4.5 mm + 4.5 mm double-BBO. The Strehl ratio is 0.65.

### LBO in broadband configuration

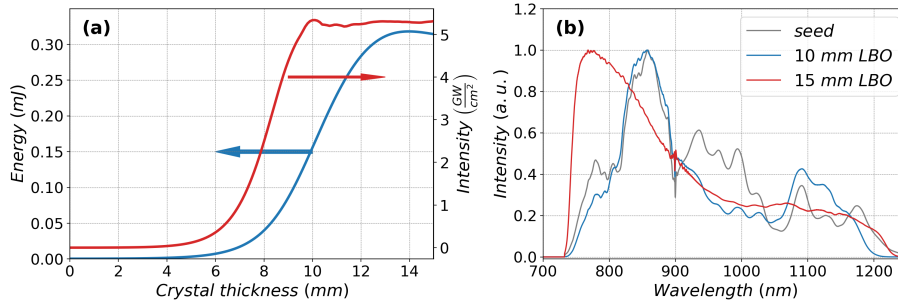


**Fig. 3.20.** (a) Energy (blue) and intensity (red) evolution of the signal during amplification in LBO. (b) Spectrum of the signal before amplification (grey), after 10 mm (blue) and 15 mm (red) thick LBO.

The energy evolution in LBO, oriented in the broadband phase-matching configuration, is plotted in Fig. 3.20 (a) by the blue curve. According to this, energy saturation is reached in case of a 15 mm thick LBO crystal, which provides the spectrum visualized by the red curve in Fig. 3.20 (b). This spectrum corresponds to 5.6 fs Fourier limited pulse duration, while in case of perfect phase compensation 6.8 fs compressed pulse duration can be reached. The beam profile, spatial and angular distribution of the signal spectrum are shown in Fig. 3.21 (a)-(c). From these figures it is clearly visible that a considerable portion of the signal pulse is back-converted, which leads to a hole in the beam profile and in the spatio-spectral shape (Fig. 3.21 (a) and (b)). According to the red curve in Fig. 3.20 (a), intensity peaks at 10 mm. The spectrum after a 10 mm thick LBO crystal is plotted by the blue curve in Fig. 3.20 (b). The spectrum supports 6.2 fs Fourier limited pulse duration and compressible to 6.4 fs.

The beam profile, spatial and angular distribution of the signal spectrum are shown in Fig. 3.22 (a)-(c), indicating a nice amplified signal pulse with negligible spatio-spectral couplings. The Strehl ratio in case of the 10 mm LBO crystal is 0.68, which suggests a good spatio-spectral pulse quality.

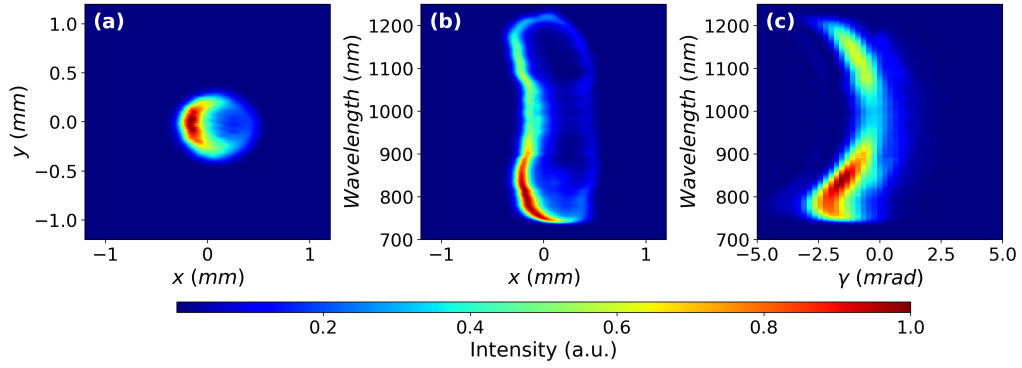


**Fig. 3.21.** Beam profile (a), spatial (b) and angular (c) distribution of the signal spectrum after amplification in a 15 mm thick LBO crystal.  $\gamma = \arcsin\left(\frac{k_x}{k}\right)$  is the propagation angle of the spectral components (angular dispersion).

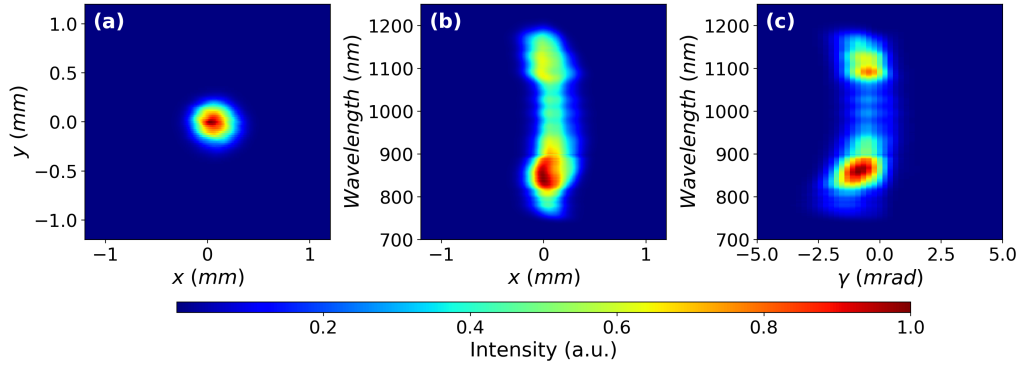


**Fig. 3.22.** Beam profile (a), spatial (b) and angular (c) distribution of the signal spectrum after amplification in a 10 mm thick LBO crystal.  $\gamma = \arcsin\left(\frac{k_x}{k}\right)$  is the propagation angle of the spectral components (angular dispersion).

### Pump recycling in a second LBO

The output parameters of the first OPCPA stage in case of the three broadband phase-matching configurations are summarized in Table 3.7. Based on the results, LBO in a broadband phase-matching geometry provides the best spatiotemporal quality, therefore it is preferred over double-BBO configurations.

**Table 3.7.** Output parameters of the three amplifier configurations

Configuration	$L_1$ (mm)	$L_2$ (mm)	E ( $\mu$ J)	F <sub>TL</sub> (fs)	$\tau_c$ (fs)	SR
Double-BBO 1	4.5	4.5	201	6	6.4	0.47
Double-BBO 2	4.5	4.5	184	6.4	6.7	0.65
broadband LBO	10	-	174	6.2	6.4	0.68

Since the pump pulse is more than twice longer than the stretched signal pulse, it can be reused in a second LBO crystal oriented in the same broadband configuration. The depleted pump after the first 10 mm thick LBO crystal is visualized in Fig. 3.23.

The pump and signal delay in the first crystal was adjusted so it would use only the first half of the pump, and leave the second half intact. In the simulations, the pump was delayed by  $-55$  ps while it propagated to the second LBO crystal so that the signal would overlap with the undepleted part.

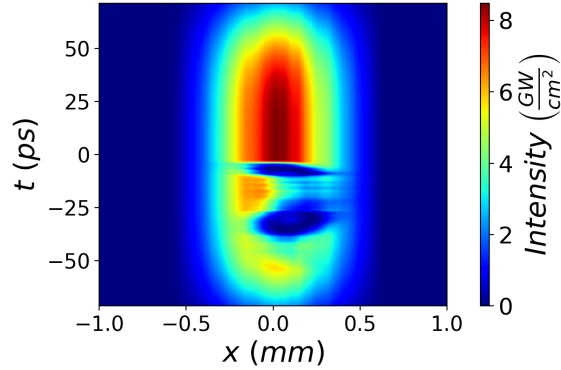


**Fig. 3.23.** Depleted pump pulse after the first LBO crystal.

The energy and peak intensity evolution in a 10 mm thick LBO crystal are plotted in Fig. 3.24 (a) by the blue and red curves, respectively. The energy saturates at 6 mm, while the intensity has a maximum at 4 mm crystal thickness. The spectrum before (grey) and after amplification using a 4 mm, 6 mm and 10 mm thick LBO crystal is shown in Fig. 3.24 (b). They support 6.4 fs, 6.2 fs and 6 fs Fourier limited pulse durations. According to these results, a longer crystal results in a shorter Fourier limited pulse duration, but poorer spatiotemporal quality. The Strehl numbers in case of 4 mm, 6 mm and 10 mm crystals are 0.61, 0.37 and 0.11. The beam profile, spatial and angular distribution of the signal spectrum after amplification in 4 mm and 6 mm thick LBO crystals are shown in Fig. 3.25 (a)-(c) and Fig. 3.26 (a)-(c), respectively. Based on these results, the pump should preferably be recycled in a 4 mm thick LBO crystal - which can provide 360  $\mu$ J pulse energy - to preserve the spatiotemporal quality.

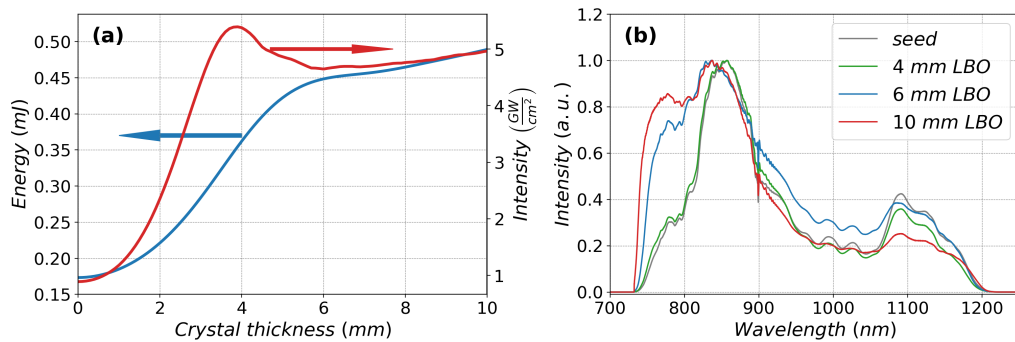


**Fig. 3.24.** (a) Energy (blue) and peak intensity (red) evolution during amplification in LBO crystals. (b) Spectrum before (grey) and after amplification in 4 mm (green), 6 mm (blue) and 10 mm (red) thick LBO crystals.

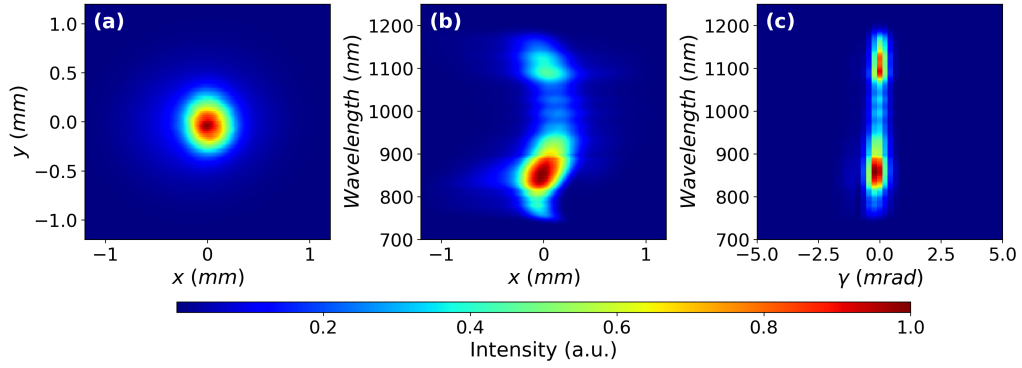


**Fig. 3.25.** Beam profile (a), spatial (b) and angular (c) distribution of the signal spectrum after amplification in a 4 mm thick LBO crystal.  $\gamma = \arcsin\left(\frac{k_x}{k}\right)$  is the propagation angle of the spectral components (angular dispersion).

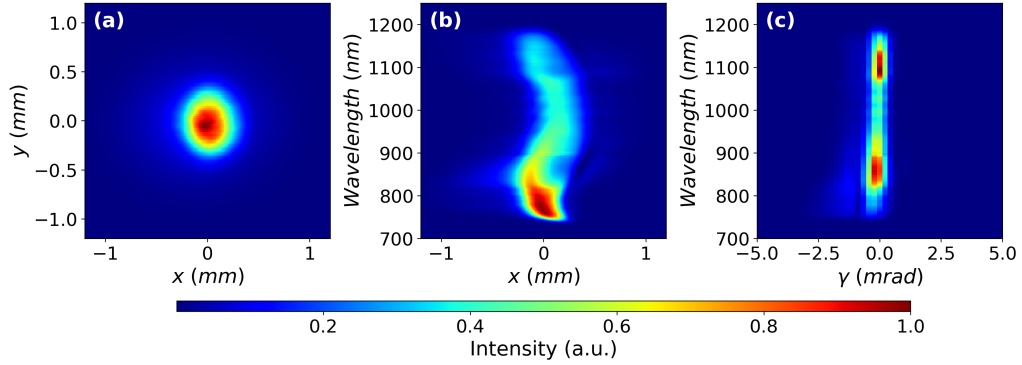


**Fig. 3.26.** Beam profile (a), spatial (b) and angular (c) distribution of the signal spectrum after amplification in a 6 mm thick LBO crystal.  $\gamma = \arcsin\left(\frac{k_x}{k}\right)$  is the propagation angle of the spectral components (angular dispersion).

### 3.2.4 Numerical examination of the second OPCPA stage

The beam profile and the spatiotemporal shape of the amplified signal pulse after the first OPCPA stage is shown in Fig. 3.27 (a) and (d). The beam diameter at  $e^{-2}$  intensity level is roughly 800  $\mu\text{m}$ . Before amplification in the second OPCPA stage, the signal beam size must be matched with the pump beam diameter. In the simulations, like in experimental conditions, the signal pulse was propagated through a Galilei-type telescope, which expands the signal beam. The beam profile and the spatiotemporal shape after beam expansion, at the plane of the second stage, is shown in Fig. 3.27 (b) and (e). As a comparison, the pump pulse shape is visualized in Fig. 3.27 (c) and (f). The parameters of the pump and signal pulses before the second OPCPA stage are summarized in Table 3.8.

The FWHM size of the pump beam is 4.5 mm. In case of a 5 mm thick BBO crystal, the lateral shift of the pump beam relative to the signal beam is 110  $\mu\text{m}$  and 460  $\mu\text{m}$  in PVWC and TPM arrangements, respectively. Consequently, in case of the numerical examination of the double-BBO, the PVWC arrangement is used to minimize spatiotemporal couplings.

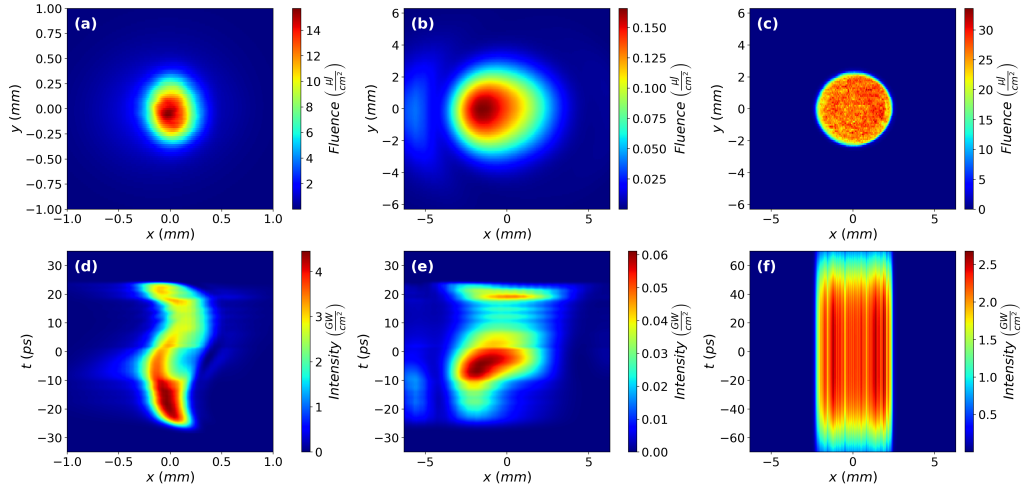


**Fig. 3.27.** Integrated pulse profile and spatiotemporal shape of the signal pulse after the first stage (a and d) and after beam expansion and propagation before the second stage (b and e). Beam profile (c) and spatiotemporal shape (f) of the pump at the the plane of the nonlinear crystal.

**Table 3.8.** Input pulse parameters of the 2<sup>nd</sup> NOPCPA stage.

	Pump	Signal
Energy (mJ)	45	0.42
Pulse duration (ps)	125	50
FWHM (mm)	4.5	4.5
Diameter at $e^{-2}$ (mm)	4.8	6.8
Intensity ( $\text{GW cm}^{-2}$ )	2.8	0.06

### Double-BBO in configuration 1

The energy evolution at the edges ( $BBO_e$ ) and central part ( $BBO_c$ ) of the spectrum is plotted in Fig. 3.28 (a). Energy saturation is reached in case of 6 mm and 5 mm thick BBO crystals. The spectrum after the amplification at the edges and the center is show by blue and red curves in Fig. 3.28. The Fourier limited signal pulse duration is 6 fs, and in case of perfect phase compensation, 6.2 fs compressed pulse duration can be reached.

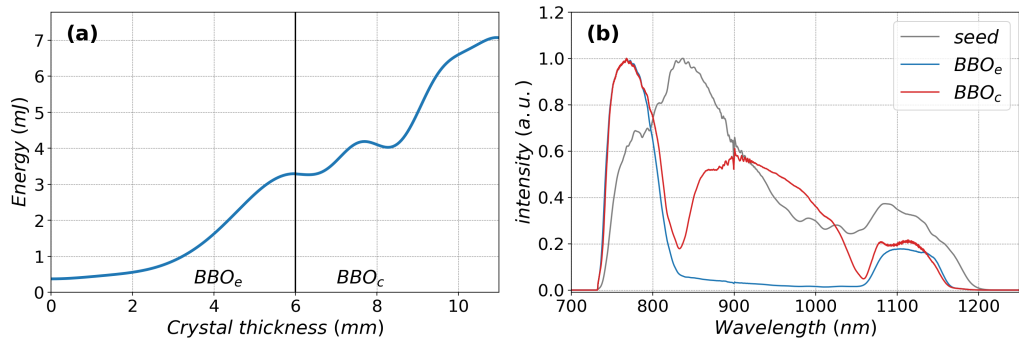


**Fig. 3.28.** (a) Energy evolution during amplification in double-BBO using the first phase-matching configuration. (b) Signal spectrum before (grey) and after amplification in  $BBO_e$  (blue) and  $BBO_c$  (red).

The beam profile, spatial and angular distribution of the amplified signal spectrum is shown in Fig. 3.29 (a)-(c). According to these figures, the signal pulse has neither spatial nor angular dispersion. The structure of the spatio-spectral shape is not symmetric about the  $x = 0$  axis in the walk-off plane, however the small deviation between the Fourier limited and compressed pulse duration indicates that the spectral phase is almost homogeneous across the beam profile. The Strehl ratio in this configuration is 0.55.

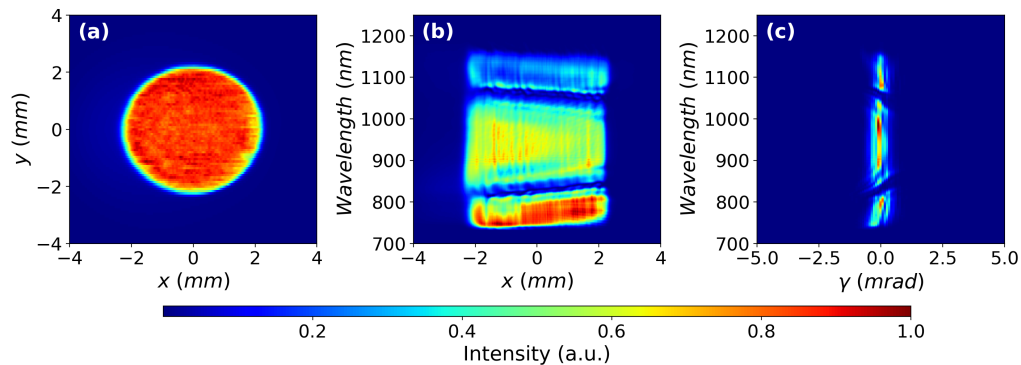


**Fig. 3.29.** Beam profile (a), spatial (b) and angular (c) distribution of the amplified signal spectrum after double-BBO.

### Double-BBO in configuration 2

The energy evolution during amplification in double-BBO oriented in the second configuration is plotted in Fig. 3.30 (a). Energy saturation is reached using two 5 mm thick BBO crystals providing 7.2 mJ after amplification. The signal spectrum before (grey) and after amplification in "BBO long" (blue) and "BBO short" (red) are shown in Fig. 3.30 (b). The duration of the Fourier limited and compressed pulses are 6.4 fs and 6.6 fs, respectively.

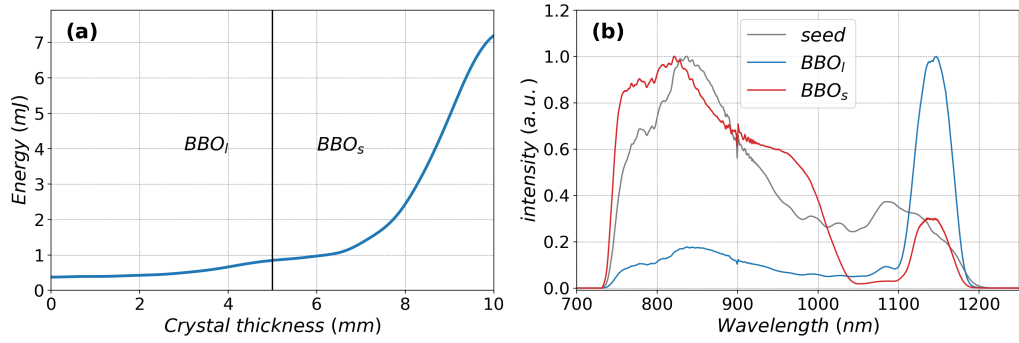


**Fig. 3.30.** (a) Energy evolution during amplification on the 1100 nm to 1200 nm ( $BBO_I$ ) and 720 nm to 1050 nm ( $BBO_S$ ) spectral range. (b) Signal spectrum before (grey) and after amplification in  $BBO_I$  (blue) and  $BBO_S$  (red).

The beam profile, spatial and angular distribution of the amplified signal pulse after double-BBO are visualized in Fig. 3.31 (a)-(c). The Strehl ratio of this configuration is 0.69.

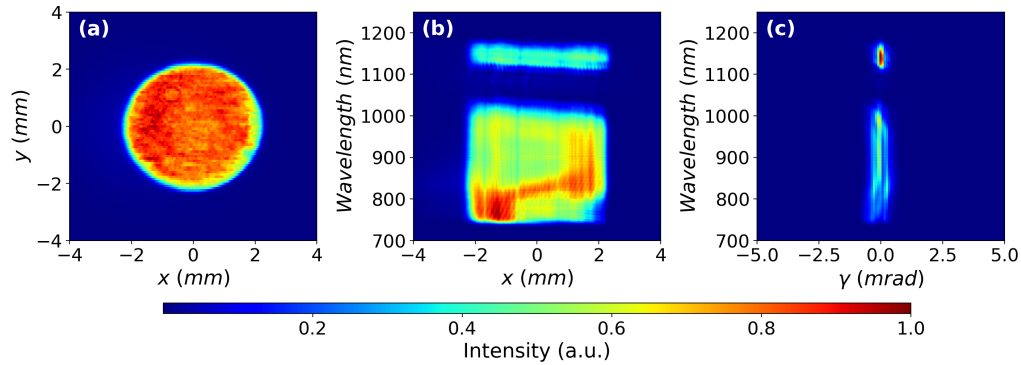


**Fig. 3.31.** Beam profile (a) spatial (b) and angular (c) distribution of the amplified signal spectrum after double-BBO using the second configuration.

### Examination of LBO

The energy evolution during amplification in LBO crystal is shown in Fig. 3.32 (a). In order to reach energy saturation, a 12 mm thick crystal is needed which provides 4.6 mJ signal pulses and the spectrum plotted in Fig. 3.32 (b). The duration of the Fourier limited and compressed pulse shapes are 6 fs and 6.5 fs. The Strehl ratio of this configuration is 0.56. The beam profile, spatial and angular distribution of the amplified signal spectrum are shown in Fig. 3.33 (a)-(c).

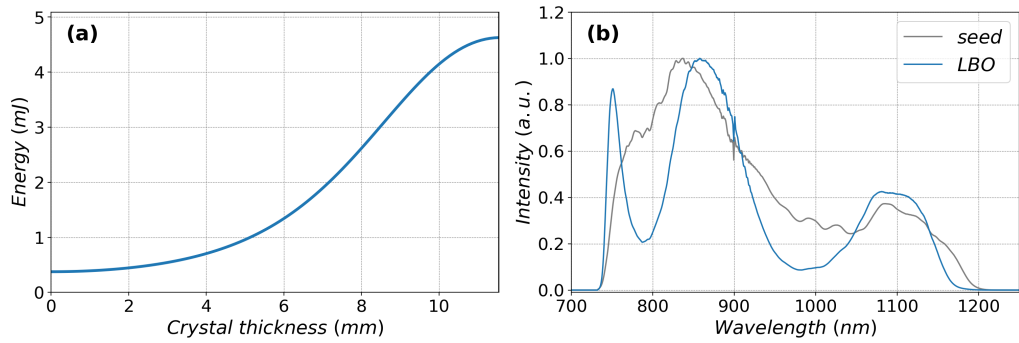


**Fig. 3.32.** (a) Energy evolution during amplification in LBO used in the broadband phase-matching orientation. (b) Signal spectrum before (grey) and after (blue) amplification.

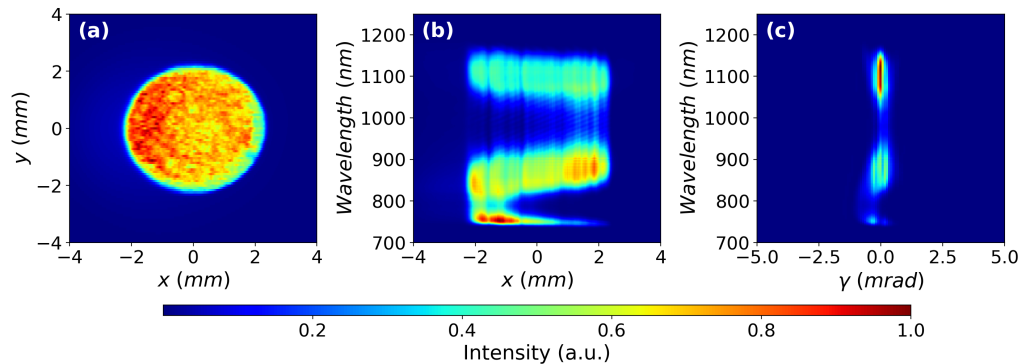


**Fig. 3.33.** Beam profile (a), spatial (b) and angular (c) distribution of the amplified signal spectrum after LBO.

## Conclusions in NOPCPA2

The output parameters of the second OPCPA stage in case of different amplifier configurations are summarized in Table 3.9. The highest pulse energy and best spatiotemporal quality is reached by using double-BBO in the second phase-matching orientation (double-BBO 2), however the Fourier limited and compressed pulse duration is longer than in the other two configurations. Double-BBO 1 and LBO can provide the same bandwidth, but the deviation of the Fourier limited and compressed pulse duration is less and the output energy is higher in the former configuration than in LBO. Therefore, the optimal broadband arrangement for the second OPCPA stage is based on the double-BBO used in the first phase-matching orientation.

**Table 3.9.** Output parameters of the second OPCPA stage in different configurations.

Configuration	$L_1$ (mm)	$L_2$ (mm)	E (mJ)	FTL (fs)	$\tau_c$ (fs)	SR
Double-BBO 1	6	5	7	6	6.2	0.55
Double-BBO 2	5	5	7.2	6.4	6.6	0.69
Broadband LBO	12	-	4.6	6	6.5	0.56

### 3.2.5 Numerical examination of the third OPCPA stage

The beam profile and spatiotemporal shape of the amplified signal pulse after double-BBO 1 in the second OPCPA stage are shown in Fig. 3.34 (a) and (d). The beam FWHM is 4.5 mm so it has to be enlarged in order to match it with the pump beam diameter (Table 3.10) in the third OPCPA stage. In order to mimic experimental conditions, the propagation of the signal pulse through a magnifying telescope and an additional 1.5 m free space was numerically simulated. This results in a diffracted beam profile and a spatiotemporal shape, as visualized in Fig. 3.34 (b) and (e). The appearance of a diffraction pattern is not critical because the local fluence (Fig. 3.34 (b)) is below  $2 \mu\text{J cm}^{-2}$ , which is much lower than the damage threshold of optical coatings. Moreover, if the third OPCPA stage is operated in the energy saturation regime, the intensity distribution will smooth out and inherit the pump pulse shape. The beam profile and spatiotemporal shape of the pump pulse at the plane of the nonlinear crystal are shown in Fig. 3.34 (c) and (f). The input parameters of the pump and signal pulses for the third OPCPA stage are summarized in Table 3.10.

In the third (and fourth) OPCPA stage the FWHM size of the pump beam is 8.5 mm. In case of a 4 mm thick BBO crystal the lateral pump beam displacement relative to the signal beam is  $90 \mu\text{m}$  and  $370 \mu\text{m}$  in the PVWC and TPM arrangements, respectively. The beam FWHM is more than twenty times larger than the lateral shift, even in TPM scheme. This allows for the utilization of the TPM scheme without significant spatiotemporal couplings. Therefore, TPM phase-matching scheme is used during the numerical examination of the double-BBOs in the last two amplifier stages. The advantage of the TPM over the PVWC scheme is that in the latter one the parasitic second-harmonic process,  $900 \text{ nm} + 900 \text{ nm} \rightarrow 450 \text{ nm}$ , is also phase-matched. In case of power amplifiers this process can be very efficient, thus creating a hole in the signal spectrum.

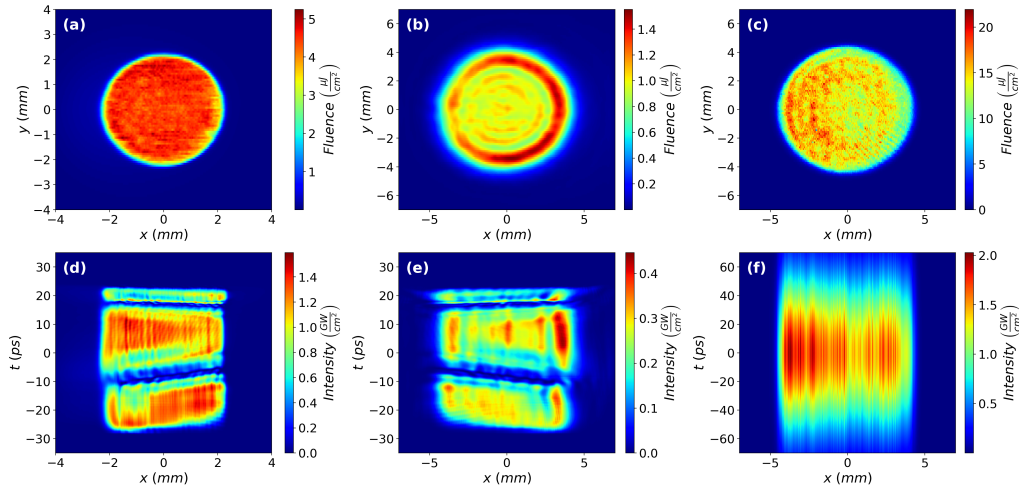


**Fig. 3.34.** Beam profile and spatiotemporal shape of the signal pulse after the second OPCPA (a & d); at the input plane of the third OPCPA (b & e); pump pulse at the input plane of the third OPCPA (c & f).

**Table 3.10.** Pulse parameters before the third OPCPA stage.

	Pump	Signal
Energy (mJ)	90	6.6
Pulse duration (ps)	90	50
FWHM (mm)	8.5	8.2
Diameter at $e^{-2}$ (mm)	9	9.4
Intensity ( $\text{GW cm}^{-2}$ )	2.5	0.5

### Double-BBO in configuration 1

The energy evolution during amplification in double-BBO oriented in the first phase-matching configuration is shown in Fig. 3.35 (a). Energy saturation is reached by using two 3.5 mm thick BBO crystals, providing 24 mJ pulse energy and the spectrum plotted by the red curve in Fig. 3.35 (b). Both the Fourier limited and compressed pulse shapes have a duration of 6.2 fs, while the Strehl ratio is 0.53. The beam profile, spatial and angular distribution of the signal spectrum are shown in Fig. 3.36 (a)-(c).

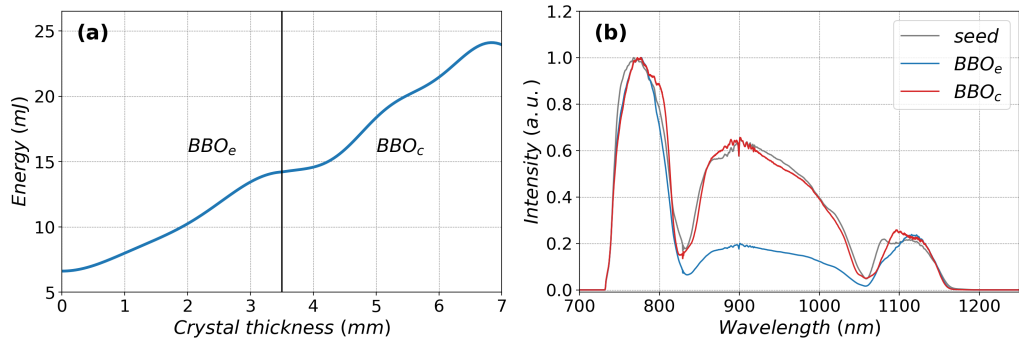


**Fig. 3.35.** (a) Energy evolution during the amplification of the edges ( $BBO_e$ ) and the central ( $BBO_c$ ) part of the signal spectrum. (b) Spectrum of the signal pulse before (grey) and after amplification in  $BBO_e$  (blue) and  $BBO_c$  (red).

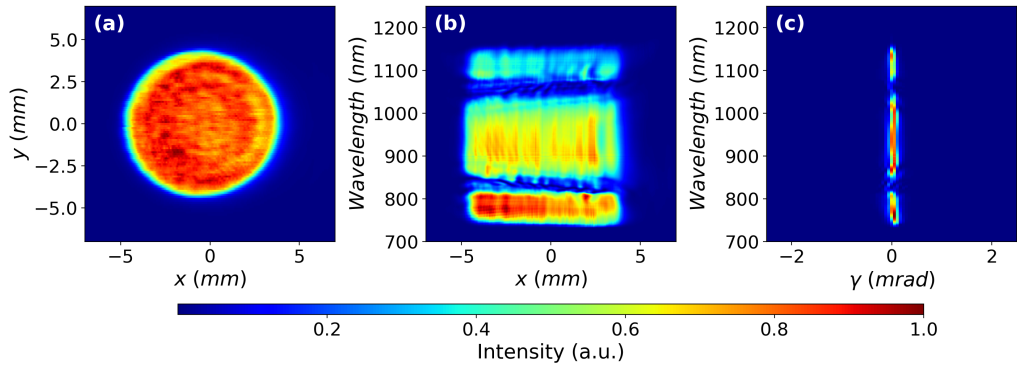


**Fig. 3.36.** Beam profile (a), spatial (b) and angular (c) distribution of the amplified signal spectrum.

## Double-BBO in configuration 2

Energy evolution during amplification in double-BBO oriented in the second phase-matching orientation is plotted in Fig. 3.37 (a). Energy saturation is reached by using 4 mm and 3 mm thick BBO crystals, providing 25.7 mJ pulse energy. The first crystal ( $BBO_s$ ) amplifies over the 720 nm to 1050 nm spectral range (blue curve in Fig. 3.37 (b)), while the second one ( $BBO_l$ ) amplifies a narrow wavelength range centered at 1100 nm (red curve in Fig. 3.37 (b)). The duration of the Fourier limited and compressed pulse shapes are 6.2 fs and 6.3 fs, respectively, while the Strehl ratio in this configuration is 0.57. The beam profile, spatial and angular distribution of the amplified signal spectrum is visualized in Fig. 3.38 (a)-(c).

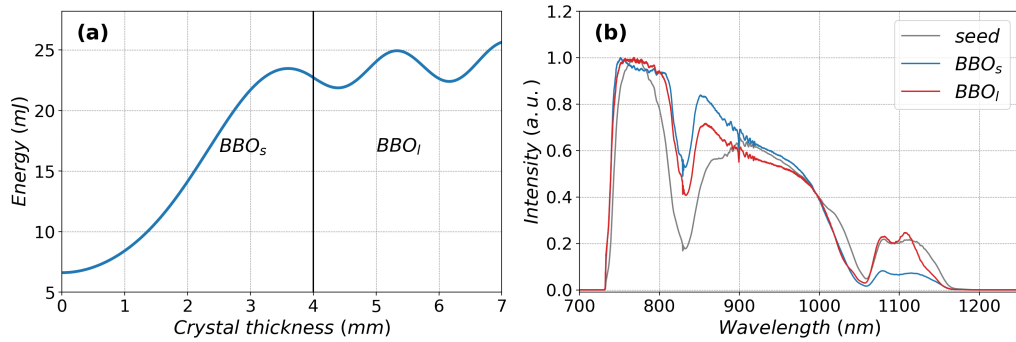


**Fig. 3.37.** (a) Energy evolution during amplification in double-BBO in the second phase-matching configuration. (b) Signal spectrum before (grey) and after amplification in  $BBO_s$  (blue) and  $BBO_l$  (red).

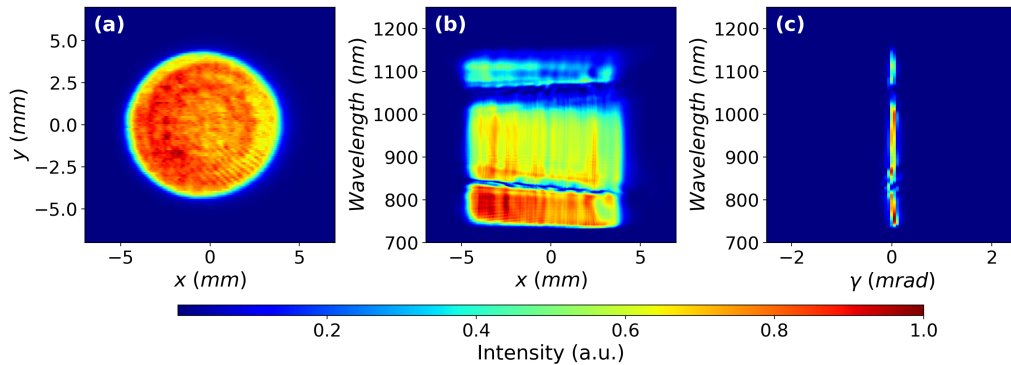


**Fig. 3.38.** Beam profile (a), spatial (b) and angular (c) distribution of the amplified signal spectrum after double-BBO in the second phase-matching configuration.

## Examination of LBO

Energy evolution during amplification in LBO in the broadband phase-matching orientation is plotted in Fig. 3.39 (a). Energy saturation is reached at the thickness of 8 mm, providing 21.8 mJ pulse energy. The spectrum before and after amplification is shown in Fig. 3.39 (b). The duration of the Fourier limited and compressed pulse shapes are 6.2 fs and 6.4 fs, respectively, while the Strehl ratio in this configuration is 0.58. The beam profile, spatial and angular distribution of the amplified signal spectrum is visualized in Fig. 3.40 (a)-(c).

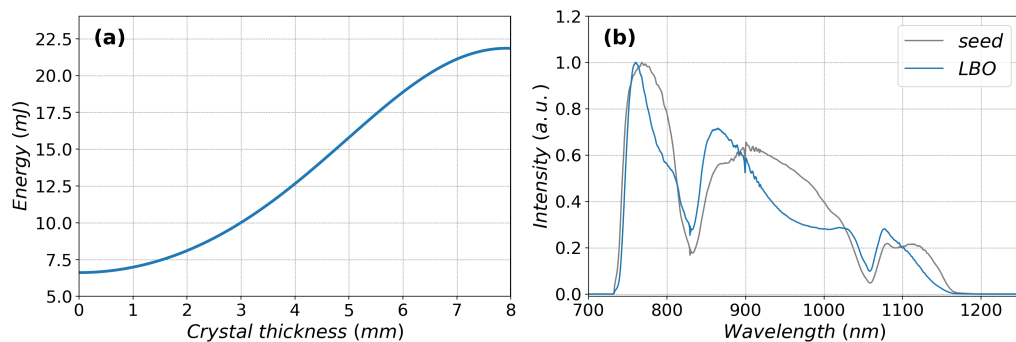


**Fig. 3.39.** (a) Energy evolution during amplification in LBO oriented in the broadband phase-matching configuration. (b) Signal spectrum before (grey) and after (blue) amplification in broadband LBO crystal.

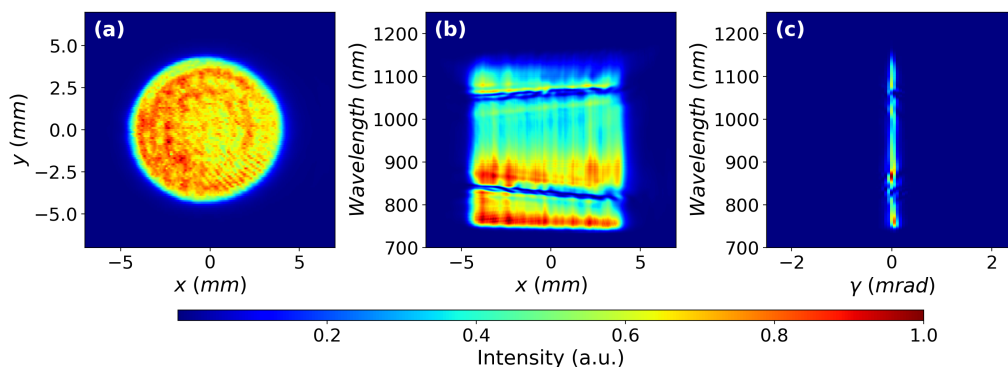


**Fig. 3.40.** Beam profile (a), spatial (b) and angular (c) distribution of the signal spectrum after amplification in LBO.

### Conclusions in NOCPA3

The output parameters of the third OPCPA stage using the three possible broadband phase-matching configurations are summarized in Table 3.11. According to the results each of the three variations provide very similar pulse parameters and each of them would be suitable for the third OPCPA stage. Since the second double-BBO arrangement achieves the highest output energy, the following stage will be supplied by the pulses amplified in this configuration.

**Table 3.11.** Output parameters of the third OPCPA stage in different configurations.

Configuration	$L_1$ (mm)	$L_2$ (mm)	E (mJ)	FTL (fs)	$\tau_c$ (fs)	SR
Double-BBO 1	3.5	3.5	24	6.2	6.2	0.53
Double-BBO 2	4	3	25.7	6.2	6.3	0.57
Broadband LBO	8	-	21.8	6.2	6.4	0.58

### 3.2.6 Numerical examination of the fourth OPCPA stage

The beam profile and spatiotemporal shape of the amplified signal pulse after double-BBO in the third OPCPA stage are shown in Fig. 3.41 (a) and (d). The pump pulse

in the fourth OPCPA stage (Fig. 3.41 (c) and (f)) has the same spatiotemporal shape as in the previous stage, only the energy, thus the peak intensity is higher. Since the pump beam diameter is the same, there is no need for the magnification of the signal beam after the third OPCPA stage. In order to simulate experimental conditions, the signal pulse was numerically propagated 0.5 m in free space, because this is the distance between the last two amplifier stages. This results in the signal beam profile and spatiotemporal shape shown in Fig. 3.41 (b) and (e) at the plane of the last OPCPA stage. The parameters of the pump and signal pulses at the front plane of the nonlinear crystal are summarized in Table 3.12.

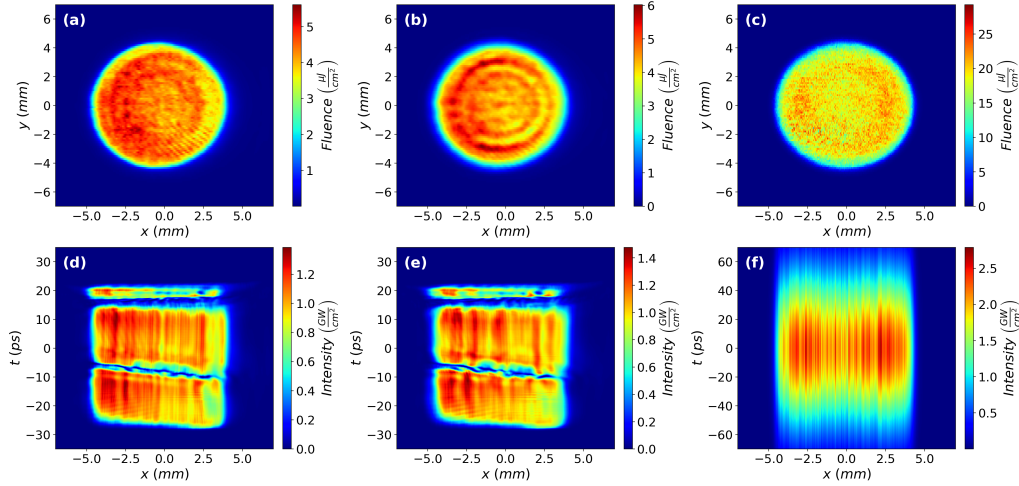


**Fig. 3.41.** Beam profile and spatiotemporal shape of the signal pulse at the rear surface of the double-BBO in the third stage (a & d) and at the front surface of the nonlinear crystal in the fourth stage (b & e). Beam profile and spatiotemporal shape of the pump pulse at the front surface of the nonlinear crystal in the fourth stage (c & f).

**Table 3.12.** Input pulse parameters of the 4<sup>th</sup> NOPCPA stage.

	Pump	Signal
Energy (mJ)	120	25.6
Pulse duration (ps)	90	50
FWHM (mm)	8.5	8.1
Diameter at $e^{-2}$ level (mm)	9	9
Intensity ( $\text{GW cm}^{-2}$ )	3.3	1.7

### Double-BBO in configuration 1

The energy evolution during amplification in double-BBO oriented in the first phase-matching orientation is plotted in Fig. 3.42 (a). Energy saturation is reached by using 2 mm and 1.5 mm thick BBO crystals, providing 49.4 mJ pulse energy. The first crystal ( $BBO_e$ ) amplifies over the 700 nm to 800 nm and 1050 nm to 1150 nm spectral ranges (blue curve in Fig. 3.42 (b)), while the second one ( $BBO_c$ ) amplifies the 800 nm to 1050 nm wavelength range (red curve in Fig. 3.42 (b)). The duration

of both the Fourier limited and compressed pulse shapes are 6.2 fs, and the Strehl ratio in this configuration is 0.38. The beam profile, spatial and angular distribution of the amplified signal spectrum is visualized in Fig. 3.43 (a)-(c).

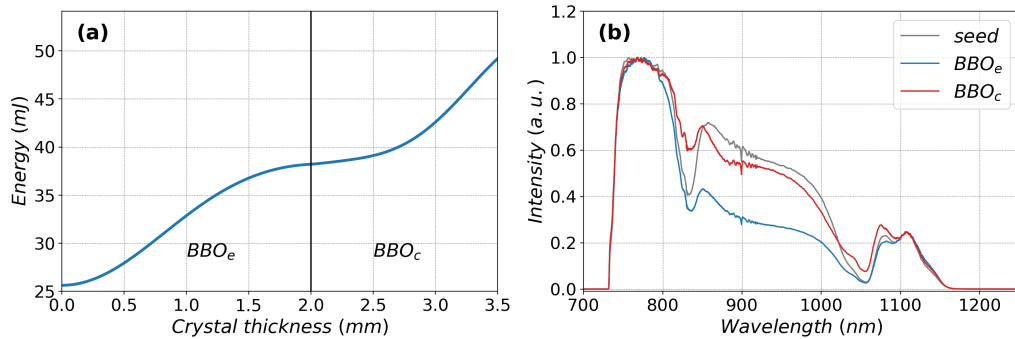


**Fig. 3.42.** (a) Energy evolution during amplification in double-BBO in the first phase-matching orientation. (b) Signal spectrum before (grey) and after amplification in  $BBO_e$  (blue) and in  $BBO_c$  (red).

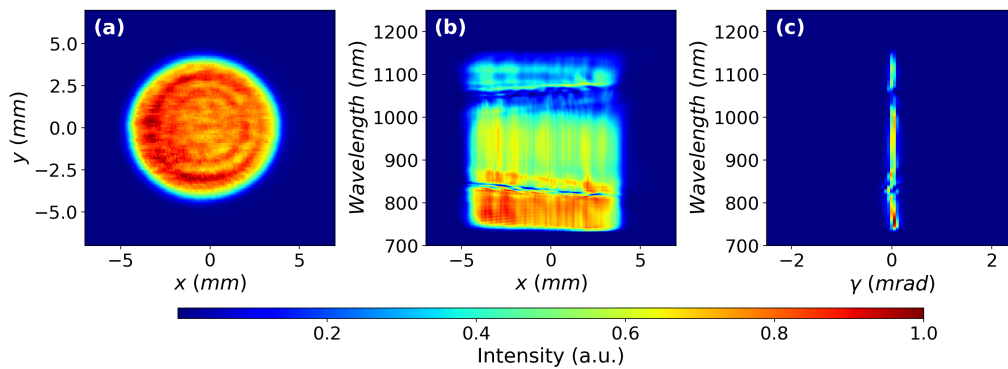


**Fig. 3.43.** Beam profile (a), spatial (b) and angular (c) distribution of the signal spectrum after amplification in double-BBO in the first phase-matching configuration.

### Double-BBO in configuration 2

Energy evolution during amplification in double-BBO oriented in the second phase-matching orientation is plotted in Fig. 3.44 (a). Energy saturation is reached by using 2.2 mm and 1 mm thick BBO crystals, providing 51.1 mJ pulse energy. The first crystal ( $BBO_s$ ) amplifies over the 720 nm to 1050 nm spectral range (blue curve in Fig. 3.44 (b)), while the second one ( $BBO_l$ ) amplifies a narrow wavelength range centered at 1100 nm (red curve in Fig. 3.44 (b)). The duration of both the Fourier limited and compressed pulse shapes are 6.4 fs, while the Strehl ratio in this configuration is 0.43. The beam profile, spatial and angular distribution of the amplified signal spectrum are visualized in Fig. 3.45 (a)-(c).

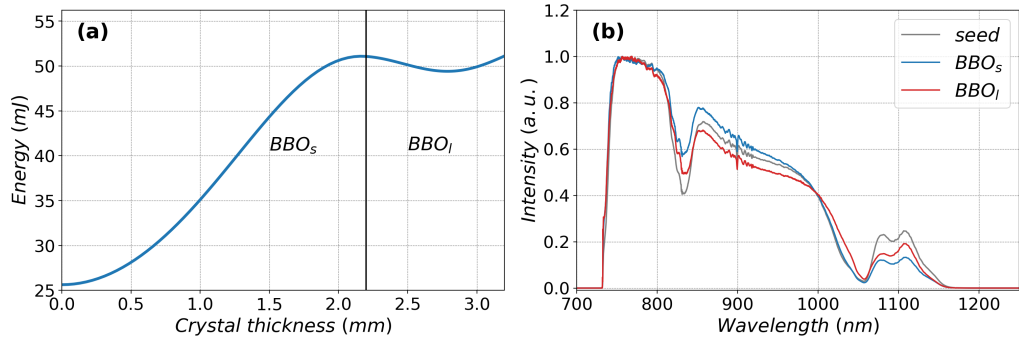


**Fig. 3.44.** (a) Energy evolution during amplification in double-BBO in the second phase-matching configuration. (b) Signal spectrum before (grey) and after amplification in  $BBO_s$  (blue) and  $BBO_l$  (red).

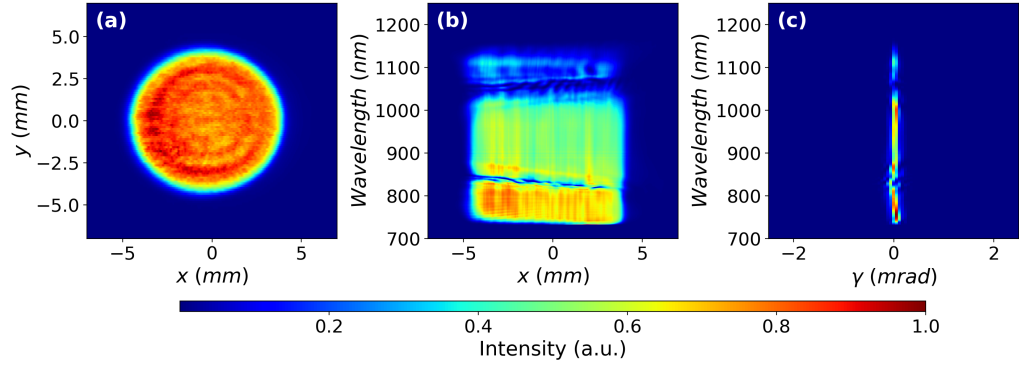


**Fig. 3.45.** Beam profile (a), spatial (b) and angular (c) distribution of the signal spectrum after amplification in double-BBO in the first phase-matching configuration.

### Examination of LBO

Energy evolution during amplification in LBO crystal in the broadband phase-matching orientation is plotted in Fig. 3.46 (a). Energy saturation is reached at the thickness of 5 mm, providing 49.7 mJ pulse energy. The spectrum before and after amplification is shown in Fig. 3.46 (b). The duration of the Fourier limited and compressed pulse shapes are 6.2 fs and 6.3 fs, while the Strehl ratio in this configuration is 0.39. The beam profile, spatial and angular distribution of the amplified signal spectrum are visualized in Fig. 3.47 (a)-(c).

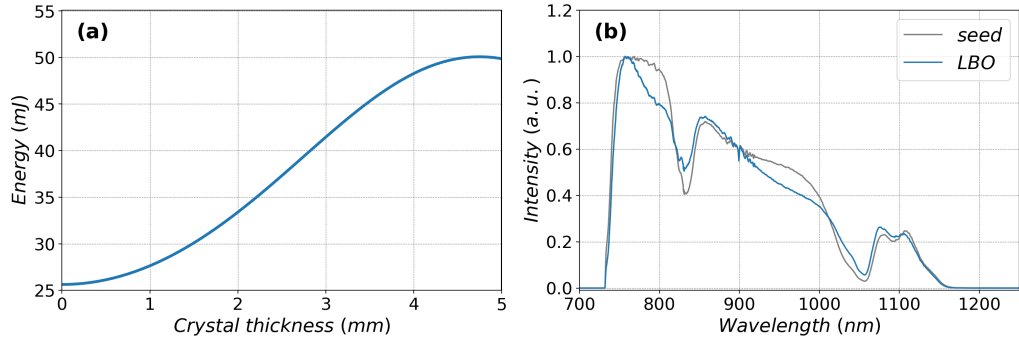


**Fig. 3.46.** (a) Energy evolution during amplification in LBO oriented in broadband phase-matching configuration. (b) Signal spectrum before (grey) and after (blue) amplification in broadband LBO crystal.

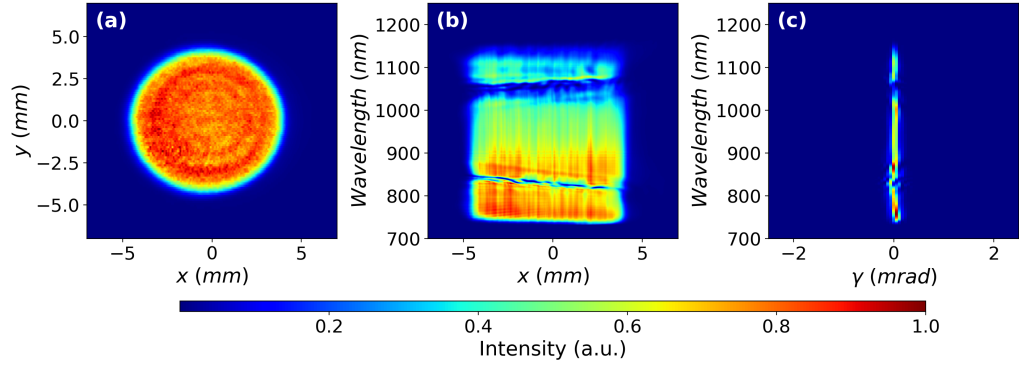


**Fig. 3.47.** Beam profile (a), spatial (b) and angular (c) distribution of the signal spectrum after amplification in double-BBO in the first phase-matching configuration.

## Conclusions in NOPCPA4

The output parameters of the last OPCPA stage using the three possible broadband phase-matching configurations are summarized in Table 3.13. Each variation can provide roughly 50 mJ pulse energy, while the first double-BBO configuration can provide the broadest bandwidth and the shortest compressed pulse duration at the same time. Therefore, this is considered as the optimal configuration in the fourth OPCPA stage.

**Table 3.13.** Output parameters of the third OPCPA stage in different configurations.

Configuration	$L_1$ (mm)	$L_2$ (mm)	E (mJ)	FTL (fs)	$\tau_c$ (fs)	SR
Double-BBO 1	2	1.5	49.4	6.2	6.2	0.38
Double-BBO 2	2.2	1	51.1	6.4	6.4	0.43
Broadband LBO	5	-	49.7	6.2	6.3	0.39

### 3.2.7 Influence of the idler in the second crystal

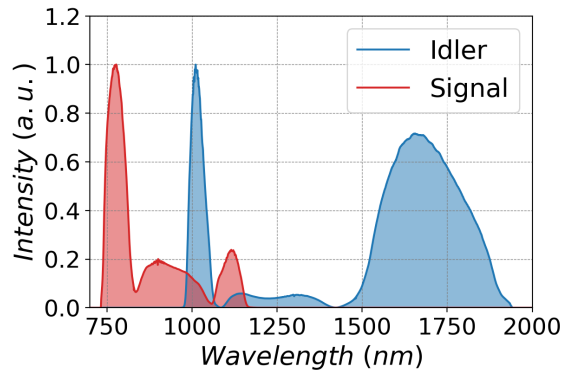


**Fig. 3.48.** Spectrum of the idler (blue) and signal (red) after the first BBO crystal.

In the double-BBO configuration, two idler pulse is generated in the two subsequent crystals. Since the crystals are close to each other, it is not possible to physically block the first idler pulse and prevent it from entering the second BBO. The usage of dichroic coating on the front surface of the second crystal, which reflects the idler and transmits the pump and signal, is not an option either, as the spectrum of the idler and signal pulses overlap in the 950 nm to 1200 nm range as it is indicated in Fig. 3.48. Consequently, the idler pulse generated in the first crystals enters the second BBO, therefore it is important to examine numerically its influence on the amplification in the second crystal. In the simulations this was done by simply zeroing the idler field before modeling OPA in the second crystal. Consequently, we could compare the output parameters of double-BBO in the presence and absence of the first idler pulse.

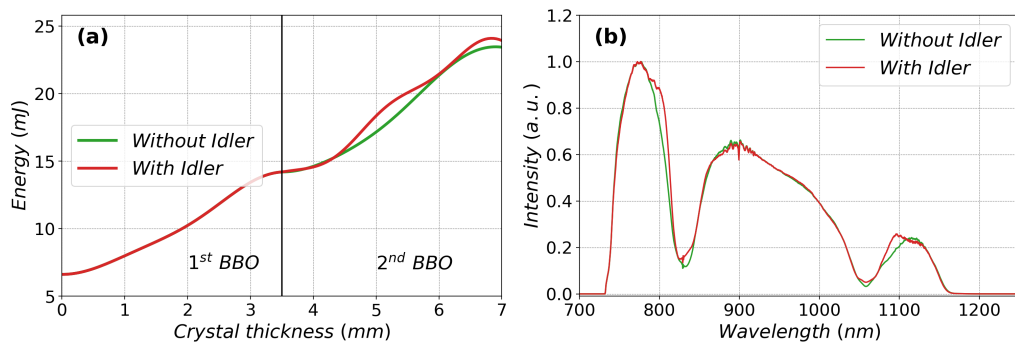


**Fig. 3.49.** Energy evolution (a) and amplified signal spectrum (b) in double-BBO in the presence (red) and absence (green) of the first idler pulse in the second BBO.

According to theoretical considerations, the idler pulse generated in the first crystal will be out of phase-matching in the second one due to the slightly detuned phase-matching angle ( $\theta$ ). Consequently, the energy and the spectral shape should remain intact in the second BBO. This is verified by Fig. 3.49 (a) and (b), which show the energy evolution and the amplified spectrum after the double-BBO in the presence and absence of the first idler pulse.

The only effect which can be observed is that the energy evolution curve becomes modulated in the presence of the idler. This can be attributed to low efficiency, back and forth energy conversion at the spectral edges caused by huge phase-mismatch in the second crystal (for example Fig. 2.6.3 on page 96. in Ref. [4]). This effect is visualized in Fig. 3.50 and in Fig. 3.51, which show the evolution of the signal spectrum during amplification in double-BBO in the presence and absence of the first idler pulse. The intensity modulations at the spectral edges in case of idler injection (Fig. 3.50 (b)) are much higher than in case of the first idler is zeroed (Fig. 3.51 (b)). In order to visualize this effect more clearly, in Fig. 3.50 (c) and Fig. 3.51 (c) a one dimensional intensity cut from (b) was taken at 750 nm and 1150 nm wavelengths and plotted as a function of the propagation distance in the second crystal ( $z_2$ ). Fig. 3.51 (c) indicates that these modulations are always present, but their amplitude increases in case of idler injection (Fig. 3.50 (c)). The most important output parameters in the two cases are summarized in Table 3.14.

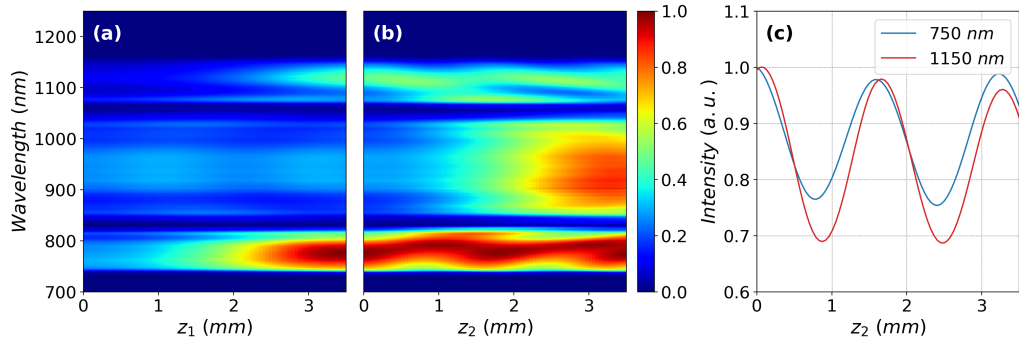


**Fig. 3.50.** *The first idler is present in the second crystal.* Evolution of the signal spectrum during amplification in the 1<sup>st</sup> (a) and 2<sup>nd</sup> (b) BBO crystals. (c) Intensity evolution of the 750 nm and 1150 nm spectral components in the second BBO. (Adopted from Ref. [T2])

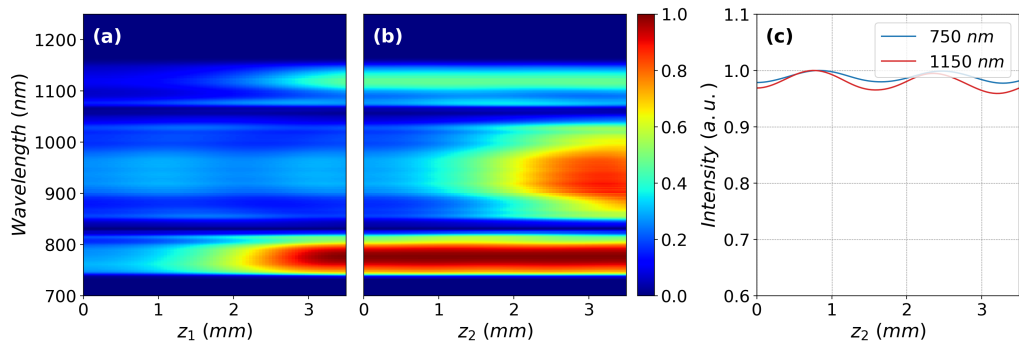


**Fig. 3.51.** *The first idler is absent in the second crystal.* Evolution of the signal spectrum during amplification in the 1<sup>st</sup> (a) and 2<sup>nd</sup> (b) BBO crystals. (c) Intensity evolution of the 750 nm and 1150 nm spectral components in the second BBO.

**Table 3.14.** Output parameters of the double-BBO in the presence and absence of the first idler in the second crystal.

	Idler Injected	Idler Zeroed
Energy (mJ)	23.9	23.4
FTL ( fs)	6.2	6.2
Strehl ratio	0.57	0.58

### 3.2.8 Possible final configuration

The first OPCPA is a high-gain preamplifier stage. The later pump beam displacement relative to the signal pulse in PVWC scheme is  $105\ \mu\text{m}$  in case of a  $4.5\ \text{mm}$  thick BBO crystal, while the FWHM size of the pump beam is  $600\ \mu\text{m}$ . Due to the high gain, the amplified signal pulse will have a similar size and the same spatial position as the pump beam due to gain guiding [182]. In case of such small beam sizes the  $105\ \mu\text{m}$  lateral displacement is not negligible and causes spatial chirp. Based on these findings the use of LBO crystals in the first OPCPA is preferable over a double-BBO.

In the second OPCPA stage the intensity gain is 27 (Table 3.15) and the size of the interacting beams is  $4.5\ \text{mm}$ . The lateral pump beam displacement relative to the signal beam in a  $5\ \text{mm}$  BBO under the PVWC scheme is  $110\ \mu\text{m}$ , which allows the utilization of a double-BBO without significant spatiotemporal couplings.

In the last two OPCPA stages the intensity gain is less than 5 and the size of the interacting beams is much bigger than the lateral pump beam displacement even in the TPM scheme. This and the higher nonlinear coefficient of BBO favors the use of double-BBO configurations instead of LBO crystals.

The parameters of the numerically optimized broadband OPCPA stages are summarized in Table 3.15. With this configuration, the numerical simulations predict  $49.4\ \text{mJ} \times 0.83 = 41\ \text{mJ}$  pulse energy at the output, where 0.83 is the transmission of the compressor.

The spectrum of the output signal pulse and the residual spectral phase after compensating the phase derivatives up to the  $7^{\text{th}}$  order are visualized in Fig. 3.52 (a) by the blue shaded area and the red curve, respectively. Another important aspect of the double-BBO configuration is the behavior of the spectral phase where the gain curves of the two crystals overlap. According to Fig. 3.52 (a), there are two phase jumps at the spectral holes, which correspond to the meeting points of the spectral gain curves (Fig. 3.10). The magnitude of these phase jumps is less than  $\pi$  and can be reduced by further fine tuning the acousto-optical programmable dispersive filter (AOPDF). Even with this modulated spectral phase, the signal pulse is compressible to  $6.6\ \text{fs}$  (2.2 cycles at  $900\ \text{nm}$ ) (Fig. 3.52 (b)), providing  $4\ \text{TW}$  peak power.

**Table 3.15.** Numerically optimized OPCPA parameters.

	OPCPA1	OPCPA2	OPCPA3	OPCPA4
Crystals	LBO+LBO	BBO+BBO	BBO+BBO	BBO+BBO
Thickness (mm)	10+4	6+5	3+4	2+1.5
$E_{IN}$ (mJ)	$0.45 \times 10^{-3}$	0.36	7	25.7
$E_{OUT}$ (mJ)	0.36	7	25.7	49.4
Energy gain	1000	15.5	3.7	1.9
$I_{IN}$ ( $\text{GW cm}^{-2}$ )	$1.5 \times 10^{-3}$	0.06	0.5	1.7
$I_{OUT}$ ( $\text{GW cm}^{-2}$ )	4.8	1.6	1.5	3
Intensity gain	3200	27	3	1.8

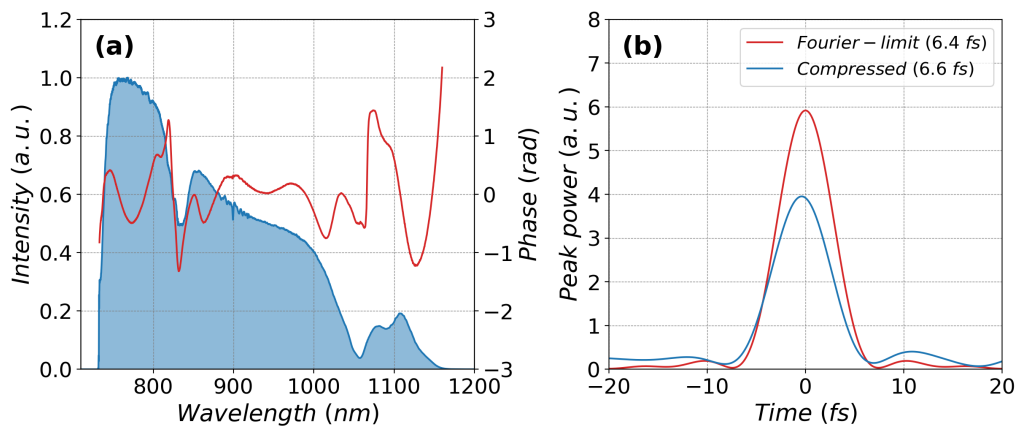


**Fig. 3.52.** (a) Output spectrum (blue shaded area) and the residual spectral phase (red curve) after compensating the phase derivatives up to the 7<sup>th</sup> order. (b) Fourier limited and compressed pulse shape after 7<sup>th</sup> order phase compensation. The value of the peak power is already multiplied by the throughput (83%) of the compressor.

### 3.2.9 Summary

**T2** I have shown that double-BBO configuration introduces spatiotemporal couplings if the two following two conditions are satisfied [T2]:

1. The lateral pump displacement in noncollinear geometry is comparable to the size of the interacting beams.
2. The intensity gain is high, thus the pump guides the signal pulse during amplification.

**T3** I have modeled and determined the optimal configuration of an OPCPA system to provide 2.2-cycle, TW-class pulses [T2].

### 3.3 Comparative study

#### 3.3.1 Generation of CEP-stabilized few-cycle mid-IR pulses

The generation of CEP-stable, ultrashort mid-IR pulses relies on the frequency down-conversion of energetic near-IR pulses by DFG. These near-IR driving pulses are usually provided by Yb:YAG laser amplifiers, which can provide energetic, 1030 nm pulses with 1 ps pulse duration [34, 183–186].

The first step towards the production of mid-IR wavelengths is to generate a broadband short-wave infrared (SWIR) signal pulse. This can be achieved by using the fraction of the available pump energy for supercontinuum generation in YAG [88, 187] or by frequency downshifting a fraction of the 1  $\mu\text{m}$  output of a master oscillator in photonic crystal fibers [89, 188, 189]. In either case, optical synchronization is ensured as both pump and seed pulses originate from the same source. Moreover, this solution provides passive CEP stability for the resulting mid-IR idler pulse after DFG.

It is desired by many applications, especially strong-field physics, to boost the energy of the mid-IR pulses. This can be done in two ways and both of them utilize OPCPA (Fig. 3.53). The first option is to amplify the signal pulse in a multistage OPCPA, which is followed by a last DFG stage, from where the CEP-stable idler is delivered (Fig. 3.53. (b)). The second option is to first introduce DFG to provide a low energy, CEP-stable idler pulse, which is then amplified in the following OPCPA chain (Fig. 3.53. (a)). During my work I named the first and second case as "signal scheme" and "idler scheme", depending on which pulse is amplified using OPCPA.

During the implementation of a mid-IR system it is always a question which scheme should be used. Usually the construction of one scheme rules out switching to the other option since optics designed for mid-IR wavelength does not work at the SWIR spectral range, where the signal is located. Thus changing from one scheme to another would cause additional costs and efforts, which is not desired if a well operating system is demonstrated. Furthermore, according to the number of mid-IR systems presented in literature, both schemes are used approximately equally frequently. Without claiming completeness, the signal and idler scheme is used in systems described in [171–174, 190–195] and [88, 89, 196–202], respectively. These systems have different configurations, so it is not straightforward to compare those which utilize idler scheme to those which use the signal scheme. Due to these reasons, the easiest way to draw conclusions about the two schemes is to numerically simulate both versions under the same conditions. The strategy in my work is to first optimize the signal chirp in both cases on the highest output peak power and then to compare various pulse parameters, i.e. energy, energy stability, peak power, pulse duration and CEP-stability.

#### 3.3.2 Description of the modelled system

The structure of the modelled mid-IR system is based on the ELI-ALPS MIR laser, which is well described in Ref. [88]. It is driven by an Yb:YAG thin-disk regenerative amplifier, which provides 1030 nm, 1.1 ps long, 2 mJ pulses at 100 kHz repetition rate. From the available pump, 9  $\mu\text{J}$  is used for continuum generation in a YAG crystal, which is then filtered by a low-pass filter ("F" in Fig. 3.53) and stretched in bulk material. These are followed by the AOPDF which is used for fine tuning

the spectral phase and amplitude shaping. As a result, a seed pulse is generated in the  $1.35\ \mu\text{m}$  to  $1.75\ \mu\text{m}$  range, which is shown in Fig 3.54 (a). In the idler scheme, which is also used in Ref.[88], the mid-IR pulse at  $3.1\ \mu\text{m}$  is generated in the first DFG stage and then amplified in three consecutive OPA stages (Fig.3.53.(a)). In the signal scheme the seed is first amplified in three OPA stages and then the idler is generated in the last DFG stage (Fig.3.53.(b)). In both schemes the pulses are compressed using bulk materials.

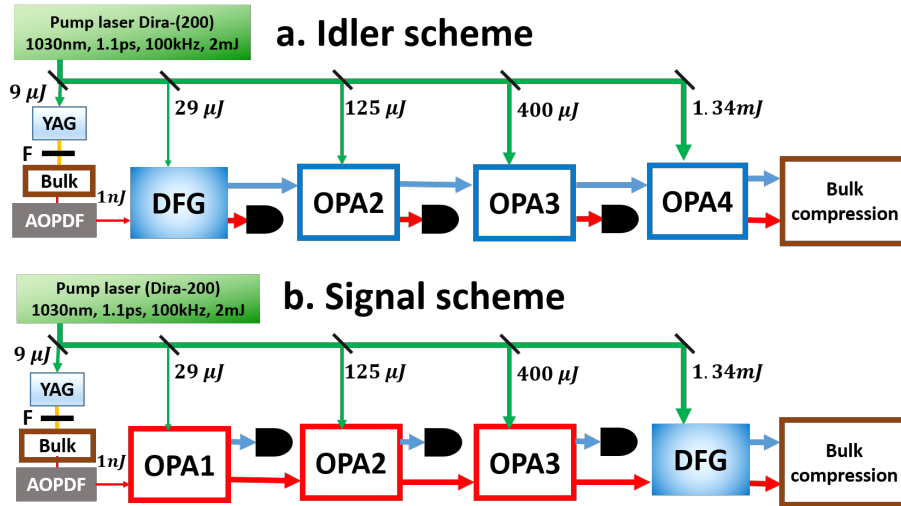


**Fig. 3.53.** Schematics of a mid-IR system utilizing idler (a) and signal (b) scheme. The structure is based on the MIR laser of ELI-ALPS[88]. YAG - yttrium aluminum garnet crystal, Sa- bulk sapphire, AOPDF - acousto-optic programmable dispersive filter, DFG - difference frequency generation, OPA - optical parametric amplification, Si - bulk silicone. [Adapted] with permission from [Ref. [T3]] © The Optical Society.

The seed spectrum (Fig. 3.54 (a)) is obtained from a real measurement in the laboratory, while the spectral phase was calculated from the Sellmeier polynomial of the bulk stretcher and the phase derivatives added by the AOPDF. When we applied the calculated spectral phase on the measured spectrum, the simulation was supplied with a realistic temporal shape. In Fig. 3.54 (b) the temporal shape of the stretched signal pulse is shown in a case when the signal is stretched to approximately half of the pump duration. The spatial shape of the signal in the first stage (DFG in the idler scheme or OPA1 in the signal scheme) was approximated by 2D Gaussian distribution. This is justified by the fact that the nonlinear crystal is placed at the focal plane of the lens used for focusing the seed beam. The 3D complex signal electric field was constructed using these distributions in a way that the spatial and temporal integral of the distribution would equal to 1 nJ, which is approximately the seed energy after the stretcher.

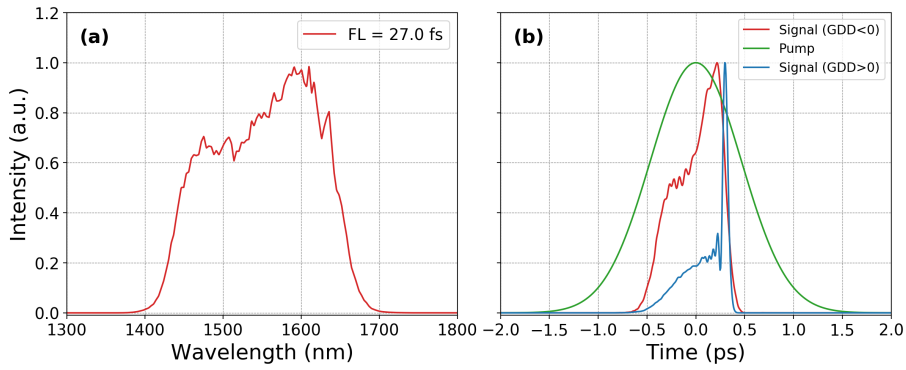


**Fig. 3.54.** (a) The spectrum of the signal pulse before OPCPA which supports 27 fs Fourier limited (FL) pulse duration. (b) Temporal shape of the signal pulse before OPCPA in case of negative (red curve) and positive (blue curve) chirp using a 60 cm and a 32 cm long sapphire stretcher, respectively. The RMS pulse duration is the same in both cases. The green curve corresponds to the temporal shape of the pump pulse. [Adapted] with permission from [Ref. [T3]] © The Optical Society.

Thin-disk lasers typically have Gaussian temporal and spatial near-field intensity distribution [185], so the spatiotemporal shape of the pump pulses was approximated to a 3D Gaussian function in case of every stage. The temporal shape of the pump is shown in Fig. 3.54 (b). The peak intensity of the pump pulse was fixed at  $150 \text{ GW cm}^{-2}$  on the surface of every nonlinear crystal. The spatial size of the pump pulses on the surface of the nonlinear crystals are calculated from the fixed peak intensity and the known energy distribution among the four stages (Fig 3.53). These parameters are summarized in Table 3.16.

After constructing the 3D complex electric field of the pump and signal pulses, TWMM was simulated using the advanced OPCPA code described in Section 2.8.1. As the output of the numerical code, the 3D complex electric field of the generated idler, amplified signal and depleted pump pulses are provided. Depending on the simulated scheme, the propagation of the idler (idler scheme) or the signal (signal scheme) pulse from one crystal to another was simulated using the methods described in Section 2.8.2. The spatio-spectral phase shift introduced by the lenses or mirrors was also taken into account, as it is described in Section 2.2.2. Using these Python functions, I numerically simulated the imaging of the signal or the idler pulse from one crystal to another. In case of each crystal, the spatial size of the signal or idler beam was matched to the size of the pump beam. These data are also summarized in Table 3.16.

All these steps ensured a realistic simulation of the entire OPCPA chain and allowed for the optimization of various parameters on the highest output signal and idler peak power.

### Nonlinear crystal parameters

During the simulations, a KTA crystal was used instead of quasi-phase-matching (QPM) and lithium niobate crystals[88]. The reasons for choosing KTA are the following:

- KTA in collinear, type II phase-matching geometry in the  $(\theta, \phi) = (41^\circ, 0^\circ)$

**Table 3.16.** Pump parameters and spatial size of the seed beam in the OPA stages.

	OPA1	OPA2	OPA3	OPA4
Pump intensity ( $\text{GW cm}^{-2}$ )	150	150	150	150
Pump energy ( $\mu\text{J}$ )	29	124	403	1387
Pump beam FWHM ( $\mu\text{m}$ )	120	250	440	820
Seed beam FWHM ( $\mu\text{m}$ )	132	275	484	902

crystallographic direction allows for the amplification of a broad signal and idler bandwidth.

- In collinear geometry the idler (signal) in the signal (idler) scheme will be angular dispersion free, which provides more straightforward comparison than noncollinear geometry. In the latter case, angular dispersion has to be compensated for [174].
- Collinear geometry results in a simple, dual-channel ( $1.54 \mu\text{m}$  and  $3.2 \mu\text{m}$ ) system where the pulses are synchronized. This can be useful for many scientific applications, like two-color HHG [203].
- It was reported in [193, 195, 204, 205] that KTA has a high damage threshold when pumped by ps or sub-ps pulses.

All of these properties favor their usage over noncollinear lithium niobate crystals and QPM gratings. QPM gratings are also operated in collinear geometry, however they suffer from beam degradation in case of high peak and average powers [192, 201, 204].

### Dispersion of the system

**Table 3.17.** Dispersion coefficients of sapphire, silicon and KTA crystal at the signal and idler central wavelengths.

	$\lambda_c$ ( $\mu\text{m}$ )	1.54	3.11
Sapphire	GDD ( $\text{fs}^2 \text{mm}^{-1}$ )	-31	-626
	TOD ( $\text{fs}^3 \text{mm}^{-1}$ )	193	3774
	FOD ( $\text{fs}^4 \text{mm}^{-1}$ )	-565	-32028
Silicon	GDD ( $\text{fs}^2 \text{mm}^{-1}$ )	1128	500
	TOD ( $\text{fs}^3 \text{mm}^{-1}$ )	1420	871
	FOD ( $\text{fs}^4 \text{mm}^{-1}$ )	5441	238
KTA	GDD ( $\text{fs}^2 \text{mm}^{-1}$ )	73	-306
	TOD ( $\text{fs}^3 \text{mm}^{-1}$ )	200	2319
	FOD ( $\text{fs}^4 \text{mm}^{-1}$ )	-327	-75580

Many of the commonly used glasses (fused silica, sapphire) have anomalous dispersion at the mid-IR spectral range (Table 3.17.). So the idler can be compressed

in bulk even if it is chirped positively. The signal on the other hand is located in the SWIR spectral range and the central wavelength is very close to the zero dispersion point of the commonly used glasses. Sapphire, for example, introduces a small amount of negative GDD at the signal central wavelength (Table 3.17). Therefore, a very long glass would be needed to stretch it to the right temporal duration or to compress it to the Fourier limit after amplification. During compression the pulse energy is high, and in case of long propagation nonlinear effects (SPM) can occur. Therefore, it is more advantageous to use a long glass as a stretcher rather than a compressor.

Due to this reasoning, the initial plan was to chirp the signal pulse negatively in a bulk sapphire stretcher. In order to maximize the transmission of the AOPDF (Dazzler), the GDD setting has to be around  $15\,000\text{ fs}^2$ . This amount of GDD compensates 460 mm sapphire. In other words, if the length of the sapphire stretcher is more or less than 460 mm, the signal chirp is negative or positive, respectively. This is illustrated in Fig 3.57.

### 3.3.3 OPCPA optimization

#### Optimization of crystal thickness

The thickness of nonlinear materials is an essential parameter of every OPCPA system because it will determine the overall conversion efficiency, energy stability and quality of the amplified pulses. Crystals shorter than the optimal value will provide low efficiency, while longer crystals will spoil the spatiotemporal shape and phase of the pulses. In the current case, crystal thickness was optimized on the highest energy. The optimal crystal thickness is mainly influenced by the ratio of the seed and pump intensities. Since the pump intensity is fixed, the optimal crystal thicknesses mainly depend on seed intensity, which is determined by the stretching ratio. Consequently, it is expected that the optimal size of the crystals is influenced by the thickness of the bulk stretcher.

In order to identify the optimal thickness of KTA crystals, the amplification in the OPCPA chain was simulated at five different sapphire thicknesses in both schemes (Tables 3.18 and 3.19). These five values are chosen to have two positively and two negatively chirped cases and a middle one when the GDD equals zero. This way it was possible to see how the sign and absolute value of the chirp influence the optimal crystal thickness.

According to the results summarized in Tables 3.18 and 3.19, the chirp has just a minor influence on the optimal lengths of the nonlinear crystals in a given stage, and there is no significant difference between the two schemes. This can be explained with the fact that the first stage is a high gain pre-amplification stage, which operates in an intensity saturation regime, as illustrated in Fig. 3.55. In Fig. 3.55, the peak intensity evolution of the signal pulse is plotted as a function of crystal thickness at different chirp values. With the exception of the un-chirped case ( $L_{Sa} = 460\text{ mm}$ ), intensity saturates after  $2.2\text{ mm}$  propagation. This means that the first stage equalizes the intensity of the signal and idler pulses. Consequently, the following stages will be supplied with approximately the same pulse intensity, which will result in similar optimal crystal thicknesses at different chirp values.

**Table 3.18.** Optimal crystal thicknesses in the idler scheme at different chirp values.  $L_{Sa}$  - thickness of the sapphire stretcher, GDD - group delay dispersion of the sapphire stretcher,  $\tau_{RMS}$  - RMS pulse duration of the stretched pulse,  $L_i$  ( $i = 1, 2, 3, 4$ ) are the optimal thickness of the KTA crystals in the 1<sup>st</sup>, 2<sup>nd</sup>, 3<sup>rd</sup> and 4<sup>th</sup> stage.

$L_{Sa}$ (mm)	GDD (fs <sup>2</sup> )	$\tau_{RMS}$ (fs)	$L_1$	$L_2$	$L_3$	$L_4$
120	10500	550	3.4	1.7	1.3	1.3
330	4260	230	3.1	1.7	1.3	1.4
460	0	54	2.8	1.9	1.6	1.4
600	-4440	230	3.1	1.6	1.3	1.4
800	-10500	550	3.4	1.6	1.2	1.3

**Table 3.19.** Optimal crystal thicknesses in the signal scheme at different chirp values.  $L_{Sa}$  - thickness of the sapphire stretcher, GDD - group delay dispersion of the sapphire stretcher,  $\tau_{RMS}$  - RMS pulse duration of the stretched pulse,  $L_i$  ( $i = 1, 2, 3, 4$ ) are the optimal thickness of the KTA crystals in the 1<sup>st</sup>, 2<sup>nd</sup>, 3<sup>rd</sup> and 4<sup>th</sup> stage.

$L_{Sa}$ (mm)	GDD (fs <sup>2</sup> )	$\tau_{RMS}$ (fs)	$L_1$	$L_2$	$L_3$	$L_4$
0	10500	550	4	1.6	1.2	1.1
170	4260	230	3.8	1.6	1.2	1.1
300	4260	230	3.5	1.6	1.2	1.2
460	-4440	230	3.2	1.7	1.7	1.4
620	-10500	550	3.5	1.6	1.2	1.2
750	-10500	550	3.8	1.7	1.2	1.2
920	-10500	550	3.9	1.7	1.2	1.2

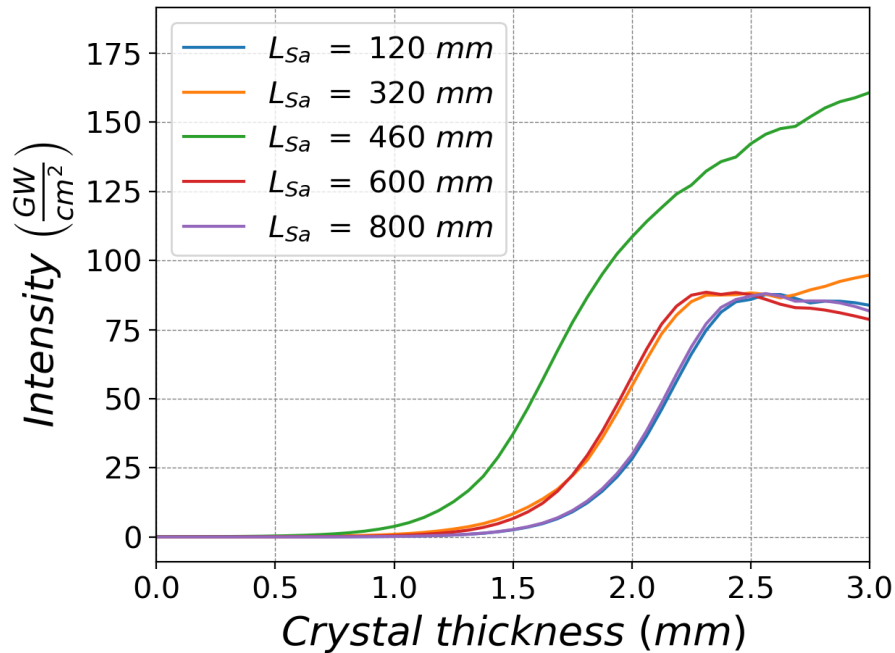


**Fig. 3.55.** Intensity evolution of the signal pulse in the 1<sup>st</sup> stage as a function of the crystal thickness at different chirp values.  $L_{Sa}$  - thickness of the sapphire stretcher

Based on the results, the chosen crystal thicknesses are 3 mm, 1.5 mm, 1.2 mm and 1 mm in the 1<sup>st</sup>, 2<sup>nd</sup>, 3<sup>rd</sup> and 4<sup>th</sup> stages. These values are somewhat shorter than those summarized in Tables 3.18 and 3.19, which prevents the final stages from entering the back-conversion regime.

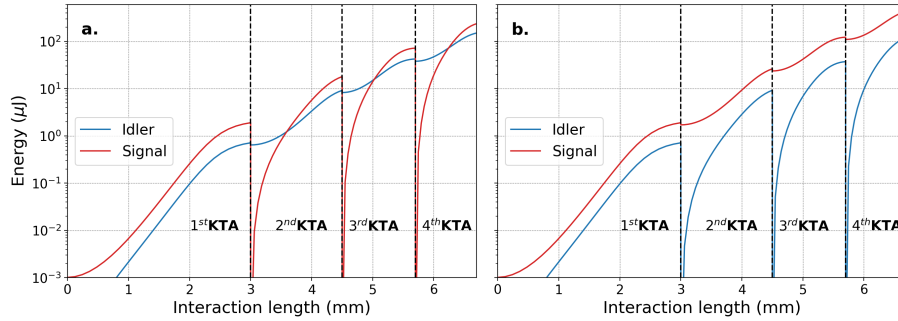


**Fig. 3.56.** Energy evolution of the idler (blue curves) and signal (red curves) pulses in the idler (a) and signal (b) schemes. The vertical dashed lines indicate the boundaries of the KTA crystals of each stage. [Adapted] with permission from [Ref. [T3]] © The Optical Society.

Energy evolution as a function of the propagation distance inside the crystals is plotted in Fig.3.56 on the logarithmic scale in the idler (a) and signal (b) schemes. This illustrates that the energy saturates even with slightly shorter crystals, which ensures efficient and stable operation for the OPCPA system, while the quality of the pulses are preserved.

### Chirp optimization

The duration of the stretched seed pulse has a huge impact on the output characteristics of every OPCPA system. The optimal stretching ratio with respect to the pump pulse duration depends on the unique properties of an OPCPA, furthermore it depends on the desired output parameters[59, 60, 83]. Different duration ratios are necessary to reach the highest efficiency, bandwidth or efficiency-bandwidth product (peak-power). For these reasons, it is essential to numerically optimize the chirp in the current case for both amplification schemes. During experiments, the peak intensity or the peak power is the most important parameter. Consequently, in the simulated mid-IR system the chirp is optimized on the highest achievable peak power.

It was mentioned under Section 3.3.2 that from a practical point of view the use of a negatively chirped signal is preferable, however it is not a determining factor and the optimal chirp sign will be revealed by optimization.

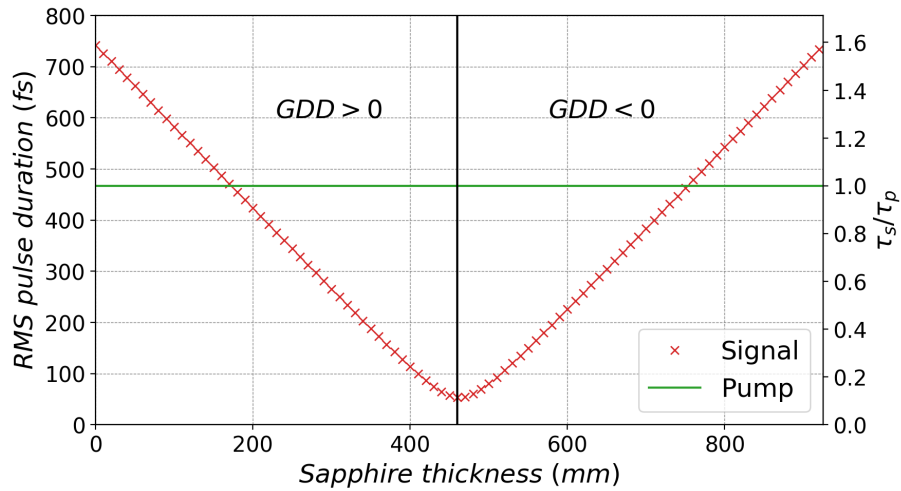


**Fig. 3.57.** Root-mean-square value of the stretched signal pulse (RMS pulse duration) as a function of the length of the sapphire stretcher (red crosses). The green line indicates the RMS duration of the pump. The stretched pulse duration is also expressed by the duration ratio of the signal and pump pulses (right y-axis). The black vertical line at 46 cm indicates the shortest chirped pulse duration. [Adapted] with permission from [Ref. [T3]] © The Optical Society.

In order to optimize the chirp, the thickness of the sapphire stretcher was varied from 0 mm to 920 mm in 10 mm steps. The root-mean-square value of the stretched signal pulse (RMS duration) as a function of the stretcher thickness is visualized in Fig.3.57. The green horizontal line indicates the RMS duration of the pump pulse, while the black vertical line indicates the position of the minimum pulse duration which occurs at 460 mm. Shorter and longer bulk results in a positively ( $GDD > 0$ ) and negatively ( $GDD < 0$ ) chirped signal pulse, respectively.

In case of each stretcher thickness, the entire OPCPA chain was simulated in both amplification scenarios. After the last stage, the Fourier limited pulse shapes ( $P(t)$ ) of both the signal and idler pulses were calculated. The Fourier limited pulse duration and peak power was obtained by taking the FWHM and maximum value of  $P(t)$ , while the energy was calculated by the integration of  $P(t)$  over time. These values are plotted versus the thickness of the sapphire stretcher in the idler (Fig.3.58) and signal (Fig.3.59) schemes.

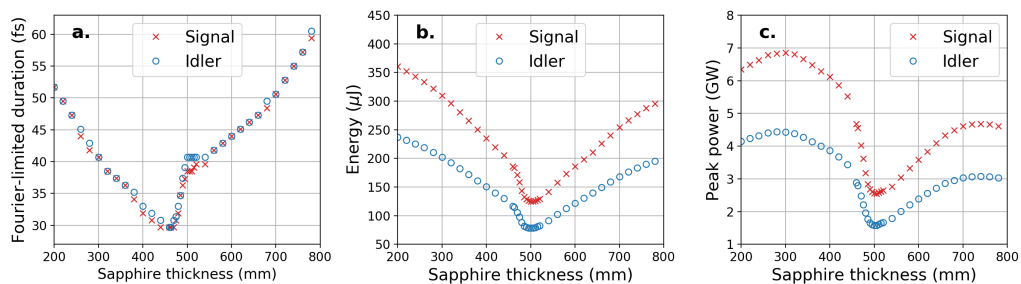


**Fig. 3.58.** Fourier limited pulse duration (a) pulse energy (b) and peak power (c) of the signal (red crosses) and idler (blue circles) after the OPCPA chain in the idler scheme as a function of stretcher thickness. [Adapted] with permission from [Ref. [T3]] © The Optical Society.

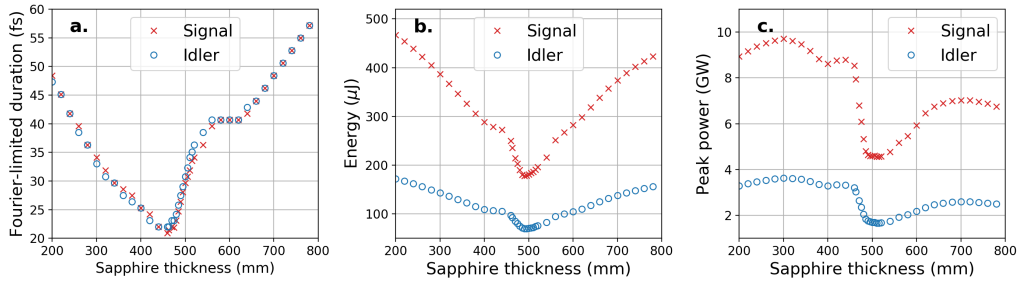


**Fig. 3.59.** Fourier limited pulse duration (a) pulse energy (b) and peak power (c) of the signal (red crosses) and idler (blue circles) after the OPCPA chain in the signal scheme as a function of stretcher thickness. [Adapted] with permission from [Ref. [T3]] © The Optical Society.

If the seed pulse duration is increased either in the positive ( $< 460$  mm) or negative ( $> 460$  mm) chirp direction, the temporal overlap improves between the interacting pulses. Consequently, conversion efficiency increases, which is shown in Fig. 3.58 (b) and Fig. 3.59 (b) in the idler and signal schemes, respectively. On the other hand, the bandwidth of the amplified pulses reduces due to gain narrowing, which results in an increasing Fourier limited pulse duration (Fig. 3.58 (a) and Fig. 3.59 (a)). Since the peak power is proportional to the energy and inversely proportional to the pulse duration, there will be an optimal stretched pulse duration which will provide the highest output peak power. In case of both schemes this is achieved at  $L_{Sa} = 300$  mm and  $L_{Sa} = 720$  mm thick sapphire in the  $GDD > 0$  and  $GDD < 0$  regions, respectively. The parameters of the stretched seed pulse at these stretcher thicknesses are summarized in Table 3.20.

**Table 3.20.** Parameters of the stretched seed pulse at the optimal sapphire thickness ( $L_{Sa}$ ) which results in the highest output peak power in the positively and negatively chirped regions.  $RMS_s$  and  $RMS_p$  are the RMS duration of the stretched seed and pump pulses, respectively.

$L_{Sa}$ (mm)	GDD (fs <sup>2</sup> )	$RMS_s$ (fs)	$\frac{RMS_s}{RMS_p}$
300	4880	265.5	0.57
700	-7552	384	0.82

Apart from the previously described effects, Figs. 3.58 and 3.59 illustrate an unexpected phenomena. All three quantities (FWHM of the Fourier limited shape, energy and peak power) are asymmetric with respect to chirp reversal. The detailed investigation of the effect is presented in the following section.

From the chirp optimization it is obvious that the output peak power (Figs. 3.58.c. and 3.59.c.) is higher in case of a positively chirped signal pulse in both schemes. Therefore, the performance of the idler and signal schemes will be compared in case of the 300 mm thick sapphire stretcher, which provides a 0.57 seed and pump duration ratio.

### 3.3.4 Investigation of peak power asymmetry

In order to reveal the source of peak power asymmetry (Figs. 3.58 (c) and 3.59 (c)), the OPCPA chain was simulated with simplified parameters. Firstly, instead of the

1 ps, Gaussian pump pulse a  $10^{\text{th}}$  order super-Gaussian pulse shape was applied, which had 5 ps duration and the same  $150 \text{ GW cm}^{-2}$  peak intensity. This prevented gain narrowing and its influence on the output results. Secondly, phase derivatives higher than second order (TOD, FOD, etc.) were canceled in the spectral phase of the input signal pulse. High order terms, especially TOD, result in an asymmetric temporal shape, which could be one reason for the peak power asymmetry.

According to Figs. 3.58 and 3.59, the asymmetric behavior of the output peak power is still observable in both the "signal" and "idler" schemes and the tendency is similar in case of both signal and idler pulses. Therefore, in this section I only present the results of the numerical investigation for the idler pulse, which is amplified in "idler scheme".

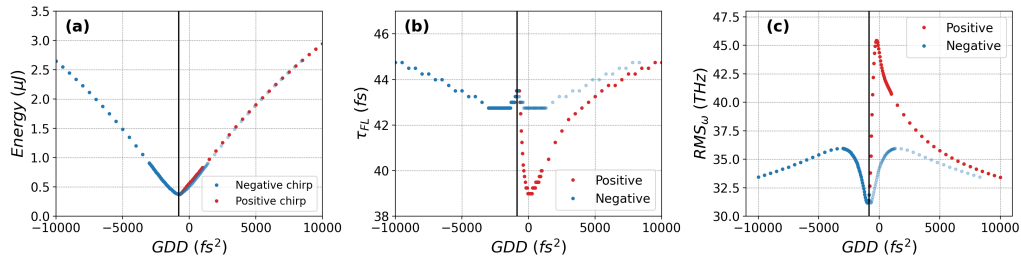


**Fig. 3.60.** Energy (a), Fourier limited duration (b) and root mean square deviation (c) of the idler pulse after the first KTA crystal as a function of the input signal chirp. The black vertical line indicates the position of the minimum output energy.

The influence of the first high-gain OPA stage was examined separately from the last three power amplifier stages. The idler pulse energy after the first KTA crystal as a function of the GDD is plotted in Fig. 3.60. (a). The black vertical line at  $-850 \text{ fs}^2$  indicates the position of the minimum energy, which corresponds to the minimum temporal overlap between the pump, signal and idler pulses, therefore it will be the new axis of symmetry instead of  $0 \text{ fs}^2$ . This shift of the symmetry axis is the consequence of the dispersion of the KTA crystal. According to Table 3.17, the first 3 mm thick crystal adds  $220 \text{ fs}^2$  and  $-1086 \text{ fs}^2$  at the signal and idler central wavelengths, respectively. This means that the idler and signal pulses will have  $0 \text{ fs}^2$  GDD by the end of the KTA crystal if the input signal pulse has  $-1086 \text{ fs}^2$  and  $-220 \text{ fs}^2$  GDD, respectively. Therefore, the minimal temporal overlap during amplification should be between  $-1086 \text{ fs}^2$  and  $-220 \text{ fs}^2$  input signal chirp, as it is provided by the numerical simulation.

In Fig. 3.60 (a)-(c), the values corresponding to the negative input signal chirp (blue dots) are mirrored into the positive quadrant and indicated by the faded blue dots, therefore they can be obviously compared to the positively chirped values (red dots).

According to the results shown in Fig. 3.60 (a), by deviating from the black vertical line in either the positive or negative direction energy increases due to the improving temporal overlap between the three interacting pulses. Furthermore, the output energy values in case of a negative (blue dots) and positive (red dots) input signal GDD have reflection symmetry on the black vertical line, which indicates that efficiency is not influenced by the input chirp sign.

The Fourier limited pulse duration ( $\tau_{FL}$ ) and the root mean square deviation of

the idler spectrum ( $RMS_{\omega}$ ) as a function of the input signal chirp are plotted in Figs. 3.60 (b) and (c). The results indicate that in case of a positive input signal chirp the output idler (and also signal) pulse has a shorter Fourier limited duration (Fig. 3.60 (a)) and a broader bandwidth (Fig. 3.60 (c)). The biggest deviation in the Fourier limited pulse durations is 4 fs, which occurs at  $0 \text{ fs}^2$  and  $-1700 \text{ fs}^2$  input signal chirp respectively, while the output energy in case of these values is the same.

Fig. 3.61 illustrates the idler spectrum after the first stage in case of  $-2700 \text{ fs}^2$  and  $1000 \text{ fs}^2$  input signal chirp. In case of these two input chirp values the output pulse energy is equally  $0.8 \mu\text{J}$ . It must be noted that the bandwidth deviation is not large and during experimental conditions it is hard to observe since usually it is not trivial to reverse the input chirp, and the small difference can also be attributed to measurement errors.

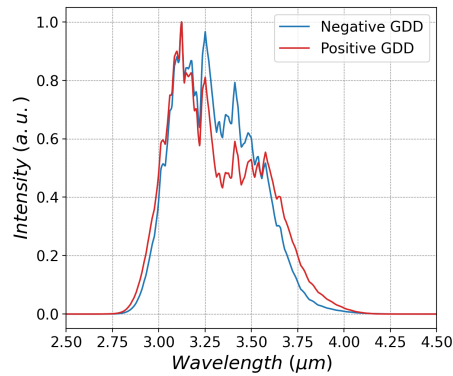


**Fig. 3.61.** Spectrum of the idler pulse after the first KTA crystal in case of  $1000 \text{ fs}^2$  (red) and  $-2700 \text{ fs}^2$  (blue) input signal chirp.

The output energy, Fourier limited pulse duration and bandwidth of the idler pulse after the last OPA stage is shown in Fig. 3.62 (a)-(c). The sum of the KTA crystal thicknesses is 6.7 mm, which adds  $491 \text{ fs}^2$  and  $-2427 \text{ fs}^2$  GDD at the signal and idler central wavelengths, respectively. Consequently, the position of the minimum output energy is further shifted. According to the numerical simulations, a  $-1450 \text{ fs}^2$  input signal GDD minimizes the temporal overlap between the idler, signal and pump pulses during amplification in the four OPA stages (black line in Fig. 3.62 (a)).

In contrast to the first stage, there is a significant difference ( $\approx 80 \mu\text{J}$ ) in the output pulse energy in case of negative and positive input signal GDD. This energy difference is, however, an indirect consequence of the chirp sign, as it was not observable after the first crystal. The reason for this energy difference is that the first KTA crystal introduces bandwidth asymmetry in case of positive and negative input signal chirp values. Since the bandwidth is larger in case of a positive GDD, the stretched pulse duration is also longer. Thus the temporal overlap is better in the power amplifier stages, which results in higher conversion efficiency.

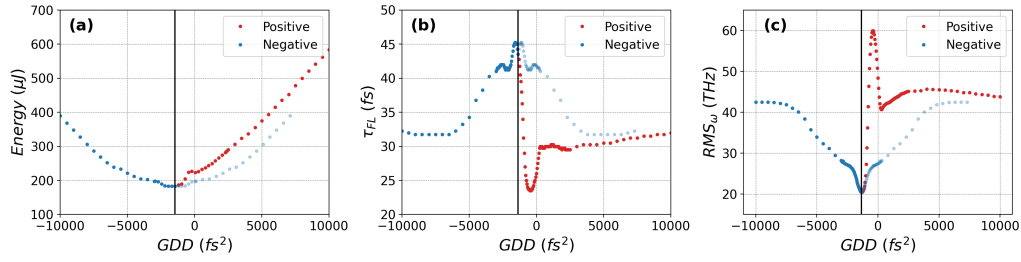


**Fig. 3.62.** Energy (a), Fourier limited duration (b) and root mean square deviation (c) of the idler pulse after the last KTA crystal as a function of the input signal chirp. The black vertical line indicates the position of the minimum output energy.

The deviation in the Fourier limited pulse duration (Fig. 3.62 (b)) and bandwidth (Fig. 3.62 (c)) in case of negative and positive input signal chirp values is even more emphasized after the last stage. The shorter pulse duration and the higher output pulse energy leads to higher peak power in the positively chirped region, as it is indicated in Fig. 3.63.

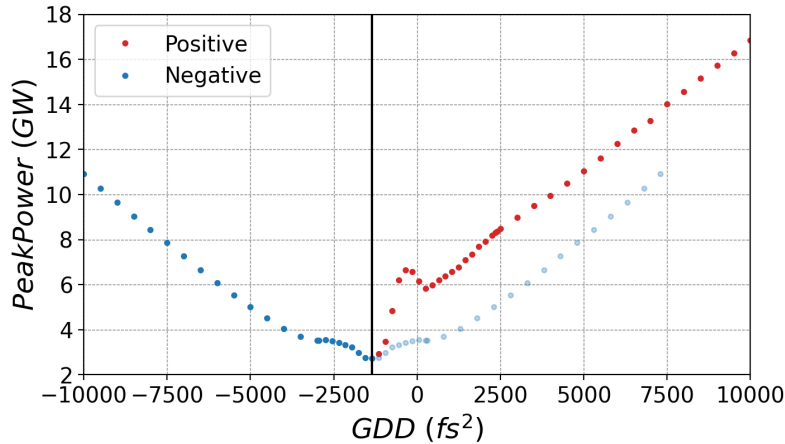


**Fig. 3.63.** Peak power of the Fourier limited idler pulse shape after the OPA chain. The black vertical line indicates the position of the minimum output energy. The values corresponding to a negative input signal chirp are mirrored into the positive quadrant (faded blue dots).

The asymmetry in the amplified bandwidth is the consequence of the dispersion properties of the KTA crystal. According to Table 3.17, KTA has positive and negative GDD at the signal and idler central wavelengths, respectively. Therefore, if the input signal pulse is chirped positively, the temporal duration will increase during propagation through the KTA crystal. The idler chirp in this case will be negative. Since KTA has a negative GDD at the idler central wavelength, the idler will also broaden temporally. This is visualized in Fig. 3.64 (a), where the blue continuous and dashed curves represent the idler pulse shape at  $z_0$  and  $z_0 + 2$  mm spatial positions inside the KTA crystal. The green shaded area represents the pump pulse, which is almost depleted. The vertical blue and red lines mark the temporal locations of the  $2.8 \mu\text{m}$  and  $3.5 \mu\text{m}$  spectral components under the envelope of the negatively chirped idler pulse. After 2 mm propagation, these spectral components

will move away from the depleted pump region, as it is indicated by the dashed lines and arrows in Fig. 3.64 (a). This way the spectral edges will be amplified efficiently.

If the input signal pulse has negative chirp, the opposite thing will occur, which is illustrated in Fig. 3.64 (b). The temporal duration of both signal and idler pulses will be shorter during propagating through KTA crystals, and the spectral edges will move towards the depleted pump region, hence they will experience a smaller intensity gain than in the previous situation.

Due to the previously described phenomena, the bandwidth of the amplified pulses will be narrower when the idler and signal pulses shorten in time during amplification. This effect, to the best of my knowledge, has not been identified so far, therefore I have named it "depletion induced gain narrowing", and it is responsible for peak power asymmetry.

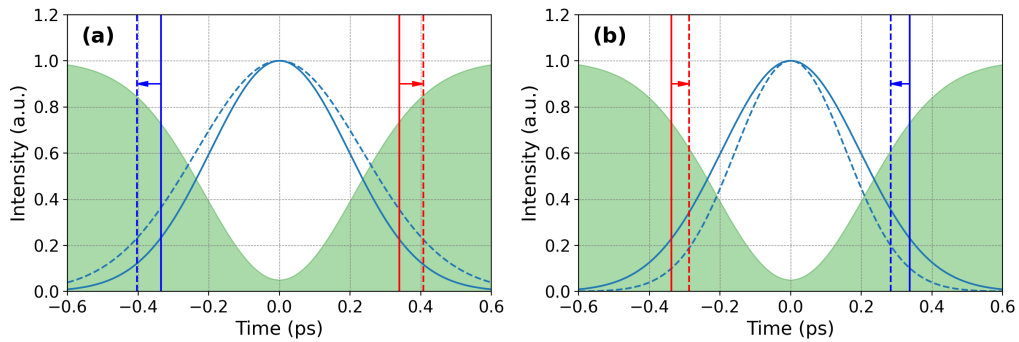


**Fig. 3.64.** Visualization of depletion induced gain narrowing. (a) The duration of the chirped signal and idler pulses increase, so the blue and red spectral components move away from the depleted region and thus enhance efficiency. (b) The pulses get shorter in time, so the spectral edges move towards the depleted region and the gain bandwidth decreases.

### 3.3.5 Comparison of the idler and signal schemes

#### Energy and energy stability

The energy values of the idler and signal pulses after each stage, the pump-to-signal and pump-to-idler conversion efficiencies and energy stability of the two schemes are summarized in Table 3.21. From the energy values ( $E_{1,2,3,4}$ ) and the conversion efficiencies ( $\eta_{p-s,i}$ ) it can be concluded that the idler (signal) is generated more efficiently in the idler scheme (signal scheme). This can be attributed to the fact that in the signal scheme, approximately 50  $\mu\text{J}$  idler is discarded before the last stage. Similarly, in the idler scheme, a roughly 113  $\mu\text{J}$  signal is dumped before OPA4.

The pump extraction efficiency ( $\eta_{p-s+i}$ ) is slightly higher in the idler scheme than in the signal scheme. The reason for this is that KTA is more dispersive in the mid-IR than in the SWIR spectral range. Therefore, the idler in the idler scheme will be longer in time than the signal in the signal scheme by the end of the OPCPA system (note the chirped pulse duration in Table 3.22). Consequently, in the idler scheme the temporal overlap of the three pulses will be higher than in the signal scheme, which results in slightly improved extraction efficiency.

A very crucial point of every OPCPA system is the energy stability of the amplified pulses. The main source of energy instabilities is the fluctuations of the pump

intensity. The stability is defined by Eq.3.1, where  $\sigma$  is the standard deviation and  $\mu$  is the mean value of the pump energy.

$$Stability = \frac{\sigma}{\mu} \cdot 100 \quad (3.1)$$

It is assumed that the fluctuations of the pump intensity follow normal distribution. To reveal which scheme is less sensitive on pump instabilities the standard deviation of the pump intensity was varied from  $0 \text{ GW cm}^{-2}$  to  $4 \text{ GW cm}^{-2}$ . According to Eq.3.1, this translates to a 0% to 2.67% stability interval. Therefore, in the simulations the pump intensity in the last stage was varied from  $148 \text{ GW cm}^{-2}$  to  $152 \text{ GW cm}^{-2}$  in  $0.4 \text{ GW cm}^{-2}$  steps, and in each case OPA and DFG was simulated in the idler and signal schemes. In this small intensity range the output energy of the signal and idler pulses depend linearly on pump intensity, and it is assumed that the output energy values also follow normal distribution. The energy stability of the idler and signal pulses in the two schemes are compared in Fig.3.65 (a) and (b). From this we can conclude that the stability of the idler (signal) is better in the idler scheme (signal scheme).

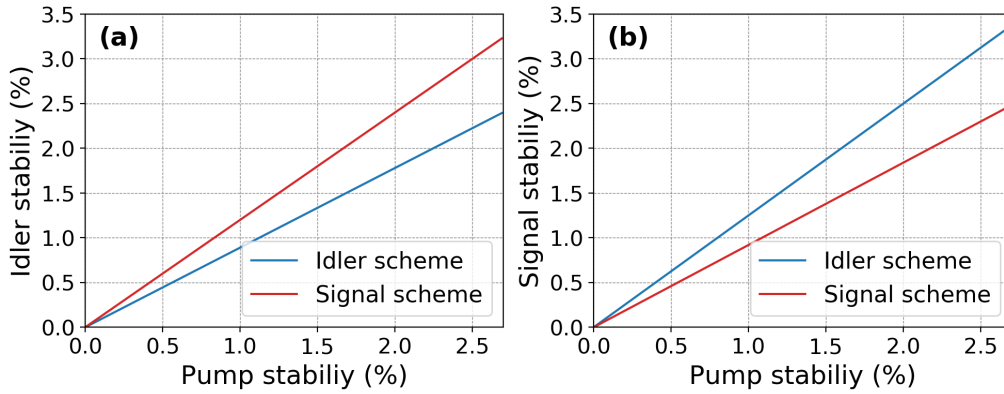


**Fig. 3.65.** Stability of the idler (a) and signal (b) as a function of pump stability in the idler (blue) and signal (red) schemes. [Adapted] with permission from [Ref. [T3]] © The Optical Society.

### Spectral and temporal characteristics

The spectral and temporal characteristics of the idler and signal pulses in the two schemes are compared in Table 3.22. The duration of the chirped pulses ( $\tau_{chirped}$ ) after the final stage is longer in the idler scheme than in the signal scheme, which is the consequence of the larger dispersion of KTA crystals at the idler central wavelength (Table 3.17). This is also indicated by the larger absolute value of the dispersion coefficients (GDD, TOD and FOD in Table 3.22) in the idler scheme. According to Table 3.21, this results in a slightly improved energy extraction efficiency. On the other hand, due to the longer stretched pulse duration, pulses in the idler scheme are affected more by gain narrowing than in the signal scheme. As a result, the Fourier limited pulse duration ( $\tau_{FL}$  in Table 3.22) is longer in the idler than in the signal scheme. According to Fig.3.66, this difference means only a little deviation in the shape of the spectrum and during experimental conditions it can be overcome by the slight detuning of subsequent crystals.

**Table 3.21.** Comparison of the energy ( $E_{1,2,3,4}$ ) after each stage, overall pump-to-signal or pump-to-idler conversion efficiency ( $\eta_{p-s,i}$ ) and energy stability of the two schemes.

-	Idler Scheme		Signal Scheme	
	Signal	Idler	Signal	Idler
$E_1$ ( $\mu\text{J}$ )	2.4	1.2	2.4	1.2
$E_2$ ( $\mu\text{J}$ )	20.9	11.4	21.6	9.65
$E_3$ ( $\mu\text{J}$ )	90	55	99	39
$E_4$ ( $\mu\text{J}$ )	314	205	364	136
$\eta_{p-s,i}$ (%)	15.7	10.25	18.2	6.8
$\eta_{p-s+i}$ (%)	25.95		25	
Stability*(%)	1.25	0.89	0.92	1.2

\* at 1% pump stability

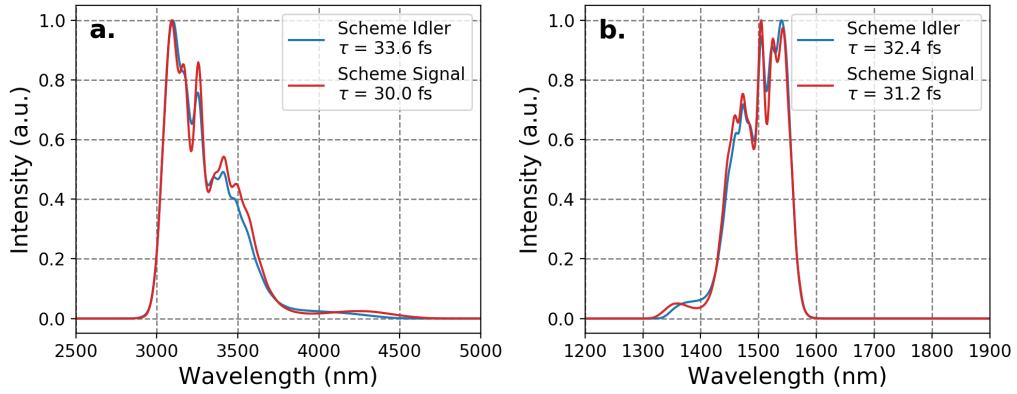


**Fig. 3.66.** Comparison of the idler (a) and signal (b) spectra produced in the idler scheme (blue) and the signal scheme (red). The Fourier limited pulse duration ( $\tau$ ) is indicated in the legend. [Adapted] with permission from [Ref. [T3]] © The Optical Society.

Chirp optimization revealed that higher peak power can be achieved when the signal is chirped positively. In accordance with this, the idler pulse will be chirped negatively. Therefore, the signal and idler pulses can be compressed in bulk sapphire and silicon, respectively (Table 3.22). The RMS duration of the signal pulse is minimized by 237 mm and 196 mm long sapphire in the idler and signal schemes, respectively (Fig.3.67.a.). In case of silicon, which is used for the compression of the idler pulse (Fig.3.67.b.), these values are 11.4 mm and 9 mm (Table 3.22).

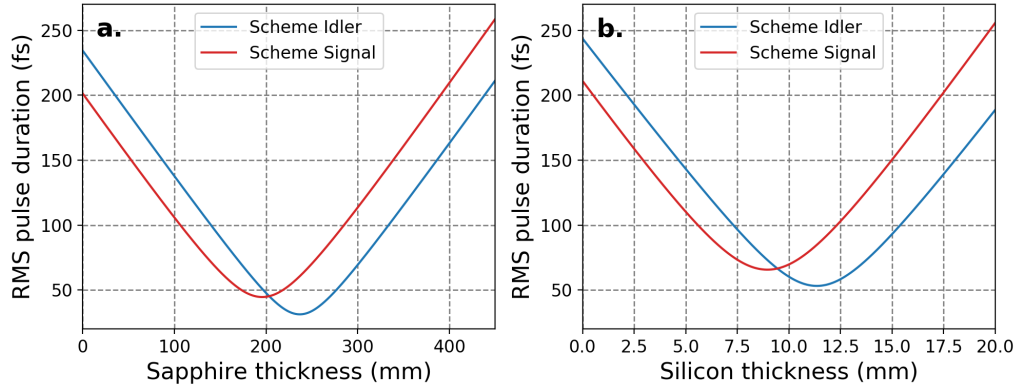


**Fig. 3.67.** RMS pulse duration in idler (blue) and signal (red) scheme as a function of the thickness of the sapphire (a) and silicon (b) compressor.

The shortest compressed pulse duration cannot be achieved solely by the bulk compressors. Some residual spectral phase will always be present, which, however, can be pre-compensated by the AOPDF at the beginning of the OPCPA system. The compressed duration of the signal and idler pulses are summarized in Table 3.22. The values indicate that in the signal scheme the compressed pulse duration is slightly shorter than in the idler scheme, but the deviation is negligible.

The peak power of the compressed pulses are summarized in the last row of Table 3.22. Since the difference in the duration of the compressed pulses is negligible, these values correlate with the energy of the amplified pulses after the last stage (Table 3.21). According to this, the peak power of the idler (signal) is higher in the idler (signal) scheme than in the signal scheme.

**Table 3.22.** Spectral and temporal characteristics of the signal and idler pulses in the idler and signal schemes.

-	Idler Scheme		Signal Scheme	
	Signal	Idler	Signal	Idler
$\tau_{chirped}^a$ (fs)	568	588	508	520
$GDD$ (fs <sup>2</sup> )	4841	-4994	3953	-4038
$TOD \cdot 10^3$ (fs <sup>3</sup> )	-34	-48	-22	-31
$FOD \cdot 10^6$ (fs <sup>4</sup> )	5.3	-5.8	4.9	-5.1
$\tau_{FL}^b$ (fs)	32.4	33.6	31.2	30
Compressor material	Sapphire	Silicon	Sapphire	Silicon
Compressor thickness (mm)	237	11.4	196	9
Compressed pulse duration <sup>c</sup> (fs)	34.2	35.4	33.6	33
Peak power (GW)	7.7	4.8	8.3	3.3

<sup>a</sup> FWHM of the stretched pulses

<sup>b</sup> FWHM of the Fourier limited pulse shape

<sup>c</sup> Perfect phase compensation at the center of mass of the beam profile

### CEP-stability

The CEP stability of the mid-IR pulses is influenced by several factors (such as air turbulence, mechanical vibrations and temperature instabilities) which are present

regardless of the applied amplification scheme. On the other hand, CEP-stability is also sensitive to the fluctuations of pump intensity, which can cause differences in the two schemes. Therefore, pump intensity was varied from  $148 \text{ GW cm}^{-2}$  to  $152 \text{ GW cm}^{-2}$  in  $0.2 \text{ GW cm}^{-2}$  steps and in each case the amplification was simulated in the 4<sup>th</sup> OPA or DFG stage. For every pump intensity, the spectral phase of the idler pulse was extracted and by fitting a fourth-order polynomial the phase derivatives were obtained at the central frequency  $\omega_0$  up to the 4<sup>th</sup> order. From  $\phi(\omega_0)$  and  $GD(\omega_0)$  the CEP was calculated according to Eq.2.41 [82].

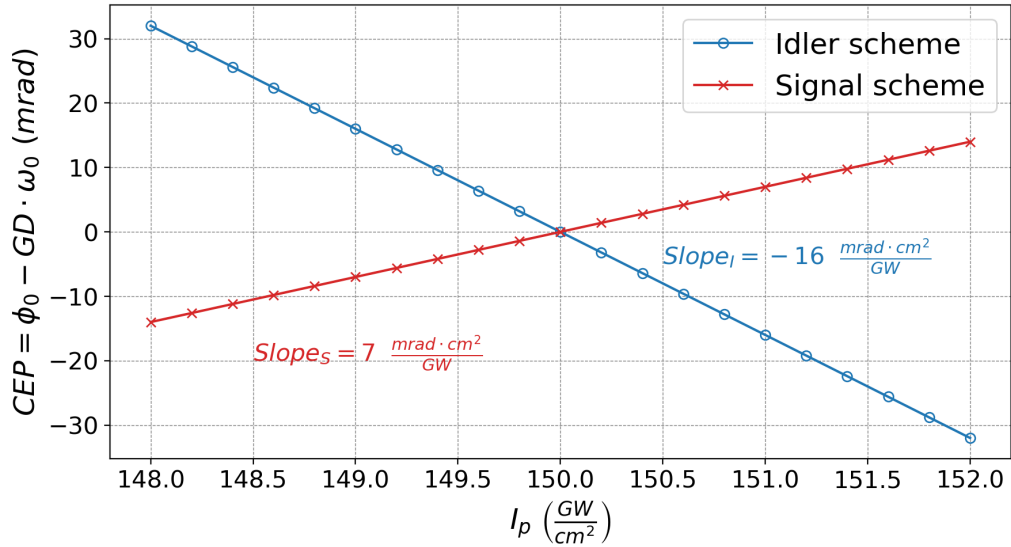


**Fig. 3.68.** CEP as a function of the pump intensity in the last stage in the idler (blue circles) and signal (red crosses) schemes. The slopes of the fitted lines are indicated in the figure. [Adapted] with permission from [Ref. [T3]] © The Optical Society.

The CEP as a function of pump intensity is shown in Fig. 3.68. According to the obtained data, there is a linear correlation between the pump intensity and the CEP of the idler pulses in both schemes. The slopes of the fitted lines are  $-16 \text{ mrad cm}^2 \text{ GW}^{-1}$  and  $7 \text{ mrad cm}^2 \text{ GW}^{-1}$  in the idler and signal schemes, respectively. According to this result, the CEP of the idler is less sensitive to pump intensity fluctuations in the signal scheme. The energy stability of typical pump lasers is better than 1%. If the average intensity value is  $150 \text{ GW cm}^{-2}$ , then this stability, according to Eq.3.1, corresponds to  $1.5 \text{ GW cm}^{-2}$  standard deviation. Based on the calculated slopes, this standard deviation translates to 23.4 mrad and 11 mrad CEP noise in the idler and signal schemes, respectively.

### 3.3.6 Summary

**T4** I have numerically optimized the performance of two CEP-stabilized mid-IR systems, which are different in the order of amplification (OPCPA) and frequency conversion (DFG) stages and revealed that the overall conversion efficiency is slightly better and the peak power of the idler is higher if DFG is placed before OPCPA, while CEP-stability is somewhat better and the compressed pulses are shorter if OPCPA is done prior DFG [T3]. Due to the small differences, the applicable scheme could be decided by an overall cost-benefit analysis.

**T5** I revealed, to my knowledge for the first time, that the interplay of pump depletion and the shortening of stretched pulses during amplification results in gain narrowing and due to this lower peak power can be achieved at the output of the OPCPA system [T3].

# Chapter 4

## Summary

In my thesis I used a 4D numerical code for the modeling of various OPCPA systems. The code utilizes a special algorithm for calculating the fast Fourier-transform of highly chirped pulses [67]. The numerical simulation of OPCPA, especially in case of a broadband signal and long ( $\geq 10$  ps) pump pulses, is challenging because of the fine temporal resolution and large temporal grid size, which are needed to resolve both the Fourier-limited signal pulse and accommodate the long pump pulse. In the advanced algorithm the quadratic phase term is factored out, thus resulting in two subsequent Fourier-transforms and separate temporal grids for the transform-limited and stretched signal pulses. This way the requirements on the temporal grid size are relaxed. The method enables the numerical simulation of OPCPA on desktop computers without approximations and with acceptable computational time.

The OPCPA concept has many advantages compared to conventional, laser amplifier based CPA systems. It can provide large gain bandwidth, exceptional pulse contrast and can be scaled to high average powers. Yet, PW-scale systems are rather based on conventional CPA, mainly due to the two-fold increase in conversion efficiency provided by Ti:sapphire.

Therefore, my aim was to examine the idea of a special OPA arrangement which could potentially increase conversion efficiency.

**T1** I have numerically examined the properties of the cascaded-extraction optical parametric amplifier (CE-OPA) design and revealed that CE-OPA increases conversion efficiency by at least 10%, without deteriorating the spatiotemporal shape of the amplified signal[T1].

The production of pulses as short as a single oscillation cycle under the field envelope is mainly motivated by isolated attosecond pulse generation. Such short pulses can be generated by using post-compression techniques, however, currently they are limited to a few-mJ energy level. On the other hand, few-tens-mJ, three-cycle pulses are directly accessible from OPCPA systems. Therefore, the other way of reaching single-cycle duration is to find a method to increase the gain bandwidth of OPCPA.

Consequently, my aim was to examine the properties of a few broadband OPCPA configurations which could potentially broaden the gain spectrum.

**T2** I have shown that double-BBO configuration introduces spatiotemporal couplings if the two following two conditions are satisfied [T2]:

1. The lateral pump displacement in noncollinear geometry is comparable to the size of the interacting beams.
2. The intensity gain is high, thus the pump guides the signal pulse during amplification.

The first development phase of the ELI-ALPS Single Cycle Laser (SYLOS 1) was the first 1 kHz repetition rate TW-class OPCPA system, delivering CEP-stabilized, three-cycle pulses [36]. During the second development phase, called SYLOS 2, the aim was to shorten the pulse duration close to 2-cycle, while keeping the peak power at the same level.

Therefore, my aim was to determine the optimal OPCPA configuration during the upgrade of the Single-Cycle Laser (SYLOS 2) laser in ELI-ALPS.

**T3** I have modeled and determined the optimal configuration of an OPCPA system to provide 2.2-cycle, TW class pulses [T2].

In the past few years, OPCPA systems operating in the mid-IR have rapidly proliferated due to the recognition that many strong field physical experiments can benefit from the long wavelength driving pulses. CEP-stabilized, mid-IR pulses are generated as the difference frequency of the pump and signal pulses. There are two options to increase the energy of the mid-IR pulses: the first is to amplify the idler pulse after DFG; the second is to amplify the signal prior DFG. During my work, I named these two scenarios as "idler scheme" and "signal scheme", respectively. According to the mid-IR systems reported so far, the two schemes are utilized approximately equally, without reasoning about the chosen amplification scheme. In laboratory conditions it is not straightforward, and in some cases it is even impossible, to switch from one scheme to the other under the same experimental conditions.

Therefore, my aim was to optimize a mid-IR OPCPA in case of both schemes and provide an answer to the previous question.

**T4** I have numerically optimized the performance of two CEP-stabilized mid-IR systems, which are different in the order of amplification (OPCPA) and frequency conversion (DFG) stages and revealed that the overall conversion efficiency is slightly better and the peak power of the idler is higher if DFG is placed before OPCPA, while CEP-stability is somewhat better and the compressed pulses are shorter if OPCPA is done prior DFG [T3]. Due to the small differences, the applicable scheme could be decided by an overall cost-benefit analysis.

**T5** I revealed, to my knowledge for the first time, that the interplay of pump depletion and the shortening of stretched pulses during amplification results in gain narrowing and due to this lower peak power can be achieved at the output of the OPCPA system [T3].

# Chapter 5

## Magyar nyelvű összefoglaló

### 5.1 Bevezetés

A XIX. század elejéig a Nap volt a legintenzívebb fényforrás, amellyel kísérletezni tudtak. Ennek alapján írták le a fény terjedésének ma is használatos, alapvető törvényeit, mint például az egyenes vonalú terjedést, fénytörést és a diszperziót (az anyag törésmutatójának a fény hullámhosszától való függése). Mindezt egy olyan fényforrás segítségével tették, melynek átlagos intenzitása a Föld felszínén  $0,14 \text{ W cm}^{-2}$ . Ennél az intenzitásszintnél az anyagok optikailag lineáris viselkedést mutatnak. Ez azt jelenti, hogy az anyag nem létesít kölcsönhatást a fény különböző frekvencia komponensei között. Ezzel szemben, a lézerek 1960-ban történő sikeres kísérleti megvalósítását követően [1] lehetőség nyílt tízmilliószor nagyobb (több  $\text{MW cm}^{-2}$ ) intenzitás elérésére. Ekkora fényintenzitás már nemlineáris viselkedést vált ki az anyagban. Az első ilyen nemlineáris jelenséget, a másodharmonikus keltést (SHG), már 1961-ben, nagyjából egy évvel a lézer felfedezése után demonstrálták [2].

A lézerekben a fény erősítése indukált emisszió révén jön létre miközben a fény áthalad az erősítő közegen, amely az energiát tárolja. Az energiatárolást az aktív anyagok speciálisan elhelyezkedő, valós energianívói teszik lehetővé. Az aktív anyagok gerjesztése, pumpálása során a lézeraktív atomok átkerülnek a lézerműködéshez szükséges felső energiaszintre, létrehozva a populáció inverziót. Ezen energiaszintek élettartama, szilárdtest lézerek esetén, a néhány mikroszekundum ( $1 \mu\text{s} = 1 \times 10^{-6} \text{ s}$ ) és a néhány milliszekundum ( $1 \text{ ms} = 1 \times 10^{-3} \text{ s}$ ) közötti időtartományba esik. Ezzel szemben a másod-harmonikus keltés és ehhez hasonló nemlineáris folyamatokban valós energiaszintek nem vesznek részt. Az ilyen folyamatokat parametrikus folyamatoknak nevezzük. A parametrikus folyamatok során az anyag atomjai, a Heisenberg-féle határozatlansági reláció ( $\Delta t \Delta E \geq \hbar/2$ ) által megszabott  $\Delta t$  időtartamig felkerülnek egy virtuális energiaszintre. Ezen virtuális szintek élettartama egy látható tartománybeli foton esetén a néhány száz attoszekundum ( $1 \text{ as} = 1 \times 10^{-18} \text{ s}$ ) időtartományába esik. Emiatt a parametrikus folyamatok lejátszódása a femtoszekundumtól ( $1 \text{ fs} = 1 \times 10^{-15} \text{ s}$ ) nagyobb időintervallumokon, ahol ezeket jelenleg hasznosítani és tanulmányozni lehet, pillanatszerűnek tekinthető.

A másod-harmonikus keltés kísérleti megvalósítását követően a tudósok vizsgálni kezdték a fény nemlineáris folyamatokkal történő erősítését [5]. Ez a módszer az úgy nevezett optikai parametrikus erősítés (OPA), amelyet kísérletileg először 1965-ben igazoltak [6]. A folyamat során a pumpa impulzusból pillanatszerű energiatranszfer történik a jel impulzusba. A pumpa és a jel impulzusok foton energia különbsége egy harmadik, úgynevezett "idler" impulzus megjelenését eredményezi. Megjegyzendő,

hogy lézerek esetén ez az energiakülönbség hő formájában akkumulálódik és az aktív közeget fűti.

Az impulzusüzemű lézerek lehetőséget adtak extrém kísérleti körülmények létrehozására, valamint hasznosnak bizonyultak időbontott és ultragyors folyamatok vizsgálatánál is. Ebből kifolyólag a cél a minél rövidebb és minél nagyobb energiájú impulzusok előállítása volt. Hamarosan felfedeztek két módszert, a Q-kapcsolást és a módusszinkronizációt, amelyek lehetővé tették a nagy energiájú nanoszekundum ( $1 \text{ ns} = 1 \times 10^{-9} \text{ s}$ ) időtartamú, illetve kisebb energiájú és pikoszekundum alatti ( $1 \text{ ps} = 1 \times 10^{-12} \text{ s}$ ) időtartamú impulzusok előállítását. A gyors technológiai fejlődésnek köszönhetően a lézerek olyan intenzitás szintet produkáltak, amelynél az anyagok törésmutatója intenzitásfüggővé vált. Ez olyan effektusok felfedezéséhez vezetett, mint az önfázis moduláció (SPM) és az önfókuszálódás (Kerr-effektus), illetve ezek következményeként a lézernyaláb terjedés közben történő felbomlása. Mindezen jelenségek megakadályozták az impulzusok energiájának további növelését. A problémára bő két évtizeden át nem találtak megoldást, mígnem 1985-ben Donna Strickland és Gérard Mourou sikeresen alkalmazták a fázismodulált impulzusú erősítés ("chirped pulse amplification"), rövidítve CPA, módszerét lézerpulzusokra [10]. A módszer lényege, hogy az ultrarövid impulzusok időtartamának növelésével lecsökkentjük a csúcshintenzitást. Így erősítés közben nem lépnek fel az előbb említett, nemkívánt nemlineáris jelenségek. Az erősítést az impulzusok időbeli összenyomása követi. A ma működő titán-zafír alapú CPA rendszerekben 100 fs alatti időtartamú impulzusokat, akár 1 ns időtartamra nyújtják, ami lehetővé teszi az impulzusok energiájának akár 12 nagyságrenddel történő növelését. Így, az impulzusok csúcsteljesítménye az időbeli összenyomásukat követően a petawattos (PW) szintet is elérheti. Ezzel a módszerrel nemrégiben 5,4 PW csúcsteljesítményű ( $1 \text{ PW} = 1 \times 10^{15} \text{ W}$ ), 24 fs időtartamú lézerpulzust produkáltak [12].

Azokat a CPA rendszereket, melyekbe lézerekristály helyett optikai parametrikus erősítésnél használatos nemlineáris kristályt helyeznek, optikai parametrikus fázismodulált impulzusú erősítőknak ("optical parametric chirped pulse amplification", OPCPA) nevezik. A lézerekristályokkal ellentétben, az OPA pillanatszerű mivolta miatt, az OPCPA megvalósításához sokkal szigorúbb időzítési feltételeket kell teljesíteni. Biztosítani kell a jel és pumpa impulzusok tér- és időbeli átfedését. Az OPCPA első sikeres demonstrálása 1992-ben történt (Dubietis és tsi. [13]), majd nemsokkal később a TW-os határt is sikerült átlépni velük [14]. Nemrégiben egy teljesen OPCPA alapú rendszerrel 4,9 PW csúcsteljesítményű és 18,6 fs időtartamú impulzusok előállítását valósították meg [15].

Az OPCPA első és egyben legfontosabb előnye a lézerekristályon alapuló CPA módszerhez képest, hogy a pumpa és jel fotonok energiakülönbsége egy harmadik foton formájában távozik a kristályból. Így a nemlineáris kristályokban nagyságrendekkel kisebb hőterhelés lép fel, mint a lézerekristályokban. Ebből kifolyólag az OPCPA könnyebben skálázható nagy átlagteljesítményű impulzussorozatok létrehozására. Továbbá a lézerekristályokban fellép egy parazitikus folyamat, az úgynevezett erősített spontán emisszió (ASE) jelensége. Ez az erősített impulzusok előtt és után egy hosszan elnyúló zajszintet okoz, ami negatívan befolyásolja a kísérletek lefolyását. Időtartamát a lézereközeg gerjesztett energiaszintjének lecsengési ideje szabja meg. Az ennek megfelelő jelenség a parametrikus erősítőknél az úgynevezett parametrikus szuperfluoreszcencia (PSF), amely az elektromágneses tér vákuum fluktuációjából származik [150]. Ennek időtartamát a pumpaipulzus időtartama

szabja meg. Így, ha a pumpa és jel impulzusok időtartama közel azonos, akkor az OPCPA módszerrel nagyobb kontraszttal (jobb jel-zaj viszonytal) rendelkező impulzus állítható elő. Nem utolsósorban a parametrikus erősítők sáv szélessége általában nagyobb, mint a lézeraktív közegek emissziós sáv szélessége. Ezért az OPCPA rendszerek 10 fs időtartamú impulzusok előállítását is lehetővé teszik, míg a titán-zafír alapú CPA rendszerekben az elérhető impulzushossz, speciális technikák hiányában, a 40 fs és 50 fs közötti tartományba esik.

Előnyös tulajdonságai mellett az OPCPA működéséhez sokkal szigorúbb körülmények szükségesek. A legfontosabb követelmény a pumpa és jel impulzusok szinkronizációja. Továbbá az erősített jel impulzus igen érzékeny a pumpa impulzus téridőbeli alakjára, ami sokáig nagy kihívások elé állította a pumpalézer technológiát. Mindezek mellett az energiakonverzió tipikus hatásfoka OPCPA-ban a 10% és 25% közötti tartományba esik, míg titán-zafír CPA rendszerekben kisebb erőfeszítésekkel 50% is elérhető. Ez utóbbi az oka annak, hogy a PW csúcsteljesítményű impulzusokat előállító CPA rendszerek többsége lézererősítő kristályon alapul.

Az utóbbi két évtizedben az 1  $\mu\text{m}$  központi hullámhosszú impulzusokat előállító pumpalézer technológia [28, 34, 35] nagy fejlődésen esett át, amelynek következtében egyre több működő OPCPA rendszert demonstrálnak világszerte.

Az OPCPA rendszerekkel olyan nagy átlag és csúcsteljesítményű ultrarövid impulzusok előállítása vált lehetővé melyek a fény elektromos terének csupán néhány oszcillációs ciklusból állnak [36]. Ezeket a szakirodalomban néhány-ciklusú impulzusoknak nevezik (ez általában 1-5 ciklust jelent). Az ilyen paraméterekkel bíró impulzusok kiemelt fontosságúak az izolált attoszekundumos impulzusok keltésénél [43–45].

Az OPCPA rendszerek másik fő jelentősége, hogy erősítési spektrumukat a nemlineáris kristályok átláthatósági tartománya szabja meg, míg ezt lézerek esetén az aktív anyagok emissziós spektruma korlátozza. Ez lehetőséget nyújt olyan OPCPA rendszerek megvalósítására, amelyek a közép-infravörös (mid-IR) tartományban működnek. Az utóbbi évtizedben megfigyelték, hogy számos atomfizikai kísérlet lefolyása előnyösebb, ha a kísérletet meghatjő lézerimpulzus hullámhossza a közép-infravörös (mid-IR) tartományban van. Például ilyen fényimpulzusokkal keltették az eddig mért legrövidebb (43 as) attoszekundumos fényimpulzust [47]. Továbbá, számos molekula rotációs és vibrációs spektruma is a közép-infravörös tartományban van, így ezeket a forrásokat elsősorban alkalmazták például biológiai minták vizsgálatánál és lélegzet analízis során [52].

### 5.1.1 Munkám motivációja és célja

Az előzőekben felsorolt kísérletek megkövetelik a nagy csúcs- és átlagteljesítményű, ultrarövid impulzusok előállítását a közeli- és közép-infravörös (near-IR és mid-IR) spektrális tartományokban. Jelenleg erre az OPCPA módszer az egyik legalkalmasabb erősítési technika. Ennél fogva munkám motivációját az OPCPA rendszerek fejlesztése jelentette.

Egy OPCPA rendszer fejlesztése során rengeteg a szabad paraméter, amelyek optimalizálásához elengedhetetlen a széleskörű numerikus módszerekkel történő vizsgálat. A numerikus szimulációk segítségével nagymértékben csökkenthetőek a rendszer kifejlesztéséhez szükséges költségek. Továbbá a szimulációk révén információ nyer-

hető az impulzusok téridőbeli alakjáról, melynek mérése nem mindig kivitelezhető kísérleti körülmények között.

Az OPCPA modellezéséhez fejlesztett numerikus kódok, amelyek a folyamat minden egyes tulajdonságát figyelembe veszik, meglehetősen összetettek [56–58]. Ezen felül a modellezéshez szükséges számításgigák a nyalábméret és az impulzusidő növelésével exponenciálisan növekednek. Ennek következményeként a tudományos folyóiratokban eddig közölt numerikus szimulációknak két esete figyelhető meg, amelyekkel csökkenthető a szimulációhoz szükséges számítási teljesítmény. Az első esetben, közelítésekkel élve, csak kétdimenziós (terjedési távolság és idő) modelleket alkalmaznak [59, 60]. A második esetben egy négydimenziós  $(x, y, z, t)$  modellt használva, 10 ps időtartamnál nem hosszabb impulzusokkal és/vagy kis méretű nyalábokkal végeznek számításokat [62–65].

Munkám során egy olyan négydimenziós, numerikus kódot használtam OPCPA modellezéshez, amely speciális módszerrel számítja ki a szélessávú, nyújtott impulzusok Fourier-transzformáltját. A módszernek köszönhetően lecsökken a numerikus modellezéshez szükséges számítási igény, így lehetőséget ad olyan OPCPA rendszerek közelítés nélküli modellezésére, amelyben a nyújtott impulzusok hossza meghaladja a 10 ps időtartamot. A legjobb tudomásom szerint, a tudományos közlemények alapján, ehhez hasonló szimulációs eredményeket még nem demonstráltak.

Munkám során a következő célokat tűztem ki:

- Egy olyan OPA elrendezés numerikus vizsgálata és optimalizálása, amelynek segítségével növelhető a jelenlegi energiakonverziós hatások.
- Egy olyan OPCPA elrendezés numerikus vizsgálata, amelynek segítségével növelhető az erősített impulzusok sáv szélessége.
- Az ELI-ALPS SYLOS 2 lézerrendszerében lévő szélessávú OPCPA fokozatok numerikus optimalizációja.
- A közép-infravörös ultrarövid lézerimpulzusok két féle előállítási módjának numerikus összehasonlító elemzése.

A dolgozatomban a bevezető után az új tudományos eredményeim megértéséhez szükséges tudományos előzmények rész következnek. Itt részletesen taglalom az ultrarövid impulzusok lineáris és nemlineáris közegben történő terjedését, az optikai parametrikus erősítés folyamatát és a különböző fázisillesztési módszereket. Az egyes fázisillesztési módszereket a munkám során használt nemlineáris kristályok példáján szemléltetem. Vázolom az OPCPA rendszerek numerikus szimulációjának módszereit és szót ejtek a parametrikus erősítőkből fellépő impulzus torzulásokról is. Ezt követően részletezem az új tudományos eredményeimet.

## 5.2 Tudományos előzmények

### 5.2.1 Impulzusok jellemző mennyiségei

Dolgozatomban az elektromos hullámok komplex írásmódját használtam, amely az Euler-formula alapján felírható a tér abszolút értékének és a fázisát tartalmazó exponens szorzataként. Az elektromágneses hullámokat tekinthetjük tér- és időképpen, valamint transzverzális hullámszám- és frekvenciatérben. Az idő- és frekvenciakép,

illetve a tér és transzverzális hullámszám reprezentáció között a Fourier-transzformáció teremt kapcsolatot. Az ultrarövid impulzusok elektromos tere felbontható egy lassan változó burkoló függvényre és egy gyorsan oszcilláló vivőhullámra. A vivőhullám frekvenciája tetszőleges lehet, ennek általában az impulzus spektrumának tömegközéppontját választják. Az impulzus intenzitása arányos az elektromos térerősség abszolút értékének négyzetével, mértékegysége a  $W\text{ cm}^{-2}$ . Az intenzitás függ a térkoordinátáktól és az időtől, és ez jellemzi az impulzus tér-időbeli alakját. Az intenzitásfüggvény idő szerinti integrálja adja meg az impulzus energiasűrűségét, amelynek mértékegysége  $J\text{ cm}^{-2}$ . Gyakran előforduló mennyiség még az impulzus csúcsteljesítménye, amelyet az intenzitás tér-dimenziók szerinti integrálásával kaphatunk meg. Így megkapjuk a csúcsteljesítményt az impulzusidő függvényében. Az impulzus időtartamát a csúcsteljesítmény maximumának félértékszélessége jellemzi, amelyet az *FWHM* rövidítés jelöl. Amennyiben az impulzus időbeli alakja mellékcúcsokat is tartalmaz, akkor az impulzus időtartamát célszerű az impulzusidő szórásával megadni. Ezt dolgozatomban a  $\tau_{RMS}$  mennyiség jelöli.

## 5.2.2 Impulzusok terjedése

**Hullámegyenlet** Az impulzusok terjedését általános esetben a Maxwell-egyenletekből levezethető nemlineáris hullámegyenlet írja le.

**Az anyag polarizációja** A fény-anyag kölcsönhatást a hullámegyenletben az elektromos és mágneses polarizációs vektor fejezi ki (ez nem összekeverendő a fény polarizációjával, azaz a hullámok rezgési irányával). Dolgozatomban nem mágneses anyagokkal foglalkozom, ezért a mágneses polarizáció értéke zérus. Az elektromos polarizációs vektor és az elektromos térerősség vektorok között az elektromos szuszceptibilitás tenzor teremt kapcsolatot, amely izotróp anyagok esetén skalármennyiség. Az elektromos polarizációs vektor felbontható lineáris és nemlineáris részre, amelyek lehetőséget adnak az impulzus terjedése közben fellépő lineáris és nemlineáris effektusok leírására. Ennek megfelelően az elektromos szuszceptibilitás tenzornak van lineáris és nemlineáris része. A lineáris részből vezethető be az anyagok törésmutatója.

**Egyirányú impulzusterjedés** A hullámegyenlet lineáris részének megoldása egy pozitív és egy negatív irányba terjedő hullám összegeként írható fel. A dolgozatomban vizsgált lineáris és nemlineáris jelenségek során nincs visszafelé (negatív irányba) terjedő hullám, így ennek amplitúdója zérus. Ezért a hullámegyenlet egy elsőrendű nemlineáris parciális differenciálegyenletté egyszerűsödik, amelyet egyirányú impulzusterjedési egyenletnek neveznek és az UPPE ("unidirection pulse propagation equation") rövidítés jelöl. Az egyenlet nem alkalmazza a paraxiális és lassan változó burkoló közelítést, továbbá könnyedén implementálható numerikus megoldó algoritmusokban.

**Lineáris terjedés** Alacsony fényintenzitásnál a nemlineáris polarizáció elhanyagolható és ekkor lineáris impulzusterjedésről beszélünk. Lineáris terjedés közben az impulzusok diffraktálódnak, illetve az anyagok diszperziója miatt időben kinyúlnak. Lineáris esetben a Fourier-térben (transzverzális hullámszám és frekvenciater) felírt UPPE egyenlet analitikusan megoldható, majd a Fourier-transzformáció segítségével az elektromos tér felírható a tér-idő képben. Ez lehetőséget ad az impulzus lineáris terjedésének modellezésére valós lézerrendszerekben.

**Diszperzió** A diszperzió az anyagok törésmutatójának frekvenciától való függése.

Normális diszperzió esetén a törésmutató a frekvencia monoton növekvő függvénye. Az impulzusok anyagon történő áthaladásuk közben, a diszperzió miatt, spektrális fázistolást szenvednek, ami a spektrális fázis Taylor-sorának együtthatóival, azaz a fázis deriváltakkal jellemezhető. Ezeket általában negyedrendig szokás felírni. A nulladik tag a vivőhullám burkoló alatti fázisváltozásával ekvivalens. Az első tag a csoportkésés ( $GD$ ), ami megadja az impulzus adott hosszúságú anyagon történő áthaladásához szükséges időtartamot. A második tag, a csoportkésés diszperzió ( $GDD$ ), amely az impulzusok időbeli kinyúlásáért felelős. A harmadik és negyedik tagot a  $TOD$  és  $FOD$  rövidítések jelölik és mellékcsúcsok, illetve talpak megjelenéséhez vezet az impulzus időbeli alakjában.

**Térbeli fázistolás** Az impulzusok valós optikai rendszerekben történő terjedésük során, miközben lencséken haladnak keresztül, illetve gömbtükréről reflektálódnak, térbeli fázistolást szenvednek. A térbeli fázistolás bevezetésével modellezhető az impulzusok fókuszálása, illetve nyalábtágító teleszkópokon történő áthaladása.

**Lineáris terjedés anizotróp kristályban** Anizotróp kristályokban az elektromos térerősség és elektromos eltolás vektorok között a dielektromos tenzor létesít kapcsolatot. A dielektromos tenzor mátrixa szimmetrikus, ami az energia megmaradásának következménye. Ebből kifolyólag sajátértékei valósak és a mátrix a sajátvektorai által alkotott bázisban diagonális. Ezt nevezik dielektromos főtengelerendszernek. A sajátértékek megegyeznek a főtengelelhez tartozó törésmutató négyzetével. Ebből és a Maxwell-egyenletekből következik, hogy az elektromos eltolás, elektromos térerősség, a hullámnormális és az energiaterjedés iránya (Poyting-vektor) egy síkban vannak. Az elektromos térerősség vektor és a Poyting-vektor, valamint az elektromos eltolás vektor és a hullámnormális páronként merőlegesek. A hullámnormális és a Poyting-vektor által bezárt szöget a szakirodalomban "walk-off" szögnek is nevezik. Belátható továbbá, hogy egy adott terjedési irányban két lehetséges fázissebesség léphet fel, amelyekhez két egymásra és a terjedési irányra merőleges elektromos eltolás vektor tartozik. Ezeket nevezzük gyors és lassú hullámoknak, illetve gyors és lassú polarizációs irányoknak. Azokat a kristályokat, amelyek dielektromos tenzorának két sajátértéke megegyezik, egytengelyű (unaxiális) kristályoknak nevezzük. Ilyen kristály például a beta-bárium-borát (BBO) és kálium-dihidrogén-foszfát (KDP). Amennyiben a dielektromos tenzor mindhárom sajátértéke különböző, akkor kéttengelyű (biaxiális) kristályokról beszélünk. Ilyen például a kálium-titanil-arsenát (KTA) illetve a lítium-triborát (LBO). A főtengelekhez tartozó törésmutatók nagyság szerinti elrendezése miatt a biaxiális kristályokban az optikai tengelyek az XZ fősík első és második negyedében helyezkednek el és azonos szöget zárnak be a Z főtengelel. Unaxiális kristályok esetén az optikai tengely iránya egybeesik a Z főtengelel irányával. Unaxiális kristályokban a lassú és gyors hullámok helyett ordinárius és extraordinárius hullámokról beszélünk. Az extraordinárius hullám törésmutatója függ a terjedési iránytól, valamint az energiaterjedés iránya nem egyezik meg a hullámnormális irányával, míg az ordinárius hullám úgy viselkedik, mintha izotróp kristályban terjedne.

### 5.2.3 Nemlineáris folyamatok

**Másodrendű nemlineáris folyamatok** Egy másodrendű nemlineáris kristályban a nemlineáris polarizáció több új frekvenciakomponens forrása lehet. Két bemenő monokromatikus komponens esetén a kimeneten jelentkezhet mindkét hullám

másodharmonikusa, amelyek a bejövő hullámok kétszeres frekvenciáin rezegnek. Ezt nevezik másod-harmonikus keltésnek (SHG). Keletkezhet továbbá a két frekvenciakomponens összege, amit összefrekvencia-keltésnek neveznek (SFG). Amennyiben a két bemenő frekvenciakomponens különbsége jön létre, akkor különbségi frekvenciakeltésről (DFG) beszélünk. Az utóbbi két esetben (SFG és DFG), ha az egyik tér frekvenciája zérus, akkor ezek a Pockles-effektust írják le. Optikai rektifikációról (OR) akkor beszélünk, ha a kimeneten egy állandó elektromos tér (DC tér) jelenik meg.

**Optikai parametrikus erősítés** Az optikai parametrikus erősítés egy olyan másodrendű nemlineáris folyamat, amelyben egy magasabb és egy alacsonyabb frekvenciájú hullám (pumpa és jel) belépnek egy nemlineáris közegbe, ahol első lépésben különbségi frekvenciakeltés jön létre. Ezután az újonnan keltett hullám ("idler") is kölcsönhatásba lép a pumpával, ami viszont egy újabb, a jel frekvenciáján keletkező hullám megjelenéséhez vezet. Ezáltal a jel amplitúdója növekedni fog a terjedés folyamán, azaz erősítés lép fel. Abban a speciális esetben, amikor a jel amplitúdója zérus, akkor optikai parametrikus keltésről (OPG) beszélünk, ami az elektromágneses tér vákuumfluktuációjának erősítése. Ez a folyamat okozza az optikai parametrikus erősítőkben fellépő parametrikus szuperfluoreszcencia jelenségét (PSF). Amennyiben az OPG egy rezonátorban keletkezik, ahol a keletkező fotonok koherens módon összeadódnak, optikai parametrikus oszcillátorról beszélünk (OPO).

**Effektív nemlineáris együttható** A másodrendű nemlineáris folyamatok erősségét a nemlineáris szuszceptibilitás tenzor elemeinek nagysága illetve lineáris kombinációjuk határozza meg. Három impulzus kölcsönhatása során az impulzusok polarizációja meghatározza, hogy a nemlineáris tenzor mely elemei, mekkora hányaddal vesznek részt a kölcsönhatásban. Amennyiben a három hullám polarizációja adott, úgy meg lehet határozni a nemlineáris tenzor effektív értékét.

**Passzív vivő-burkoló fázis stabilizálás** A vivő-burkoló fázis, amelyet a CEP (carrier envelope phase) rövidítés jelöl, az ultrarövid impulzus burkolójának és a gyorsan oszcilláló elektromos térerősség maximumának a fáziskülönbségét jelenti [82]. A CEP felbontható egy statikus fázis eltolódásra és egy impulzusról impulzusra változó fázisfluktuációra. Számos kísérlet szempontjából, mint például a magas-harmonikus-keltés (HHG), elengedhetetlen a CEP állandó értéken tartása, stabilizálása. Létezik aktív és passzív CEP stabilizálás. Az aktív stabilizálást főként magas ismétlési frekvenciájú lézeroszcillátorok esetén alkalmazzák, ahol egy aktív visszacsatoló körrel szabályozzák az oszcillátor frekvenciafésűjének eltolódását az oszcillátor ismétlési frekvenciájának felharmonikusaihoz képest [70]. A passzív CEP stabilizálás során egy másodrendű nemlineáris folyamatot, a különbségi frekvenciakeltést (DFG) használják ki. A különbségi frekvencia fázisa a pompa és a jel bemenő fázisának különbségével áll lineáris kapcsolatban. Amennyiben a jel- és a pumpaimpulzusok CEP fluktuációja lövésről lövésre ugyanannyival változik, akkor a különbségi frekvencia fázisa állandó értéket vesz fel. Ehhez az szükséges, hogy a jel- és pumpaimpulzusok ugyanazon forrásból származzanak. Ezt a gyakorlatban úgy valósítják meg, hogy a jelet a pumpaimpulzusból generálják, fehérfényt keltéssel.

#### 5.2.4 Fázisillesztés

A korábban felsorolt másodrendű nemlineáris folyamatok hatásfokát a fázisillesztési feltételek teljesülése szabja meg. Megmutatható, hogy a normális diszperzió tar-

tományában nem érhető el fázisillesztés. Ebből kifolyólag erre a célra anizotróp, kettősen törő kristályokat alkalmaznak. A kettősen törő kristályokban a bemenő hullámok polarizációjának szabályozásával elérhető, hogy a három hullám mindegyike "lassú" (s) vagy "gyors" (f) hullámként viselkedjen. Belátható, hogy a fázisillesztés biztosítása érdekében a legnagyobb frekvenciával rendelkező hullám csak és kizárólag "gyors" (f) polarizációval rendelkezhet. Így a két alacsonyabb frekvenciájú hullám polarizációjára három lehetőség adódik, amelyek a "lassú-lassú" (ss), "lassú-gyors" (sf), vagy pedig "gyors-lassú" (fs) kombinációk. Amikor a két alacsonyabb frekvenciájú hullám polarizációja megegyezik, akkor azt I. típusú, ellenkező esetben II. típusú fázisillesztésnek nevezzük.

**Szöggel történő hangolás** Három tetszőleges frekvenciakomponens esetén a fázisillesztés teljesülését a kettősen törő kristály orientációjának hangolásával lehet elérni. A nyaláb terjedési irányát a kristályhoz rögzített főtengely rendszerben gömbi koordinátákkal, polár és azimutális szögekkel célszerű megadni. Unaxiális kristályokban az extraordinárius hullám törésmutatója, így fázis sebessége a polárszög változtatásával hangolható. Biaxiális kristályokban egy tetszőleges irányba terjedő hullám esetén mind a "gyors", mind pedig a "lassú" hullám fázis sebessége függ a terjedési iránytól, azaz két extraordinárius hullámról beszélünk. A kristálytani fősíkokban azonban a helyzet hasonló az unaxiális kristályok esetéhez. Ilyenkor egyik hullám ordinárius, még a másik extraordinárius viselkedést mutat. Gyakorlatban a fázisillesztés biaxiális kristályok esetén a kristálytani fősíkokban történik. A szöggel történő hangolás egyik hátránya, hogy az extraordinárius hullám normálisa és energiaterjedési iránya eltérő. Ez azt jelenti, hogy az extraordinárius hullám térben lemászik az ordinárius hullámról. Ezt nevezik walk-off jelenségnek, és másodharmonikus-keltés, vagy parametrikus erősítés folyamán aszimmetrikus nyalábprofil eredményez.

**Hőmérséklettel történő hangolás** A fázisillesztési feltételt a kristály hőmérsékletének hangolásával is el lehet érni. Ilyenkor a hullámok az egyik főtengely mentén terjednek, mivel ebben az esetben a "walk-off" szög zérus. Így elkerülhető az aszimmetrikus nyalábprofil, illetve növelhető a konverzió hatásfoka.

**Kvázi fázisillesztés** Léteznek olyan erősen nemlineáris kristályok, amelyek esetében a kettőtörésen alapuló fázisillesztés nem alkalmazható izotróp mivoltuk miatt. Más esetekben pedig a nemlineáris tenzor legnagyobb értékű eleme nem járul hozzá az effektív nemlineáris együtthatóhoz. Ilyen esetekben alkalmazható a kvázi fázisillesztés módszere, amelynek lényege, hogy a nemlineáris együttható előjelét minden koherenciahossz után változtatják. A koherenciahossz az a távolság, mely esetén egy adott nemlineáris folyamat, fázisillesztés hiányában a maximum értékét éri el. Ezzel a módszerrel fázisillesztés nélkül is magas konverziós hatásfok érhető el. Hátránya, hogy általában kisebb erősítési sáv szélességet biztosít, mint a kettőtörésen alapuló fázisillesztés, illetve a technológia jelenlegi állása szerint csak kisebb méretű (néhány mm átmérőjű) periodikus kristályokat tudnak előállítani, így nem alkalmazhatók nagy energiájú impulzusok erősítésekor.

**Nem kollineáris fázisillesztés** A kettőtörésen alapuló fázisillesztés úgy is megvalósítható, hogy a három hullám terjedési iránya enyhén eltérő. Ezt nevezik nem kollineáris fázisillesztésnek.

**Szélessávú fázisillesztés** Általában, három monokromatikus komponensre biztosítható a fázisillesztés feltétele. Azonban széles spektrumú impulzusok erősítésekor elengedhetetlen, hogy a fázisillesztés a lehető legszélesebb frekvenciatar-

ományon teljesüljön. Ezt nevezik szélessávú fázisillesztésnek. A feltételeit a fázisillesztetlenség Taylor-sorba fejtésével, és a sor együtthatóinak nullával történő ki-egyenlítésével kaphatjuk meg. A sor nulladik tagja a központi frekvenciák fázisillesztési feltétlét szabja meg. A jel és "idler" impulzusok csoportsebességének illesztésével elérhető, hogy a sor első tagja is nullával legyen egyenlő. A csoportsebesség illesztése nem kollineáris geometriában vagy degenerált erősítés esetén teljesül, amikor a jel és "idler" impulzusok központi hullámhossza azonos. Ultra-szélessávú szinkronizációnak nevezzük azt az esetet, amikor a sor második tagjának együtthatója is zérus. Csoportsebesség-illesztés tetszőleges pumpa- és jelimpulzusok estében általában teljesíthető. Az ultra szélessávú szinkronizáció azonban kikötést jelent a pumpa hullámhosszára nézve, ami kísérletileg általában nehezen biztosítható.

### 5.2.5 OPCPA rendszerek modellezése

Egy több erősítőfokozatból álló rendszer modellezése két részre osztható. Az egyik az optikai parametrikus erősítés modellezése nemlineáris kristályokban. A másik feladat pedig az erősítőkristályok közötti lineáris terjedés, nyalábtágító teleszkópok modellezése.

**Parametrikus erősítés modellezése** A fázismodulált optikai parametrikus erősítés (OPCPA) numerikus modellezéséhez egy c++ írt kódot használtam fel, amelyet az Orosz Tudományos Akadémia Alkalmazott Fizika Intézetében fejlesztettek ki. Az OPCPA kód a tetszőleges másodrendű nemlineáris folyamatot leíró csatolt UPPE egyenletrendszerrel oldja meg a másodrendű "split-step" módszer segítségével. A lineáris terjedést Fourier-térben (transzverzális hullámszám-frekvenciatér) kezeli, míg az egyenletek nem lineáris részét a másodrendű Runge-Kutta módszerrel oldja meg. A kód figyelembe veszi a diffrakciót, diszperziót, nem kollineáris terjedést és a fénytörést a kristályok ki- és belépő felületein, a kristály anizotrópiáját (walk-off, aszimmetrikus diffrakció [56]) és a parametrikus szuperfluoreszcencia jelenségét is. A kölcsönhatásban részt vevő impulzusok ("idler", jel és pumpa) komplex elektromos tere három bináris fájlban kerül kimentésre. E fájlok használhatók egy következő erősítőfokozat modellezéséhez. A numerikus kód különlegessége, hogy egy nemrégiben közölt, speciális módszert használ a split-step algoritmus során a gyors Fourier-transzformáció kiszámításához [67]. Ennek következtében az OPCPA modellezéséhez szükséges memóriaigények drasztikusan lecsökkennek. Ez lehetőséget nyújt olyan OPCPA rendszerek modellezéséhez, amelyekben a nyújtott jel- és a pumpaimpulzusok hossza 10 ps felett van, illetve az impulzusok térbeli kiterjedése meghaladja az 1 cm-t.

**Lineáris terjedés modellezése** Az erősítő fokozatok közötti lineáris terjedés modellezéséhez az UPPE egyenletet használtam fel a transzverzális hullámszám-frekvenciatérben. Ezt követően, az erősítő kristályok, illetve a gömbtükrök síkjában Fourier-transzformáció segítségével meghatároztam az impulzus terének téridőbeli alakját. A terjedés számítása közben figyelembe vettem a gömbtükrök térbeli fázistolását is. Mindezt egy saját fejlesztésű Python kód segítségével végeztem el. A terjedés során a transzverzális hullámszám és a valós tér közötti váltást a kétdimenziós Fourier-transzformáció segítségével lehet végrehajtani. Ennek kiszámítása hasonlóan memóriaigényes, mint a nyújtott impulzusok alakjának spektrumból történő számítása. Emiatt a két-dimenziós Fourier-transzformáció során alkalmaztam a nu-

merikus megoldó kódban is használt módszert, amellyel csökkentek a terjedés modellezéséhez szükséges számítási igények.

Az OPCPA kód, illetve az impulzusok erősítő fokozatok közötti terjedésének modellezése lehetővé tette az OPCPA rendszerek valóság-hű szimulációját.

### 5.2.6 Az impulzus alakjának torzulásai

**Pumpakiürülés** Optikai parametrikus erősítés során számos tényező befolyásolhatja az erősített impulzusok téridőbeli alakját. Az egyik ilyen tényező a pumpa impulzus kiürülése, ami után az erősítési folyamat megfordul, a jel és "idler" fotonok rekombinálódnak és egy pumpafoton keletkezik belőlük. Ez a jelimpulzus energiájának csökkenéséhez vezet, illetve a pumpa nyaláb téridőbeli burkolójának változásai miatt az erősített jel impulzus torzulásához vezet.

**Walk-off** Erősítés közben fellép a walk-off effektus, amelynek következtében a nyalábok leválnak egymásról. Ez aszimmetrikus nyaláb profilt eredményezhet.

**Nem kollineáris geometria** Ultrarövid impulzusok nem kollineáris erősítése az impulzusok frontjának dőlését és térbeli diszperzióját eredményezi. E téridőbeli csatolások hosszú pumpaimpulzusok esetén eltűnnek [78, 145, 146]. Dolgozatomban az impulzusok téridőbeli és fázisfront torzulásait a Strehl-szám módosított definíciójával jellemezem [77].

## 5.3 Eredmények

Munkám során egy négydimenziós numerikus kódot használtam különböző paraméterekkel rendelkező OPCPA rendszerek valóság-hű modellezéséhez.

Az OPCPA rendszerek számos előnyös tulajdonsággal bírnak a hagyományos CPA rendszerekkel szemben. Fontos kivétel ez alól a konverziós hatások, amely a hagyományos titán-zafír alapú CPA rendszerekben 50%, viszont OPCPA-ban tipikusan 10-20% körüli érték. Ez a fő oka annak, hogy a ma működő PW csúcsteljesítményű impulzusokat előállító rendszerek jelentős hányada lézerezésen alapuló CPA rendszert alkalmaz. Ezért céлом egy olyan OPA elrendezés numerikus vizsgálata és optimalizálása volt, amelynek segítségével növelhető a jelenlegi energiakonverziós hatások.

**T1** Numerikus módszerekkel megvizsgáltam és optimalizáltam egy úgynevezett "cascaded extraction OPA" (CE-OPA) erősítő elrendezést és kimutattam, hogy a CE-OPA módszer legalább 10%-al növeli meg a pumpából jelimpulzusba történő energiakonverzió hatásfokát [T1].

A több millijoule energiával rendelkező, egy optikai ciklusból álló impulzusok előállítását főként az izolált attoszekundumos impulzusok generálásra motiválja. Az egyciklusú impulzusok előállításának egyik módja az OPCPA erősítő kritikus sáv szélességének növelése lehet. Ezért céлом egy olyan OPCPA elrendezés numerikus vizsgálata volt, amelynek segítségével növelhető az erősített impulzusok sáv szélessége.

**T2** Numerikus módszerekkel megvizsgáltam és optimalizáltam egy dupla BBO kristályból álló erősítő elrendezést, amellyel két optikai ciklusból álló impulzusok előállításához szükséges sáv szélességet lehet erősíteni. Modelleztem, hogy ezt az

elrendezést milyen feltételek esetén lehet alkalmazni és megállapítottam, hogy az alábbi két feltétel teljesülése esetén ez az erősítő konfiguráció az impulzusok tér-időbeli torzulásához vezet [T2]:

1. A pumpaimpulzus erősítés közben fellépő laterális elmozdulása összemérhető a pumpa és jel nyalábok méretével.
2. Az erősítés nagy és így a pumpa módosítja ("vezeti") a jelimpulzus terjedését az erősítő közegben.

Az ELI-ALPS kutató központban található Egyciklusú Lézerrendszer első fejlesztési fázisa, SYLOS 1, volt az első olyan rendszer amely 1 kHz ismétlési frekvencián állított elő TW csúcsteljesítményű, vivő-burkoló fázis stabilizált lézerimpulzusokat [36]. A második fejlesztési szakasz (SYLOS 2) célja az impulzushossz 2 optikai ciklusra történő csökkentése volt a csúcsteljesítmény megtartása mellett. Ezért céлом az ELI-ALPS SYLOS 2 lézerrendszerében lévő szélessávú OPCPA fokozatok numerikus optimalizációja volt.

**T3** Modelleztem és optimalizáltam az ELI-ALPS Egyciklusú Lézerrendszerének (SYLOS) OPCPA rendszerét, ami jelenleg 2,2 optikai ciklusú (6,4 fs) időtartamú TW csúcsteljesítményű impulzusokat állít elő [T2].

A CEP-stabilizált közép-infravörös impulzusokat különbségi frekvenciakeltés segítségével hozzák létre. Azonban ezek energiáját növelni kell, aminek két lehetséges módja van. Az egyik a közép-infravörös impulzusok DFG-t követő optikai parametrikus erősítése (OPA). Dolgozatomban ezt "idler módszernek" neveztem el. A másik módszer ennek fordítottja, azaz a DFG-t megelőzi a jelimpulzus erősítése OPA-ban. Ezt munkám során "jel módszernek" hívtam. A tudományos közlemények alapján a két módszert egyenlő arányban alkalmazzák, azonban nincs indokolva, hogy miért az adott módszerre esett a választás. Ez bizonyos szempontból érthető, hiszen laboratóriumi körülmények között az átállás egyik módszerről a másikra nehezen kivitelezhető, egyes esetekben nem is lehetséges. Így célul tűztem ki a közép-infravörös ultrarövid lézerimpulzusok két féle előállítási módjának numerikus összehasonlító elemzését.

**T4** Modelleztem és optimalizáltam egy közép-infravörös tartományban működő OPCPA rendszert az "idler módszert" és a "jel módszert" alkalmazva és összehasonlítottam az erősített impulzusok paramétereit. Kimutattam, hogy a pumpa energia kinyerésének hatásfoka kicsivel jobb és a közép-infravörös impulzus csúcsteljesítménye magasabb az "idler módszert" alkalmazva, míg a CEP-stabilitás jobb és a kompresszált impulzusok időtartama kicsivel rövidebb a "jel módszer" használatával [T3].

**T5** Kimutattam, legjobb tudomásom szerint először, hogy a pumpaimpulzus kiürülése és a fázismodulált impulzusok időtartamának erősítés közben történő csökkenése spektrális beszűkülést és alacsonyabb csúcsteljesítményt eredményezi az OPCPA rendszer kimenetén [T3].

# References

- [1] T. H. Maiman, “Stimulated Optical Radiation in Ruby,” *Nature*, vol. 187, pp. 493–494, 4736 1960. DOI: [10.1038/187493a0](https://doi.org/10.1038/187493a0).
- [2] P. A. Franken, A. E. Hill, C. W. Peters, and G. Weinreich, “Generation of Optical Harmonics,” *Phys. Rev. Lett.*, vol. 7, pp. 118–119, 4 1961. DOI: [10.1103/PhysRevLett.7.118](https://doi.org/10.1103/PhysRevLett.7.118).
- [3] A. Siegman, *Lasers*. University Science Books, 1986, ISBN: 9780935702118.
- [4] R. Boyd and D. Prato, *Nonlinear Optics*. Elsevier Science, 2008.
- [5] J. A. Armstrong, N. Bloembergen, J. Ducuing, and P. S. Pershan, “Interactions between light waves in a nonlinear dielectric,” *Phys. Rev.*, vol. 127, no. 6, pp. 1918–1939, 1962. DOI: [10.1103/PhysRev.127.1918](https://doi.org/10.1103/PhysRev.127.1918).
- [6] C. C. Wang and G. W. Racette, “Measurement of parametric gain accompanying optical difference frequency generation,” *Applied Physics Letters*, vol. 6, no. 8, pp. 169–171, 1965. DOI: [10.1063/1.1754219](https://doi.org/10.1063/1.1754219).
- [7] F. J. McClung and R. W. Hellwarth, “Giant optical pulsations from ruby,” *Journal of Applied Physics*, vol. 33, no. 3, pp. 828–829, 1962. DOI: [10.1063/1.1777174](https://doi.org/10.1063/1.1777174).
- [8] L. E. Hargrove, R. L. Fork, and M. A. Pollack, “Locking of he–ne laser modes induced by synchronous intracavity modulation,” *Applied Physics Letters*, vol. 5, no. 1, pp. 4–5, 1964. DOI: [10.1063/1.1754025](https://doi.org/10.1063/1.1754025).
- [9] G. Agrawal, *Nonlinear Fiber Optics*, ser. Optics and Photonics. Elsevier Science, 2013, ISBN: 9780123970237.
- [10] D. Strickland and G. Mourou, “Compression of amplified chirped optical pulses,” *Optics Communications*, vol. 56, no. 3, pp. 219–221, 1985. DOI: [https://doi.org/10.1016/0030-4018\(85\)90120-8](https://doi.org/10.1016/0030-4018(85)90120-8).
- [11] G. A. Mourou, T. Tajima, and S. V. Bulanov, “Optics in the relativistic regime,” *Rev. Mod. Phys.*, vol. 78, pp. 309–371, 2 2006. DOI: [10.1103/RevModPhys.78.309](https://doi.org/10.1103/RevModPhys.78.309).
- [12] Z. Gan, L. Yu, S. Li, C. Wang, X. Liang, Y. Liu, W. Li, Z. Guo, Z. Fan, X. Yuan, L. Xu, Z. Liu, Y. Xu, J. Lu, H. Lu, D. Yin, Y. Leng, R. Li, and Z. Xu, “200 J high efficiency Ti:sapphire chirped pulse amplifier pumped by temporal dual-pulse,” *Optics Express*, vol. 25, no. 5, pp. 5169–5178, 2017. DOI: [10.1364/OE.25.005169](https://doi.org/10.1364/OE.25.005169).
- [13] A. D. G. J. A. Piskarskas, “Powerful femtosecond pulse generation by chirped and stretched pulse parametric amplification in BBO crystal,” *Optics Communications*, vol. 88, 4-6 1992. DOI: [10.1016/0030-4018\(92\)90070-8](https://doi.org/10.1016/0030-4018(92)90070-8).

- [14] I. N. Ross, J. L. Collier, P. Matousek, C. N. Danson, D. Neely, R. M. Allott, D. A. Pepler, C. Hernandez-Gomez, and K. Osvay, "Generation of terawatt pulses by use of optical parametric chirped pulse amplification," *Appl. Opt.*, vol. 39, no. 15, pp. 2422–2427, 2000. DOI: [10.1364/AO.39.002422](https://doi.org/10.1364/AO.39.002422).
- [15] X. Zeng, K. Zhou, Y. Zuo, Q. Zhu, J. Su, X. Wang, X. Wang, X. Huang, X. Jiang, D. Jiang, Y. Guo, N. Xie, Z. W. S. Zhou and, J. Mu, H. Peng, and F. Jing, "Multi-petawatt laser facility fully based on optical parametric chirped-pulse amplification," *Optics Letters*, vol. 42, no. 10, pp. 2014–2017, 2017. DOI: [10.1364/OL.42.002014](https://doi.org/10.1364/OL.42.002014).
- [16] K. Yamakawa, M. Aoyama, S. Matsuoka, T. Kase, Y. Akahane, and H. Takuma, "100-TW sub-20-fs Ti:sapphire laser system operating at a 10-Hz repetition rate," *Opt. Lett.*, vol. 23, no. 18, pp. 1468–1470, 1998. DOI: [10.1364/OL.23.001468](https://doi.org/10.1364/OL.23.001468).
- [17] A. A. Eilanlou, Y. Nabekawa, K. L. Ishikawa, H. Takahashi, and K. Midorikawa, "Direct amplification of terawatt sub-10-fs pulses in a CPA system of Ti:sapphire laser," *Opt. Express*, vol. 16, no. 17, pp. 13 431–13 438, 2008. DOI: [10.1364/OE.16.013431](https://doi.org/10.1364/OE.16.013431).
- [18] M. Kalashnikov, H. Cao, K. Osvay, and V. Chvykov, "Polarization-encoded chirped pulse amplification in Ti:sapphire: a way toward few-cycle petawatt lasers," *Opt. Lett.*, vol. 41, no. 1, pp. 25–28, 2016. DOI: [10.1364/OL.41.000025](https://doi.org/10.1364/OL.41.000025).
- [19] T. J. Yu, S. K. Lee, J. H. Sung, J. W. Yoon, T. M. Jeong, and J. Lee, "Generation of high-contrast, 30 fs, 1.5 PW laser pulses from chirped-pulse amplification Ti:sapphire laser," *Optics Express*, vol. 20, no. 10, pp. 10 807–10 815, 2012. DOI: [10.1364/OE.20.010807](https://doi.org/10.1364/OE.20.010807).
- [20] A. M. F. Tavella and F. Krausz, "Investigation of the superfluorescence and signal amplification in an ultrabroadband multiterawatt optical parametric chirped pulse amplifier system," *New Journal of Physics*, vol. 8, no. 10, p. 219, 2006. DOI: [10.1088/1367-2630/8/10/219](https://doi.org/10.1088/1367-2630/8/10/219).
- [21] F. G. Patterson, J. Bonlie, D. Price, and B. White, "Suppression of parasitic lasing in large-aperture Ti:sapphire laser amplifiers," *Optics Letters*, vol. 24, no. 14, pp. 963–965, 1999. DOI: [10.1364/OL.24.000963](https://doi.org/10.1364/OL.24.000963).
- [22] M. P. Kalashnikov, E. Risse, H. Schönengel, and W. Sandner, "Double chirped-pulse-amplification laser: a way to clean pulses temporally," *Optics Letters*, vol. 30, no. 8, pp. 923–925, 2005. DOI: [10.1364/OL.30.000923](https://doi.org/10.1364/OL.30.000923).
- [23] V. Chvykov, P. Rousseau, S. Reed, G. Kalinchenko, and V. Yanovsky, "Generation of  $10^{11}$  contrast 50 TW laser pulses," *Optics Letters*, vol. 30, no. 8, pp. 923–925, 2005. DOI: [10.1364/OL.30.000923](https://doi.org/10.1364/OL.30.000923).
- [24] N. Forget, A. Cotel, E. Brambrink, P. Audebert, C. L. Blanc, A. Jullien, O. Albert, and G. Chériaux, "Pump-noise transfer in optical parametric chirped-pulse amplification," *Optics Letters*, vol. 30, no. 21, pp. 2921–2923, 2005. DOI: [10.1364/OL.30.002921](https://doi.org/10.1364/OL.30.002921).
- [25] V. Pajer and M. Kalashnikov, "Contrast degradation in OPCPA systems induced by a pump with a post-pulse," *Laser Physics Letters*, vol. 15, no. 9, p. 095 402, 2018. DOI: [10.1088/1612-202X/aaccb1](https://doi.org/10.1088/1612-202X/aaccb1).

- [26] J. Adamonis, A. Aleknavičius, K. Michailovas, S. Balickas, V. Petrauskienė, T. Gertus, and A. Michailovas, “Implementation of a SVWP-based laser beam shaping technique for generation of 100-mJ-level picosecond pulses,” *Applied Optics*, vol. 55, no. 28, pp. 8007–8015, 2016. DOI: [10.1364/AO.55.008007](https://doi.org/10.1364/AO.55.008007).
- [27] J. Adamonis, R. Antipenkov, J. Kolenda, A. Michailovas, A. P. Piskarkas, A. Varanavicius, and A. Zaukevicus, “Formation of flat-top picosecond pump pulses for OPCPA systems by cascade second harmonic generation,” *Lithuanian Journal of Physics*, vol. 52, no. 3, pp. 193–202, 2012. DOI: [10.3952/physics.v52i3.2470](https://doi.org/10.3952/physics.v52i3.2470).
- [28] J. Adamonis, R. Antipenkov, J. Kolenda, A. Michailovas, A. P. Piskarkas, and A. Varanavicius, “High-energy Nd:YAG-amplification system for OPCPA pumping,” *Quantum Electronics*, vol. 42, no. 7, pp. 567–574, 2012. DOI: [10.1070/QE2012v042n07ABEH014689](https://doi.org/10.1070/QE2012v042n07ABEH014689).
- [29] L. YU, X. LIANG, L. XU, W. LI, C. PENG, Z. HU, C. WANG, X. LU, Y. CHU, Z. GAN, X. LIU, Y. LIU, X. WANG, H. LU, D. YIN, Y. LENG, R. LI, and Z. XU, “Optimization for high-energy and high-efficiency broadband optical parametric chirped-pulse amplification in LBO near 800 nm,” *Optics Letters*, vol. 40, no. 14, pp. 3412–3415, 2015. DOI: [10.1364/OL.40.003412](https://doi.org/10.1364/OL.40.003412).
- [30] L. Xu, L. Yu, X. Liang, Y. Chu, Z. Hu, L. Ma, Y. Xu, C. Wang, X. Lu, H. Lu, Y. Yue, Y. Zhao, F. Fan, H. Tu, Y. Leng, R. Li, and Z. Xu, “High-energy noncollinear optical parametric–chirped pulse amplification in LBO at 800 nm,” *Optics Letters*, vol. 38, no. 22, pp. 4837–4840, 2013. DOI: [10.1364/OL.38.004837](https://doi.org/10.1364/OL.38.004837).
- [31] V. V. Lozhkarev, G. I. Freidman, V. N. Ginzburg, E. V. Katin, E. A. Khazanov, A. V. Kirsanov, G. A. Luchinin, A. N. Mal’shakov, M. A. Martyanov, O. V. Palashov, A. K. Poteomkin, A. M. Sergeev, A. A. Shaykin, and I. V. Yakovlev, “Compact 0.56 Petawatt laser system based on optical parametric chirped pulse amplification in KD\*P crystals,” *Laser Physics Letters*, vol. 4, no. 6, pp. 421–427, 2007. DOI: [10.1002/lap1.200710008](https://doi.org/10.1002/lap1.200710008).
- [32] W. Li, Z. Gan, L. Yu, C. Wang, Y. Liu, Z. Guo, L. Xu, M. Xu, Y. Hang, Y. Xu, J. Wang, P. Huang, H. Cao, B. Yao, X. Zhang, L. Chen, Y. Tang, S. Li, X. Liu, S. Li, M. He, D. Yin, X. Liang, Y. Leng, R. Li, and Z. Xu, “339 J high-energy Ti:sapphire chirped-pulse amplifier for 10 PW laser facility,” *Optics Letters*, vol. 43, no. 22, pp. 5681–5684, 2018. DOI: [10.1364/OL.43.005681](https://doi.org/10.1364/OL.43.005681).
- [33] Y. Chu, X. Liang, L. Yu, Y. Xu, L. Xu, L. Ma, X. Lu, Y. Liu, Y. Leng, R. Li, and Z. Xu, “High-contrast 2.0 Petawatt Ti:sapphire laser system,” *Optics Express*, vol. 21, no. 24, pp. 29 231–29 239, 2013. DOI: [10.1364/OE.21.029231](https://doi.org/10.1364/OE.21.029231).
- [34] L. E. Zapata, F. Reichert, M. Hemmer, and F. X. Kärtner, “250 W average power, 100 kHz repetition rate cryogenic Yb:YAG amplifier for OPCPA pumping,” *Opt. Lett.*, vol. 41, no. 3, pp. 492–495, 2016. DOI: [10.1364/OL.41.000492](https://doi.org/10.1364/OL.41.000492).

- [35] W. Huang, J. Wang, X. Lu, T. Huang, J. Guo, W. Fan, and X. Li, “LD-pumped gas-cooled multislabs Nd:glass laser amplification to joule level,” *High Power Laser Science and Engineering*, vol. 6, e15, 2018. DOI: [10.1017/hpl.2018.7](https://doi.org/10.1017/hpl.2018.7).
- [36] R. Budriūnas, T. Stanislauskas, J. Adamonis, A. Aleknavičius, G. Veitas, D. Gadonas, S. Balickas, A. Michailovas, and A. Varanavičius, “53 W average power CEP-stabilized OPCPA system delivering 5.5 TW few cycle pulses at 1 kHz repetition rate,” *Optics Express*, vol. 25, no. 5, pp. 5797–5806, 2017. DOI: [10.1364/OE.25.005797](https://doi.org/10.1364/OE.25.005797).
- [37] S. Steinke, A. Henig, M. Schnürer, T. Sokollik, P. Nickles, D. Jung, D. Kiefer, R. Hörlein, J. Schreiber, T. Tajima, and et al., “Efficient ion acceleration by collective laser-driven electron dynamics with ultra-thin foil targets,” *Laser and Particle Beams*, vol. 28, no. 1, pp. 215–221, 2010. DOI: [10.1017/S0263034610000157](https://doi.org/10.1017/S0263034610000157).
- [38] P. Antici, J. Fuchs, E. d’Humières, E. Lefebvre, M. Borghesi, E. Brambrink, C. A. Cecchetti, S. Gaillard, L. Romagnani, Y. Sentoku, T. Toncian, O. Willi, P. Audebert, and H. Pépin, “Energetic protons generated by ultra-high contrast laser pulses interacting with ultrathin targets,” *Physics of Plasmas*, vol. 14, no. 3, p. 030 701, 2007. DOI: [10.1063/1.2480610](https://doi.org/10.1063/1.2480610).
- [39] D. Guénot, D. Gustas, A. Vernier, B. Beaurepaire, F. Böhle, M. Bocoum, M. Lozano, A. Jullien, R. Lopez-Martens, A. Lifschitz, and J. Faure, “Relativistic electron beams driven by kHz single-cycle light pulses,” *Nature Photonics*, vol. 11, pp. 293–296, 5 2017. DOI: [10.1038/nphoton.2017.46](https://doi.org/10.1038/nphoton.2017.46).
- [40] R. J. D. Miller, “Femtosecond Crystallography with Ultrabright Electrons and X-rays: Capturing Chemistry in Action,” *Science*, vol. 343, no. 6175, pp. 1108–1116, 2014. DOI: [10.1126/science.1248488](https://doi.org/10.1126/science.1248488).
- [41] H. Kuramochi, S. Takeuchi, and T. Tahara, “Femtosecond time-resolved impulsive stimulated Raman spectroscopy using sub-7-fs pulses: Apparatus and applications,” *Review of Scientific Instruments*, vol. 87, no. 4, p. 043 107, 2016. DOI: [10.1063/1.4945259](https://doi.org/10.1063/1.4945259).
- [42] M. Liebel, C. Schnedermann, T. Wende, and P. Kukura, “Principles and applications of broadband impulsive vibrational spectroscopy,” *J. Phys. Chem. A*, vol. 119, pp. 9506–9517, 36 2015. DOI: [10.1021/acs.jpca.5b05948](https://doi.org/10.1021/acs.jpca.5b05948).
- [43] G. Sansone, E. Benedetti, F. Calegari, C. Vozzi, L. Avaldi, R. Flammini, L. Poletto, P. Villoresi, C. Altucci, R. Velotta, S. Stagira, S. De Silvestri, and M. Nisoli, “Isolated single-cycle attosecond pulses,” *Science*, vol. 314, no. 5798, pp. 443–446, 2006. DOI: [10.1126/science.1132838](https://doi.org/10.1126/science.1132838).
- [44] S. Gilbertson, Y. Wu, S. D. Khan, M. Chini, K. Zhao, X. Feng, and Z. Chang, “Isolated attosecond pulse generation using multicycle pulses directly from a laser amplifier,” *Phys. Rev. A*, vol. 81, p. 043 810, 4 2010. DOI: [10.1103/PhysRevA.81.043810](https://doi.org/10.1103/PhysRevA.81.043810).
- [45] M. Chini, K. Zhao, and Z. Chang, “The generation, characterization and applications of broadband isolated attosecond pulses,” *Nature Photonics*, vol. 8, pp. 178–186, 3 2014. DOI: [10.1038/nphoton.2013.362](https://doi.org/10.1038/nphoton.2013.362).

- [46] B. Wolter, M. G. Pullen, M. Baudisch, M. Sclafani, M. Hemmer, A. Sentsleben, C. D. Schröter, J. Ullrich, R. Moshhammer, and J. Biegert, “Strong-Field Physics with Mid-IR Fields,” *Phys. Rev. X*, vol. 5, p. 021034, 2015. DOI: [10.1103/PhysRevX.5.021034](https://doi.org/10.1103/PhysRevX.5.021034).
- [47] T. Gaumnitz, A. Jain, Y. Pertot, M. Huppert, I. Jordan, F. Ardana-Lamas, and H. J. Wörner, “Streaking of 43-attosecond soft-X-ray pulses generated by a passively CEP-stable mid-infrared driver,” *Opt. Express*, vol. 25, no. 22, pp. 27506–27518, 2017. DOI: [10.1364/OE.25.027506](https://doi.org/10.1364/OE.25.027506).
- [48] X. Ren, J. Li, Y. Yin, K. Zhao, A. Chew, Y. Wang, S. Hu, Y. Cheng, E. Cunningham, Y. Wu, M. Chini, and Z. Chang, “Attosecond light sources in the water window,” *Journal of Optics*, vol. 20, no. 2, p. 023001, 2018. DOI: [10.1088/2040-8986/aaa394](https://doi.org/10.1088/2040-8986/aaa394).
- [49] T. Popmintchev, M.-C. Chen, D. Popmintchev, P. Arpin, S. Brown, S. Alisauskas, G. Andriukaitis, T. Balciunas, O. D. Mucke, A. Pugzlys, A. Baltuska, B. Shim, S. E. Schrauth, A. Gaeta, C. Hernandez-Garcia, L. Plaja, A. Becker, A. Jaron-Becker, M. M. Murnane, and H. C. Kapteyn, “Bright Coherent Ultrahigh Harmonics in the keV X-ray Regime from Mid-Infrared Femtosecond Lasers,” *Science*, vol. 336, no. 6086, pp. 1287–1291, 2012. DOI: [10.1126/science.1218497](https://doi.org/10.1126/science.1218497).
- [50] A. V. Mitrofanov, D. A. Sidorov-Biryukov, M. V. Rozhko, S. V. Ryabchuk, A. A. Voronin, and A. M. Zheltikov, “High-order harmonic generation from a solid-surface plasma by relativistic-intensity sub-100-fs mid-infrared pulses,” *Opt. Lett.*, vol. 43, no. 22, pp. 5571–5574, 2018. DOI: [10.1364/OL.43.005571](https://doi.org/10.1364/OL.43.005571).
- [51] D. Woodbury, L. Feder, V. Shumakova, C. Gollner, R. Schwartz, B. Miao, F. Salehi, A. Korolov, A. Pugžlys, A. Baltuška, and H. M. Milchberg, “Laser wakefield acceleration with mid-IR laser pulses,” *Opt. Lett.*, vol. 43, no. 5, pp. 1131–1134, 2018. DOI: [10.1364/OL.43.001131](https://doi.org/10.1364/OL.43.001131).
- [52] F. Tittel, D. Richter, and A. Fried, “Mid-infrared laser applications in spectroscopy,” in *Solid-State Mid-Infrared Laser Sources*, I. Sorokina and K. Vodopyanov, Eds., vol. 89, Springer, 2003. DOI: [10.1007/3-540-36491-9\\_11](https://doi.org/10.1007/3-540-36491-9_11).
- [53] W. Petrich, “Mid-infrared and raman spectroscopy for medical diagnostics,” *Applied Spectroscopy Reviews*, vol. 36, no. 2-3, pp. 181–237, 2001. DOI: [10.1081/ASR-100106156](https://doi.org/10.1081/ASR-100106156).
- [54] C. Wang and P. Sahay, “Breath analysis using laser spectroscopic techniques: Breath biomarkers, spectral fingerprints, and detection limits,” *Sensors*, vol. 9, no. 10, pp. 8230–8262, 2009. DOI: [10.3390/s91008230](https://doi.org/10.3390/s91008230).
- [55] M. Pushkarsky, M. Weida, T. Day, D. Arnone, and R. Pritchett, “Compact mid-IR Breath Analysis System,” *2007 IEEE Sensors*, pp. 20–23, 2007.
- [56] G. Arisholm, “General numerical methods for simulating second-order nonlinear interactions in birefringent media,” *J. Opt. Soc. Am. B*, vol. 14, no. 10, pp. 2543–2549, 1997. DOI: [10.1364/JOSAB.14.002543](https://doi.org/10.1364/JOSAB.14.002543).

- [57] A. V. Smith, W. J. Alford, T. D. Raymond, and M. S. Bowers, “Comparison of a numerical model with measured performance of a seeded, nanosecond KTP optical parametric oscillator,” *J. Opt. Soc. Am. B*, vol. 12, no. 11, pp. 2253–2267, 1995. DOI: [10.1364/JOSAB.12.002253](https://doi.org/10.1364/JOSAB.12.002253).
- [58] A. V. Smith and M. S. Bowers, “Phase distortions in sum- and difference-frequency mixing in crystals,” *J. Opt. Soc. Am. B*, vol. 12, no. 1, pp. 49–57, 1995. DOI: [10.1364/JOSAB.12.000049](https://doi.org/10.1364/JOSAB.12.000049).
- [59] S. Witte, R. Zinkstok, W. Hogervorst, and K. Eikema, “Numerical simulations for performance optimization of a few-cycle terawatt NOPCPA system,” *Applied Physics B*, vol. 87, pp. 677–684, 4 2007. DOI: [10.1007/s00340-007-2640-8](https://doi.org/10.1007/s00340-007-2640-8).
- [60] J. Moses, C. Manzoni, S.-W. Huang, G. Cerullo, and F. X. Kärtner, “Temporal optimization of ultrabroadband high-energy OPCPA,” *Opt. Express*, vol. 17, no. 7, pp. 5540–5555, 2009. DOI: [10.1364/OE.17.005540](https://doi.org/10.1364/OE.17.005540).
- [61] J. Hu, X. Wang, Y. Xu, L. Yu, F. Wu, Z. Zhang, X. Yang, P. Ji, P. Bai, X. Liang, Y. Leng, and R. Li, “Numerical analysis of the DKDP-based high-energy optical parametric chirped pulse amplifier for a 100 PW class laser,” *Appl. Opt.*, vol. 60, no. 13, pp. 3842–3848, 2021. DOI: [10.1364/AO.423191](https://doi.org/10.1364/AO.423191).
- [62] H. Fattahi, “Yb:YAG-Pumped, Few-Cycle Optical Parametric Amplifiers,” in *High Energy and Short Pulse Lasers*, R. Viskup, Ed., IntechOpen, 2016, ch. 3. DOI: [10.5772/64438](https://doi.org/10.5772/64438).
- [63] P. S. J. B. C. H. G. A. U. Keller, “Design of a sub-13-fs, multi-gigawatt chirped pulse optical parametric amplification system,” *Applied Physics B: Lasers and Optics*, vol. 79, 3 2004. DOI: [10.1007/s00340-004-1532-4](https://doi.org/10.1007/s00340-004-1532-4).
- [64] A. Thai, C. Skrobol, P. K. Bates, G. Arisholm, Z. Major, F. Krausz, S. Karsch, and J. Biegert, “Simulations of petawatt-class few-cycle optical-parametric chirped-pulse amplification, including nonlinear refractive index effects,” *Opt. Lett.*, vol. 35, no. 20, pp. 3471–3473, 2010. DOI: [10.1364/OL.35.003471](https://doi.org/10.1364/OL.35.003471).
- [65] A. Zaukevicus, *The use of angular dispersion for formation of high peak power and ultrashort pulsed light beams in nonlinear interactions*. Vilnius University, 2012.
- [66] G. Pariente, V. Gallet, A. Borot, O. Gobert, and F. Quéré, “Space-time characterization of ultra-intense femtosecond laser beams,” *Nature Photonics*, vol. 10, pp. 547–553, 8 2016. DOI: [10.1038/nphoton.2016.140](https://doi.org/10.1038/nphoton.2016.140).
- [67] A. Andrianov, A. Szabo, A. Sergeev, A. Kim, V. Chvykov, and M. Kalashnikov, “Computationally efficient method for Fourier transform of highly chirped pulses for laser and parametric amplifier modeling,” *Optics Express*, vol. 24, no. 23, pp. 25 974–25 982, 2016. DOI: [10.1364/OE.24.025974](https://doi.org/10.1364/OE.24.025974).
- [68] J. Diels, W. Rudolph, P. Liao, and P. Kelley, *Ultrashort Laser Pulse Phenomena*, ser. Optics and photonics. Elsevier Science, 2006.
- [69] G. Cerullo, A. Baltuška, O. Mücke, and C. Vozzi, “Few-optical-cycle light pulses with passive carrier-envelope phase stabilization,” *Laser & Photonics Reviews*, vol. 5, no. 3, pp. 323–351, 2011. DOI: <https://doi.org/10.1002/lpor.201000013>.

- [70] D. J. Jones, S. T. Cundiff, T. M. Fortier, J. L. Hall, and J. Ye, “Carrier-envelope phase stabilization of single and multiple femtosecond lasers,” in *Few-Cycle Laser Pulse Generation and Its Applications*, F. X. Kärtner, Ed. Berlin, Heidelberg: Springer Berlin Heidelberg, 2004, pp. 317–343, ISBN: 978-3-540-39849-3. DOI: [10.1007/978-3-540-39849-3\\_8](https://doi.org/10.1007/978-3-540-39849-3_8).
- [71] F. X. Kärtner, “Few-cycle laser pulse generation and its applications,” in 2004, vol. 10.1007/b88427. DOI: [10.1007/978-3-540-39849-3\\_1](https://doi.org/10.1007/978-3-540-39849-3_1).
- [72] J. Goodman, *Introduction to Fourier Optics*, ser. McGraw-Hill physical and quantum electronics series. W. H. Freeman, 2005, ISBN: 9780974707723.
- [73] S. Akturk, X. Gu, P. Bowlan, and R. Trebino, “Spatio-temporal couplings in ultrashort laser pulses,” *Journal of Optics*, vol. 12, no. 9, p. 093001, 2010. DOI: [10.1088/2040-8978/12/9/093001](https://doi.org/10.1088/2040-8978/12/9/093001).
- [74] V. N. Mahajan, “Strehl ratio for primary aberrations: Some analytical results for circular and annular pupils,” *J. Opt. Soc. Am.*, vol. 72, no. 9, pp. 1258–1266, 1982. DOI: [10.1364/JOSA.72.001258](https://doi.org/10.1364/JOSA.72.001258).
- [75] B. C. Platt and R. Shack, “History and Principles of Shack-Hartmann Wavefront Sensing,” *Journal of Refractive Surgery*, vol. 17, no. 5, S573–S577, 2001. DOI: [10.3928/1081-597X-20010901-13](https://doi.org/10.3928/1081-597X-20010901-13).
- [76] N. Varkentina, G. Dovillaire, J. Legrand, G. Beaugrand, I. Stefanon, P. Treimany, and X. Levecq, “New adaptive optics control strategy for petawatt-class laser chains,” *Quantum Electronics*, vol. 47, no. 8, pp. 711–717, 2017. DOI: [10.1070/qe116429](https://doi.org/10.1070/qe116429).
- [77] A. Giree, M. Mero, G. Arisholm, M. J. J. Vrakking, and F. J. Furch, “Numerical study of spatiotemporal distortions in noncollinear optical parametric chirped-pulse amplifiers,” *Opt. Express*, vol. 25, no. 4, pp. 3104–3121, 2017. DOI: [10.1364/OE.25.003104](https://doi.org/10.1364/OE.25.003104).
- [78] J. Bromage, C. Dorrer, and J. D. Zuegel, “Angular-dispersion-induced spatiotemporal aberrations in noncollinear optical parametric amplifiers,” *Opt. Lett.*, vol. 35, no. 13, pp. 2251–2253, 2010. DOI: [10.1364/OL.35.002251](https://doi.org/10.1364/OL.35.002251).
- [79] A. Yariv and P. Yeh, in *Optical Waves in Crystals: Propagation and Control of Laser Radiation*, John Wiley & Sons, 2002, ISBN: 978-0-471-43081-0.
- [80] A. Couairon, E. Brambilla, T. Corti, D. Majus, O. Ramirez-Gongora, and M. Kolesik, “Practitioner’s guide to laser pulse propagation models and simulation,” *The European Physical Journal Special Topics*, vol. 199, Nov. 2011. DOI: [10.1140/epjst/e2011-01503-3](https://doi.org/10.1140/epjst/e2011-01503-3).
- [81] S. Guha, *Laser Beam Propagation in Nonlinear Optical Media*. CRC Press, 2017, ISBN: 9781439866399.
- [82] A. Borzsonyi, A. Kovács, and K. Osvay, “What we can learn about ultrashort pulses by linear optical methods,” *Applied Sciences*, vol. 3, pp. 515–544, 2013. DOI: [10.3390/app3020515](https://doi.org/10.3390/app3020515).
- [83] I. N. Ross, P. Matousek, G. H. C. New, and K. Osvay, “Analysis and optimization of optical parametric chirped pulse amplification,” *Journal of the Optical Society of America B*, vol. 19, no. 12, pp. 2945–2956, 2002. DOI: [10.1364/JOSAB.19.002945](https://doi.org/10.1364/JOSAB.19.002945).

- [84] R. Sutherland, *Handbook of Nonlinear Optics*. Taylor & Francis, 2003, ISBN: 9780824742430.
- [85] I. Ross, P. Matousek, M. Towrie, A. Langley, and J. Collier, “The prospects for ultrashort pulse duration and ultrahigh intensity using optical parametric chirped pulse amplifiers,” *Optics Communications*, vol. 144, pp. 125–133, 1997.
- [86] A. Baltuška, T. Fuji, and T. Kobayashi, “Controlling the Carrier-Envelope Phase of Ultrashort Light Pulses with Optical Parametric Amplifiers,” *Phys. Rev. Lett.*, vol. 88, p. 133 901, 13 2002. DOI: [10.1103/PhysRevLett.88.133901](https://doi.org/10.1103/PhysRevLett.88.133901).
- [87] S. T. Cundiff, “Phase stabilization of ultrashort optical pulses,” *Journal of Physics D: Applied Physics*, vol. 35, no. 8, R43–R59, 2002. DOI: [10.1088/0022-3727/35/8/201](https://doi.org/10.1088/0022-3727/35/8/201).
- [88] N. Thiré, R. Maksimenka, B. Kiss, C. Ferchaud, G. Gitzinger, T. Pinoteau, H. Jousset, S. Jarosch, P. Bizouard, V. D. Pietro, E. Cormier, K. Osvay, and N. Forget, “Highly stable, 15 W, few-cycle, 65 mrad CEP-noise mid-IR OPCPA for statistical physics,” *Optics Express*, vol. 26, no. 21, p. 26 907, 2018. DOI: [10.1364/OE.26.026907](https://doi.org/10.1364/OE.26.026907).
- [89] U. Elu, M. Baudisch, H. Pires, F. Tani, M. H. Frosz, F. Köttig, A. Ermolov, P. S. Russell, and J. Biegert, “High average power and single-cycle pulses from a mid-IR optical parametric chirped pulse amplifier,” *Optica*, vol. 4, no. 9, pp. 1024–1029, 2017. DOI: [10.1364/OPTICA.4.001024](https://doi.org/10.1364/OPTICA.4.001024).
- [90] T. Skauli, K. L. Vodopyanov, T. J. Pinguet, A. Schober, O. Levi, L. A. Eyres, M. M. Fejer, J. S. Harris, B. Gerard, L. Becouarn, E. Lallier, and G. Arisholm, “Measurement of the nonlinear coefficient of orientation-patterned GaAs and demonstration of highly efficient second-harmonic generation,” *Opt. Lett.*, vol. 27, no. 8, pp. 628–630, 2002. DOI: [10.1364/OL.27.000628](https://doi.org/10.1364/OL.27.000628).
- [91] I. Shoji, T. Kondo, A. Kitamoto, M. Shirane, and R. Ito, “Absolute scale of second-order nonlinear-optical coefficients,” *J. Opt. Soc. Am. B*, vol. 14, no. 9, pp. 2268–2294, 1997. DOI: [10.1364/JOSAB.14.002268](https://doi.org/10.1364/JOSAB.14.002268).
- [92] D. S. Hum and M. M. Fejer, “Quasi-phasematching,” *Comptes Rendus Physique*, vol. 8, no. 2, pp. 180–198, 2007. DOI: <https://doi.org/10.1016/j.crhy.2006.10.022>.
- [93] N. Boeuf, D. A. Branning, I. Chaperot, E. Dauler, S. Guerin, G. S. Jaeger, A. Muller, and A. L. Migdall, “Calculating characteristics of noncollinear phase matching in uniaxial and biaxial crystals,” *Optical Engineering*, vol. 39, no. 4, pp. 1016–1024, 2000. DOI: [10.1117/1.602464](https://doi.org/10.1117/1.602464).
- [94] C. Skrobol, *High-intensity, picosecond-pumped, few-cycle OPCPA*. Fakultät für Physik der Ludwig-Maximilians-Universität, 2014.
- [95] R. Dabu, “Very broad gain bandwidth parametric amplification in nonlinear crystals at critical wavelength degeneracy,” *Opt. Express*, vol. 18, no. 11, pp. 11 689–11 699, 2010. DOI: [10.1364/OE.18.011689](https://doi.org/10.1364/OE.18.011689).

- [96] D. Tang, J. Ma, J. Wang, B. Zhou, G. Xie, P. Yuan, H. Zhu, and L. Qian, “Temperature- and wavelength-insensitive parametric amplification enabled by noncollinear achromatic phase-matching,” *Scientific Reports*, vol. 6, no. 1, p. 36 059, 2016. DOI: [10.1038/srep36059](https://doi.org/10.1038/srep36059).
- [97] J. Limpert, C. Aguergaray, S. Montant, I. Manek-Hönniger, S. Petit, D. Descamps, E. Cormier, and F. Salin, “Ultra-broad bandwidth parametric amplification at degeneracy,” *Opt. Express*, vol. 13, no. 19, pp. 7386–7392, 2005. DOI: [10.1364/OPEX.13.007386](https://doi.org/10.1364/OPEX.13.007386).
- [98] A. Kessel, V. E. Leshchenko, O. Jahn, M. Krüger, A. Münzer, A. Schwarz, V. Pervak, M. Trubetskov, S. A. Trushin, F. Krausz, Z. Major, and S. Karsch, “Relativistic few-cycle pulses with high contrast from picosecond-pumped OPCPA,” *Optica*, vol. 5, no. 4, pp. 434–442, 2018. DOI: [10.1364/OPTICA.5.000434](https://doi.org/10.1364/OPTICA.5.000434).
- [99] S. Prinz, M. Schnitzenbaumer, D. Potamianos, M. Schultze, S. Stark, M. Häfner, C. Y. Teisset, C. Wandt, K. Michel, R. Kienberger, B. Bernhardt, and T. Metzger, “Thin-disk pumped optical parametric chirped pulse amplifier delivering CEP-stable multi-mJ few-cycle pulses at 6 kHz,” *Opt. Express*, vol. 26, no. 2, pp. 1108–1124, 2018. DOI: [10.1364/OE.26.001108](https://doi.org/10.1364/OE.26.001108).
- [100] S. Witte and K. S. E. Eikema, “Ultrafast Optical Parametric Chirped-Pulse Amplification,” *IEEE Journal of Selected Topics in Quantum Electronics*, vol. 18, no. 1, pp. 296–307, 2012. DOI: [10.1109/JSTQE.2011.2118370](https://doi.org/10.1109/JSTQE.2011.2118370).
- [101] V. Bagnoud, I. A. Begishev, M. J. Guardalben, J. Puth, and J. D. Zuegel, “5 Hz , >250 mJ optical parametric chirped-pulse amplifier at 1053 nm,” *Optics Letters*, vol. 30, no. 14, pp. 1843–1845, 2005. DOI: [10.1364/OL.30.001843](https://doi.org/10.1364/OL.30.001843).
- [102] L. J. Waxer, V. Bagnoud, I. A. Begishev, M. J. Guardalben, J. Puth, and J. D. Zuegel, “High-conversion-efficiency optical parametric chirped-pulse amplification system using spatiotemporally shaped pump pulses,” *Optics Letters*, vol. 28, no. 14, pp. 1245–1247, 2003. DOI: [10.1364/OL.28.001245](https://doi.org/10.1364/OL.28.001245).
- [103] J. A. Fülöp, Z. Major, B. Horváth, F. Tavella, A. Baltuska, and F. Krausz, “Shaping of picosecond pulses for pumping optical parametric amplification,” *Applied Physics B*, vol. 87, no. 1, pp. 79–84, 2007. DOI: [10.1007/s00340-006-2488-3](https://doi.org/10.1007/s00340-006-2488-3).
- [104] M. D. Skeldon, “A high-bandwidth electrical waveform generator based on an aperture-coupled stripline,” *Review of Scientific Instruments*, vol. 71, no. 9, pp. 3559–3566, 2000. DOI: [10.1063/1.1288254](https://doi.org/10.1063/1.1288254).
- [105] L. J. Waxer, J. H. Kelly, J. Rothenberg, A. Babushkin, C. Bibeau, A. Bayramian, and S. Payne, “Precision spectral sculpting for narrow-band amplification of broadband frequency-modulated pulses,” *Optics Letters*, vol. 27, no. 16, pp. 1427–1429, 2002. DOI: [10.1364/OL.27.001427](https://doi.org/10.1364/OL.27.001427).
- [106] M. J. Guardalben, J. Keegan, L. J. Waxer, V. Bagnoud, I. A. Begishev, J. Puth, and J. D. Zuegel, “Design of a highly stable, high-conversion-efficiency, optical parametric chirped-pulse amplification system with good beam quality,” *Optics Express*, vol. 11, no. 20, pp. 2511–2524, 2003. DOI: [10.1364/OE.11.002511](https://doi.org/10.1364/OE.11.002511).

- [107] I. A. Begishev, A. A. Gulamov, E. A. Erofeev, E. A. Ibragimov, S. R. Kamalov, T. usmanov, and A. D. Khadzhaev, “Highly efficient parametric amplification of optical beams. I. optimization of the profiles of interacting waves in parametric amplification,” *Sov. J. Quantum Electron.*, vol. 20, no. 9, pp. 1100–1103, 1990. DOI: [10.1070/QE1990v020n09ABEH007413](https://doi.org/10.1070/QE1990v020n09ABEH007413).
- [108] I. A. Begishev, A. A. Gulamov, E. A. Erofeev, E. A. Ibragimov, and S. R. Kamalov, “Highly efficient parametric amplification of optical beams. II. Parametric interaction of waves with conformal profiles,” *Soviet Journal of Quantum Electronics*, vol. 20, no. 9, pp. 1104–1106, 1990. DOI: [10.1070/QE1990v020n09ABEH007414](https://doi.org/10.1070/QE1990v020n09ABEH007414).
- [109] P. Matousek, B. Rus, and I. N. Ross, “Design of a multi-petawatt optical parametric chirped pulse amplifier for the iodine laser ASTERIX IV,” *IEEE Journal of Quantum Electronics*, vol. 36, no. 2, pp. 158–163, 2000. DOI: [10.1109/3.823461](https://doi.org/10.1109/3.823461).
- [110] J. Ma, J. Wang, P. Yuan, G. Xie, K. Xiong, Y. Tu, X. Tu, E. Shi, Y. Zheng, and L. Qian, “Quasi-parametric amplification of chirped pulses based on a Sm<sup>3+</sup>-doped yttrium calcium oxyborate crystal,” *Optica*, vol. 2, no. 11, pp. 1006–1009, 2015. DOI: [10.1364/OPTICA.2.001006](https://doi.org/10.1364/OPTICA.2.001006).
- [111] Y. Li, H. Zhong, J. Yang, S. Wang, and D. Fan, “Versatile backconversion-inhibited broadband optical parametric amplification based on an idler-separated QPM configuration,” *Optics Letters*, vol. 42, no. 14, pp. 2806–2809, 2017. DOI: [10.1364/OL.42.002806](https://doi.org/10.1364/OL.42.002806).
- [112] Y. Deng and F. Krausz, *Method and device for optical parametric chirped pulse amplification*, 2013.
- [113] M. Schultze, T. Binhammer, G. Palmer, M. Emons, T. Lang, and U. Morgner, “Multi- $\mu$ J, CEP-stabilized, two-cycle pulses from an OPCPA system with up to 500 kHz repetition rate,” *Optics Express*, vol. 18, no. 26, pp. 27 291–27 297, 2010. DOI: [10.1364/OE.18.027291](https://doi.org/10.1364/OE.18.027291).
- [114] P. Wnuk, Y. Stepanenko, and C. Radzewicz, “Multi-terawatt chirped pulse optical parametric amplifier with a time-shear power amplification stage,” *Optics Express*, vol. 17, no. 17, pp. 15 264–15 273, 2009. DOI: [10.1364/OE.17.015264](https://doi.org/10.1364/OE.17.015264).
- [115] H. Fattahi, C. Skrobol, M. Ueffing, Y. Deng, A. Schwarz, Y. Kida, V. Pervak, T. Metzger, Z. Major, and F. Krausz, “High efficiency, multi-mJ, sub 10 fs, optical parametric amplifier at 3 kHz,” in *Conference on Lasers and Electro-Optics 2012*, Optical Society of America, 2012, CTh1N.6. DOI: [10.1364/CLEO\\_SI.2012.CTh1N.6](https://doi.org/10.1364/CLEO_SI.2012.CTh1N.6).
- [116] J. Ma, J. Wang, B. Zhou, P. Yuan, G. Xie, K. Xiong, Y. Zheng, H. Zhu, and L. Qian, “Broadband, efficient, and robust quasi-parametric chirped-pulse amplification,” *Optics Express*, no. 21, pp. 25 149–25 164, 2017. DOI: [10.1364/OE.25.025149](https://doi.org/10.1364/OE.25.025149).
- [117] C. Aguergaray, O. Schmidt, J. Rothhardt, D. Schimpf, D. Descamps, S. Petit, J. Limpert, and E. Cormier, “Ultra-wide parametric amplification at 800 nm toward octave spanning,” *Opt. Express*, vol. 17, no. 7, pp. 5153–5162, 2009. DOI: [10.1364/OE.17.005153](https://doi.org/10.1364/OE.17.005153).

- [118] S. Adachi, N. Ishii, T. Kanai, A. Kosuge, J. Itatani, Y. Kobayashi, D. Yoshitomi, K. Torizuka, and S. Watanabe, “5-fs, multi-mJ, CEP-locked parametric chirped-pulse amplifier pumped by a 450-nm source at 1 kHz,” *Opt. Express*, vol. 16, no. 19, pp. 14 341–14 352, 2008. DOI: [10.1364/OE.16.014341](https://doi.org/10.1364/OE.16.014341).
- [119] H. Fattahi, H. G. Barros, M. Gorjan, T. Nubbemeyer, B. Alsaif, C. Y. Teisset, M. Schultze, S. Prinz, M. Haefner, M. Ueffing, A. Alismail, L. Vámos, A. Schwarz, O. Pronin, J. Brons, X. T. Geng, G. Arisholm, M. Ciappina, V. S. Yakovlev, D.-E. Kim, A. M. Azzeer, N. Karpowicz, D. Sutter, Z. Major, T. Metzger, and F. Krausz, “Third-generation femtosecond technology,” *Optica*, vol. 1, no. 1, pp. 45–63, 2014. DOI: [10.1364/OPTICA.1.000045](https://doi.org/10.1364/OPTICA.1.000045).
- [120] D. E. Rivas, A. Borot, D. E. Cardenas, G. Marcus, X. Gu, D. Herrmann, J. Xu, J. Tan, D. Kormin, G. Ma, W. Dallari, G. D. Tsakiris, I. B. Földes, S.-w. Chou, M. Weidman, B. Bergues, T. Wittmann, H. Schröder, P. Tzallas, D. Charalambidis, O. Razskazovskaya, V. Pervak, F. Krausz, and L. Veisz, “Next generation driver for attosecond and laser-plasma physics,” *Scientific Reports*, vol. 7, p. 5224, 1 2017. DOI: [10.1038/s41598-017-05082-w](https://doi.org/10.1038/s41598-017-05082-w).
- [121] K. Yamane, T. Tanigawa, T. Sekikawa, and M. Yamashita, “Angularly-dispersed optical parametric amplification of optical pulses with one-octave bandwidth toward monocycle regime,” *Optics Express*, vol. 16, no. 22, pp. 18 345–18 353, 2008. DOI: [10.1364/OE.16.018345](https://doi.org/10.1364/OE.16.018345).
- [122] G. Arisholm, J. Biegert, P. Schlup, C. P. Hauri, and U. Keller, “Ultra-broadband chirped-pulse optical parametric amplifier with angularly dispersed beams,” *Opt. Express*, vol. 12, no. 3, pp. 518–530, 2004. DOI: [10.1364/OPEX.12.000518](https://doi.org/10.1364/OPEX.12.000518).
- [123] G. Tóth, L. Pálfalvi, L. Tokodi, J. Hebling, and J. A. Fülöp, “Scalable broadband OPCPA in Lithium Niobate with signal angular dispersion,” *Optics Communications*, vol. 370, pp. 250–255, 2016, ISSN: 0030-4018. DOI: <https://doi.org/10.1016/j.optcom.2016.03.025>.
- [124] X. Zou, H. Liang, S. Qu, K. Liu, C. Liu, Q. J. Wang, and Y. Zhang, “High-energy single-cycle pulse generation in a parametric amplifier with the optimized angular dispersion,” *Applied Physics B*, vol. 125, no. 3, p. 36, 2019. DOI: [10.1007/s00340-019-7152-9](https://doi.org/10.1007/s00340-019-7152-9).
- [125] D. Herrmann, L. Veisz, R. Tautz, F. Tavella, K. Schmid, V. Pervak, and F. Krausz, “Generation of sub-three-cycle, 16 TW light pulses by using noncollinear optical parametric chirped-pulse amplification,” *Opt. Lett.*, vol. 34, no. 16, pp. 2459–2461, 2009. DOI: [10.1364/OL.34.002459](https://doi.org/10.1364/OL.34.002459).
- [126] S. Witte, R. T. Zinkstok, A. L. Wolf, W. Hogervorst, W. Ubachs, and K. S. E. Eikema, “A source of 2 terawatt, 2.7 cycle laser pulses based on noncollinear optical parametric chirped pulse amplification,” *Opt. Express*, vol. 14, no. 18, pp. 8168–8177, 2006. DOI: [10.1364/OE.14.008168](https://doi.org/10.1364/OE.14.008168).

- [127] G. Tamošauskas, A. Dubietis, G. Valiulis, and A. Piskarskas, “Optical parametric amplifier pumped by two mutually incoherent laser beams,” *Applied Physics B*, vol. 90, no. 2, pp. 305–307, 2008. DOI: [10.1007/s00340-008-2984-8](https://doi.org/10.1007/s00340-008-2984-8).
- [128] S. Ališauskas, R. Butkus, V. Pyragaitė, V. Smilgevičius, A. Stabinis, and A. Piskarskas, “Prospects for increasing average power of optical parametric chirped pulse amplifiers via multi-beam pumping,” *Optics Communications*, vol. 283, no. 3, pp. 469–473, 2010. DOI: <https://doi.org/10.1016/j.optcom.2009.10.029>.
- [129] A. Dubietis, R. Danielius, G. Tamošauskas, and A. Piskarskas, “Combining effect in a multiple-beam-pumped optical parametric amplifier,” *J. Opt. Soc. Am. B*, vol. 15, no. 3, pp. 1135–1139, 1998. DOI: [10.1364/JOSAB.15.001135](https://doi.org/10.1364/JOSAB.15.001135).
- [130] G. Mennerat, B. Tropheme, and B. Boulanger, “Experimental demonstration of five-beam-pumped optical parametric amplification,” *Opt. Lett.*, vol. 38, no. 17, pp. 3319–3321, 2013. DOI: [10.1364/OL.38.003319](https://doi.org/10.1364/OL.38.003319).
- [131] D. Herrmann, R. Tautz, F. Tavella, F. Krausz, and L. Veisz, “Investigation of two-beam-pumped noncollinear optical parametric chirped-pulse amplification for the generation of few-cycle light pulses,” *Opt. Express*, vol. 18, no. 5, pp. 4170–4183, 2010. DOI: [10.1364/OE.18.004170](https://doi.org/10.1364/OE.18.004170).
- [132] K. Ogawa, M. Aoyama, Y. Akahane, K. Tsuji, J. Kawanaka, T. Hari moto, H. Nishioka, M. Fujita, and K. Yamakawa, “Bandwidth enhancement of optical parametric chirped pulse amplification by temporally delayed two pump beams,” *Japanese Journal of Applied Physics*, vol. 47, no. 6, pp. 4592–4594, 2008. DOI: [10.1143/jjap.47.4592](https://doi.org/10.1143/jjap.47.4592).
- [133] C. Wang, Y. Leng, B. Zhao, Z. Zhang, and Z. Xu, “Extremely broad gain spectra of two-beam-pumped optical parametric chirped-pulse amplifier,” *Optics Communications*, vol. 237, no. 1, pp. 169–177, 2004. DOI: <https://doi.org/10.1016/j.optcom.2004.03.074>.
- [134] E. Žeromskis, A. Dubietis, G. Tamošauskas, and A. Piskarskas, “Gain bandwidth broadening of the continuum-seeded optical parametric amplifier by use of two pump beams,” *Optics Communications*, vol. 203, no. 3, pp. 435–440, 2002. DOI: [https://doi.org/10.1016/S0030-4018\(02\)01182-3](https://doi.org/10.1016/S0030-4018(02)01182-3).
- [135] D. Herrmann, C. Homann, R. Tautz, M. Scharrer, P. S. Russell, F. Krausz, L. Veisz, and E. Riedle, “Approaching the full octave: Noncollinear optical parametric chirped pulse amplification with two-color pumping,” *Opt. Express*, vol. 18, no. 18, pp. 18 752–18 762, 2010. DOI: [10.1364/OE.18.018752](https://doi.org/10.1364/OE.18.018752).
- [136] A. P. Piskarskas, A. P. Stabinis, and V. Pyragaitė, “Ultrabroad bandwidth of optical parametric amplifiers,” *IEEE Journal of Quantum Electronics*, vol. 46, no. 7, pp. 1031–1038, 2010.
- [137] V. Pyragaitė, R. Butkus, G. Archipovaitė, D. Kezys, A. Stabinis, A. Piskarskas, and V. Smilgevičius, “Minimization of parametric diffraction effect in two-beam pumped optical parametric amplification,” *Optics Communications*, vol. 309, pp. 344–348, 2013. DOI: <https://doi.org/10.1016/j.optcom.2013.08.008>.

- [138] R. Danielius, P. D. Trapani, A. Dubietis, A. Piskarskas, D. Podenas, and G. P. Banfi, “Self-diffraction through cascaded second-order frequency-mixing effects in beta-barium borate,” *Opt. Lett.*, vol. 18, no. 8, pp. 574–576, 1993. DOI: [10.1364/OL.18.000574](https://doi.org/10.1364/OL.18.000574).
- [139] B. E. Schmidt, N. Thiré, M. Boivin, A. Laramée, F. Poitras, G. Lebrun, T. Ozaki, H. Ibrahim, and F. Légaré, “Frequency domain optical parametric amplification,” *Nature Communications*, vol. 5, p. 3643, 1 2014. DOI: [10.1038/ncomms4643](https://doi.org/10.1038/ncomms4643).
- [140] A. Wirth, M. T. Hassan, I. Grguraš, J. Gagnon, A. Moulet, T. T. Luu, S. Pabst, R. Santra, Z. A. Alahmed, A. M. Azzeer, V. S. Yakovlev, V. Pervak, F. Krausz, and E. Goulielmakis, “Synthesized light transients,” *Science*, vol. 334, no. 6053, pp. 195–200, 2011. DOI: [10.1126/science.1210268](https://doi.org/10.1126/science.1210268).
- [141] G. M. Rossi, R. E. Mainz, Y. Yang, F. Scheiba, M. A. Silva-Toledo, S.-H. Chia, P. D. Keathley, S. Fang, O. D. Mücke, C. Manzoni, G. Cerullo, G. Cirmi, and F. X. Kärtner, “Sub-cycle millijoule-level parametric waveform synthesizer for attosecond science,” *Nature Photonics*, vol. 14, no. 10, pp. 629–635, 2020. DOI: [10.1038/s41566-020-0659-0](https://doi.org/10.1038/s41566-020-0659-0).
- [142] G. Arisholm, R. Paschotta, and T. Südmeyer, “Limits to the power scalability of high-gain optical parametric amplifiers,” *J. Opt. Soc. Am. B*, vol. 21, no. 3, pp. 578–590, 2004. DOI: [10.1364/JOSAB.21.000578](https://doi.org/10.1364/JOSAB.21.000578).
- [143] S. Akturk, X. Gu, P. Gabolde, and R. Trebino, “The general theory of first-order spatio-temporal distortions of Gaussian pulses and beams,” *Opt. Express*, vol. 13, no. 21, pp. 8642–8661, 2005. DOI: [10.1364/OPEX.13.008642](https://doi.org/10.1364/OPEX.13.008642).
- [144] S. Akturk, X. Gu, E. Zeek, and R. Trebino, “Pulse-front tilt caused by spatial and temporal chirp,” *Opt. Express*, vol. 12, no. 19, pp. 4399–4410, 2004. DOI: [10.1364/OPEX.12.004399](https://doi.org/10.1364/OPEX.12.004399).
- [145] O. Isaienko and E. Borguet, “Pulse-front matching of ultrabroadband near-infrared noncollinear optical parametric amplified pulses,” *J. Opt. Soc. Am. B*, vol. 26, no. 5, pp. 965–972, 2009. DOI: [10.1364/JOSAB.26.000965](https://doi.org/10.1364/JOSAB.26.000965).
- [146] A. Zaukevičius, V. Jukna, R. Antipenkov, V. Martinėnaitė, A. Varanavičius, A. P. Piskarskas, and G. Valiulis, “Manifestation of spatial chirp in femtosecond noncollinear optical parametric chirped-pulse amplifier,” *J. Opt. Soc. Am. B*, vol. 28, no. 12, pp. 2902–2908, 2011. DOI: [10.1364/JOSAB.28.002902](https://doi.org/10.1364/JOSAB.28.002902).
- [147] A. Shirakawa, I. Sakane, M. Takasaka, and T. Kobayashi, “Sub-5-fs visible pulse generation by pulse-front-matched noncollinear optical parametric amplification,” *Applied Physics Letters*, vol. 74, no. 16, pp. 2268–2270, 1999. DOI: [10.1063/1.123820](https://doi.org/10.1063/1.123820).
- [148] T. H. Dou, R. Tautz, X. Gu, G. Marcus, T. Feurer, F. Krausz, and L. Veisz, “Dispersion control with reflection gratings of an ultra-broadband spectrum approaching a full octave,” *Opt. Express*, vol. 18, no. 26, pp. 27 900–27 909, 2010. DOI: [10.1364/OE.18.027900](https://doi.org/10.1364/OE.18.027900).

- [149] I. V. Yakovlev, “Stretchers and compressors for ultra-high power laser systems,” *Quantum Electronics*, vol. 44, no. 5, pp. 393–414, 2014. DOI: [10.1070/qe2014v044n05abeh015429](https://doi.org/10.1070/qe2014v044n05abeh015429).
- [150] S. N. Bagayev, V. I. Trunov, E. V. Pestryakov, V. E. Leshchenko, S. A. Frolov, and V. A. Vasiliev, “Optimisation of wide-band parametric amplification stages of a femtosecond laser system with coherent combining of fields,” *Quantum Electronics*, vol. 44, no. 5, pp. 415–425, 2014. DOI: [10.1070/qe2014v044n05abeh015437](https://doi.org/10.1070/qe2014v044n05abeh015437).
- [151] W. Press, W. H. S. Teukolsky, W. Vetterling, S. A. and B. Flannery, *Numerical Recipes 3rd Edition: The Art of Scientific Computing*. Cambridge University Press, 2007, ISBN: 9780521880688.
- [152] E. Treacy, “Optical pulse compression with diffraction gratings,” *IEEE Journal of Quantum Electronics*, vol. 5, no. 9, pp. 454–458, 1969. DOI: [10.1109/JQE.1969.1076303](https://doi.org/10.1109/JQE.1969.1076303).
- [153] G. Cheriaux, P. Rousseau, F. Salin, J. P. Chambaret, B. Walker, and L. F. Dimauro, “Aberration-free stretcher design for ultrashort-pulse amplification,” *Opt. Lett.*, vol. 21, no. 6, pp. 414–416, 1996. DOI: [10.1364/OL.21.000414](https://doi.org/10.1364/OL.21.000414).
- [154] R. Akbari and A. Major, “Optical, spectral and phase-matching properties of BIBO, BBO and LBO crystals for optical parametric oscillation in the visible and near-infrared wavelength ranges,” *Laser Physics*, vol. 23, no. 3, p. 035 401, 2013. DOI: [10.1088/1054-660x/23/3/035401](https://doi.org/10.1088/1054-660x/23/3/035401).
- [155] D. Eimerl, L. Davis, S. Velsko, E. K. Graham, and A. Zalkin, “Optical, mechanical, and thermal properties of barium borate,” *Journal of Applied Physics*, vol. 62, no. 5, pp. 1968–1983, 1987. DOI: [10.1063/1.339536](https://doi.org/10.1063/1.339536).
- [156] D. Zhang, Y. Kong, and J.-y. Zhang, “Optical parametric properties of 532-nm-pumped beta-barium-borate near the infrared absorption edge,” *Optics Communications*, vol. 184, no. 5, pp. 485–491, 2000. DOI: [https://doi.org/10.1016/S0030-4018\(00\)00968-8](https://doi.org/10.1016/S0030-4018(00)00968-8).
- [157] D. N. Nikogosyan, “Beta barium borate (BBO),” *Applied Physics A*, vol. 52, no. 6, pp. 359–368, 1991. DOI: [10.1007/BF00323647](https://doi.org/10.1007/BF00323647).
- [158] R. C. Eckardt, H. Masuda, Y. X. Fan, and R. L. Byer, “Absolute and relative nonlinear optical coefficients of KDP, KD\*P,  $BaB_2O_4$ ,  $LiIO_3$ ,  $MgO:LiNbO_3$ , and KTP measured by phase-matched second-harmonic generation,” *IEEE Journal of Quantum Electronics*, vol. 26, no. 5, pp. 922–933, 1990. DOI: [10.1109/3.55534](https://doi.org/10.1109/3.55534).
- [159] I. Shoji, H. Nakamura, K. Ohdaira, T. Kondo, R. Ito, T. Okamoto, K. Tatsuki, and S. Kubota, “Absolute measurement of second-order nonlinear-optical coefficients of beta-BaB2O4 for visible to ultraviolet second-harmonic wavelengths,” *J. Opt. Soc. Am. B*, vol. 16, no. 4, pp. 620–624, 1999. DOI: [10.1364/JOSAB.16.000620](https://doi.org/10.1364/JOSAB.16.000620).

- [160] F. Batysta, R. Antipenkov, J. Novák, J. T. Green, J. A. Naylor, J. Horáček, M. Horáček, Z. Hubka, R. Boge, T. Mazanec, B. Himmel, P. Bakule, and B. Rus, “Broadband OPCPA system with 11 mJ output at 1 kHz, compressible to 12 fs,” *Opt. Express*, vol. 24, no. 16, pp. 17 843–17 848, 2016. DOI: [10.1364/OE.24.017843](https://doi.org/10.1364/OE.24.017843).
- [161] N. Ishii, L. Turi, V. S. Yakovlev, T. Fuji, F. Krausz, A. Baltuška, R. Butkus, G. Veitas, V. Smilgevičius, R. Danielius, and A. Piskarskas, “Multimillijoule chirped parametric amplification of few-cycle pulses,” *Opt. Lett.*, vol. 30, no. 5, pp. 567–569, 2005. DOI: [10.1364/OL.30.000567](https://doi.org/10.1364/OL.30.000567).
- [162] V. G. Dmitriev, G. G. Gurzadyan, and D. N. Nikogosyan, *Handbook of Nonlinear Optical Crystals*. Springer-Verlag Berlin Heidelberg, 1999. DOI: [10.1007/978-3-540-46793-9](https://doi.org/10.1007/978-3-540-46793-9).
- [163] X. Cai, X. Lin, G. Li, J. Lu, Z. Hu, and G. Zheng, “Rapid growth and properties of large-aperture 98%-deuterated DKDP crystals,” *High Power Laser Science and Engineering*, vol. 7, e46, 2019. DOI: [10.1017/hpl.2019.24](https://doi.org/10.1017/hpl.2019.24).
- [164] V. Lozhkarev, G. I. Freidman, V. Ginzburg, E. Khazanov, O. Palashov, A. Sergeev, and I. Yakolev, “Study of Broadband Optical Parametric Chirped Pulse Amplification in a DKDP Crystal Pumped by the Second Harmonic of a Nd:YLF Laser,” *Laser Physics*, vol. 15, no. 9, pp. 1319–1333, 2005.
- [165] G. Ghosh and G. Bhar, “Temperature dispersion in ADP, KDP, and KD\*P for nonlinear devices,” *IEEE Journal of Quantum Electronics*, vol. 18, no. 2, pp. 143–145, 1982. DOI: [10.1109/JQE.1982.1071501](https://doi.org/10.1109/JQE.1982.1071501).
- [166] K. Kato, “Temperature-tuned 90° phase-matching properties of LiB3O5,” *IEEE Journal of Quantum Electronics*, vol. 30, no. 12, pp. 2950–2952, 1994. DOI: [10.1109/3.362711](https://doi.org/10.1109/3.362711).
- [167] D. A. Roberts, “Simplified characterization of uniaxial and biaxial nonlinear optical crystals: a plea for standardization of nomenclature and conventions,” *IEEE Journal of Quantum Electronics*, vol. 28, no. 10, pp. 2057–2074, 1992. DOI: [10.1109/3.159516](https://doi.org/10.1109/3.159516).
- [168] G. Hansson, H. Karlsson, S. Wang, and F. Laurell, “Transmission measurements in KTP and isomorphic compounds,” *Appl. Opt.*, vol. 39, no. 27, pp. 5058–5069, 2000. DOI: [10.1364/AO.39.005058](https://doi.org/10.1364/AO.39.005058).
- [169] K. Kato and N. Umemura, “Sellmeier and Thermo-Optic Dispersion Formulas for KTiOAsO4,” in *Conference on Lasers and Electro-Optics/ International Quantum Electronics Conference and Photonic Applications Systems Technologies*, 2004, CThT35.
- [170] M. V. Pack, D. J. Armstrong, and A. V. Smith, “Measurement of the  $\chi^{(2)}$  tensors of KTiOPO4, KTiOAsO4, RbTiOPO4, and RbTiOAsO4 crystals,” *Appl. Opt.*, vol. 43, no. 16, pp. 3319–3323, 2004. DOI: [10.1364/AO.43.003319](https://doi.org/10.1364/AO.43.003319).

- [171] G. Andriukaitis, T. Balčiūnas, S. Ališauskas, A. Pugžlys, A. Baltuška, T. Popmintchev, M.-C. Chen, M. M. Murnane, and H. C. Kapteyn, “90 GW peak power few-cycle mid-infrared pulses from an optical parametric amplifier,” *Opt. Lett.*, vol. 36, no. 15, pp. 2755–2757, 2011. DOI: [10.1364/OL.36.002755](https://doi.org/10.1364/OL.36.002755).
- [172] F. Lu, P. Xia, Y. Matsumoto, T. Kanai, N. Ishii, and J. Itatani, “Generation of sub-two-cycle CEP-stable optical pulses at 3.5  $\mu\text{m}$  from a KTA-based optical parametric amplifier with multiple-plate compression,” *Opt. Lett.*, vol. 43, no. 11, pp. 2720–2723, 2018. DOI: [10.1364/OL.43.002720](https://doi.org/10.1364/OL.43.002720).
- [173] Z. Heiner, V. Petrov, G. Steinmeyer, M. J. J. Vrakking, and M. Mero, “100-kHz, dual-beam OPA delivering high-quality, 5-cycle angular-dispersion-compensated mid-infrared idler pulses at 3.1  $\mu\text{m}$ ,” *Opt. Express*, vol. 26, no. 20, pp. 25 793–25 804, 2018. DOI: [10.1364/OE.26.025793](https://doi.org/10.1364/OE.26.025793).
- [174] M. Mero, Z. Heiner, V. Petrov, H. Rottke, F. Branchi, G. M. Thomas, and M. J. J. Vrakking, “43 W, 1.55  $\mu\text{m}$  and 12.5 W, 3.1  $\mu\text{m}$  dual-beam, sub-10 cycle, 100 kHz optical parametric chirped pulse amplifier,” *Opt. Lett.*, vol. 43, no. 21, pp. 5246–5249, 2018. DOI: [10.1364/OL.43.005246](https://doi.org/10.1364/OL.43.005246).
- [175] P. Mason, M. Divoký, K. Ertel, J. Pilař, T. Butcher, M. Hanuš, S. Banerjee, J. Phillips, J. Smith, M. D. Vido, A. Lucianetti, C. Hernandez-Gomez, C. Edwards, T. Mocek, and J. Collier, “Kilowatt average power 100 J-level diode pumped solid state laser,” *Optica*, vol. 4, no. 4, pp. 438–439, 2017. DOI: [10.1364/OPTICA.4.000438](https://doi.org/10.1364/OPTICA.4.000438).
- [176] A. Lucianetti, M. Sawicka, O. Slezak, M. Divoky, J. Pilar, V. Jambunathan, S. Bonora, R. Antipenkov, and T. Mocek, “Design of a kJ-class HiLASE laser as a driver for inertial fusion energy,” *High Power Laser Science and Engineering*, vol. 2, e13, 2014. DOI: [10.1017/hpl.2014.15](https://doi.org/10.1017/hpl.2014.15).
- [177] C. Skrobol, I. Ahmad, S. Klingebiel, C. Wandt, S. A. Trushin, Z. Major, F. Krausz, and S. Karsch, “Broadband amplification by picosecond OPCPA in DKDP pumped at 515 nm,” *Optics Express*, vol. 20, no. 4, pp. 4619–4629, 2012. DOI: [10.1364/OE.20.004619](https://doi.org/10.1364/OE.20.004619).
- [178] R. Budriūnas, T. Stanislauskas, and A. Varanavičius, “Passively CEP-separated frontend for few cycle terawatt OPCPA system,” *Journal of Optics*, vol. 17, no. 9, p. 094008, 2015. DOI: [10.1088/2040-8978/17/9/094008](https://doi.org/10.1088/2040-8978/17/9/094008).
- [179] V. Bagnoud and F. Wagner, “Ultra-high temporal contrast performance of the PHELIX petawatt facility,” *High Power Laser Science and Engineering*, vol. 4, e39, 2016. DOI: [10.1017/hpl.2016.38](https://doi.org/10.1017/hpl.2016.38).
- [180] F. Verluise, V. Laude, Z. Cheng, C. Spielmann, and P. Tournois, “Amplitude and phase control of ultrashort pulses by use of an acousto-optic programmable dispersive filter: Pulse compression and shaping,” *Opt. Lett.*, vol. 25, no. 8, pp. 575–577, 2000. DOI: [10.1364/OL.25.000575](https://doi.org/10.1364/OL.25.000575).
- [181] A. L. Oien, I. T. McKinnie, P. Jain, N. A. Russell, D. M. Warrington, and L. A. W. Gloster, “Efficient, low-threshold collinear and noncollinear beta-barium borate optical parametric oscillators,” *Opt. Lett.*, vol. 22, no. 12, pp. 859–861, 1997. DOI: [10.1364/OL.22.000859](https://doi.org/10.1364/OL.22.000859).

- [182] G. Arisholm, R. Paschotta, and T. Südmeyer, “Limits to the power scalability of high-gain optical parametric amplifiers,” *J. Opt. Soc. Am. B*, vol. 21, no. 3, pp. 578–590, 2004. DOI: [10.1364/JOSAB.21.000578](https://doi.org/10.1364/JOSAB.21.000578).
- [183] B. A. Reagan, A. H. Curtis, K. A. Wernsing, F. J. Furch, B. M. Luther, and J. J. Rocca, “Development of High Energy Diode-Pumped Thick-Disk Yb:YAG Chirped-Pulse-Amplification Lasers,” *IEEE Journal of Quantum Electronics*, vol. 48, no. 6, pp. 827–835, 2012.
- [184] S. Klingebiel, C. Wandt, C. Skrobol, I. Ahmad, S. A. Trushin, Z. Major, F. Krausz, and S. Karsch, “High energy picosecond Yb:YAG CPA system at 10 Hz repetition rate for pumping optical parametric amplifiers,” *Opt. Express*, vol. 19, no. 6, pp. 5357–5363, 2011. DOI: [10.1364/OE.19.005357](https://doi.org/10.1364/OE.19.005357).
- [185] T. Nubbemeyer, M. Kaumanns, M. Ueffing, M. Gorjan, A. Alismail, H. Fattahi, J. Brons, O. Pronin, H. G. Barros, Z. Major, T. Metzger, D. Sutter, and F. Krausz, “1 kW, 200 mJ picosecond thin-disk laser system,” *Opt. Lett.*, vol. 42, no. 7, pp. 1381–1384, 2017. DOI: [10.1364/OL.42.001381](https://doi.org/10.1364/OL.42.001381).
- [186] M. Schulz, R. Riedel, A. Willner, T. Mans, C. Schnitzler, P. Russbuedt, J. Dolkemeyer, E. Seise, T. Gottschall, S. Hädrich, S. Duesterer, H. Schlarb, J. Feldhaus, J. Limpert, B. Faatz, A. Tünnermann, J. Rossbach, M. Drescher, and F. Tavella, “Yb:YAG Innoslab amplifier: efficient high repetition rate subpicosecond pumping system for optical parametric chirped pulse amplification,” *Opt. Lett.*, vol. 36, no. 13, pp. 2456–2458, 2011. DOI: [10.1364/OL.36.002456](https://doi.org/10.1364/OL.36.002456).
- [187] I. Gražulevičiūtė, M. Skeivytė, E. Keblytė, J. Galinis, G. Tamošauskas, and A. Dubietis, “Supercontinuum generation in yag and sapphire with picosecond laser pulses,” *Lithuanian Journal of Physics*, vol. 55, no. 2, pp. 110–116, 2015. DOI: [10.3952/physics.v55i2.3101](https://doi.org/10.3952/physics.v55i2.3101).
- [188] M. F. Saleh and F. Biancalana, “Tunable frequency-up/down conversion in gas-filled hollow-core photonic crystal fibers,” *Opt. Lett.*, vol. 40, no. 18, pp. 4218–4221, 2015. DOI: [10.1364/OL.40.004218](https://doi.org/10.1364/OL.40.004218).
- [189] E. E. Serebryannikov, A. M. Zheltikov, N. Ishii, C. Y. Teisset, S. Köhler, T. Fuji, T. Metzger, F. Krausz, and A. Baltuška, “Soliton self-frequency shift of 6-fs pulses in photonic-crystal fibers,” *Applied Physics B*, vol. 81, pp. 585–588, 5 2005. DOI: [10.1007/s00340-005-1929-8](https://doi.org/10.1007/s00340-005-1929-8).
- [190] B. W. Mayer, C. R. Phillips, L. Gallmann, M. M. Fejer, and U. Keller, “Sub-four-cycle laser pulses directly from a high-repetition-rate optical parametric chirped-pulse amplifier at 3.4  $\mu\text{m}$ ,” *Opt. Lett.*, vol. 38, no. 21, pp. 4265–4268, 2013. DOI: [10.1364/OL.38.004265](https://doi.org/10.1364/OL.38.004265).
- [191] B. W. Mayer, C. R. Phillips, L. Gallmann, and U. Keller, “Mid-infrared pulse generation via achromatic quasi-phase-matched OPCPA,” *Opt. Express*, vol. 22, no. 17, pp. 20 798–20 808, 2014. DOI: [10.1364/OE.22.020798](https://doi.org/10.1364/OE.22.020798).
- [192] P. Rigaud, A. V. de Walle, M. Hanna, N. Forget, F. Guichard, Y. Zaouter, K. Guesmi, F. Druon, and P. Georges, “Supercontinuum-seeded few-cycle mid-infrared OPCPA system,” *Opt. Express*, vol. 24, no. 23, pp. 26 494–26 502, 2016. DOI: [10.1364/OE.24.026494](https://doi.org/10.1364/OE.24.026494).

- [193] Y. Chen, Y. Li, W. Li, X. Guo, and Y. Leng, “Generation of high beam quality, high-energy and broadband tunable mid-infrared pulse from a KTA optical parametric amplifier,” *Optics Communications*, vol. 365, pp. 7–13, 2016. DOI: <https://doi.org/10.1016/j.optcom.2015.12.001>.
- [194] L. von Grafenstein, M. Bock, D. Ueberschaer, K. Zawilski, P. Schunemann, U. Griebner, and T. Elsaesser, “5  $\mu\text{m}$  few-cycle pulses with multi-gigawatt peak power at a 1 kHz repetition rate,” *Opt. Lett.*, vol. 42, no. 19, pp. 3796–3799, 2017. DOI: [10.1364/OL.42.003796](https://doi.org/10.1364/OL.42.003796).
- [195] H. He, Z. Wang, C. Hu, J. Jiang, S. Qin, P. He, N. Zhang, P. Yang, Z. Li, and Z. Wei, “520- $\mu\text{J}$  mid-infrared femtosecond laser at 2.8  $\mu\text{m}$  by 1-kHz KTA optical parametric amplifier,” *Applied Physics B*, vol. 124, p. 31, 2 2018. DOI: [10.1007/s00340-018-6896-y](https://doi.org/10.1007/s00340-018-6896-y).
- [196] T. Feng, A. Heilmann, M. Bock, L. Ehrentraut, T. Witting, H. Yu, H. Stiel, S. Eisebitt, and M. Schnürer, “27 W 2.1  $\mu\text{m}$  OPCPA system for coherent soft X-ray generation operating at 10 kHz,” *Opt. Express*, vol. 28, no. 6, pp. 8724–8733, 2020. DOI: [10.1364/OE.386588](https://doi.org/10.1364/OE.386588).
- [197] H. Pires, M. Baudisch, D. Sanchez, M. Hemmer, and J. Biegert, “Ultrashort pulse generation in the mid-IR,” *Progress in Quantum Electronics*, vol. 43, pp. 1–30, 2015. DOI: <https://doi.org/10.1016/j.pquantelec.2015.07.001>.
- [198] O. Chalus, A. Thai, P. K. Bates, and J. Biegert, “Six-cycle mid-infrared source with 3.8  $\mu\text{J}$  at 100 kHz,” *Opt. Lett.*, vol. 35, no. 19, pp. 3204–3206, 2010. DOI: [10.1364/OL.35.003204](https://doi.org/10.1364/OL.35.003204).
- [199] F. Silva, P. K. Bates, A. Esteban-Martin, M. Ebrahim-Zadeh, and J. Biegert, “High-average-power, carrier-envelope phase-stable, few-cycle pulses at 2.1  $\mu\text{m}$  from a collinear  $\text{BiB}_3\text{O}_6$  optical parametric amplifier,” *Opt. Lett.*, vol. 37, no. 5, pp. 933–935, 2012. DOI: [10.1364/OL.37.000933](https://doi.org/10.1364/OL.37.000933).
- [200] M. Baudisch, H. Pires, H. Ishizuki, T. Taira, M. Hemmer, and J. Biegert, “Sub-4-optical-cycle, 340 MW peak power, high stability mid-IR source at 160 kHz,” *Journal of Optics*, vol. 17, no. 9, p. 094 002, 2015. DOI: [10.1088/2040-8978/17/9/094002](https://doi.org/10.1088/2040-8978/17/9/094002).
- [201] Y. Shamir, J. Rothhardt, S. Hädrich, S. Demmler, M. Tschernajew, J. Limpert, and A. Tünnermann, “High-average-power 2  $\mu\text{m}$  few-cycle optical parametric chirped pulse amplifier at 100 kHz repetition rate,” *Opt. Lett.*, vol. 40, no. 23, pp. 5546–5549, 2015. DOI: [10.1364/OL.40.005546](https://doi.org/10.1364/OL.40.005546).
- [202] N. Bigler, J. Pupeikis, S. Hrisafov, L. Gallmann, C. R. Phillips, and U. Keller, “High-power OPCPA generating 1.7 cycle pulses at 2.5  $\mu\text{m}$ ,” *Opt. Express*, vol. 26, no. 20, pp. 26 750–26 757, 2018. DOI: [10.1364/OE.26.026750](https://doi.org/10.1364/OE.26.026750).
- [203] Y. Oishi, M. Kaku, A. Suda, F. Kannari, and K. Midorikawa, “Generation of extreme ultraviolet continuum radiation driven by a sub-10-fs two-color field,” *Opt. Express*, vol. 14, no. 16, pp. 7230–7237, 2006. DOI: [10.1364/OE.14.007230](https://doi.org/10.1364/OE.14.007230).

- [204] M. Baudisch, M. Hemmer, H. Pires, and J. Biegert, “Performance of MgO:-PPLN, KTA, and KNbO<sub>3</sub> for mid-wave infrared broadband parametric amplification at high average power,” *Opt. Lett.*, vol. 39, no. 20, pp. 5802–5805, 2014. DOI: [10.1364/OL.39.005802](https://doi.org/10.1364/OL.39.005802).
- [205] V. Petrov, F. Noack, and R. Stolzenberger, “Seeded femtosecond optical parametric amplification in the mid-infrared spectral region above 3  $\mu\text{m}$ ,” *Appl. Opt.*, vol. 36, no. 6, pp. 1164–1172, 1997. DOI: [10.1364/AO.36.001164](https://doi.org/10.1364/AO.36.001164).

# Own publications related to the thesis

- [T1] H. Cao, S. Toth, M. Kalashnikov, V. Chvykov, and K. Osvay, “Highly efficient, cascaded extraction optical parametric amplifier,” *Optics Express*, vol. 26, no. 6, pp. 7516–7527, 2018. DOI: [10.1364/OE.26.007516](https://doi.org/10.1364/OE.26.007516).
- [T2] S. Toth, T. Stanislaukas, I. Balciunas, R. Budriunas, J. Adamonis, R. Danilevicius, K. Viskontas, D. Lengvinas, G. Veitas, D. Gadonas, A. Varanavicius, J. Csontos, T. Somoskoi, L. Toth, A. Borzsonyi, and K. Osvay, “SYLOS lasers - the frontier of few-cycle, multi-TW, kHz lasers for ultrafast applications at extreme light infrastructure attosecond light pulse source,” *Journal of Physics: Photonics*, vol. 2, no. 4, p. 045003, 2020. DOI: [10.1088/2515-7647/ab9fe1](https://doi.org/10.1088/2515-7647/ab9fe1).
- [T3] S. Toth, R. Flender, B. Kiss, M. Kurucz, A. Andrianov, L. Haizer, E. Cormier, and K. Osvay, “Comparative study of an ultrafast, CEP-stable, dual-channel mid-IR OPCPA system,” *Journal of the Optical Society of America B*, vol. 36, no. 12, pp. 3538–3546, 2019. DOI: [10.1364/JOSAB.36.003538](https://doi.org/10.1364/JOSAB.36.003538).

## Other own publications

- [O1] M. Kurucz, R. Flender, L. Haizer, R. S. Nagymihaly, W. Cho, K. T. Kim, S. Toth, E. Cormier, and B. Kiss, “2.3-cycle mid-infrared pulses from hybrid thin-plate post-compression at 7 W average power,” *Optics Communications*, vol. 472, p. 126 035, 2020, ISSN: 0030-4018. DOI: <https://doi.org/10.1016/j.optcom.2020.126035>.
- [O2] M. Kurucz, S. Tóth, R. Flender, L. Haizer, B. Kiss, B. Persielle, and E. Cormier, “Single-shot CEP drift measurement at arbitrary repetition rate based on dispersive Fourier transform,” *Opt. Express*, vol. 27, no. 9, pp. 13 387–13 399, 2019. DOI: [10.1364/OE.27.013387](https://doi.org/10.1364/OE.27.013387).
- [O3] C. Medina, D. Schomas, N. Rendler, M. Debatin, D. Uhl, A. Ngai, L. B. Ltaief, M. Dumergue, Z. Filus, B. Farkas, R. Flender, L. Haizer, B. Kiss, M. Kurucz, B. Major, S. Toth, F. Stienkemeier, R. Moshhammer, T. Pfeifer, S. R. Krishnan, A. Heidenreich, and M. Mudrich, “Single-shot electron imaging of dopant-induced nanoplasmas,” *New Journal of Physics*, vol. 23, no. 5, p. 053 011, 2021. DOI: [10.1088/1367-2630/abf7f9](https://doi.org/10.1088/1367-2630/abf7f9).

## Conference presentations (Oral)

- [CO1] T. Stanislauskas, I. Balciunas, R. Budriunas, G. Veitas, D. Gadonas, J. Adamonis, A. Michailovas, A. Borzsonyi, **Sz. Toth**, J. Csontos, and K. Osvay, “Chirped pulse parametric amplifier producing 5-tw, 2.1-cycle, CEP stable pulses at 1 kHz repetition rate,” Optical Society of America, 2019, cg\_p-16. DOI: [10.1364/CLEO\\_EUROPE.2019.cg\\_p\16](https://doi.org/10.1364/CLEO_EUROPE.2019.cg_p\16).
- [CO2] K. Osvay, A. Börzsönyi, H. Cao, E. Cormier, J. Csontos, P. Jójárt, M. Kalashnikov, B. Kiss, R. Lopez-Martens, **Sz. Toth**, and Z. Varallyay, “Development status and operation experiences of the few cycle high average power lasers of ELI-ALPS (Conference Presentation),” in *Short-pulse High-energy Lasers and Ultrafast Optical Technologies*, International Society for Optics and Photonics, vol. 11034, SPIE, 2019. DOI: [10.1117/12.2523057](https://doi.org/10.1117/12.2523057).
- [CO3] **Sz. Toth\***, R. Nagymihaly, A. Andrianov, B. Kiss, R. Flender, M. Kurucz, L. Haizer, E. Cormier, and K. Osvay, “Conceptual study of a 1 kHz 10 mJ-class mid-IR OPCPA system with thermal aspects,” in *Ultrafast Optics 2019*, International Society for Optics and Photonics, vol. 11370, SPIE, 2019, pp. 77–80. DOI: [10.1117/12.2562972](https://doi.org/10.1117/12.2562972).
- [CO4] **Sz. Toth\***, T. Stanislauskas, I. Balciunas, A. Andrianov, R. Budriunas, G. Veitas, J. Csontos, A. Borzsonyi, L. Toth, T. Somoskoi, and K. Osvay, “Design study of two-cycle bandwidth, single-color pumped OPCPA chain,” in *Ultrafast Optics 2019*, International Society for Optics and Photonics, vol. 11370, SPIE, 2019, pp. 81–83. DOI: [10.1117/12.2562972](https://doi.org/10.1117/12.2562972).
- [CO5] T. Stanislauskas, I. Balciunas, J. Adamonis, R. Budriunas, G. Veitas, D. Lengvinas, D. Gadonas, **Sz. Toth\***, J. Csontos, A. Borzsonyi, L. Toth, T. Somoskoi, and K. Osvay, “Performance test results of ELI-ALPS SYLOS lasers,” in *Ultrafast Optics 2019*, International Society for Optics and Photonics, vol. 11370, SPIE, 2019, pp. 177–180. DOI: [10.1117/12.2562972](https://doi.org/10.1117/12.2562972).
- [CO6] T. Stanislauskas, I. Balciunas, R. Budriunas, J. Adamonis, **Sz. Toth**, A. Borzsonyi, K. Osvay, A. Michailovas, G. Veitas, and D. Gadonas, “Towards Sub-2 cycle, Several-TW, 1kHz OPCPA System Based on Yb:KGW and Nd:YAG Lasers,” Optical Society of America, 2018, STu40.1. DOI: [10.1364/CLEO\\_SI.2018.STu40.1](https://doi.org/10.1364/CLEO_SI.2018.STu40.1).
- [CO7] T. Stanislauskas, R. Budriūnas, G. Veitas, D. Gadonas, J. Adamonis, A. Aleknavičius, G. Masian, Z. Kuprionis, D. Hoff, G. G. Paulus, A. Borzsonyi, **Sz. Toth**, M. Kovacs, J. Csontos, R. López-Martens, and K. Osvay, “Performance tests of the 5 TW, 1 kHz, passively CEP-stabilized ELI-ALPS SYLOS few-cycle laser system (Conference Presentation),” in *High-Power, High-Energy, and High-Intensity Laser Technology III*, International So-

ciety for Optics and Photonics, vol. 10238, SPIE, 2017, pp. 87–87. DOI:  
[10.1117/12.2265775](https://doi.org/10.1117/12.2265775).

\* - presenting author

## Conference presentations (Poster)

- [CP1] **Sz. Toth\***, T. Stanislauskas, I. Balciunas, R. Budriunas, G. Veitas, D. Gadonas, J. Csontos, A. Borzsonyi, T. Somoskoi, L. Toth, and K. Osvay, “Numerical investigation of broadband opcpa configurations for direct amplification of tw-level, two-cycle pulses,” in *2019 Conference on Lasers and Electro-Optics Europe and European Quantum Electronics Conference*, Optical Society of America, 2019, cf\_p\_31.
- [CP2] **Sz. Toth\***, R. S. Nagymihaly, R. Flender, B. Kiss, M. Kurucz, L. Haizer, E. Cormier, and K. Osvay, “Design of a 10 khz, mj-level mid-ir opcpa system,” in *2019 Conference on Lasers and Electro-Optics Europe and European Quantum Electronics Conference*, Optical Society of America, 2019, cf\_p\_34.
- [CP3] M. Kurucz, **Sz. Toth\***, R. Flender, L. Haizer, B. Kiss, B. Perseille, and E. Cormier, “High-accuracy single-shot CEP noise measurement at arbitrary repetition rate,” in *Ultrafast Optics 2019*, International Society for Optics and Photonics, vol. 11370, SPIE, 2019, pp. 293–295. DOI: [10.1117/12.2562972](https://doi.org/10.1117/12.2562972).
- [CP4] R. Flender, M. Kurucz, L. Haizer, R. Nagymihaly, **Sz. Toth**, A. Borzsonyi, E. Cormier, and B. Kiss, “Two-cycle pulses in the mid-IR based on hybrid thin plate compression at high average power,” in *Ultrafast Optics 2019*, International Society for Optics and Photonics, vol. 11370, SPIE, 2019, pp. 293–295. DOI: [10.1117/12.2562972](https://doi.org/10.1117/12.2562972).
- [CP5] **Sz. Toth\***, H. Cao, M. Kalashnikov, V. Chvykov, and K. Osvay, “Cascaded extraction opcpa – a highly efficient power amplifier design,” Optical Society of America, 2018, JT5A.20. DOI: [10.1364/EUVXRAY.2018.JT5A.20](https://doi.org/10.1364/EUVXRAY.2018.JT5A.20).
- [CP6] A. Borzsonyi, A. Aleknavicius, D. Gadonas, D. Hoff, G. Veitas, G. G. Paulus, G. Masian, J. Adamonis, J. Csontos, K. Osvay, M. Kovacs, R. Budriunas, R. Lopez-Martens, **Sz. Toth**, T. Stanislauskas, and Z. Kuprionis, “Performance evaluation during the trial operation period of the 5 TW, 1 kHz few-cycle SYLOS laser system of ELI-ALPS,” in *ICEL 2017 - International Conference on Extreme Light*, 2017.
- [CP7] **Sz. Toth\***, H. Cao, M. Kalashnikov, V. Chvykov, and K. Osvay, “Highly efficient, chirped pulse amplification in a cascaded extraction optical parametric amplifier design,” in *ICEL 2017 - International Conference on Extreme Light*, 2017.

- [CP8] **Sz. Toth\***, M. Kovács, T. Stanislauskas, R. Budriunas, J. Adamonis, A. Aleknavicius, Á. Börzsönyi, J. Csontos, G. Shayeganrad, G. Veitas, R. Lopez-Martens, and K. Osvay, “Simulation of Optical Parametris Amplifier Stages of ELI-ALPS SYLOS Laser,” in *ICEL 2017 - International Conference on Extreme Light*, 2017.
- [CP9] A. Andrásik, **Sz. Toth**, R. S. Nagymihály, P. Jójárt, R. Flender, Á. Börzsönyi, and K. Osvay, “Development of few cycle Ti:Sapphire and NOPA amplifiers at 80MHz repetition rate,” in *SPIE Optics + Optoelectronics*, 2017.
- [CP10] A. Andrásik, P. Jójárt, **Sz. Toth**, R. S. Nagymihály, Á. Börzsönyi, and K. Osvay, “10 W multipass Ti:S amplifier for 80 MHz repetition rate,” in *7th EPS-QEOD Europhoton Conference*, 2017, PO–1.29.
- [CP11] **Sz. Toth\***, R. S. Nagymihály, R. Flender, P. Jojart, A. Andrásik, A. Börzsönyi, and K. Osvay, “Development of an 80 MHz Repetition Rate tuneable amplifier system for In-Vivo Deep Brain Imaging Microscopy,” in *7th International Conference on Ultrahigh Intensity Lasers*, 2016.
- [CP12] **Sz. Toth\***, R. Flender, R. S. Nagymihály, P. Jojart, A. Andrásik, A. Börzsönyi, and K. Osvay, “Modelling and Development of an 80 MHz Repetition Rate tuneable OPCPA system for In-Vivo Deep Brain Imaging Microscopy,” in *7th EPS-QEOD EUROPHOTON CONFERENCE*, 2016.
- [CP13] A. Andrasik, P. Jojart, **Sz. Toth**, R. S. Nagymiahly, A. Borzsonyi, and K. Osvay, “10 W-os többpasszos Ti:S erősítő 80 MHz-es ismétlődési frekvencián,” in *Magyar Fizikus Vándorgyűlés*, 2016.
- [CP14] **Sz. Toth\***, R. S. Nagymihaly, P. Jojart, R. Flender, A. Andrasik, A. Borzsonyi, and K. Osvay, “80 MHz ismétlési frekvencián működő optikai parametrikus erősítő fejlesztése,” in *Magyar Fizikus Vándorgyűlés*, 2016.

\* - presenting author

# Hungarian science publications

- [S1] Á. Börzsönyi, R. Nagymihály, S. Tóth, and K. Osvay, “A csörpölt (lézer)impulzus-erősítés,” *Fizikai szemle*, vol. 12, pp. 403–407, 2018.

# Appendix A

## Undepleted pump approximation

The differential equations describing TWM (Eq. 2.69) can have a very simple and interpretable solution in case of OPA/DFG if the amplitude of the pump wave is considered to be constant ( $A_3(z) = A_3(0)$ ) during interaction. This is called the undepleted pump approximation and Eqs. 2.69 are reducing to Eqs. A.1 and A.2, where the constants  $K_1$  and  $K_2$  are defined in Eq. A.3 [84].

$$\frac{dA_1}{dz} = K_1 A_2^* e^{i\Delta kz} \quad (\text{A.1})$$

$$\frac{dA_2}{dz} = K_2 A_1^* e^{i\Delta kz} \quad (\text{A.2})$$

$$K_1 = \frac{i2\omega_1^2 d_{eff}}{c^2 k_1} A_3(0) \quad K_2 = \frac{i2\omega_2^2 d_{eff}}{c^2 k_2} A_3(0) \quad K^2 = K_2 K_1^* = \frac{8\pi^2 d_{eff}^2 I_p}{\epsilon_0 c n_1 n_2 n_3 \lambda_1 \lambda_2} \quad (\text{A.3})$$

Equations A.1 and A.2 can be decoupled by taking the derivative of A.2 and introducing A.1 into the resulting equation, which yields Eq. A.4.

$$\frac{d^2 A_2}{dz^2} = K^2 A_2 - i\Delta k \frac{dA_2}{dz} \quad (\text{A.4})$$

By introducing variables  $x_1 = A_2$  and  $x_2 = \dot{A}_2$ , where the dot indicates the derivative according to  $z$ , Eq. A.4, which is a second order differential equation, can be decoupled into two first order one as it is done in Eq. A.5.

$$\dot{\vec{x}} = \begin{pmatrix} \dot{x}_1 \\ \dot{x}_2 \end{pmatrix} = \begin{pmatrix} 0 & 1 \\ K^2 & -i\Delta k \end{pmatrix} \begin{pmatrix} x_1 \\ x_2 \end{pmatrix} = \mathbf{A} \vec{x} \quad (\text{A.5})$$

Eq. A.5 is a linear first order differential equation which has a solution in the form of  $\vec{x}(z) = \vec{x}_0 e^{\mathbf{A}z}$ . The matrix of  $e^{\mathbf{A}z}$  can be determined by using the Cayley-Hamilton theorem. For this one needs to find the eigenvalues of the  $\mathbf{A}$  matrix which are indicated in Eq. A.6, where the constant  $g$  is defined by Eq. A.7.

$$\lambda_{1,2} = -i\frac{\Delta k}{2} \pm g \quad (\text{A.6})$$

$$g = \sqrt{K^2 - \frac{\Delta k^2}{4}} \quad (\text{A.7})$$

Using the eigenvalues (Eq. A.6) and Cayley-Hamilton theorem the matrix of  $e^{\mathbf{A}z}$  is given by Eq. A.8 and from the initial conditions  $\vec{x}_0 = [A_{20}, 0]$ .

$$e^{\mathbf{A}z} = \begin{pmatrix} e^{\lambda_1 z} - \frac{\lambda_1}{2g} (e^{\lambda_1 z} - e^{\lambda_2 z}) & \frac{e^{\lambda_1 z} - e^{\lambda_2 z}}{2g} \\ K^2 \frac{e^{\lambda_1 z} - e^{\lambda_2 z}}{2g} & e^{\lambda_1 z} - (e^{\lambda_1 z} - e^{\lambda_2 z}) \left( \frac{\lambda_1 + i\Delta k}{2g} \right) \end{pmatrix} \quad (\text{A.8})$$

Repeating the same procedure also for the idler amplitude ( $A_1$ ), the evolution of the idler and signal waves can be obtained according to Eqs. A.9 and A.10.

$$A_1(z) = i \frac{4\pi d_{eff}}{\lambda_1 n_1} \frac{\sinh gz}{g} A_{30} A_{20}^* e^{-i \frac{\Delta k z}{2}} \quad (\text{A.9})$$

$$A_2(z) = \left[ \cosh gz + i \frac{\Delta k}{2g} \sinh gz \right] A_{20} e^{-i \frac{\Delta k z}{2}} \quad (\text{A.10})$$

In practice it is more convenient to use equations which are formulating the intensity and phase evolution separately. The intensity evolution can be obtained by inserting Eqs. A.9 and A.10 into Eq. 2.6, which yields Eqs. A.11 and A.12.

$$I_1(z) = I_{20} \frac{\lambda_2 K^2}{\lambda_1 g^2} \sinh^2 gz \quad (\text{A.11})$$

$$I_2(z) = I_{20} + I_{20} \frac{K^2}{g^2} \sinh^2 gz \quad (\text{A.12})$$

The phase evolution can be simply obtained by extracting the argument of Eqs. A.9 and A.10 which yields Eqs. A.13 and A.14, describing the phase of the idler and signal waves respectively [83].

$$\phi_1(z) = \frac{\pi}{2} + \phi_{30} - \phi_{20} - \frac{\Delta k z}{2} \quad (\text{A.13})$$

$$\phi_2(z) = \phi_{20} - \frac{\Delta k z}{2} + \arctan \left( \frac{\Delta k}{2g} \tanh gz \right) \quad (\text{A.14})$$

From the equations which are describing the intensity evolution it is practical to express the intensity gain according to Eqs. A.15 and A.16 [84, 85].

$$G_i = \frac{I_1(z)}{I_{20}} = \frac{\lambda_2}{\lambda_1} (G_s - 1) \quad (\text{A.15})$$

$$G_s = \frac{I_2(z)}{I_{20}} = 1 + \frac{K^2}{g^2} \sinh^2 gz \quad (\text{A.16})$$

According to Eq. 2.1, a wave packet can be considered as the superposition of monochromatic waves. Therefore, by applying Eqs. A.15 and A.16 for each monochromatic component of a broadband pulse, a frequency dependent gain distribution can be obtained. These are called spectral gain curves [84, 85]. The spectral gain curves are particularly useful for the gain bandwidth optimization during the development of few-cycle OPCPA systems.

# Appendix B

## Analytical solution of TWM

$$A_j = A_0 \frac{v_j e^{i\phi_j}}{\sqrt{n_j \lambda_j}} \quad \xi = \frac{z}{L} \quad \sigma = \Delta k L \quad (\text{B.1})$$

By introducing the dimensionless field amplitude  $v_j$ , propagation coordinate  $\xi$  and wave vector mismatch  $\sigma$  defined by Eq. B.1, where  $A_0$  is an arbitrary normalization constant having the same dimension as  $A_j$ , and  $L$  is the length of the nonlinear material, the equations describing the evolution of the field and phase can be separated according to Eq. B.2. The constant  $K$  and the function  $\theta$  are defined in Eqs. B.3 [5, 81].

$$\begin{aligned} \frac{\partial v_1}{\partial \xi} &= -K v_2 v_3 \sin \theta & v_1 \frac{\partial \phi_1}{\partial \xi} &= K v_2 v_3 \cos \theta \\ \frac{\partial v_2}{\partial \xi} &= -K v_1 v_3 \sin \theta & v_2 \frac{\partial \phi_2}{\partial \xi} &= K v_1 v_3 \cos \theta \\ \frac{\partial v_3}{\partial \xi} &= K v_1 v_2 \sin \theta & v_3 \frac{\partial \phi_3}{\partial \xi} &= K v_1 v_2 \cos \theta \end{aligned} \quad (\text{B.2})$$

$$K = \frac{4\pi d_{eff} A_0 L}{\sqrt{n_1 n_2 n_3 \lambda_1 \lambda_2 \lambda_3}} \quad \theta(\xi) = \sigma \xi + \phi_3 - \phi_2 - \phi_1 \quad (\text{B.3})$$

The equations describing the phase evolution can be combined into a single equation according to Eq. B.4 [5, 81].

$$\frac{\partial \theta}{\partial \xi} = \sigma + K \cos \theta \left[ \frac{v_1 v_2}{v_3} - \frac{v_3 v_1}{v_2} - \frac{v_3 v_2}{v_1} \right] \quad (\text{B.4})$$

The direction of the energy flow during TWM processes are governed by the phase function  $\theta(\xi)$ . It can be seen from the amplitude equations in Eq. B.2, that if  $0 < \theta < \pi$  then the amplitude of the two low frequency field ( $v_1$  and  $v_2$ ) decreases. This means that the energy from  $v_1$  and  $v_2$  fields flows into  $v_3$  field. If  $-\pi < \theta < 0$ , then the mixing process is reversed and the energy from the high frequency field flows into the two low frequency fields. Consequently, the direction of the energy flow during all second order nonlinear processes is periodic in the interaction length.

From the equations describing the amplitude evolution (Eq. B.2) one get Eqs. B.5 which are describing three quantities ( $m_1, m_2, m_3$ ) which are constant during

interaction [5, 81].

$$\begin{aligned}
 v_1 \frac{\partial v_1}{\partial \xi} - v_2 \frac{\partial v_2}{\partial \xi} &= \frac{1}{2} \frac{\partial}{\partial \xi} (v_1^2 - v_2^2) = \frac{1}{2} \frac{\partial}{\partial \xi} m_3 = 0 \\
 v_2 \frac{\partial v_2}{\partial \xi} + v_3 \frac{\partial v_3}{\partial \xi} &= \frac{1}{2} \frac{\partial}{\partial \xi} (v_2^2 + v_3^2) = \frac{1}{2} \frac{\partial}{\partial \xi} m_1 = 0 \\
 v_1 \frac{\partial v_1}{\partial \xi} + v_3 \frac{\partial v_3}{\partial \xi} &= \frac{1}{2} \frac{\partial}{\partial \xi} (v_1^2 + v_3^2) = \frac{1}{2} \frac{\partial}{\partial \xi} m_2 = 0
 \end{aligned} \tag{B.5}$$

The square of the field amplitude ( $v_j^2$ ) is proportional to the number of photons which are crossing a unite area plane per unit time ( $N$ ) according to Eq. B.6, where  $h$  is the Planck constant [5, 81].

$$v_j^2 = \frac{h}{2\epsilon_0 A_0^2} N_j \tag{B.6}$$

Therefore, Eq. B.5 can be expressed by the photon numbers according to Eqs. B.7. These are the Manley-Rowe relations which are expressing the conservation of photon numbers during TWM processes [5, 81].

$$\begin{aligned}
 \frac{\partial}{\partial \xi} (N_1 - N_2) &= 0 & \Leftrightarrow & \Delta N_1 = \Delta N_2 \\
 \frac{\partial}{\partial \xi} (N_2 + N_3) &= 0 & \Leftrightarrow & \Delta N_2 = -\Delta N_3 \\
 \frac{\partial}{\partial \xi} (N_1 + N_3) &= 0 & \Leftrightarrow & \Delta N_1 = -\Delta N_3
 \end{aligned} \tag{B.7}$$

According to Eq. B.7, the change rate of the two lower energy photons ( $\Delta N_1$  and  $\Delta N_2$ ) is equal and opposite to the change rate of the highest energy photon ( $\Delta N_3$ ) [5, 81].

By inserting the amplitude equations from Eq. B.2 into Eq. B.4 and by combining the resulting expression with the  $\partial_\xi v_3$  amplitude equation in Eq. B.2, one can get Eq. B.8 which introduces a new interaction constant  $\Gamma$  [5, 81].

$$\begin{aligned}
 \frac{\partial}{\partial \xi} \left( v_1 v_2 v_3 \cos \theta + \frac{\sigma}{2K} v_3^2 \right) &= 0 \\
 v_1 v_2 v_3 \cos \theta + \frac{\sigma}{2K} v_3^2 &= \Gamma
 \end{aligned} \tag{B.8}$$

Using the constants ( $m_1$ ,  $m_2$ ,  $m_3$  and  $\Gamma$ ) it is possible to decouple the amplitude equations in Eq. B.2 as it is done in Eq. B.9, where  $s_a < s_b < s_c$  are the roots of the expression under the square root [5, 81].

$$\begin{aligned}
 v_3 \frac{\partial v_3}{\partial \xi} &= K v_1 v_2 v_3 \sin \theta = \\
 &= K \sqrt{(v_1 v_2 v_3)^2 - (v_1 v_2 v_3 \cos \theta)^2} = \\
 &= K \sqrt{(m_2 - v_3^2)(m_1 - v_3^2)v_3^2 - \left( \Gamma - \frac{\sigma}{2K} v_3^2 \right)^2} = \\
 &= K \sqrt{(v_3^2 - s_a)(v_3^2 - s_b)(v_3^2 - s_c)}
 \end{aligned} \tag{B.9}$$

By introducing new variables defined in Eq. B.10, Eq. B.9 can be written in the form of Eq. B.11 [5, 81].

$$s = v_3^2 \quad y^2 = \frac{s - s_a}{s_b - s_a} \quad \gamma^2 = \frac{s_b - s_a}{s_c - s_a} \quad U = K\sqrt{s_c - s_a} \quad (\text{B.10})$$

$$\frac{\partial y}{\partial \xi} = U\sqrt{(1 - y^2)(1 - \gamma^2 y^2)} \quad (\text{B.11})$$

The differential equation in Eq. B.11 has analytical solution which can be expressed by the Jacobian elliptic functions ( $sn(u, \gamma^2)$ ,  $cn(u, \gamma^2)$  and  $dn(u, \gamma^2)$ ), according to Eq. B.12 [5, 81].

$$y(L) = \frac{y(0) cn(U, \gamma^2) dn(U, \gamma^2) + sn(U, \gamma^2) \sqrt{1 - y(0)^2} \sqrt{1 - \gamma^2 y(0)^2}}{1 - \gamma^2 y(0)^2 sn^2(U, \gamma^2)} \quad (\text{B.12})$$

Using Eq. B.12 and the Manley-Rowe relations (Eq. B.5) the solution for  $v_3^2$ ,  $v_2^2$  and  $v_1^2$  can be written according to Eqs. B.13 [5, 81].

$$\begin{aligned} v_3(L)^2 &= (s_b - s_a) y(L)^2 + s_a \\ v_2(L)^2 &= v_2(0)^2 + v_3(0)^2 - (s_b - s_a) y(L)^2 - s_a \\ v_1(L)^2 &= v_1(0)^2 + v_3(0)^2 - (s_b - s_a) y(L)^2 - s_a \end{aligned} \quad (\text{B.13})$$

Combining Eq. B.8 and the phase equations in Eqs. B.2 and by integrating according to  $\xi$ , yields Eq. B.14 which is the phase of the  $j$ -th wave after interaction length  $L$  [5, 83].

$$\phi_j(L) = \phi_j(0) + K \int_0^1 \frac{\Gamma - \frac{\sigma}{2K} v_3^2(\xi)}{v_j^2(\xi)} d\xi \quad (\text{B.14})$$

According to Eq. B.14, in the knowledge of the intensity evolution ( $v_3^2$ ,  $v_2^2$  and  $v_1^2$ ), the phase of each wave can be determined [5, 83].

The previously presented equations can be applied in case of OPA and DFG to provide analytical solutions for the intensity and phase evolution. The waves oscillating at frequencies  $\omega_3 > \omega_2 > \omega_1$  are called pump, signal and idler respectively. In case of both OPA and DFG the intensity of idler is zero at the entrance of the nonlinear material, thus  $v_1^2(0) = 0$ . The interaction constants ( $m_1$ ,  $m_2$ ,  $m_3$  and  $\Gamma$ ) and the roots ( $s_a$ ,  $s_b$ ,  $s_c$ ) in this case are given by Eqs. B.15, B.16 and B.17

$$m_1 = v_2^2(0) + v_3^2(0) \quad m_2 = v_3^2(0) \quad m_3 = -v_2^2(0) \quad \Gamma = \frac{\sigma}{2K} v_3^2(0) \quad (\text{B.15})$$

$$s_a = \frac{1}{2} \left( v_2^2(0) + v_3^2(0) + \frac{\sigma^2}{4K^2} - D \right) \quad s_b = v_3^2(0) \quad s_c = \frac{1}{2} \left( v_2^2(0) + v_3^2(0) + \frac{\sigma^2}{4K^2} + D \right) \quad (\text{B.16})$$

$$D = \sqrt{(v_2^2(0) + v_3^2(0))^2 + \frac{\sigma^2}{2K^2} (v_2^2(0) - v_3^2(0)) + \frac{\sigma^4}{16K^4}} \quad (\text{B.17})$$

The term containing the Jacobi elliptic functions reduces to Eq. B.18.

$$y(L) = \frac{cn(U, \gamma^2) dn(U, \gamma^2)}{1 - \gamma^2 sn^2(U, \gamma^2)} \quad (\text{B.18})$$

From the first line of Eqs. B.2, it can be deduced that due to the initially zero idler field ( $v_1^2(0) = 0$ ), the initial value of the phase function (Eq. B.3) has to be  $\theta(0) = -\frac{\pi}{2}$ . Using this fact, the initial phase of the idler pulse can be calculated from Eq. B.3 according to Eq. B.19.

$$\phi_1(0) = \frac{\pi}{2} + \phi_3(0) - \phi_2(0) \quad (\text{B.19})$$

The interpretation of this is that the initial phase of the idler pulse adjusts itself to maximize the initial signal gain [83]. From Eq. B.14 and by using the constant  $\Gamma$  from Eq. B.15 the phase of the three waves can be expressed according to Eq. B.20 [83].

$$\phi_j(L) = \phi_j(0) + \frac{\Delta k L}{2} \int_0^1 \frac{v_3^2(0) - v_3^2(\xi)}{v_j^2(\xi)} d\xi \quad (\text{B.20})$$

In case of the idler pulse ( $j = 1$ ) the integrand equals to 1, therefor the idler phase after interaction is described by Eq. B.21.

$$\phi_1(L) = \frac{\pi}{2} + \phi_3(0) - \phi_2(0) + \frac{\Delta k L}{2} \quad (\text{B.21})$$

# Acknowledgements

First of all, I would like to thank my wife for her patience and support in the past year while quite substantial portion of my free time was spent on this work. I would also like to thank the support of my parents and that they have always encouraged me in many areas of life.

I owe many thanks to my supervisor, Dr. Károly Osvay for all the great research opportunities since my BSc studies. Furthermore, I am very grateful for all my colleagues, who helped me in my work. I could fill a few more pages with their names, therefore I will only name a few, whose contribution was essential during the past few years.

I would like to thank Dr. Alexey Andrianov for the OPCPA code, which was the "tool" during my research and Dr. Áron Szabó, who introduced me to the field of numerical simulations.

I would like to thank Dr. Huabao Cao for involving me in his idea which resulted in my first scientific paper.

I am very grateful for all the Lithuanian colleagues, especially for Dr. Tomas Stanislauskas for involving me into the development of the OPCPAs of SYLOS system.

I owe many thanks for the SYLOS laser team in ELI-ALPS, namely Dr. Ádám Börzsönyi, Dr. János Csontos, Tamás Somoskői and László Tóth for their help and flexibility during the distribution of the tremendous amount of tasks we had to deal with during the last year.

Finally, I would like to thank Roland Flender, Dr. Roland Nagymihály and Dr. Bálint Kiss for the useful scientific discussions and great ideas during my work.

The ELI-ALPS project (GINOP-2.3.6-15-2015-00001) is supported by the European Union and co-financed by the European Regional Development Fund.